ABSTRACT

SNYDER, MICHELLE GRACE. Characterization of Aerosols Using Multiwavelength Multistatic Optical Scattering Data. (Under the direction of C. Russell Philbrick and Hans Hallen.)

The study of aerosols and their effect on climate have direct application to global warming and cloud formation. The technique and instrumentation presented here aims to determine aerosol characteristics, including index of refraction, size distribution and number concentration.

Research is conducted using the multistatic multiwavelength optical scattering in conjunction with the polarization ratio method to extract aerosol characteristics. Scattering intensity is measured by a charge-coupled device imager with a field of view along the profile of co-aligned laser beams capturing scattering angles from 120 to 175 degrees. The scattered wavelengths are then separated by a diffraction grating when imaged. The polarization ratio of measured intensities is compared to theoretical Lorentz-Mie scattering calculations by an inversion process to obtain aerosol characteristics.

A rigorous analysis of the polarization ratio technique is presented as it can be applied to single mode, biomodal and trimodal distributions of aerosols. The effectiveness of this method is explored through calculations of squared error for simulated distributions both with and without noise to determine the applicability of the polarization ratio technique. This analysis includes in-depth studies into each of the five parameters that affect the polarization ratio: the mean radius, the standard width, the concentration, the real index of refraction and the imaginary index of refraction. Additionally, this analysis allows error bars to be set on inverted aerosol parameters and gain insight into the optimum wavelengths for characterization.

The inversion process is also discussed, with focus on convergence and accuracy of multiple methods. Prior research has relied upon a binary genetic algorithm, which is shown to be an improvement over a generic Monte Carlo routine. An enhancement to these is shown with the use of a continuous genetic algorithm, which is successful at resolving single mode and dual mode distrubutions.

Well-known narrow size distributions and controlled materials are used to verify the methods of inversion and characterize the errors associated with this technique. A time lapse sequence of measurements is taken as the aerosol concentration decays to examine this effect on the polarization ratio. Aerosol experiments are conducted in environmentally controlled chambers at North Carolina State University and at the Johns Hopkins University Applied Physics Laboratory. Some measurements included an aerodynamic particle sizer, which is how aerosols are currently characterized using a point measurement. The simultaneous measurement allows comparison of aerosol characteristics determined by point measurements and scattering volume

measurements. Both visible and near infrared wavelengths were used, and a preliminary study of a nonspherical bioaerosol was conducted.

Ultimately, the goal of this research is to develop a technique and analysis approach that can be directly applied to the construction of a scattering instrument for aerosol characterization. The instrument system will involve a data acquisition and inversion routine that are applicable in multiple environments and measure a large range of aerosol sizes.

This research is a step toward the end goal and significantly improves the understanding of the polarization ratio, methods of data acquisition and analysis, optimization of the technique by experimental improvements, development of an inversion routine, and touches on the applicability of this techniques to non-spherical aerosols.

Characterization of Aerosols Using Multiwavelength Multistatic Optical Scattering Data

by
Michelle Grace Snyder

A dissertation submitted to the Graduate Faculty of
North Carolina State University
in partial fulfillment of the
requirements for the Degree of
Doctor of Philosophy

Physics

Raleigh, North Carolina

2011

APPROVED BY:

C. Russell Philbrick Co-chair of Advisory Committee	Hans Hallen Co-chair of Advisory Committee
Michael Paesler	Kenan Gundogdu

Mohamed Bourham

DEDICATION

This work is dedicated to my parents, Roger and Barbarajean. Your unwavering support, encouragement, and love have shaped my character, morals and work ethic. You are more than parents, you are my best friends and biggest supporters. I am forever indebted to both of you.

BIOGRAPHY

Michelle Grace Snyder was born in Binghamton, New York on March 5, 1984. At the age of 11 she moved from Endicott, New York to Raleigh, North Carolina. After completion of high school in 2002, she attended Elon University in Elon, North Carolina. In May 2006, she received bachelors of science degrees in Physics and Mathematics. She began her graduate work at North Carolina State University in August 2006. She received an en-route masters degree in August 2009. In August 2011, she received her Doctorate of Philosophy degree in Physics. Michelle will be starting a post-doctoral position at the United States Environmental Protection Agency in Research Triangle Park, North Carolina.

After graduation, she is looking forward to re-learning violin and increasing the variety and level of her culinary skills. Her interests in outdoor activities include softball, football, disc golf, water skiing and fishing (Dad, I promise we will work out the boat and sharpen our fishing skills!).

ACKNOWLEDGEMENTS

I would like to thank all of my committee members at North Carolina State University, especially my committee chairs. Your encouragement made this work possible.

My sister, Dyana, you and I have our disagreements, but I love you and appreciate all the support and love you have given me throughout this process. You are one of the rocks in my life and I could not be half the person I am without you.

Special thanks to Andrea Brown, without your constant discussion about aspects of this work I would not have survived this process. Your friendship and support have been the catalyst in my research experience. Without your persistence and coordination with facilities and equipment at Johns Hopkins Applied Physics Laboratory a large portion of the data presented here would not have been possible.

My lab mate, Tim Wright, without you I would have spent many sleepless nights chasing fog alone and would have been left in the parking lot pushing on a very heavy platform not getting anywhere.

Keeley Stevens, Stephanie Beck, and Leigh Winfrey, your editorial comments, conversation, and scientific encouragement kept me from staying in the rabbit hole under the tree and finally seeing the forest. This work would not have the organization and flow without you.

Keren Cepero, your friendship and carefree attitude kept me grounded and focused during my research process. We have a lot of disc golf to catch up on.

Finally, I would like to thank all of my friends, for dragging me away from work and insisting that I do something less intellectually strenuous. Without all of you I would have completely lost my sanity and fallen short of completing this work.

TABLE OF CONTENTS

LIST OF TABLES

LIST OF FIGURES

Chapter 1

Introduction

1.1 Motivation

The atmosphere is an essential part of the Earth's unique ability to support plant, animal and human life on its surface. The atmosphere is vital to all aspects of human life, from the very air we breathe, to the amount of energy that plants absorb while producing the food that we eat. Thus, understanding all aspects of the Earth's atmosphere is important for our continued existence on this planet. However, one of the least understood parts of the atmosphere is the aerosol component.[1,2] Aerosols are defined as any solid particle or liquid droplet suspended in a gas, such as the mixture of N_2, O_2, and other gases comprising our atmosphere. These aerosols come in many shapes and sizes which are determined by the process that created them, see Figure 1.1.

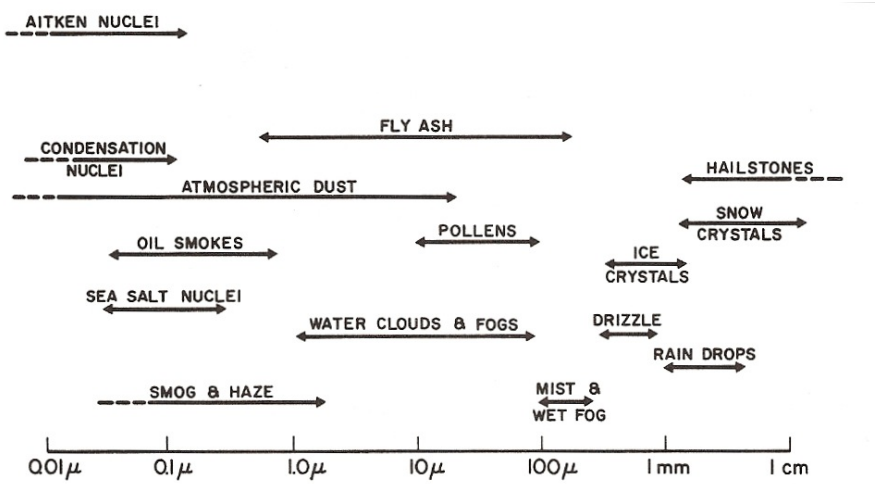

Figure 1.1: Size ranges of diameters for common aerosols, from Johnson.[3]

Aerosol diameters range from a few nanometers to a hundred microns. These are usually divided into size ranges based on their origin; three size range modes are normally recognized. The smallest size range, called the fine mode, includes aerosols from 10 nm to 100 nm. The middle size range, the accumulation mode, includes particles that are generally created by combustion processes and are often hygroscopic. These particles tend to accumulate water vapor and grow into droplets in the range from 100 nm to 1 μm. The largest size range, referred to as the coarse mode, are generally created by natural dynamical processes that disperse and re-suspend particles in the atmosphere, such as sea salt, dust and pollen. These range from 1 μm to 10 μm.[4] For a complete understanding of the atmospheric processes that affect our climate, it is important to determine the composition, concentration, and size distributions of these aerosols in the atmosphere.

Aerosols suspended in the atmosphere scatter light in all directions. Thus, aerosols affect the amount of sunlight reaches the Earth's surface effecting the human food supply. In addition, aerosols scatter light leaving Earth's atmosphere. Surface reflections and emissions are kept from exiting the atmosphere, increasing the temperature of the Earth's atmosphere.

Aerosols scatter light based on the wavelength of incident light compared to their size. One focus of this work is to characterize common scatterers, from tens of nanometers to tens of microns. The concentrations of these aerosols are many orders of magnitude ($\approx 10^{20}$) less than the atmospheric molecules, but they have a size that is 10^2 to 10^5 times the size of the molecules. Even with minuscule concentrations compared to molecules, these large aerosols dominate the optical scattering.

Recent reports by the National Oceanic and Atmospheric Administration (NOAA) and the Intergovernmental Panel on Climate Change (IPCC) have highlighted the direct and indirect impact of aerosols on climate.[1,2,5] These groups point out the effects that the climate has on humans, and the effect humans have on the environment. Aerosols affect the Earth's climate and pollution created by humans can affect the amount of aerosols in the atmosphere. These national and international panels examine the direct and indirect effects that aerosols have on climate. Aerosols directly affect the climate by scattering and absorbing in the solar spectral ranges. Indirect effects of aerosols include their role as Cloud Condensation Nuclei (CCN); once conditions permit condensation, aerosols are the catalyst for moisture to condense. This process creates a strong relation between the number of CCNs (aerosols) and the number of water droplets in clouds.[1] The direct and indirect effects of aerosols are shown in Figure 1.2, where small black dots represent aerosol particles, the larger open circles represent cloud droplets, straight lines represent the incident and reflected solar radiation, and wavy lines represent terrestrial radiation. The filled white circles indicate cloud droplet number concentration (CDNC). The unperturbed cloud contains larger cloud drops as only natural aerosols are available as cloud condensation nuclei, while the perturbed cloud contains a greater num-

ber of smaller cloud drops as both natural and anthropogenic aerosols are available as cloud condensation nuclei (CCN). The vertical gray dashes represent rainfall, and LWC refers to the liquid water content[2,6–9]

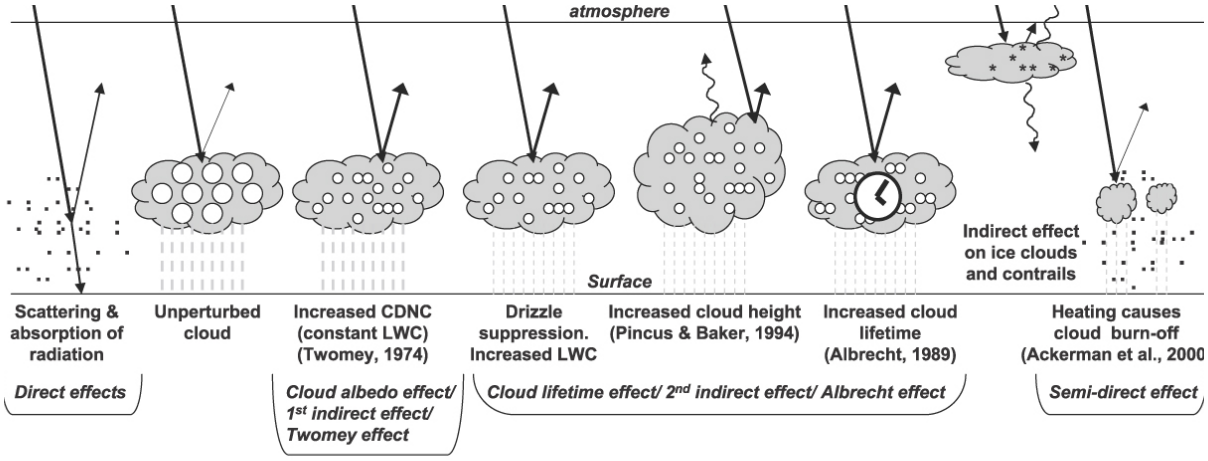

Figure 1.2: Schematic diagram showing the various radiative mechanisms associated with cloud effects that have been identified as significant effects of aerosols,[10] the references in the figure are Twomey,[6] Pinicus and Baker,[7] Alberecht,[8] Ackerman.[9]

Human impact on aerosol density can be seen in populated areas, where there may be ten times higher concentration of droplets in clouds compared to the relatively unpopulated remote marine areas. The increase in droplets is due to the CCN generation from biomass burning.[5] The increase in cloud droplets causes a rise in the Earth's albedo,[11] a measure of how much sunlight fails to reach the reach the ground. In the latest Intergovernmental Panel on Climate Change (IPCC) report,[2] the effects of aerosols produced by humans are the least understood, see Figure 1.3, where the effect of aerosol is defined by radiative forcing. Radiative forcing is a measure of how the energy balance of the Earth-atmosphere system is influenced when factors that effect climate are altered. Notice that the direct and indirect impact of aerosols have the largest error bars. Thus, studies of aerosol concentration, such as the one proposed here, are important for producing better climate forecasting models and predicting the impact of humans on the climate.

Although the impact of aerosols on the climate is large, there is a distinct lack of instrumentation available today to study aerosol size distributions. An instrument that would make widespread measurements of aerosols a possibility would need to be inexpensive, transportable, reliable, and capable of detecting a large size range. There have been several large, expensive

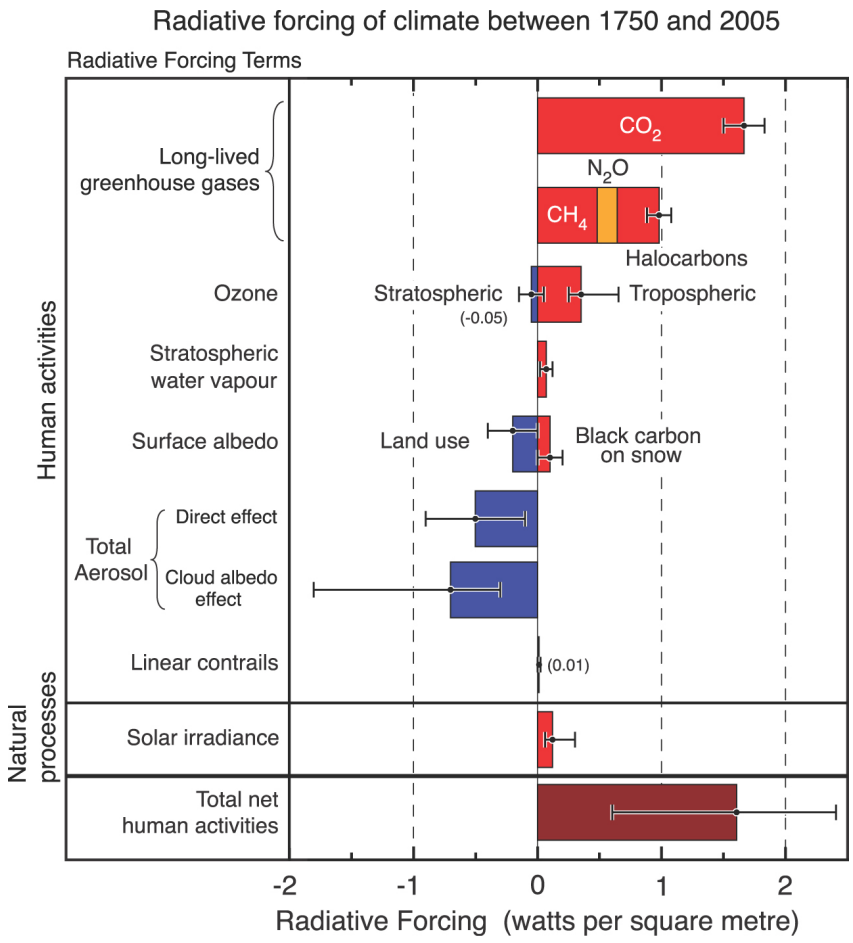

Figure 1.3: Estimates of total human impact on the radiative forcing of the atmosphere are summarized.[2]

LIght Detection And Ranging (LIDAR) systems built, as well as point measurement instruments used by many aerosol testing facilities around the world, to determine aerosol sizes and distributions.

Raman LIDARs measure the frequency shifts of scattered light to determine the concentration of molecules in large volumes of the atmosphere. Most of these systems use a high energy laser and optics to transmit the laser beam and a telescope receiver to collect the backscatter signals. They can provide simultaneous measurements of the extinction and the backscatter coefficient, which are used to investigate the aerosol properties, including chemical composition and concentrations.[12–15]

Raman systems are very large and difficult to transport, expensive to build, and require high power; these factors prevent them from taking measurements in a large number of locations. In

addition, they only measure the extinction due to aerosols, not the size distribution responsible for the extinction.

Another remote-sensing technique that is often used in conjunction with a Raman LIDAR systems is a RADAR (RAdio Detection and Ranging) system, which uses much longer wavelengths and typically detects water droplets in clouds. Again, deployment of these systems are limited by their large energy consumption.[16] The lower atmosphere is turbulent and variable, so it is essential to have an instrument that provides continuous measurements over a long period of time[17] with automated measurement capability.

Other instruments make aerosol point measurements by collecting a small volume of air, then condensing vapor onto aerosols to grow them to a size the sensor can detect. These commercially available instruments are capable of taking a limited number of samples and are expensive. They can only take point measurements, which may not be indicative of a large volume.

The system being developed is a multistatic LIDAR instrument, which would solve many of the current instrument problems. It is inexpensive, easy to operate, easy to transport, and able to take continuous measurements without modifying the environment that it measures. It is also important to test this method of volume measurement, and to test its accuracy compared to point measurements of currently available instruments. Thus, experiments described here are conducted with other aerosol measuring instruments, when possible, to help establish the accuracy of the system.

The multiwavelength, multistatic instrument has many practical real world applications. It can provide inexpensive aerosol monitoring systems to monitor concentrations of aerosol particles in the atmosphere. Aerosols of concern include smog, dust, and pollen, all of which affect the formation of clouds, change radiation transport through the atmosphere, and influence the overall climate. These measurements could provide climate modelers and forecasters with useful reference measurements to compare with computations and show a more accurate picture of the Earth's climate.

1.2 Fog Cycles: Formation, Growth and Dissipation

One major application of this instrument is to measure spherical aerosols during a fog cycle. The presence of aerosols is necessary for the formation of a fog cloud, as it provides the required cloud condensation nuclei (CCN). These CCN create the sites for the condensation of water vapor as the temperature drops below the dew point. This interrelatedness makes study of aerosols, namely their characteristics and number concentration, a suitable starting point to investigate fog formation, growth and dissipation. The following is a summary of a fog cycle:[4, 18–20]

1. SUNDOWN STAGE: Surface temperature decreases rapidly and the height of the boundary layer decreases to a few meters above the surface. Radiative cooling of the surface and turbulence decrease because of stability associated with a strong surface inversion, where temperature increases with height. This is opposite to the temperature gradient in the boundary layer is during the day, where temperature decreases with height above the ground.

2. CONDITIONING STAGE: The rate of cooling decreases, but the boundary layer thickness and turbulence increase. The turbulence transports heat toward the ground. While this is happening the relative humidity grows rapidly. A shallow ground fog is created near the surface as the dew point and temperature differences decrease and condensation begins to form on aerosols.

3. MATURE FOG STAGE: The turbulence and boundary layer height increase and the fog grows in height, liquid water content and droplet size. This is the point where it has been hypothesized that there are turbulent quasi-periodic oscillations in fog thickness and droplet size.[18]

4. DISSIPATION STAGE: With the sunrise, the fog dissipates toward the ground and only exist over a height of a few meters. The fog continues to be generated by the surface moisture and dew until the moisture is evaporated.

Instruments have been build to study the relative humidity[21] and liquid water content.[22] There have been many fog studies that highlight the complex and not well-understood microstructure[23] of fogs.

1.3 Research Methods and Objectives

The instrument developed in this work has the capability of measuring across large volumes, which give a larger and more realistic picture of the aerosols influence on the atmosphere than would point measurements. Current aerosol instruments are hindered by the fact that their measurements are restricted to small volumes. Additionally, this newer instrument does not disturb the environment under study, as opposed to point measurement instruments which extract samples into a chamber. This large scale, non-disruptive instrumentation has immediate applications in the studies of multiple concurrent size distributions of aerosols and in turbulent fogs.

The multiwavelength, multistatic instrument from previous students work[13,15,24,25]measure the scatter of multiple wavelengths from aerosols. Scattered intensity is measured at two perpendicular polarizations, the ratio of the intensities form the *polarization ratio*. The ratio is

matched to aerosol scattering calculations through an inversion process to determine aerosol distribution characteristics.

To prepare this instrument for robust aerosol research, this study examines the polarization ratio, the inversion routine, and the applicability range of this instrument. Therefore, the major objectives of this research are:

1. Explore the capabilities and limitations of the polarization ratio method through simulation and squared-error analysis;

2. Gain insights into the required wavelengths for accurate aerosols analysis through polarization ratio simulations and squared-error analysis;

3. Used a Monte Carlo type approach to determine error bars on parameter values obtained through the squared-error analysis and inverted results;

4. Develop a robust inversion routine that out preforms previous methods;

5. Test the effectiveness of the inversion routine to extract aerosol characterization parameters from measured data in well characterized, narrow single and multi-mode spherical aerosol dispersals;

6. Investigate possible applications of this system to non-spherical aerosols through experiment and calculations;

7. Use instrument and techniques on naturally occurring spherical fog particles in a less controlled environment.

Chapter 2

Optical Scattering

This chapter introduces the calculations and terminology needed to understand the optical scattering technique. A brief synopsis of the work on this subject performed by the Pennsylvania State University LIDAR Laboratory graduate students is presented. Additional descriptions, derivations and explanations are provided for a brief background in aerosols, light scattering, and remote sensing. A detailed derivation of the full scattering calculations can be found in Measures,[26] Bohren and Huffman,[27] van de Hulst,[28] and Mishchenko.[29] The relevant physics for the derivations is presented, and the resources listed can be consulted to find the step-by-step calculations.

2.1 Derivation Of Optical Scattering Equations

The equations needed to calculate the optical scattering from dielectric spheres are derived from the fundamental equations of electromagnetic theory. The boundary conditions are applied to describe constructive and destructive interference of radiation scattered at the boundaries of particles, when a photon scatters from an aerosol. This scattering process creates a complicated system of incident, internal and scattered electromagnetic fields. The scattered field depends on many things, including the incident wavelength, incident polarization, and the size, shape, and composition of the aerosol. These factors produce unique scattering signatures and absorption characteristics that spread the pattern of scatted intensity across all angles dependent on their interaction. The equations for electromagnetic scattering from a sphere first solved by Gustav Mie.[30] These calculations were independently derived by Lorentz, thus they are often referred to as Lorentz-Mie calculations.[26,27] However, to be as complete as possible and allow further expansion of scattering calculations to non-spherical particles (see Section 6.6), the scattering from an arbitrary particle is explored first, then the symmetry of a sphere is added to obtain a closed solution for a spherical scattering particle.

2.1.1 Light Scattering By a Particle

The scattering plane is defined to provide a common geometry which is used throughout this work. The scattering plane is defined by the incident light path and the detector, see Figure 2.1. Once the scattering plane is defined, each polarization and scattering angle can be defined from it.

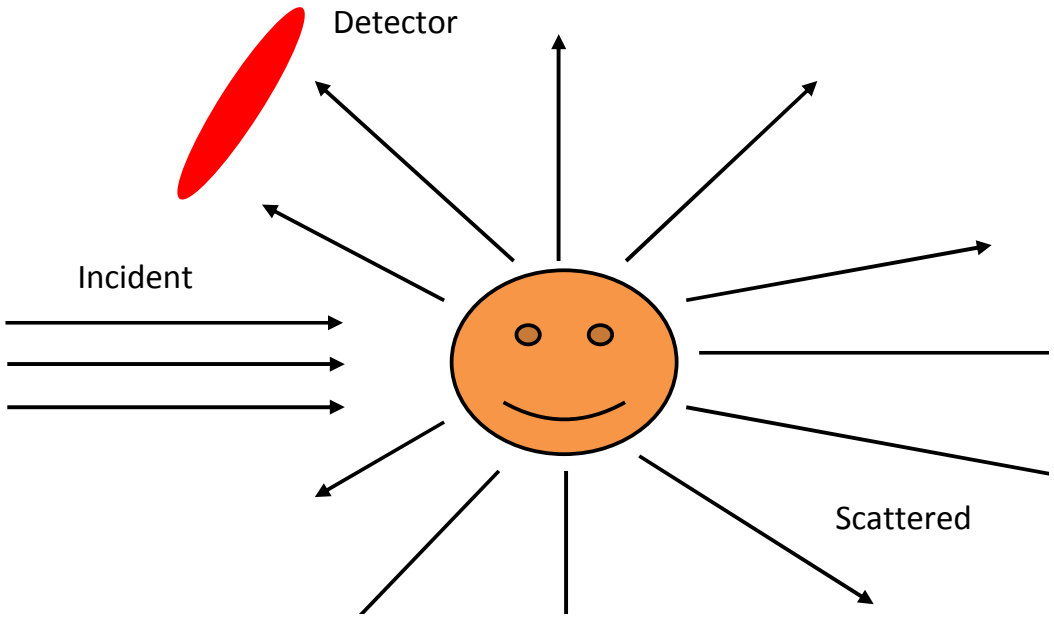

Figure 2.1: The scattering plane is defined by the incident light path in the scattering volume and the detector.

From electromagnetic theory, Maxwell's equations must be satisfied on the entire boundary of the particle, for all fields inside and outside the particle. Maxwell's equations are:

$$\nabla \cdot \vec{E} = \frac{\rho}{\epsilon_o}, \qquad \nabla \cdot \vec{H} = 0,$$
$$\nabla \times \vec{E} = \frac{-\partial \vec{H}}{\partial t}, \qquad \nabla \times \vec{H} = \vec{J} + \epsilon_o \frac{\partial \vec{E}}{\partial t}.$$

The first simplification made is to assume that the medium the particle is in does not contain electromagnetic current ($\vec{J} = 0$) and the particle is not charged ($\rho = 0$), then Maxwell's Equations are:

$$\nabla \cdot \vec{E} = 0, \quad (2.1) \qquad \nabla \cdot \vec{H} = 0, \quad (2.3)$$

$$\nabla \times \vec{E} = i\omega\mu\vec{H}, \quad (2.2) \qquad \nabla \times \vec{H} = -i\omega\epsilon\vec{E}. \quad (2.4)$$

By taking the curl of both Equations 2.2 and 2.3 and applying vector identities and substitutions, the differential wave equations are found;

$$\nabla^2\vec{E} + k^2\vec{E} = 0, \quad (2.5)$$

$$\nabla^2\vec{H} + k^2\vec{H} = 0. \quad (2.6)$$

The fields present are the incident field, the scattered field, and the internal field, all of which must satisfy Maxwell's Equations on the boundary between the inside (particle) and the outside fields (scattered + incident).

One boundary condition is that the tangential components of the electric and magnetic fields be continuous across the boundary,

$$\left[\vec{E}_{outside}(x) - \vec{E}_{inside}(x)\right] \times \hat{n} = 0, \quad (2.7)$$

$$\left[\vec{H}_{outside}(x) - \vec{H}_{inside}(x)\right] \times \hat{n} = 0, \quad (2.8)$$

where $\hat{n}$ is the unit normal vector to the scattering plane and x is a point on the scattering plane. It is also important to note that only a monochromatic wave needs to be considered here, because any wave can be considered a superposition of two orthogonal components of a polarized monochromatic wave. The simplest electric field components to choose are the ones parallel and perpendicular to the scattering plane (as defined in Figure 2.1), so all future calculations will use the notation $E_{||}$ and $E_{\perp}$ for the fields parallel and perpendicular to the scattering plane. Thus, a transformation between the usual Cartesian coordinates to spherical coordinates is needed, where $\vec{z}$ represents the direction of propagation of the incident wave, as shown in Figure 2.2.

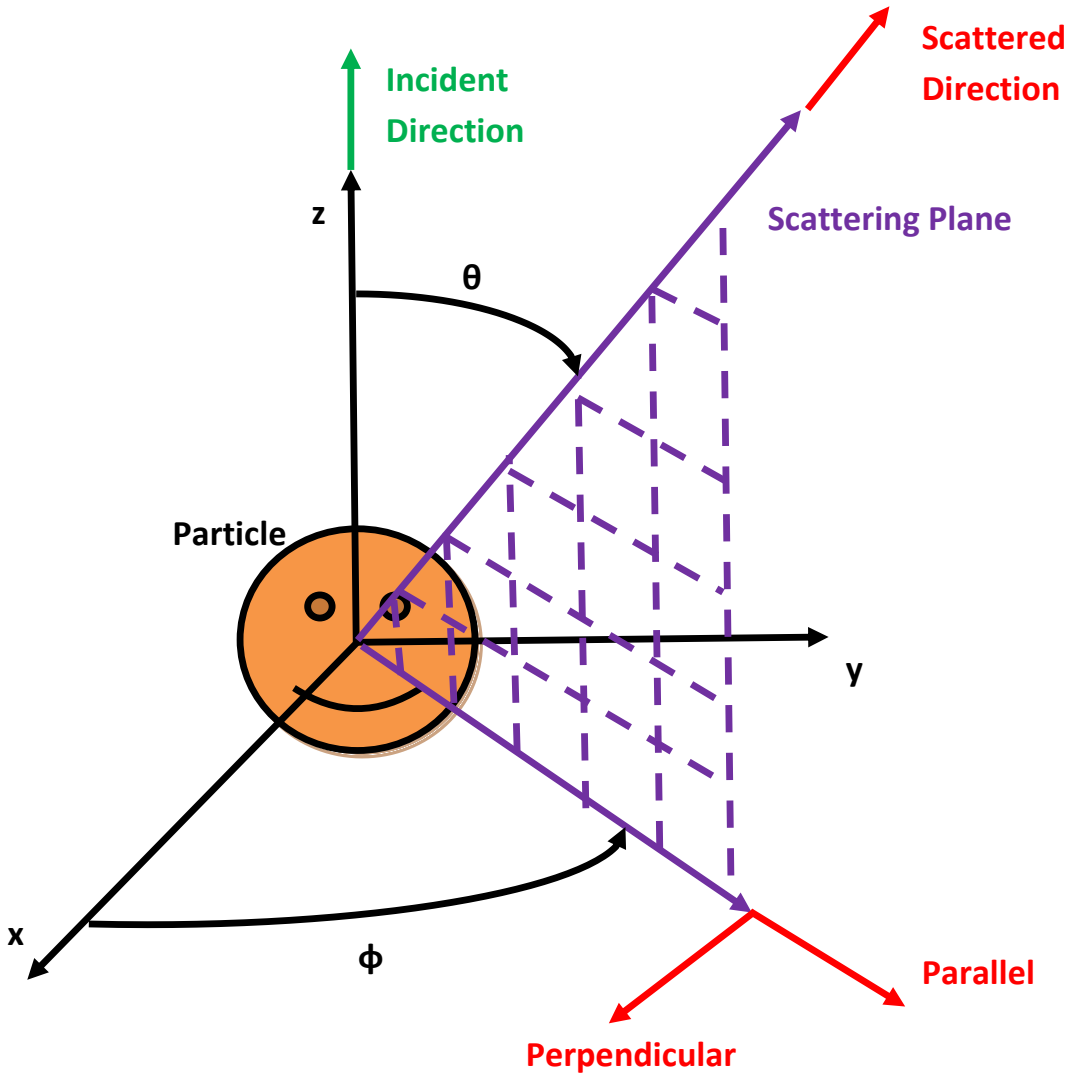

Figure 2.2: This illustrates the scattering plane and the perpendicular/parallel notation used in scattering calculations.

This transformation is represented by the following unit vectors,

$$\begin{aligned} \hat{e}_{\perp} &= \sin\phi(\hat{e}_x) - \cos\phi(\hat{e}_y), \\ \hat{e}_{||} &= \cos\phi(\hat{e}_x) - \sin\phi(\hat{e}_y). \end{aligned}$$

The electric field created by the incident wave traveling in the z-direction is,

$$\begin{aligned} E_{i\perp} &= \sin\phi E_{ix} - \cos\phi E_{iy}, \\ E_{i||} &= \cos\phi E_{ix} - \sin\phi E_{iy}. \end{aligned}$$

The angles θ and ϕ and their relationship between the x, y and z axes in the Cartesian coordinate are explicitly defined in Figure 2.2.

The particles measured are usually small compared to the wavelength, so Equation 2.5 can be approximated using the far-field limit ($kr >> 1$):

$$\vec{E}_s \approx \frac{e^{ikr}}{-ikr}\vec{A},$$

where $\vec{A} \cdot \hat{e}_r = 0$. Thus

$$\vec{E}_s = E_{s||}\hat{e}_{s||} + E_{s\perp}\hat{e}_{s\perp}.$$

This can be written more concisely in matrix notation

$$\begin{pmatrix} E_{s||} \\ E_{s\perp} \end{pmatrix} = \frac{e^{ik(r-z)}}{-ikr} \begin{pmatrix} S_2 & S_3 \\ S_4 & S_1 \end{pmatrix} \begin{pmatrix} E_{i||} \\ E_{i\perp} \end{pmatrix}, \tag{2.9}$$

where the elements $S_j (j = 1, 2, 3, 4)$ are refered to as elements of the amplitude scattering matrix and are dependent on the scattering angle (θ) and the azimuthal angle (ϕ). Finding a solution for this scattering matrix results in a description of the way light scatters from an arbitrary particle.

The field representation is somewhat impractical from an experimental perspective. Light is usually represented by a Stoke's vector in optical experiments . This is a column vector with four entries representing the intensity, horizontal or vertical polarization, $\pm 45^\circ$ polarization, and left or right circularly polarized, respectively, and is denoted as

$$\begin{pmatrix} I \\ Q \\ U \\ V \end{pmatrix}.$$

The relationship between the incident and scattered waves can be written in terms of a scattering matrix, up to a scaling factor, C, as:

$$\underbrace{\begin{pmatrix} I_s \\ Q_s \\ U_s \\ V_s \end{pmatrix}}_{\text{scattered wave}} = C \underbrace{\begin{pmatrix} S_{11} & S_{12} & S_{13} & S_{14} \\ S_{21} & S_{22} & S_{23} & S_{24} \\ S_{31} & S_{32} & S_{33} & S_{34} \\ S_{41} & S_{42} & S_{43} & S_{44} \end{pmatrix}}_{\text{scattering matrix}} \underbrace{\begin{pmatrix} I_i \\ Q_i \\ U_i \\ V_i \end{pmatrix}}_{\text{incident wave}}. \tag{2.10}$$

From here the equations can be simplified and manipulated to obtain scattering solutions for a spherical aerosol (see Section 2.1.4).

2.1.2 Scattering Terminology

The *cross section* refers to the ratio of the amount of light absorbed or scattered compared to the incident light. The cross section is described in terms of therate that energy flows in and out of a sphere of radius a and surface area A, around the arbitrary particle in Figure 2.1, and can be expressed as a work function.

$$W = -\int_A \vec{S} \cdot \hat{e}_r dA$$

where $W_{absorbed}$ is the work absorbed. Notice that $W_{absorbed}$ is always positive, since the particle is not generating energy just absorbing energy. From earlier discussions about the fields present, $W_{absorbed}$ can be split into its components.

$$W_{absorbed} = W_{incident} - W_{scattered} + W_{extinction}$$

Where these individually are

$$W_{incident} = -\int_A \vec{S}_{incident} \cdot \hat{e}_r dA, \tag{2.11}$$

$$W_{scattered} = \int_A \vec{S}_{scattered} \cdot \hat{e}_r dA, \tag{2.12}$$

$$W_{extinction} = -\int_A \vec{S}_{extinction} \cdot \hat{e}_r dA. \tag{2.13}$$

Assuming the particle is in a nonabsorbing medium, $W_{incident} = 0$, then

$$W_{extinciton} = W_{absorbed} + W_{scattered},$$

where the $W_{absorbed}$ term refers to the energy absorbed by the particle, not by the medium.

For convenience the direction of propagation for the incident light the z-direction is picked.

Thus:

$$\vec{Z} = (S_2 \cos\phi + S_3 \sin\phi)\,\hat{e}_{s||} + (S_4 \cos\phi + S_1 \sin\phi)\,\hat{e}_{s\perp},$$

will be used.

The scattered electromagnetic field in the far-field approximation can be expressed as

$$\vec{E_s} \approx \frac{e^{ik(r-z)}}{-ikr}\vec{Z}E \tag{2.14}$$

and

$$H_s \approx \frac{k}{\omega\mu}\hat{e}_r \times \vec{E}_s \tag{2.15}$$

After some manipulation an expression for the extinction term is obtained,

$$W_{extinction} = I_{incident}\frac{4\pi}{k^2} Re\left\{\left(\vec{Z}\cdot\hat{e}_x\right)_{\theta=0}\right\}.$$

This leads to the *extinction cross section*, C_{ext},

$$C_{ext} = \frac{W_{extinction}}{I_{incident}} = \frac{4\pi}{k^2} Re\left\{\left(\vec{Z}\cdot\hat{e}_x\right)_{\theta=0}\right\}.$$

Likewise, the *absorbtion cross section*, C_{abs}, and the *scattering cross section*, C_{sca} can be found.

From Equations 2.13, 2.14 and 2.15 the scattering cross section can be written,

$$C_{sca} = \int_0^{2\pi}\int_0^{\pi} \frac{|\vec{Z}^2|}{k^2}\sin\theta d\theta d\phi = \int_{4\pi} \frac{|\vec{Z}|^2}{k^2} d\Omega.$$

The *differential cross section* is the $\frac{|\vec{Z}|^2}{k^2}$ term, which is usually denoted $\frac{dC_{sca}}{d\Omega}$. The differential cross section can be thought of as the amount of light scattered in a unit solid angle in a given direction. The *phase function* is related, namely $\frac{|\vec{Z}|^2}{k^2}C_{sca}$, which is the amount of scattered intensity as a function of angle.

2.1.3 Light Scattering By Small Particles: Rayleigh Scattering

The scattering description falls into two regimes; when particles are very small,

$$ka = \frac{2\pi a}{\lambda} << 1, \tag{2.16}$$

they are considered to be in the Rayleigh regime and the scattering intensity distribution is equivalent to a dipole field, shown in Figure 2.3 . When the particles are larger than this they fall into the Mie scattering regime (section 2.1.4), which assumes that they are spherical.

Figure 2.3 was created using the BHMIE code,[27] which includes the solution of the scattering

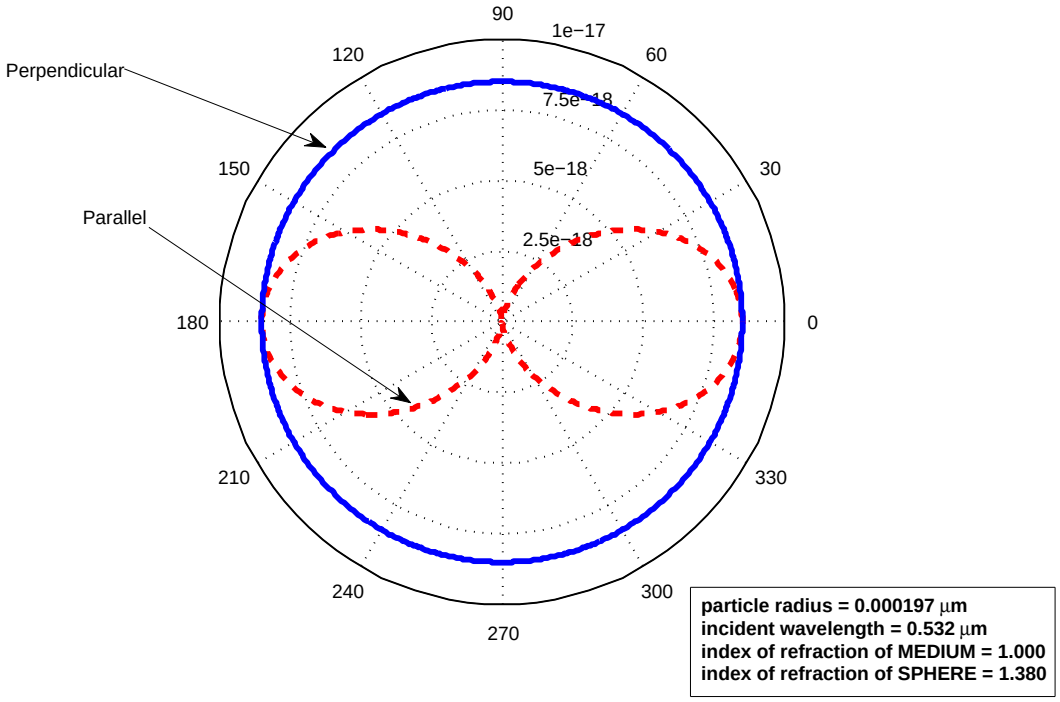

Figure 2.3: Parallel and perpendicular polarization scattering for a dipole

equations for spherical particles when $a << \lambda$. BHMIE, is the acronym for the Matlab code for the scattering equations derived in the appendix Bohren and Huffman text (in Fortran).[27] The particle radius used to make this figure was found by knowing the scattering cross section for the wavelength, assuming that an atmospheric particle has an index of refraction slightly greater than water, and then solving for the radius of particle with the desired cross section for the mix of atmospheric gases found in the troposphere.[13] The actual radius number is unimportant, except that it is much smaller than the wavelength, which produces a dipole scattered filed. This procedure was outlined by Stevens[13] to find the radius that would have the equivalent cross section of the atmospheric atomic mixture.

The primary molecules in the troposphere, the lower atmosphere. are nitrogen, N_2, and oxygen, O_2, both diatomic molecules that are in the Rayleigh scattering regime. Their concentration is approximately 2.55×10^{19} molecules/cm^3. These molecules scatter as dipoles and make up about 98% of the molecules in the troposphere.[26]

The scattering properties of these small molecules are calculated assuming there is a molecule present with an outer electron that can be treated as a harmonic oscillator. Its position, ξ, its velocity, $\dot{\xi}$, and its acceleration, $\ddot{\xi}$, are used to describe the equation of motion,

$$\ddot{\xi} + \gamma\dot{\xi} + \omega_o^2\xi = -\frac{e}{m_e}\vec{E},$$

where γ is the damping constant and ω_o is the resonant angular frequency. The electric field, $\vec{E}$, can be expressed as

$$\vec{E} = \hat{\epsilon}E_o e^{-i\omega t}. \tag{2.17}$$

.

The steady state solution of this set of equations is $\xi = \hat{\epsilon}\xi e^{-i\omega t}$, and the acceleration is

$$\dot{u} = \ddot{\xi} = -\left[\frac{\omega^2}{\omega_o^2 - \omega^2 - i\omega\gamma}\right]\frac{e}{m_e}\vec{E}. \tag{2.18}$$

The scattered electric field can be described as two components in perpendicular directions to the direction of propagation.

$$\begin{aligned} E_1^s &= -\frac{e}{4\pi\epsilon_o c^2 r}\dot{u}_1 \\ E_2^s &= -\frac{e}{4\pi\epsilon_o c^2 r}\dot{u}_2. \end{aligned}$$

If θ is defined as the scattering angle, and ϕ as the angle of polarization, then

$$\begin{aligned} \dot{u}_1 &= \dot{u}\sin\phi \\ \dot{u}_2 &= \dot{u}\cos\phi\cos\theta. \end{aligned}$$

The combined scattered electric field is

$$E_s = -\frac{e\dot{u}}{4\pi\epsilon_o c^2 r}\left[\hat{\dot{u}}_2\cos\theta\cos\phi + \hat{\dot{u}}_1\sin\phi\right]. \tag{2.19}$$

The radiation scattered power in the element of the solid angle, $d\Omega$, is

$$dP(\theta,\phi) = \frac{1}{2}\epsilon_o c|\vec{E}_s|^2 r^2 d\Omega. \tag{2.20}$$

Then the radiated scattered power per unit solid angle is,

$$\frac{dP(\theta,\phi)}{d\Omega} = \frac{1}{2}\epsilon_o c|\vec{E}_o|^2 r_e^2\left[\frac{\omega^2}{\omega_o^2 - \omega^2 - i\omega\gamma}\right]^2\{\cos^2\phi\cos^2\theta + \sin^2\phi\}. \tag{2.21}$$

The scattered power is related to the differential scattering cross section by

$$\frac{dP(\theta,\phi)}{d\Omega} = I_o \frac{d\sigma(\theta,\phi)}{d\Omega},$$

so combining with Equations 2.19 and 2.21,

$$\frac{d\sigma(\theta,\phi)}{d\Omega} = r_e^2\{\cos^2\phi\cos^2\theta + \sin^2\phi\}\left[\frac{\omega^2}{(\omega-\omega_o)^2+(\gamma/2)^2}\right].$$

The total Rayleigh scattering cross section is

$$\sigma_R(\omega) = \frac{1}{4}r_e^2\left[\frac{\omega^2}{(\omega-\omega_o)^2+(\gamma/2)^2}\right]\int_{\theta=0}^{\pi}\int_{\phi=0}^{2\pi}\{\cos^2\phi\cos^2\theta + \sin^2\phi\}\sin\theta d\theta d\phi.$$

This equation can be simplified using the square of the complex index of refraction of the molecule in air ($n_{air} = 1$),

$$n^2 = 1 + \frac{Ne^2}{\epsilon_o m_e}\left[\frac{\omega^2}{\omega_o^2-\omega^2-i\omega\gamma}\right],$$

where N is the number density of the scatters. Then the Rayleigh differential scattering cross section is

$$\frac{d\sigma_R(\theta,\phi)}{d\Omega} = \frac{\pi^2(n^2-1)^2}{N^2\lambda^4}\{\cos^2\phi\cos^2\theta + \sin^2\phi\}. \tag{2.22}$$

Notice that when $\phi = 0$ the Rayleigh scattering cross section follows a $\cos^2\theta$ shape with a coefficient determined by the aerosol concentration and wavelength; thus, the scattering phase function follows the $\cos^2\theta$ curve for the polarization that is perpendicular to the scattering plane and the particles are small compared to the wavelength.
The total Rayleigh scattering cross section is

$$\sigma_R(\lambda) = \frac{8\pi}{3}\left[\frac{\pi^2(n^2-1)^2}{N^2\lambda^4}\right].$$

The Rayleigh backscattering ($\theta = 180°$) scattering cross section is

$$\sigma_\pi^R(\lambda) = \frac{d\sigma_R(\theta=\pi)}{d\Omega} = \frac{\pi^2(n^2-1)^2}{N^2\lambda^4}.$$

The Rayleigh backscattering cross section for the mixture of atmospheric gases in the lower troposphere is approximated by,[26]

$$\sigma_\pi^R(\lambda) = 5.45\left[\frac{550}{\lambda(nm)}\right]^4 \times 10^{-28} cm^2 sr^{-1}.$$

The differential cross section is equal to the Rayleigh backscattering cross section for light

polarized parallel to the scattering plane. The differential scattering cross section is equal to the Rayleigh backscattering cross section multiplying $\cos^2\theta$ for light polarized perpendicular to the scattering plane, see Figures 2.3 and 2.4.

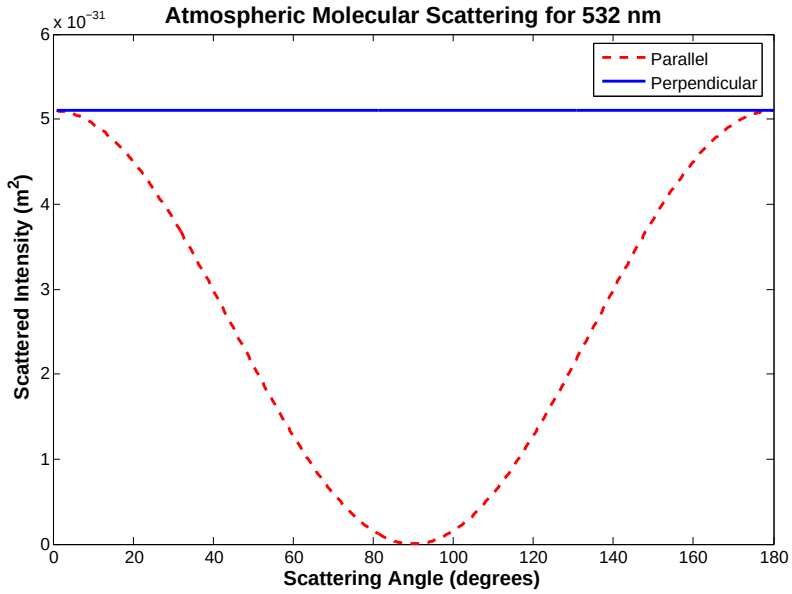

Figure 2.4: The phase function is plotted for dipole scattering of photons at 532 nm for the mix of atmospheric gases found in the troposphere. The Rayleigh backscattering cross section for this case is $5.1 \times 10^{-31} m^2$.

Figure 2.3 was created using the BHMIE routine based on the calculations of Borhen and Huffman,[27] where the diameter of the aerosol is very small compared to the wavelength of incident light. The calculated result is identical to that obtained by Rayleigh,[31] which is representative of a very small aerosol or a dipole. The scattering behavior near the lower limit of the Mie scattering regime transitions smoothly into the Rayleigh scattering range where all scattering will look like dipole scattering. The Lorentz-Mie calculations are described in Section 2.1.4. The calculations and descriptions in this section can be found elsewhere,[26–29] but are presented here for the reader to have a brief overview of aerosol scattering.

2.1.4 Light Scattering By a Sphere: Lorentz-Mie Calculations

The calculations in this section are based on Gustav Mie's original 1908 paper.[30] It is important to emphasize that these calculations are relevant when one makes the assumption

that the particles in the scattering volume are spheres. When Equtations 2.9 and 2.10 are simplified for the geometry of a sphere, the general scattering equations in matrix and Stoke's vector notation become

$$\begin{pmatrix} E_{s\|\|} \\ E_{s\perp} \end{pmatrix} = \frac{e^{ik(r-z)}}{-ikr} \begin{pmatrix} S_2 & 0 \\ 0 & S_1 \end{pmatrix} \begin{pmatrix} E_{i\|\|} \\ E_{i\perp} \end{pmatrix}, \tag{2.23}$$

$$\underbrace{\begin{pmatrix} I_s \\ Q_s \\ U_s \\ V_s \end{pmatrix}}_{\text{scattered wave}} = C \underbrace{\begin{pmatrix} S_{11} & S_{12} & 0 & 0 \\ S_{12} & S_{11} & 0 & 0 \\ 0 & 0 & S_{33} & S_{34} \\ 0 & 0 & -S_{34} & S_{44} \end{pmatrix}}_{\text{scattering matrix}} \underbrace{\begin{pmatrix} I_i \\ Q_i \\ U_i \\ V_i \end{pmatrix}}_{\text{incident wave}}.$$

The equations to convert between these representations are;

$$\begin{aligned} S_{11} &= \frac{1}{2}\left(|S_2|^2 + |S_1|^2\right), & S_{12} &= \frac{1}{2}\left(|S_2|^2 - |S_1|^2\right), \\ S_{33} &= \frac{1}{2}\left(S_2^* S_1 + S_2 S_1^*\right), & S_{34} &= \frac{i}{2}\left(S_1^* S_2 - S_2 S_1^*\right). \end{aligned}$$

Only three of these are independent since

$$S_{11}^2 = S_{12}^2 + S_{33}^2 + S_{34}^2.$$

If the light is polarized ***parallel*** to the scattering plane the Stoke's parameters are

$$\begin{aligned} I_s &= (S_{11} + S_{12})I_i = (S_2)I_i, \\ Q_s &= I_s, \\ U_s &= 0, \\ V_s &= 0. \end{aligned} \tag{2.24}$$

If the light is polarized ***perpendicular*** to the scattering plane the Stoke's parameters are

$$\begin{aligned} I_s &= (S_{11} - S_{12})I_i = (S_1)I_i, \\ Q_s &= -I_s, \\ U_s &= 0, \\ V_s &= 0. \end{aligned} \tag{2.25}$$

The scattered intensities, Equations 2.24 and 2.25, will be denoted $I_{||}$ and $I_\perp$, respectively, it is understood they represent the scattered intensities.

Pictorial Representation of Mie Scattering

Scattering from aerosols larger than the Rayleigh regime can be described by using the Lorentz-Mie calculations. The polar plot shown in Figure 2.3, allows the observer to visualize the angular scatter when the aerosol is located at the origin and the light travels from left to right toward 0 degrees. Phase functions are usually plotted as scattering angle versus scattered intensity. The scattered intensity as a function of the scattering angle is known as the *scattering phase function*. As the particles grow in size compared to the incident wavelength, i.e. $ka > 0.1$, their scattering diagrams exhibit very different features, see Figure 2.5. This figure, which was originally presented in Born and Wolf,[32] is calculated and replotted using the BHMIE code.

Figure 2.5 shows that as the size of the aerosol increases, the scattering signature deviates rapidly from the dipole scattering seen in Figure 2.3. Also notice that as ka increases to eight the scattering signature becomes highly structured. This structure is important because it contains the information on the size of the particle relative to the wavelength of the scattered light.

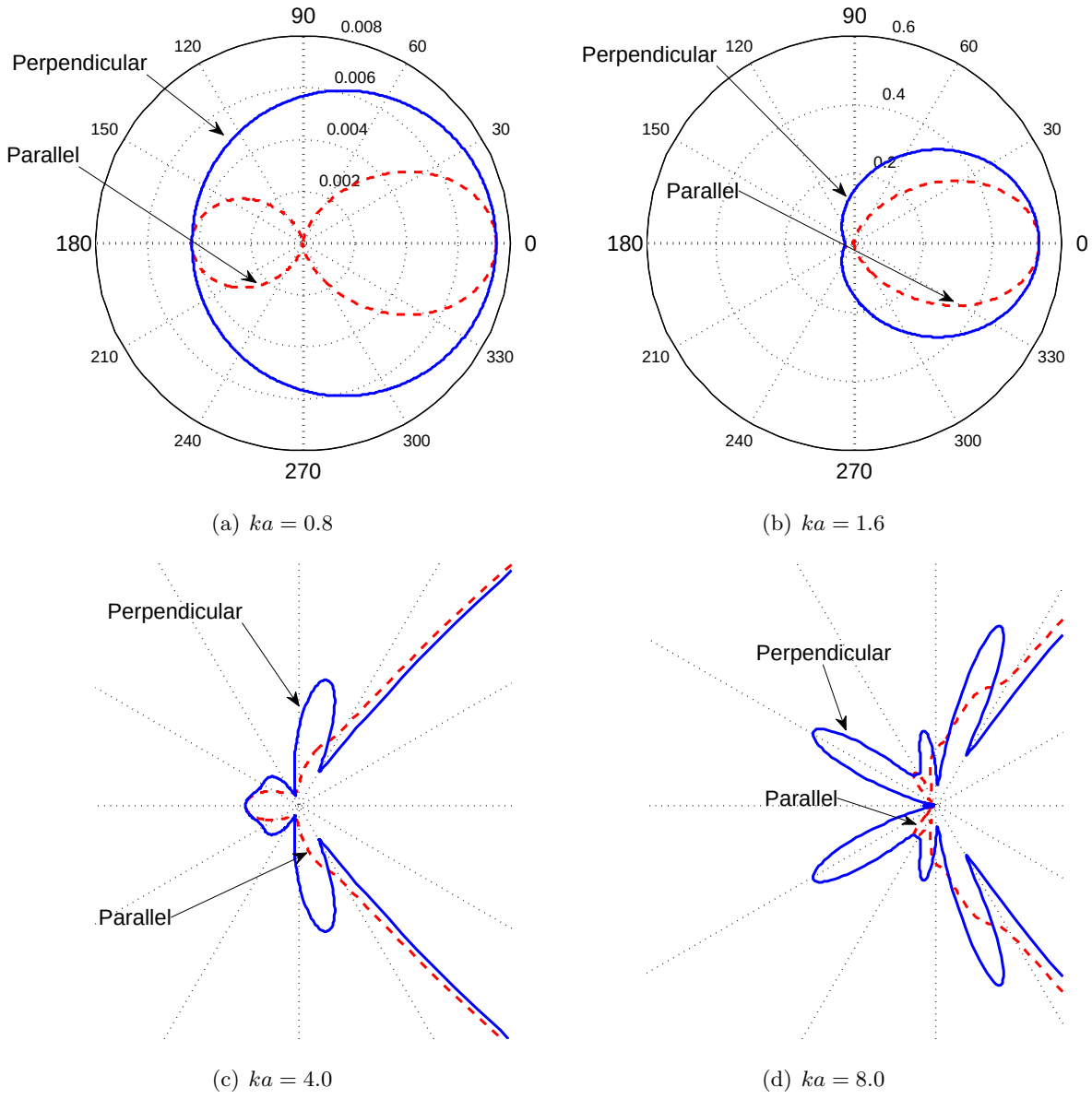

(a) $ka = 0.8$ (b) $ka = 1.6$

(c) $ka = 4.0$ (d) $ka = 8.0$

Figure 2.5: Angular scattering intensity as a function of ka for values described by Born and Wolf.[32] The solid blue lines are the perpendicular scattering and the red dashed lines are the parallel scattering.

2.2 Introduction to the Polarization Ratio

Another quantity of interest is the ratio of the calculated Mie intensities for each polarization, the *polarization ratio* (PR) is written,

$$PR = \frac{I_{||}}{I_{\perp}} = \frac{|S_2|^2 I_i}{|S_1|^2 I_i}, \tag{2.26}$$

where S_1 and S_2 are the scattering coefficients for parallel and perpendicular light from Equations 2.24 and 2.25. The scattering intensity versus angle, the phase function, was shown in Figure 2.5. The corresponding ratios formed by taking the parallel over the perpendicular scattered intensity are shown in Figure 2.6. Plots demonstrate the polarization ratio quantity calculated using the BHMIE code[27] to find the scattering phase functions, then taking the ratio of the horizontal to the vertical phase function at each angle. These plots show the characteristics of the polarization ratio using the scattering phase functions depicted in Figure 2.5. Examination of the backscattered angles, between 90 degrees and 180 degrees, shows that the two polarizations are scattered differently as ka increases, thus measuring the polarization ratio at backscattering angles is sensitive to particle size.

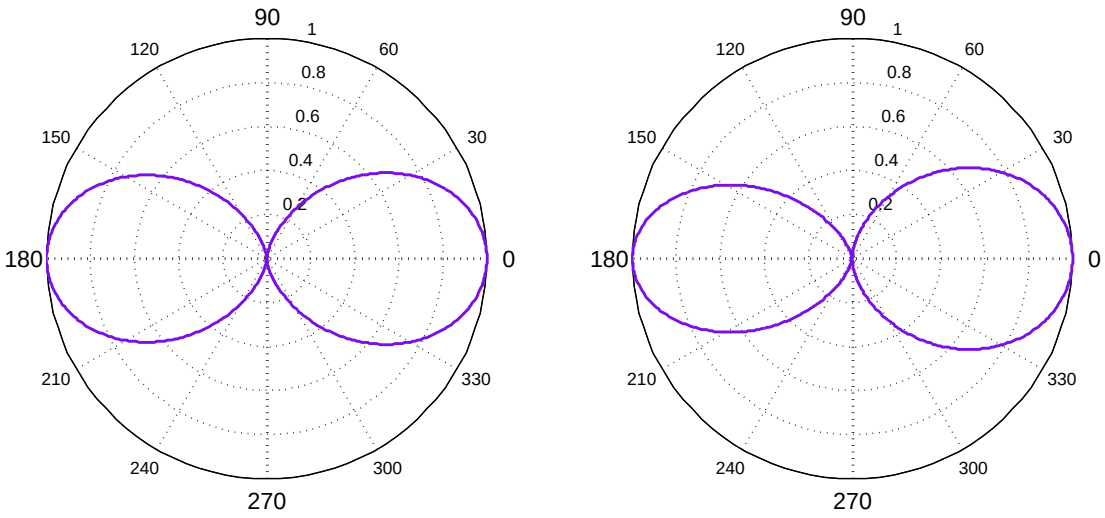

(a) $ka = 0.8$

(b) $ka = 1.6$

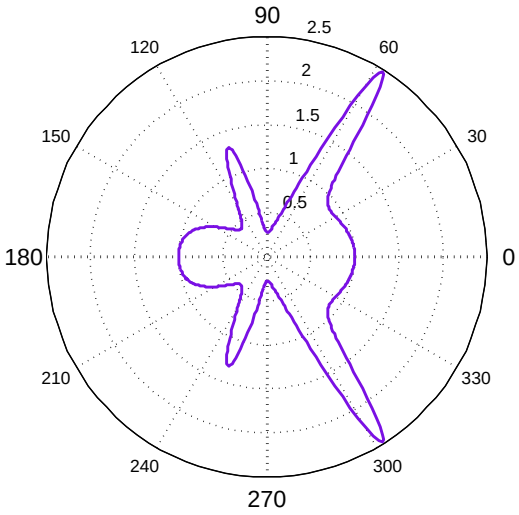

(c) $ka = 4.0$

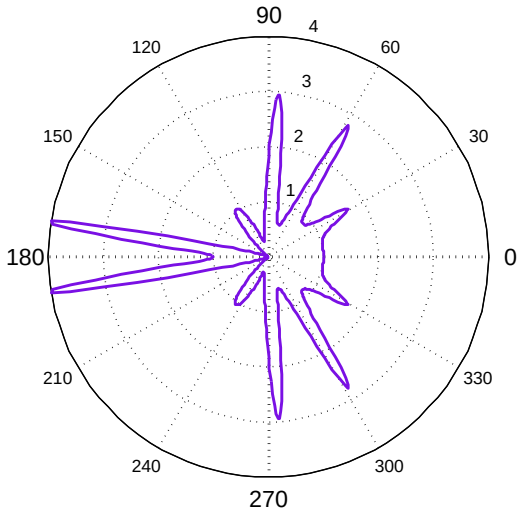

(d) $ka = 8.0$

Figure 2.6: Polarization ratios as a function of ka. The ratios are calculated at ka values identical to Figure 2.5.

2.2.1 Expansion of the Polarization Ratio Calculation to Distributions

The scattering calculations in previous sections were for an individual particle. For this method to be applicable in large volumes of aerosols, it must be expanded to find the ratio formed by a distribution of particles.

A significant amount of background knowledge is needed to describe aerosol size distribu-

tions, optical characteristics, and abundance in the atmosphere. Log-normal distributions are often used to describe aerosols; thus a short introduction to them is presented to assist the reader in understanding the later contents of this work. The majority of this discussion comes from the works of Novitsky[15] and Seinfeld and Pandis.[4]

Log-Normal Size Distributions

The variables used to characterize the log-normal distribution are mean (μ_g) and standard width (σ_g), where the g subscripts represent geometric quantities. These distributions are then normalized, so that the integral of the distribution is one. The distribution function can be multiplied by the total concentration; thus the distribution is referred to as a probability distribution function.

Many functions have been explored to attempt to match measured distributions of atmospheric aerosols, the log normal distribution function has been found to fit the measurements the best; an example is shown in Figure 2.7(a). In functional form the log-normal distribution is,

$$y(x;\mu_g,\sigma_g) = \frac{1}{log_{10}(\sigma_g)\sqrt{2\pi}} exp\left[\frac{-(log_{10}(x)-log_{10}(\mu_g))^2}{2(log_{10}(\sigma_g))^2}\right]. \tag{2.27}$$

The log normal distribution looks like a Gaussian if the sizes on the x-axis are plotted on a log scale as can be seen when comparing Figures 2.7(a) and 2.7(b).

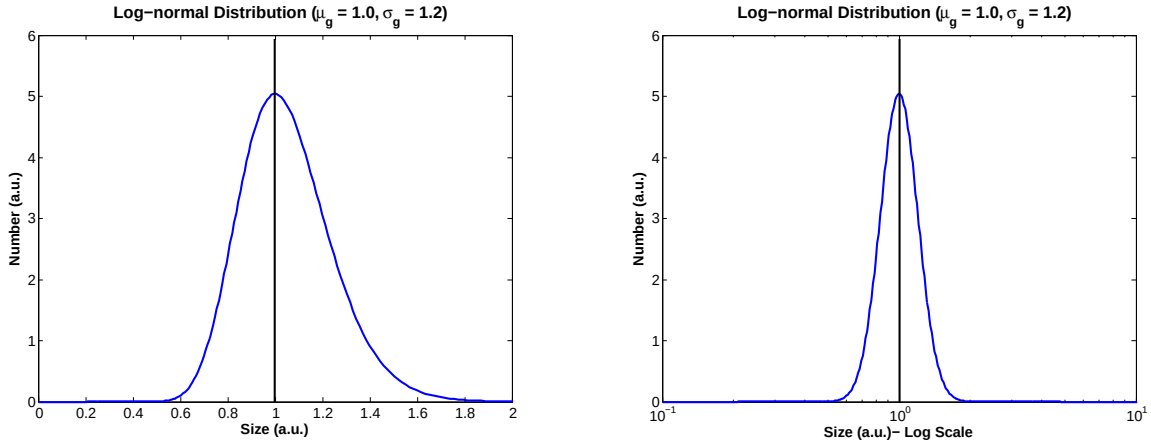

(a) Linear scale

(b) Log scale

Figure 2.7: Log normal distribution with a mean value, $\mu_g = 1$ and a standard width, $\sigma_g = 1.2$, plotted on (a) linear and (b) log scale.

The standard width, σ_g, is used to describe the "spread" of the log-normal distribution, an example of a narrow and wide distribution are shown in Figure 2.8(a) and 2.8(b), respectively.

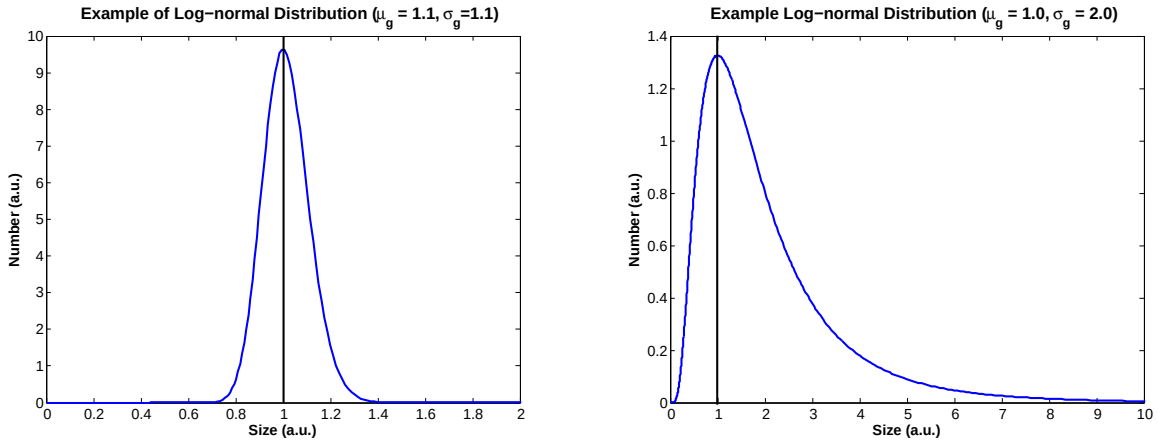

(a) Narrow

(b) Wide

Figure 2.8: Log-normal distributions with a narrow and a wide distribution width, given by σ_g.

Polarization Ratio for a Size Distribution

The size range is chosen as the size range of aerosols (in microns) that should be detected by this instrument. Sizes smaller than about 0.1λ will scatter like dipoles (see Rayleigh Scattering in Section 2.3) and aerosols much larger than about 20 μm have a significant mass and will fall too rapidly to be measured.

The best way to implement a log-normal distribution of aerosol is to use a log spaced set of points between 0.001 and 20 microns. A linearly spaced set of points are shown in Figure 2.9(a). This spacing is not selected because the fine and accumulation mode of aerosols size distributions are in the range below 1 micron, so to get accuracy in those distributions more points are needed in the smaller size range. A log spaced set of points is selected because it has many points at the smaller aerosols sizes and allows resolution in the fine and accumulation mode size ranges.

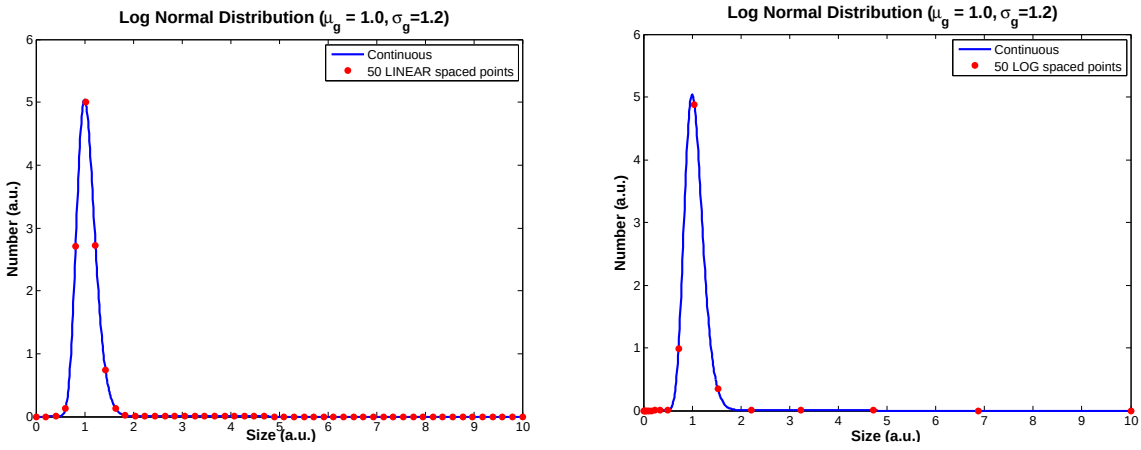

(a) 50 LINEAR spaced points

(b) 50 LOG spaced points

Figure 2.9: Log-normal distribution with $\mu_g = 1$ and $\sigma_g = 1.2$. The red dots represent spaced points, dx would be represented by the distance between the points.

In order to calculate the scattering for an entire size distribution the scattering must be calculated for all particles in that distribution and then summed to give a total scattering for the distribution. The polarization ratio (Equation 2.26) then becomes

$$PR(\theta) = \frac{I_{||}}{I_{\perp}} = \frac{\int |S_2(x,\theta)|^2 y(x) dx}{\int |S_1(x,\theta)|^2 y(x) dx}, \tag{2.28}$$

where the S_1 and S_2 notation is used to focus on the summation over all sizes, x. The angle dependence is also emphasized, since the total scattering intensity is not needed to form the scattering ratio at each angle(θ), the $y(x)$ described by the log-normal distribution (Equation 2.7(a)).

The term dx in Equation 2.28 is the size of the background size bin used. The background values and bin sizes can be spread evenly over the size ranges linearly or logarithmically. If these points are spread linearly all points and dx's are the same size, see Figure 2.9(a). However, if the points and bins are determined logarithmically then there are many points that describe the smaller size ranges and few points to describe the larger sizes, see Figure 2.9(b), here the bins, dx's, would have a varying size. Brown investigated this and determined that the difference between linear and log spaced background points was not significant enough to change the polarization ratio within the anticipated noise level.[25] The background log spaced bins are selected because they have more resolution in the fine and accumulation mode range, and less range in the broad course mode size range.

Addition of Molecular Scatter to the Polarization Ratio

To determine the concentration of aerosols it is important to take into account the number of particles and the number of molecules. The number density of molecules in the lower troposphere is approximately 2.54×10^{19} molecules/cm^3.[26] Thus to calculate the total polarization ratio the contribution of molecular(Rayleigh) scatter must be taken into account. The full polarization ratio used in this research is

$$PR(\theta) = \frac{I_{||}}{I_{\perp}} = \frac{\int N|S_2(x,\theta)|^2 y(x)dx + (2.54 \times 10^{19})S_{2molecules}(\theta)}{\int N|S_1(x,\theta)|^2 y(x)dx + (2.54 \times 10^{19})S_{1molecules}(\theta)}, \tag{2.29}$$

where N is the number concentration of aerosols in particles/cm^3.

2.2.2 Aerosol Parameter Sensitivity

The behavior of the polarization ratio is better understood as changes occur in the index of refraction, size distribution and number concentration. These are all the parameters that change the polarization ratio according to Equation 2.29. The effects on the real and imaginary part of the index of refraction on the polarization ratio are shown in Figures 2.10 and 2.11. The effect of the mean radius and standard width of the log-normal description of the aerosol distribution are shown in Figures 2.12 and 2.13. Brown[25] showed the effects of concentration changes on the polarization ratio in Figure 2.14. These five parameters will be the basis for discussions in Chapter 3, where the polarization ratio is explored as a deterministic measurement for aerosol characterization in several situations.

As seen in Figure 2.10 the polarization ratio has clearly defined structure that is shifting to increased scattering angle as the real index increases for this particular size distribution of aerosols. Figure 2.11 shows that the polarization ratio remains unchanged until the imaginary index increases beyond 0.5×10^{-3}, values higher than this indicate that the aerosol has a high absorption and this will effect the polarization ratio. Also seen in Figure 2.11 the imaginary index value does not effect the scattering angle location of the polarization ratio.

The structure in Figure 2.12 shows that when smaller aerosols (between 0.1 μm and 2.0 μm) are present the polarization ratio has a structure that increases amplitude as the scattering angle and mean size increase. Figure 2.13 shows that once the distribution spreads beyond 1.3 it loses all structure in the polarization ratio due to a particular size particle.

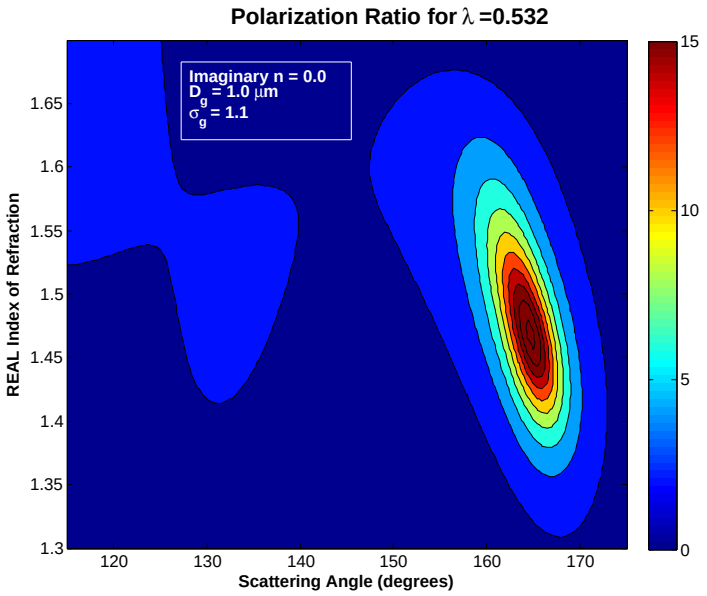

Figure 2.10: Contours show the effect of the real refractive index on the polarization ratio, for a specific case.

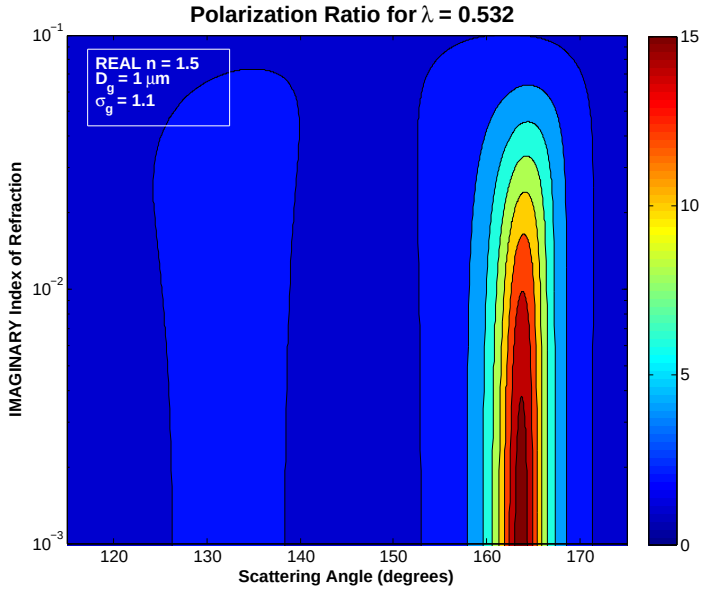

Figure 2.11: Contours show the effect of the imaginary refractive index on the polarization ratio, for a specific case.

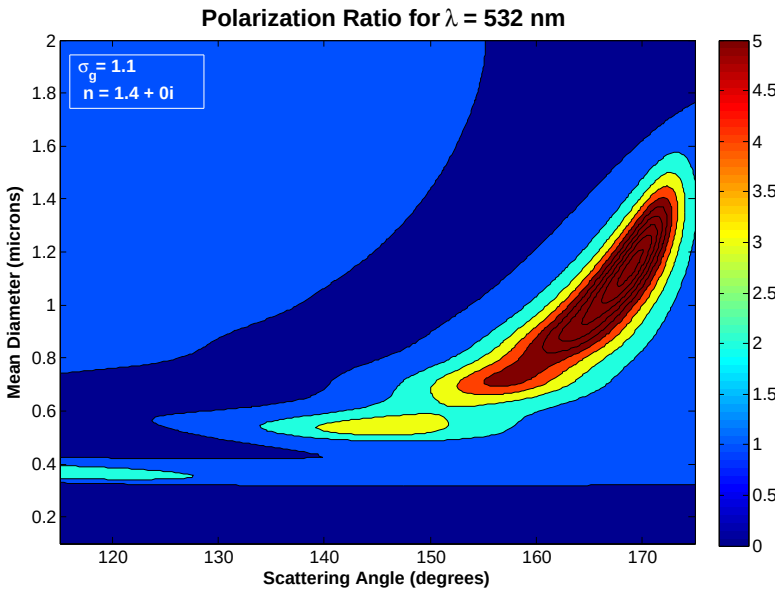

Figure 2.12: Contours show the effect of the mean diameter on the polarization ratio for aerosol sizes less than 2 microns in diameter.

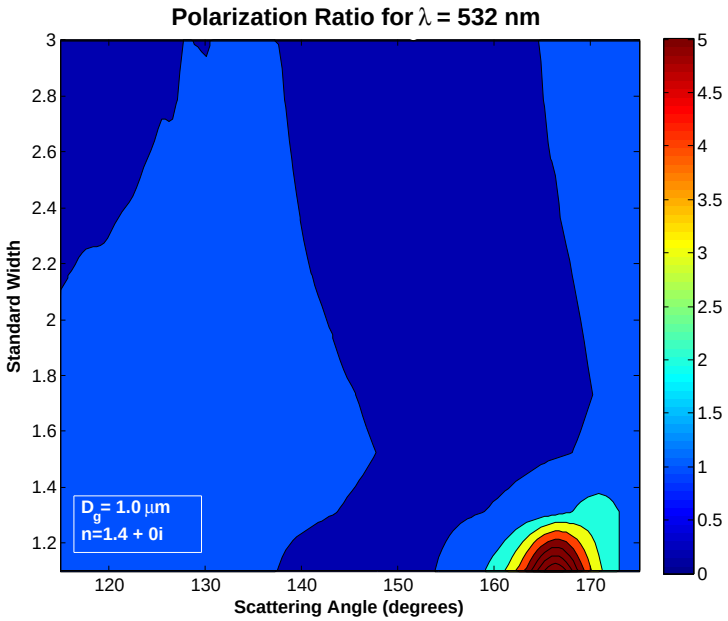

Figure 2.13: Contours show the effect of the standard width (σ_g) on the polarization ratio.

Brown[25] explored the affect of concentration on the polarization ratio and produced the results shown in Figure 2.14. At 407 nm, changes in total particle concentration, N ($\#/cm^3$) cause changes in the polarization ratio, for the selected log-normal particle size distribution ($\mu_g = 1.0\ \mu m$ and $\sigma_g = 1.1$).

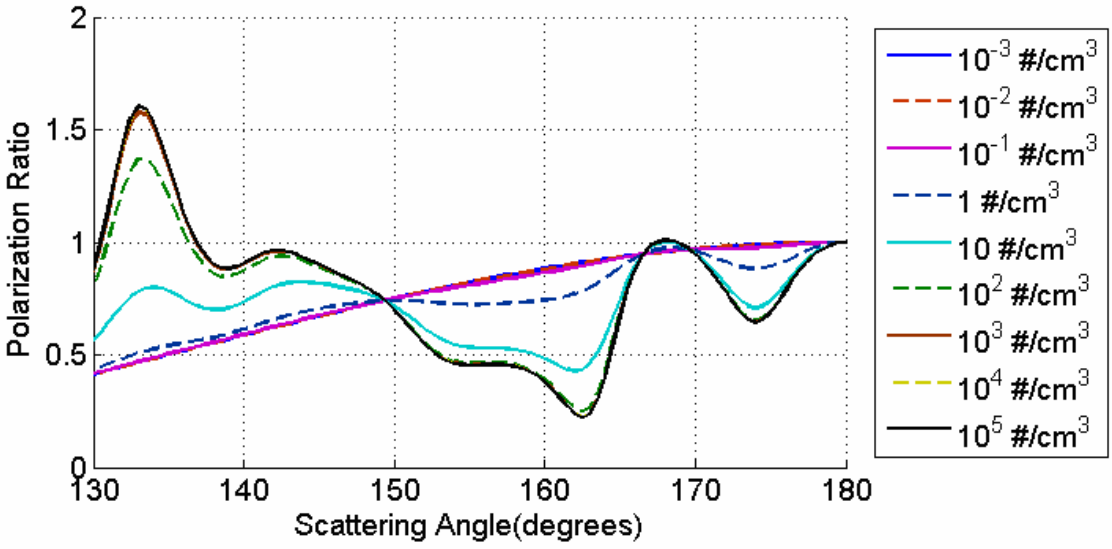

Figure 2.14: The effects of changing the concentration on the polarization ratio.[25]

2.3 Prior Instrument Development

The experimental application of these calculations was first investigated by Stevens.[13] He used the LAMP Raman LIDAR system with a horizontal beam across a 3.3 *km* path in a marine fog environment, and collected bistatic backscatter measurements to determine a size distribution of the primary aerosols present. The data was collected using a charge-coupled-device (CCD) imager to capture a range of angles, where the incident beam scatters. The scattering angle is measured from the z-axis, which is the direction of propagation for the laser beam. Typically the measurements include the backscattered angles between 120 and 175 degrees (see Figure 2.15).

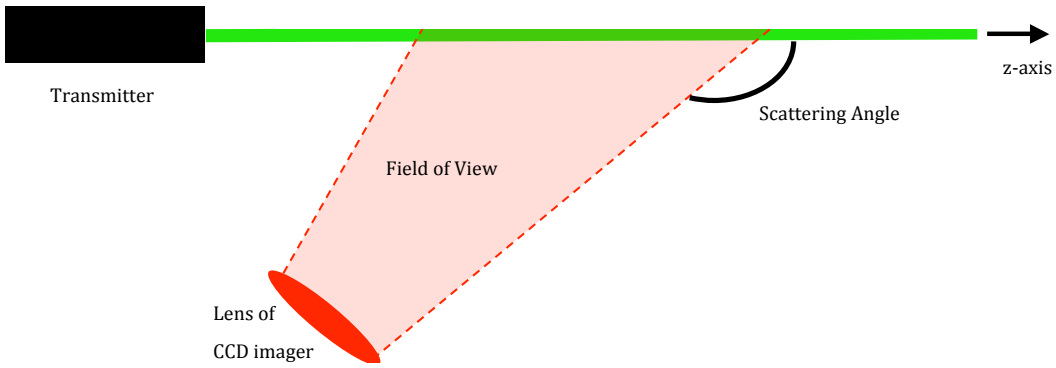

Figure 2.15: A schematic representation of the experimental set-up.

He employed a very high power laser and obtained a tri-modal distribution representing dust, marine aerosols and fog particles, in addition to the background atmospheric molecules, see Figure 2.16. Stevens laid the foundations for the bistatic scatter technique. He demonstrated that the polarization ratio is the quantity that should be examined to obtain aerosol characteristics.[13] Using the polarization ratio of the scattering phase functions of the two polarizations eliminates several sources of experimental error that would complicate the inversion process. After images of parallel and perpendicularly polarized light are taken, the polarization ratio is formed on a pixel by pixel basis to obtain the ratio at each measurement angle.

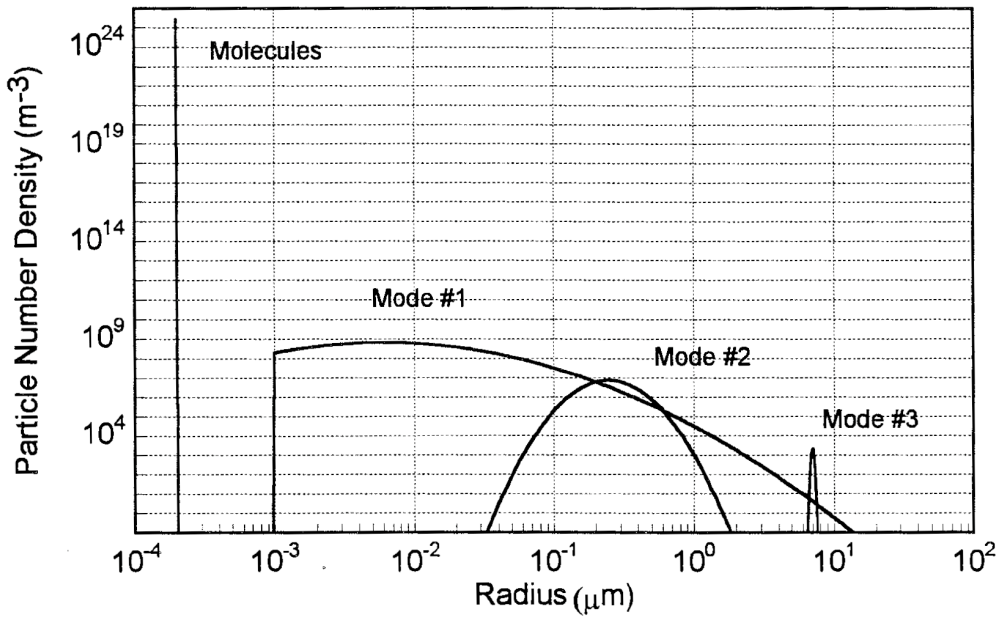

Figure 2.16: The tri-modal distribution found by Tim Stevens during a radiation fog event.[13]

The second student to investigate the backscatter technique was Novitsky.[15] He used the newer LAPS lidar system and analyzed a vertical beam. He studied several experimental techniques and analysis approaches to provide a more robust result. He explored the properties of aerosol distributions and developed a multistatic inversion algorithm to interpret the measured polarization ratio at each angle to find the size distribution of aerosols.[15]

The third student, Park, studied the multiple scattering problem.[24] He used a much lower power diode laser, but used the same angular scattering technique. He determined that if the optical depth(τ) is less than ≈ 0.3, even though the photons are scattered several times before they were collected by the receiver, they still closely follow the single scattering predictions of the Mie-Lorentz calculations for the range of backscattering angles of interest, i.e. 120 degrees to 180 degrees.[24] Figure 2.17 shows one example from his experiments. Optical depth is defined by the exponent of Beer-Lambert Law ($\tau = b_{ext} z$),

$$\frac{I}{I_o} = e^{-b_{ext} z},$$

where I is the received scattered intensity, I_o is the initial intensity from your light source, z is the path length, and b_{ext} is the extinction coefficient. The extinction coefficient is directly related to the number concentration and the extinction cross section (i.e. absorption plus scattering cross sections) of the aerosol.[4]

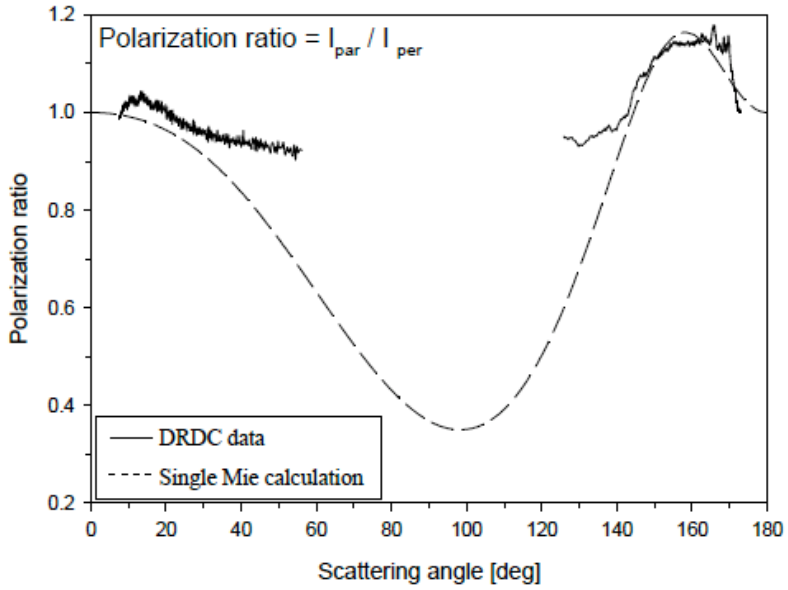

Figure 2.17: Multiple scattering measurements of the polarization ratio as compared to a calculated polarization ratio in heavy fog conditions (Park[24]).

The most recent student to study this topic was Brown,[25] who used a multi-wavelength (405 nm, 532 nm, 650 nm) transmitter with co-aligned beams. A diffraction grating was used to spatially separate the scattered beams imaged by a CCD camera, as shown in Fig. 2.18(a). This picture shows the horizontally polarized beams, another picture was taken of the vertically polarized beams as soon as possible for the polarization ratio for each wavelength shown in Figure 2.18(b). Figure 2.18(a) shows how the diffraction grating in front of the camera spatially separates the co-aligned beams.[33] The polarization ratio curves shown in Figure 2.18(b) show ratios formed from data taken during a smoke experiment at the Environmental Protection Agency (EPA) Aerosol chamber on November 24, 2009. The jaggedness on the peak of the blue curve is due to background reflections.[25]

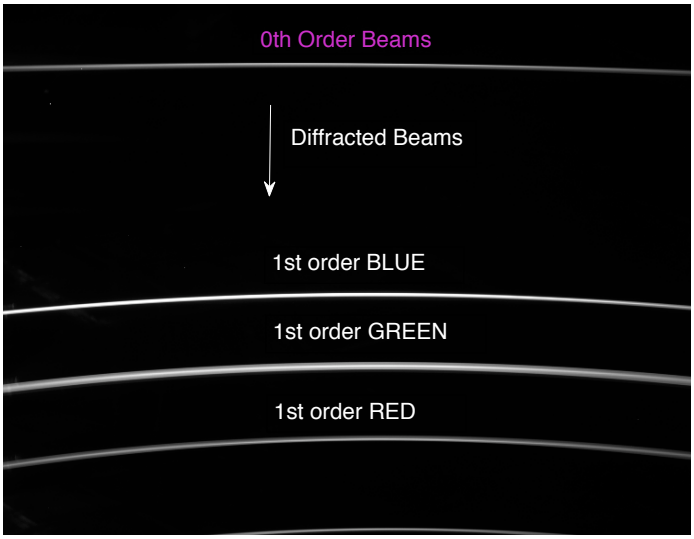

(a) Raw intensity

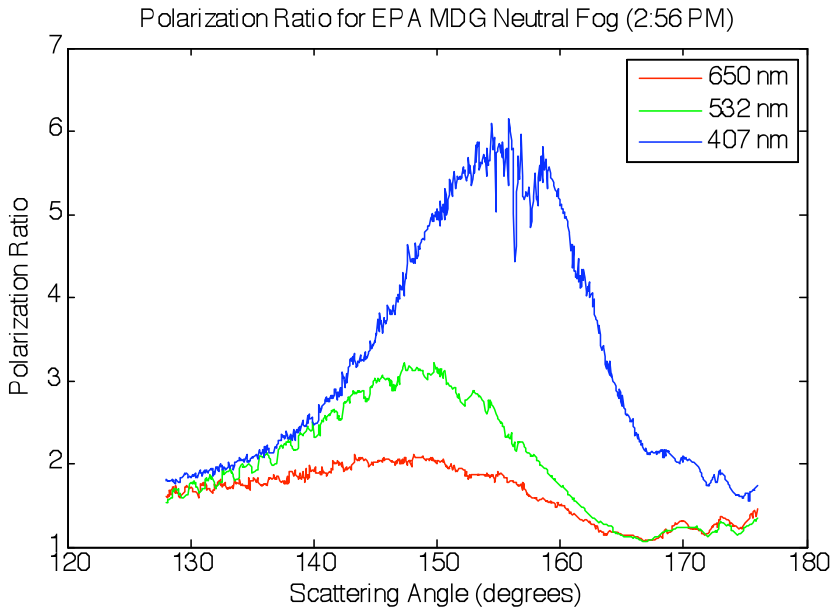

(b) Polarization ratios

Figure 2.18: Data taken at the EPA aerosol chamber during a smoke experiment by Brown.[25]

Abbreviated derivations of Rayleigh and Mie scattering are presented in this chapter as an introduction to optical scattering. Both scattering techniques are based on the polarization of the light and the size of the scatterer. The Rayleigh calculations are used to model scattering

of light from aerosols much smaller than the wavelength ($ka << 1$). The Mie calculations are implemented when the scatter is comparable to or larger than the wavelength. The larger aerosols cause more structure to appear in the scattering phase function. Phase functions are dependent on the polarization and wavelength of the incident light, the size of the aerosol, and the index of refraction of the aerosol. The calculated phase functions are used to form the polarization ratio for a single aerosol. The polarization ratio and phase functions are then extended to include a distribution of aerosol sizes, typical of atmospheric distributions. The polarization ratio for a size distribution is dependent on the mean radius, standard width, concentration, and index of refraction.

The multiwavelength multistatic instrument measures the angular scattering to form a polarization ratio. The measured polarization ratio is used to determine the aerosol distribution properties, such as mean radius, standard width, concentration and index of refraction in the following chapters.

Chapter 3

Exploration of the Polarization Ratio Method

Previous researchers[13,15,24,25] have explored the polarization ratio method as a way to characterize aerosol size distributions. This chapter is intended as a study of the applications and limitations of the polarization ratio. Polarization ratios are examined as simulated experimental noise is added and limitations of this method are discussed, including errors in the parameters for a few typical cases . In addition, the applicability of this method to analyze multi-modal aerosol distributions is explored through the use of simulated polarization ratios. After this insight is gained, the selection of optimum wavelengths for future experiments to best measure aerosols based on their size and index of refraction can be made.

3.1 Sensitivity of the Polarization Ratio in the Ideal Case

An aerosol size distribution and concentration is chosen for the exploration of the polarization ratio, see Table 3.1. This particular distribution was selected because it is in the range of possible aerosol size and number concentration likely to be measured by this instrument. The standard width selected is common for atmospheric aerosols and it is in the middle of the range of realistic values. The wavelengths used are 405 nm, 532 nm and 655 nm, because they are used in the experimental setup (described later in Chapter 5), and they are readily available laser diode wavelengths. The polarization ratios for this distribution at these three wavelengths is shown in Figure 3.1.

Table 3.1: Parameters used in the idealized simulation.

Parameter	**Mean Radius (μ_g)**	**Standard Width (σ_g)**	**Concentration (N)**
Value	0.3 μm	1.2	600 $\#/cm^3$

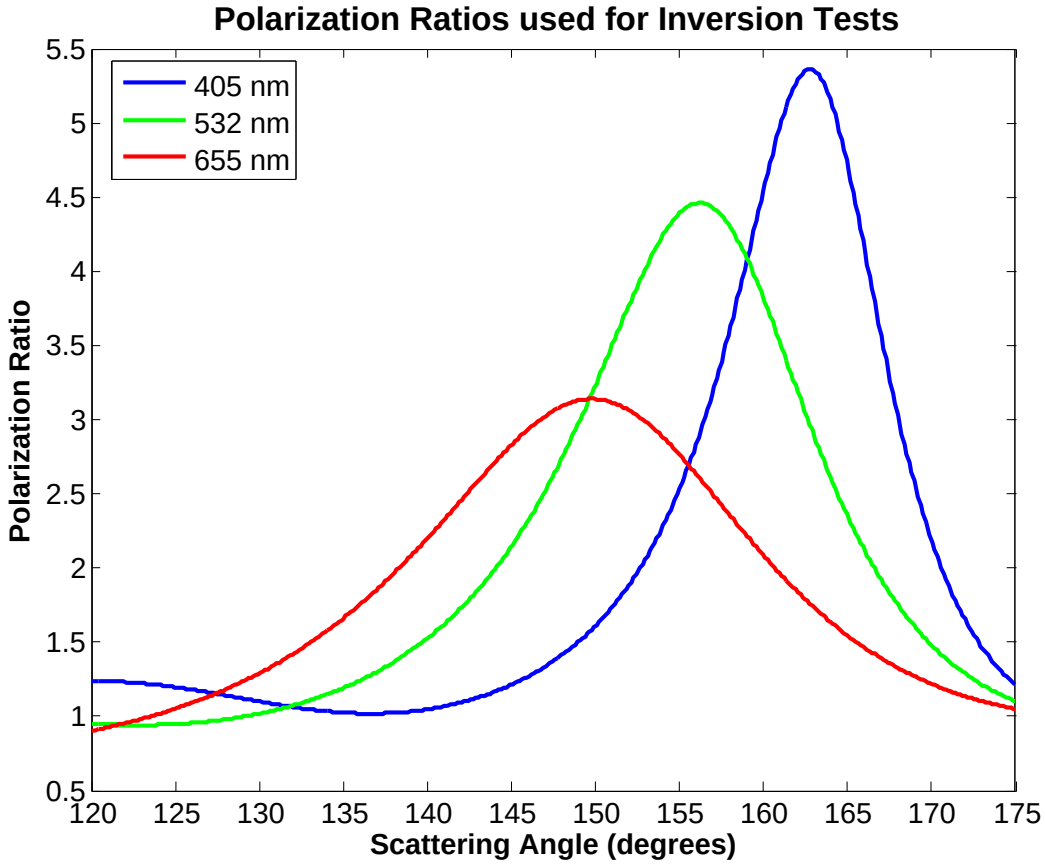

Figure 3.1: Calculated polarization ratios for idealized simulation at all three wavelengths.

From previous work,[25] the sensitivity of the aerosols size distribution and concentration should be tested to find the useful range of parameters. The concentration sensitivity tests for this aerosol distribution at all three wavelengths are shown in Figure 3.2.

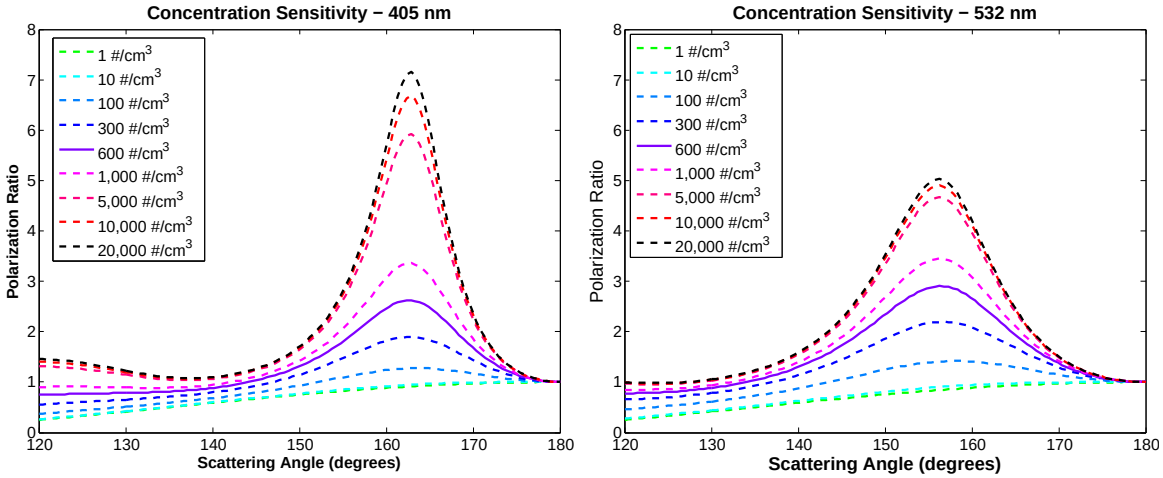

(a)

(b)

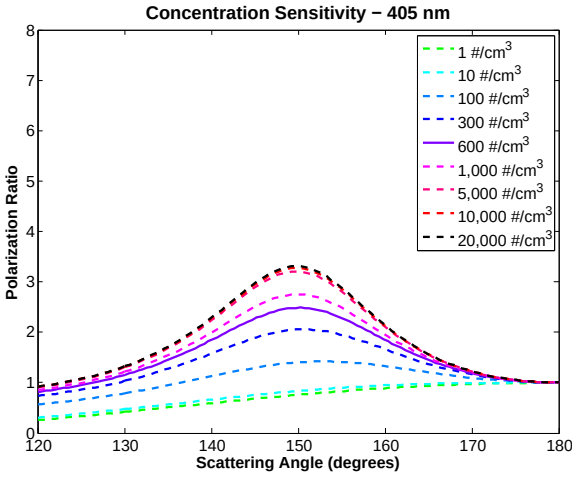

(c)

Figure 3.2: The polarization ratio calculated at multiple concentrations for each of the three wavelengths: (a) 405 nm, (b) 532 nm, and (c) 655 nm. The concentration used, 600 $\#/cm^3$, is shown in all plots as the solid line.

From Figure 3.2 it is clear that the polarization ratios for all three wavelengths change based on the concentration, and that the concentration of 600 $\#/cm^3$ is in the middle of the detectable range for all three wavelengths.

3.1.1 Singularity of Aerosol Parameters

Ultimately, the analysis procedure will need to use the measured polarization ratio and match it to calculated polarization ratios by changing the mean radius, μ_g, the standard width, σ_g and the concentration, N. Therefore, to quantitatively determine the difference between the calculated and measured polarization ratios the squared-error (SE) is defined:

$$\text{SE} = \sum_{j} \sum_{i=1}^{n} \left(PR_{calculated}(\theta_i) - PR_{measured}(\theta_i) \right)^2 , \tag{3.1}$$

where $PR_{measured}$ is the polarization ratio measure at each point, and $PR_{calculated}$ is the calculated polarization ratio with the inversion variables. The value, n, is the index over all points to be analyzed, and j is the index over the wavelengths; these values are defined by each experiment and are not a constant.

The squared-error is calculated near the exact values to examine the minimum of the squared-error to determine the uniqueness of the three parameters, see Figure 3.3. This shows that the solution for all three parameters is unique and should converge to the input parameter values.

The parabolic shapes of the squared-error in the radius and standard width are indicative of a unique converging solution, at least when the remaining parameters are fixed at the input values. The non-parabolic shape of the concentration squared error plot, shown in Figure 3.3, is an indication that the concentration is not well defined. Although the squared error converges to the input value of 600 $\#/cm^3$, noisy data sets would produce a distribution of measured concentrations, which is not symmetric; these cases would result in a tail at the larger concentrations, since the convergence is weaker in that direction. This could lead to and over estimation of the concentration in the average value.

The root of the squared-error is also defined, because it is used in later chapters as a way to measure the of a result (see Chapter 4). This quantity is referred to as the fitness value (absolute error).

$$\text{fitness} = \sum_{\lambda} \sum_{i=1}^{n} \sqrt{\left(PR_{calculated}(\theta_i) - PR_{measured}(\theta_i) \right)^2} \tag{3.2}$$

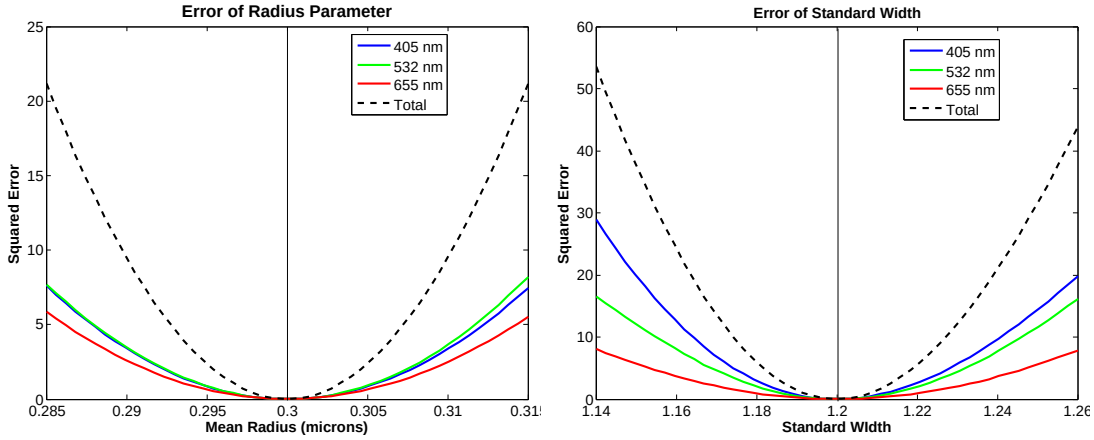

(a) (b)

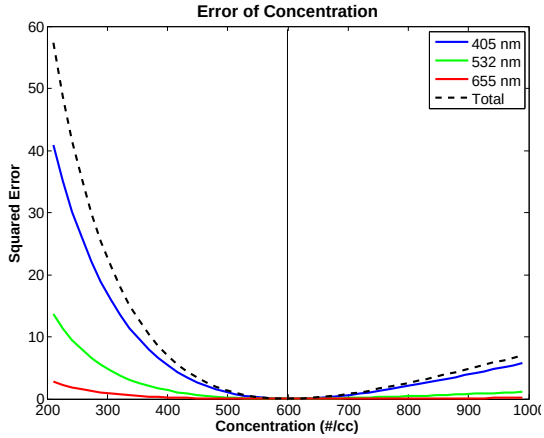

(c)

Figure 3.3: The squared-error of the polarization ratios around each of the input parameters ($\mu_g = 0.3\ \mu m$, $\sigma_g = 1.2$ and $N = 600\ \#/cc$).

The co-dependence of the parameter values can be evaluated by showing the fitness value as a function of two parameters, while the other one is held fixed. Figures 3.4, 3.5, and 3.6 show the fitness hyper-surface with one of the parameters fixed and the other two varied. All three figures show that the solution should converge to the input values, i.e. the polarization ratio is sensitive in all three parameters.

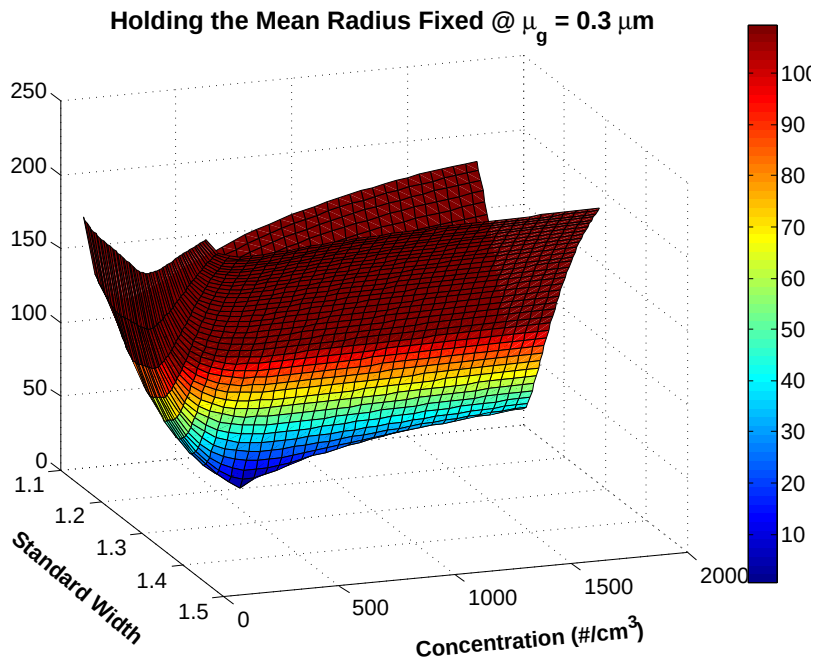

Figure 3.4: The fitness surface when the radius, μ_g, is fixed at 0.3 μm.

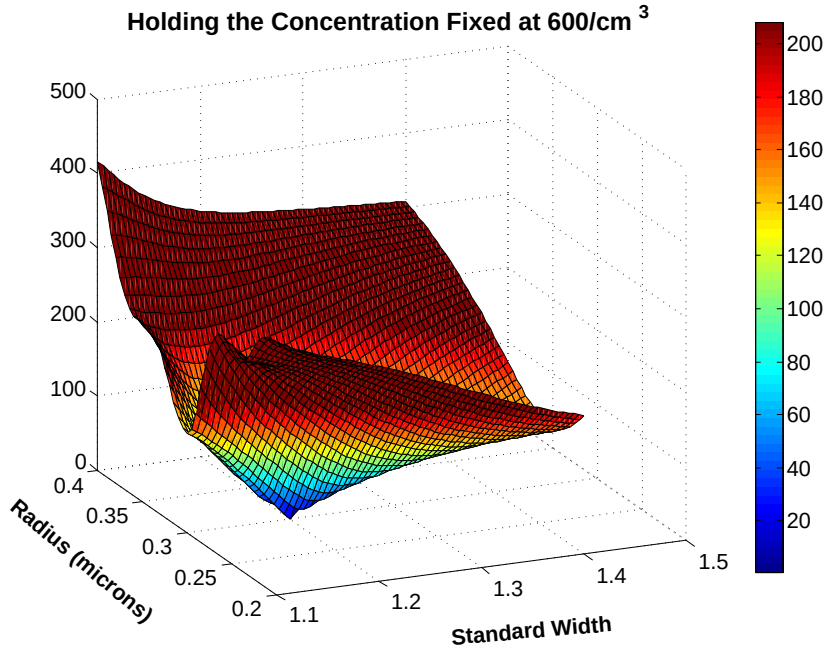

Figure 3.6: The fitness surface when the concentration is fixed at 600 #/cc.

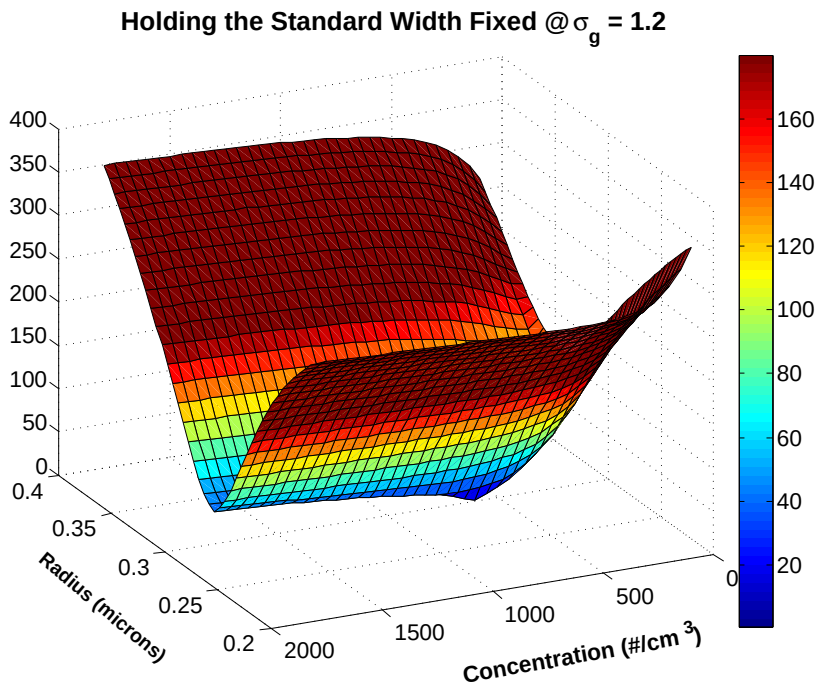

Figure 3.5: The fitness surface when the standard width, σ_g, is fixed at 1.2.

The fitness hyper-surface shows that the convergence of the polarization ratio is unique, since there is a defined point where the fitness value converges to zero, and the location of this point is consistent with the input values for each of the parameters. Therefore, this distribution appears to have no co-dependance between the three parameters, and the solution is unique for all three parameters.

Notice that when the concentration is fixed in Figure 3.6 there is a clear and steep convergence at the input radius and standard width parameters. The steepness of the convergence is distorted when the concentration is allowed to vary, shown by a valley that slowly slopes toward the input concentration, as seen in Figures 3.4 and 3.5. This shape is also present when the squared-error is calculated in Figure 3.3(c), indicative of less convergence at higher concentrations.

3.1.2 Assumptions Regarding Index of Refraction

Until this point the index of refraction value has been assumed. In an unknown environment the index of refraction of the aerosol measured is not known. Presented here is a discussion on how the index of refraction would change the calculated polarization ratio (see Figures 3.7 and 3.8).

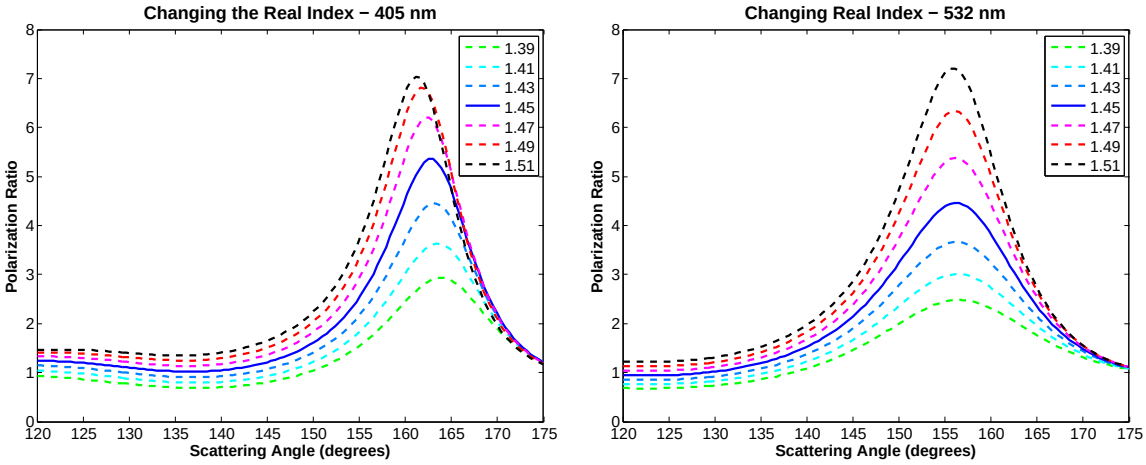

(a)

(b)

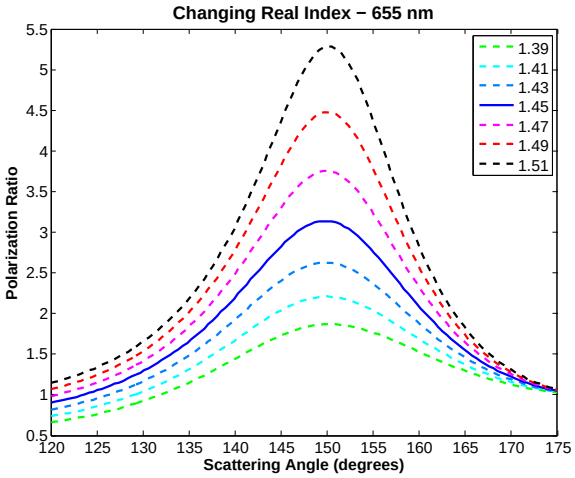

(c)

Figure 3.7: Calculated polarization ratio with a changing real index of refraction for (a) 405 nm, (b) 532 nm and (c) 655 nm . The value used in this analysis section is a solid line ($n = 1.45 + 0.001i$, all imaginary index values are $0.001i$).

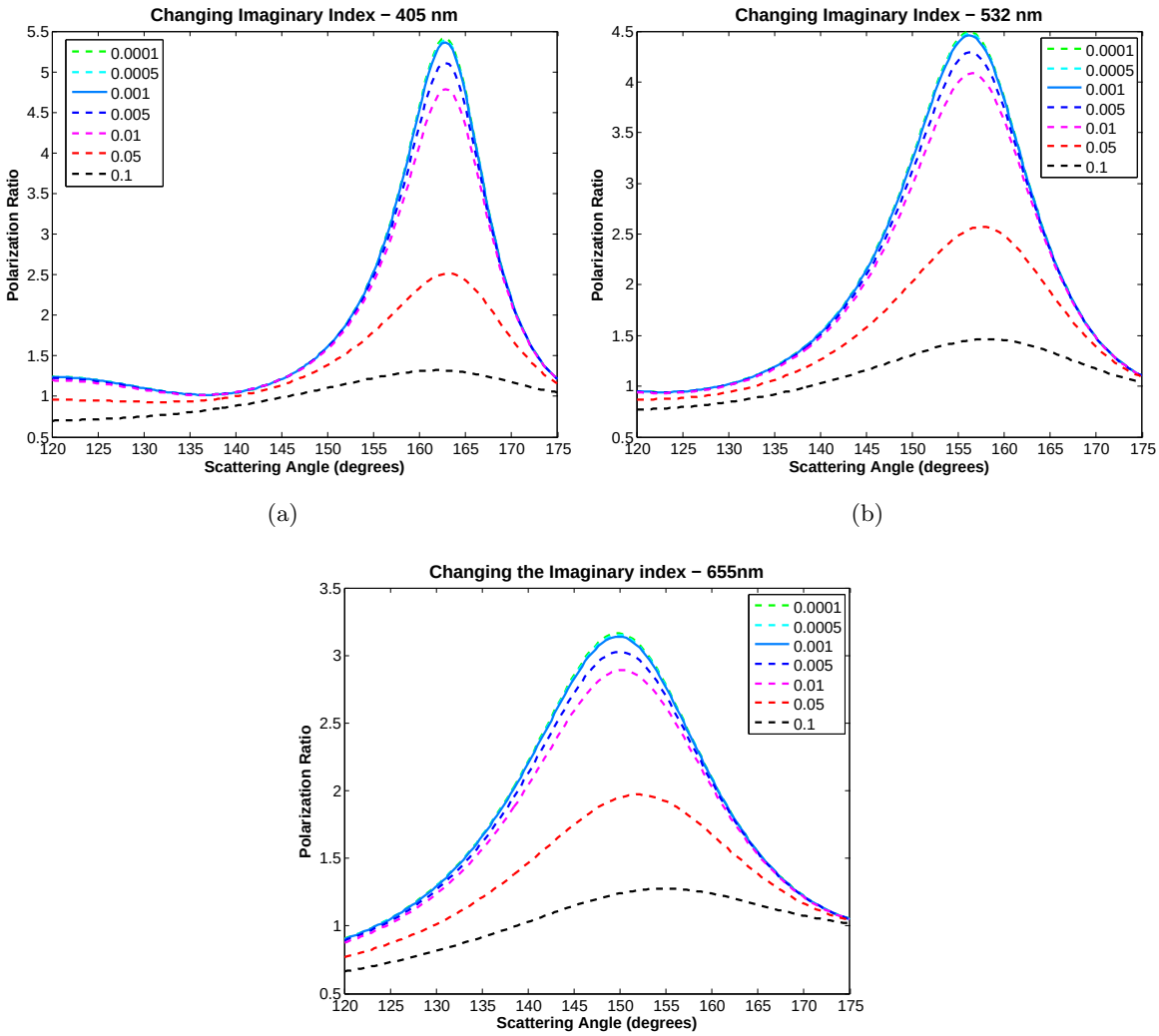

(a) (b)

(c)

Figure 3.8: The calculated polarization ratio for (a) 405 nm, (b) 532 nm and (c) 655 nm with a changing imaginary index of refraction. The value used in this analysis section is a solid line ($n = 1.45 + 0.001i$, all the real values are 1.45).

From these figures it is clear that the real index has a greater effect on the polarization ratio than the imaginary part. The imaginary index of refraction does not effect the polarization ratio until the index increases above 0.005, i.e. for high absorption. However, a smaller real index decreases the magnitude of the polarization ratio, similar to the way the concentration effects the magnitude, compare Figures 3.2 and 3.7. Since the concentration is a desired aerosol parameter to characterize the distribution the index of refraction must be assumed. The index

of refraction used in the analysis will need to be determined by another method outside of this instrument.

3.1.3 Wavelength Selection based on ka

The Mie scattering calculations in Chapter 2 were based on the ka value of the aerosol, recall that $ka = (2 \times \pi \times radius)/(wavelength)$, where the radius and wavelength are given in the same units, so ka is unit-less. The ka value is used to determine the optimum optical configuration value based on the strong squared-error convergence in the radius parameter.

The curvature of the squared-error values can be estimated by a second order polynomial (a parabola), where the coefficient of the second order is the dependance on that variable. When the coefficient is maximized the strongest convergence is obtained. This technique is similar to the second order Taylor expansion method used by Bevington[34] to examine the χ^2 error, this method has be adapted to use the squared-error in Equation 3.3.

$$SE = \frac{\partial^2 SE}{\partial r^2}(r)^2 + \frac{\partial SE}{\partial r}r + Constant \tag{3.3}$$

where SE is the squared-error, and a is radius parameter. The second order coefficient used to measure the steepness of convergence is the second derivative of the squared-error with respect to the radius parameter. Maximization of the second order coefficient of the squared-error indicates a strong convergence, therefore, in a minimization scheme the reciprocal of the second order coefficient is minimized. Maximum convergence is needed to best determine the parameter once noise is added. The reciprocal of the second order coefficient of the squared-error in terms of the ka value is shown in Figure 3.9, assuming the index of refraction is fixed at 1.45+0.001i, just as it was for the discussion in Section 3.1. This shows that there is a clear minimum of the reciprocal value, so there is a clear maximum coefficient that will provide the greatest determination of the distribution parameters.

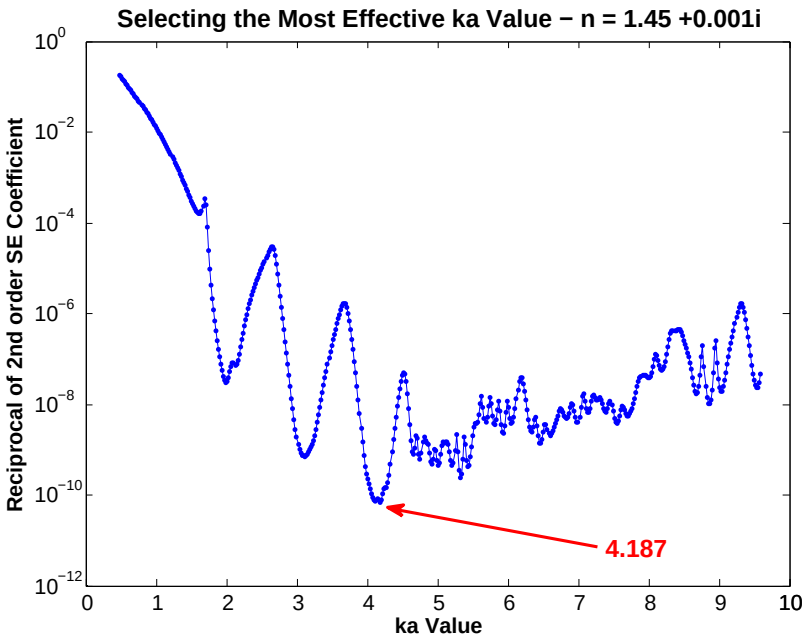

Figure 3.9: Optimum ka value for an index of refraction of 1.4 + 0.001i.

The minimum error due to the wavelength is clearly minimized at a ka value of 4.187. The ka values for the wavelengths used in Section 3.1 are shown in Table 3.2.

Table 3.2: The ka values for the visible transmitter wavelengths with a $\mu_g = 0.3\ \mu m$ aerosol.

Wavelength	**ka Value**
405 nm	4.65
532 nm	3.54
655 nm	2.88

The values for the 405 and 532 nm wavelengths are the closest to this optimum ka value and this is why they were the most deterministic in finding the radius value for the single mode distribution of 0.3 radii aerosols. By examining Figure 3.3a the 405 nm and 532 nm wavelengths are nearly on top of each other indicating that they are both equally deterministic of the radius parameter value, as is expected by their closeness to the optimum ka value. The process of

finding the optimum ka value for given values of index of refraction was repeated, a selection is shown in Figure 3.10.

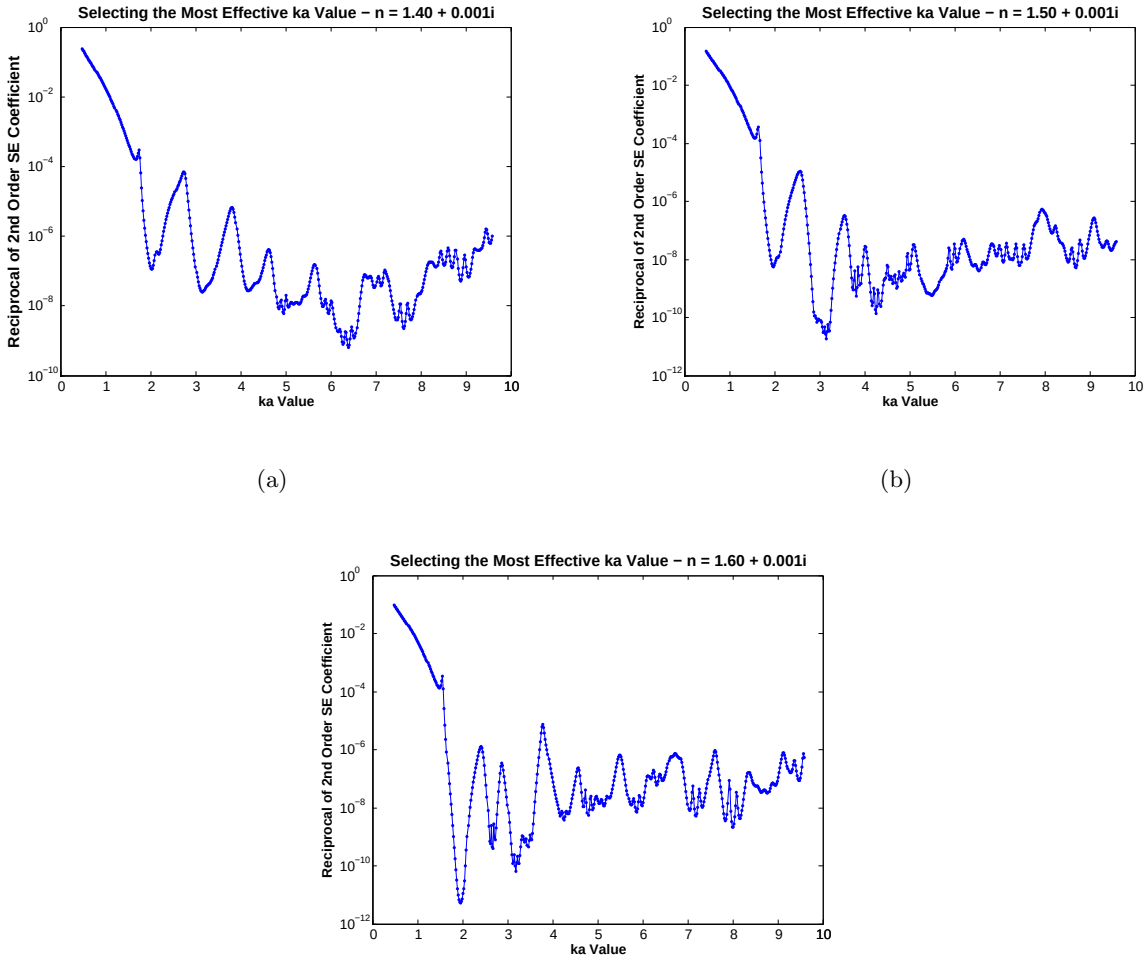

Figure 3.10: The reciprocal of the second order coefficient of the squared-error as a function of ka, for multiple indices of retraction.

This leads to a trend in optimum ka values given the index of refraction. This trend is shown for a typical range of atmospheric indices of refraction, as shown in Figure 3.11.

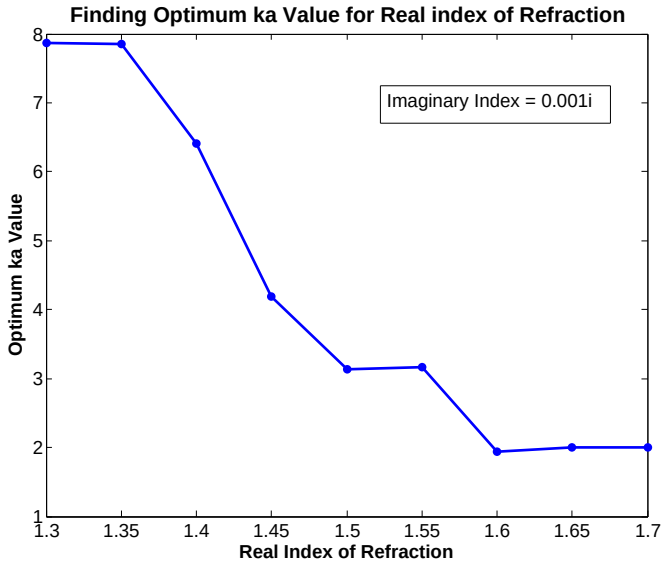

Figure 3.11: Optimum ka value as a function of real index of refraction, the imaginary index is fixed at 0.001.

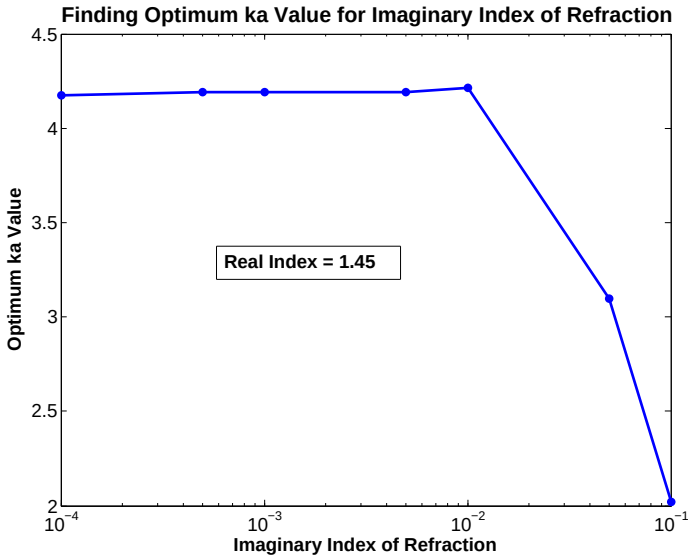

Figure 3.12: Optimum ka value as a function of imaginary index of refraction, the real index is fixed at 1.45.

The index of refraction of the aerosol measured needs to be known for the polarization ratio to be a deterministic measurement of aerosol size distributions (see Section 3.1.2). Once the index and aerosol size are determined the optimum wavelength can be found based on the ka value from Figure 3.11.

Optimum ka values were also examined based on the imaginary index of refraction, as shown in Figure 3.12.

The effect of the imaginary index does not change the optimum ka value until there is a very high absorption (≥ 0.1). Therefore, emphasis should be put on the determination of the real index of refraction to find the optimum ka value.

3.2 Polarization Ratio Sensitivity with Simulated Noise

To fully evaluate the polarization ratio as an effective value for aerosol characterization, the addition of noise that mimics the measured experimental noise must be examined. This section describes the way to computationally add noise to a calculated polarization ratio in a way that accurately represents the noise found experimentally. The polarization ratio is then re-evaluated using squared-error analysis to determine how well it can determine the aerosol characteristics with the added noise.

3.2.1 Modeling Experimental Noise

In previous work by Brown,[25] white Gaussian noise added to the polarization ratio was used to represent the experimentally measured noise. Here white Gaussian noise is again added to the polarization ratio with a signal-to-noise (SNR) of 20, as shown in Figure 3.13.

In most applications were data is measured noise is simulated in the measurements, however noise is added here to the polarization ratio even though the relative intensities are measured to form the ratio. Adding noise to the measured intensities was also explored, but provided noise on the polarization ratio that did not accurately represent that of the experimental results. Directly adding noise to the polarization ratio provided a better match. Adding noise to the measured intensities is presented in Appendix A.

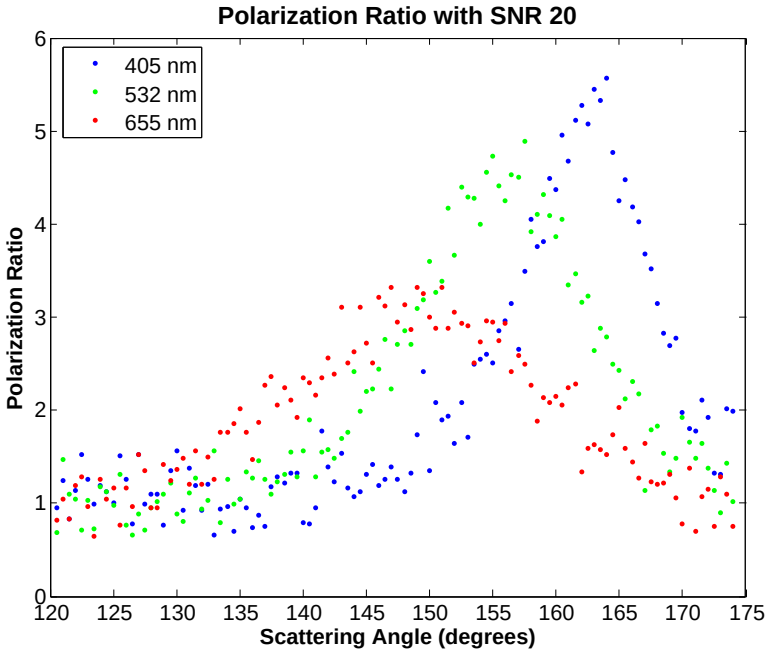

Figure 3.13: Signal to noise ratio of 20 added to the polarization ratios shown in Figure 3.1 at every half degree.

3.2.2 Re-evaluation of Polarization Ratio

Once experimental noise is added to the ratio the squared-error and fitness values are examined, to determine the convergence of a solution to the input parameter values. The squared-error plots in Figure 3.14 are made when randomly generated white Gaussian noise is added (SNR of 20) the polarization ratios. The addition of noise is always going to give a non-zero squared-error, so the squared-error has been vertically shifted till the minimum value for each of the wavelengths is zero, for easier comparison with Figure 3.3. The minimum values for the noise case are no longer at the input parameter values, but are shifted slightly, as observed in each figure. From these figures it is expected that the concentration has the largest variation, because the minimum is the broadest. This is reaffirmed in Figure 3.15 where 100 ratios were simulated with a SNR of 20 and the value that minimized the total squared-error is recorded. This is essentially a Monte-Carlo approach to evaluate the parameter errors.

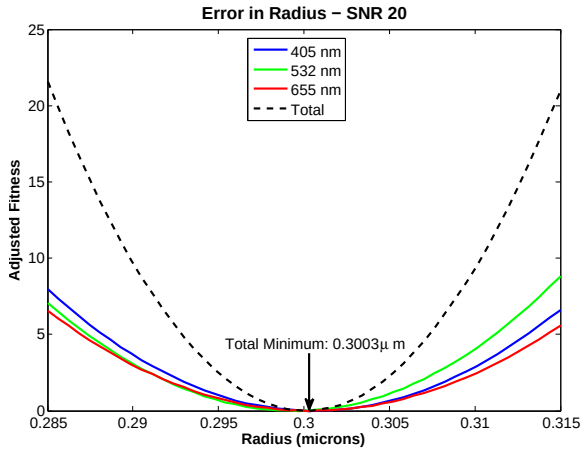

(a)

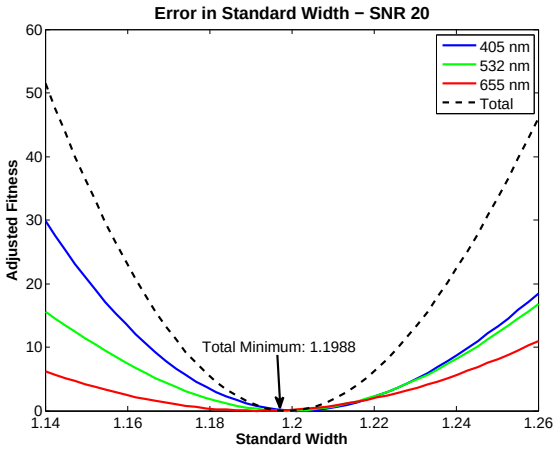

(b)

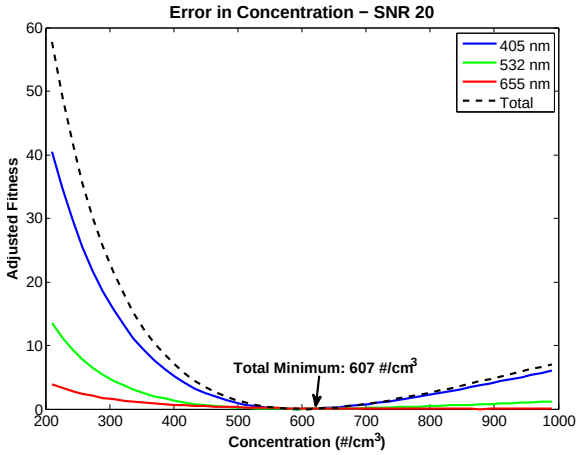

(c)

Figure 3.14: The squared-error for the three wavelengths and the total is calculated when holding all parameters fixed except one, and the minimum value vertically shifted to zero. This represents a squared-error analysis for one set polarization ratios with white Gaussian noise added.

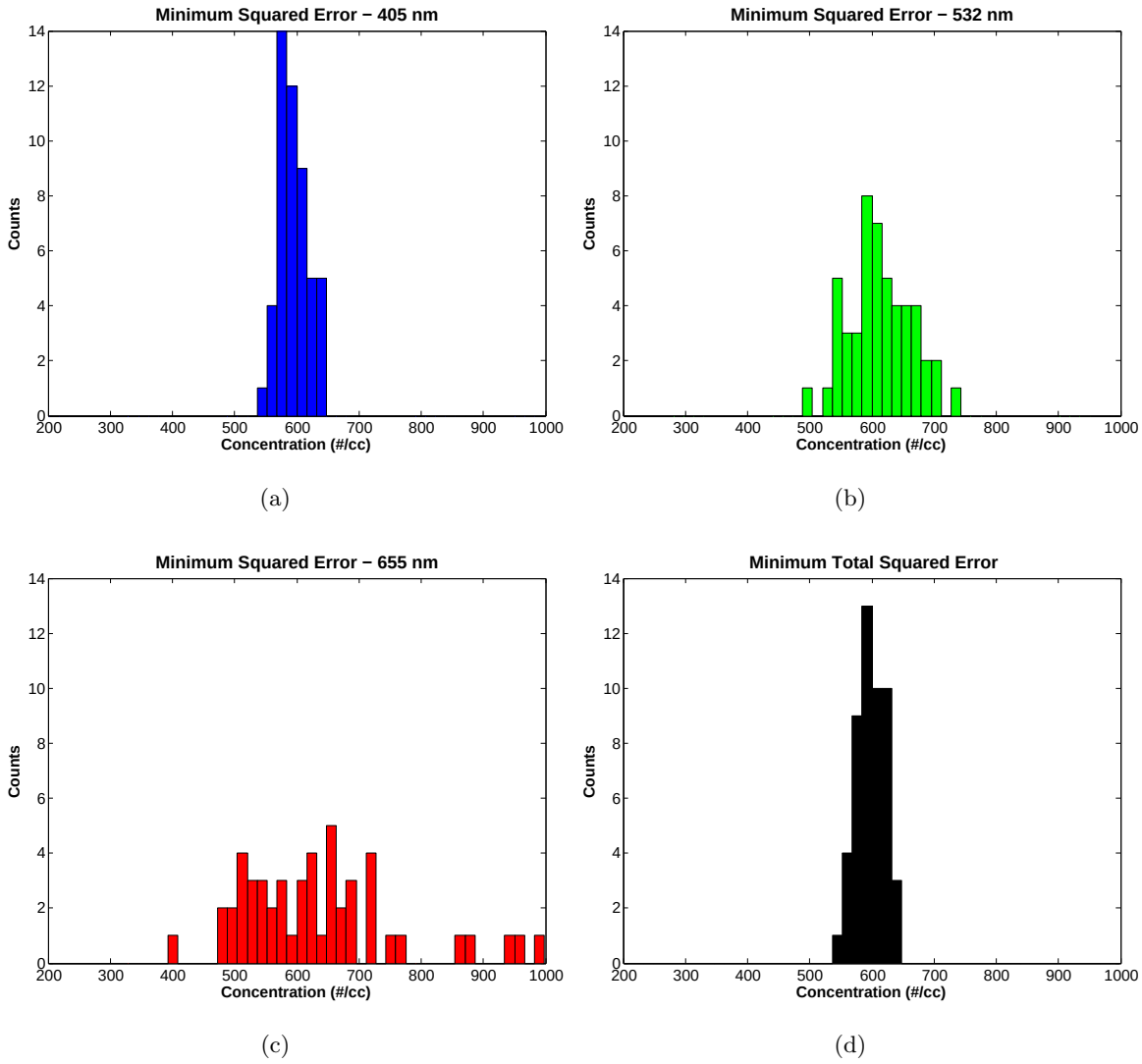

Figure 3.15: The minimum squared-error for 100 polarization ratios with a SNR of 20.

The summation of squared-errors of all three wavelengths slightly improves the location of the minimum squared-error. The 655 nm and 532 nm wavelengths show a wider spread in the minimum of the squared-error. The deviation of the minimum squared-error for the 655 nm and 532 nm wavelengths tend toward a higher concentrations. This is expected since the curvature of the squared-error of the concentration shown in Figure 3.14 has a less severe slope for higher concentrations. The physical reasons stems from the fact that the creation of the polarization ratio removes the total scattered signal strength. The polarization ratio only contains information on concentration relative to the known molecular scatter. The shorter

wavelengths are more sensitive to these molecular effects, and thus are more critical to the concentration measurement.

3.3 Application to Multi-Mode Distributions

In the previous sections, a single mode distribution of aerosols is explored. This distribution is in the accumulation mode size range. Aerosols typically occur in the fine (diameter < 0.1 microns) and course (diameter > 1 micron) modes as well. A mode in each of these size ranges is used for analysis in bi-modal and tri-modal configurations to test the applicability of the polarization ratio method to multi-mode distributions. Based on the optimum ka value, the ka values for each of the modes should be examined are shown in Table 3.4.

Table 3.3: The fine, accumulation and course mode distributions used in multi-mode exploration.

Mode	**Radius (microns)**	**Standard Width (σ_g)**	**Concentration ($\#/cm^3$)**
Fine	0.05	1.7	10,000
Accumulation	0.3	1.2	600
Course	4.0	1.01	0.01

Table 3.4: The ka values for all three modes are given for the selected wavelengths (index of refraction $n = 1.45 + 0.001i$).

Wavelength (nm)	**Fine Mode** ($\mu_g = 0.05\mu m$)	**Accumulation Mode** ($\mu_g = 0.3\mu m$)	**Coarse Mode** ($\mu_g = 4.0\mu m$)
405	0.775	4.65	62.1
532	0.591	3.54	47.2
655	0.480	2.88	38.4

Fine and Accumulation Modes

The fine and accumulation bi-modal size distributions are shown in Figure 3.16(a) with the calculated polarization ratios shown in Figure 3.16(b). The squared-error for each parameter is calculated with no noise in the polarization ratio, as shown in Figure 3.17. Each of the six parameters show convergence to the input value with no noise in the ratio. Noise is added

to the polarization ratio and the squared-error is calculated for each of the six parameters, as shown in Figure 3.18.

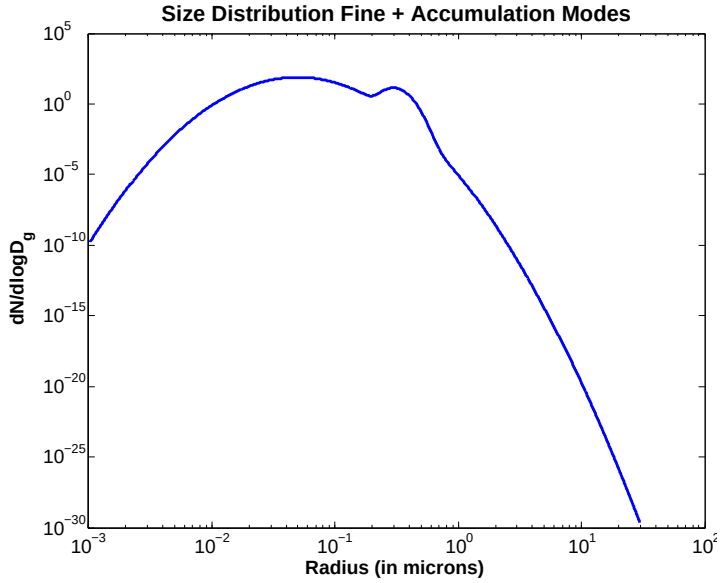

(a)

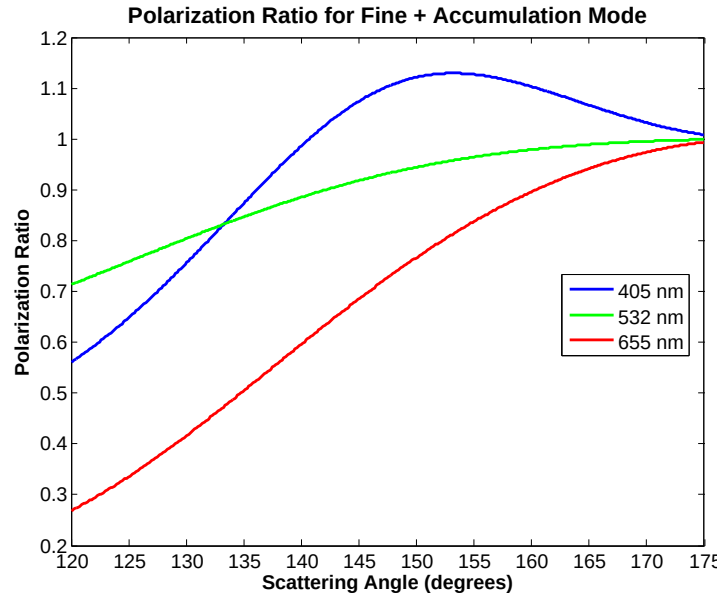

(b)

Figure 3.16: The bi-modal size distribution (a), and the polarization ratio (b) are shown for the fine and accumulation modes listed in Table 3.3.

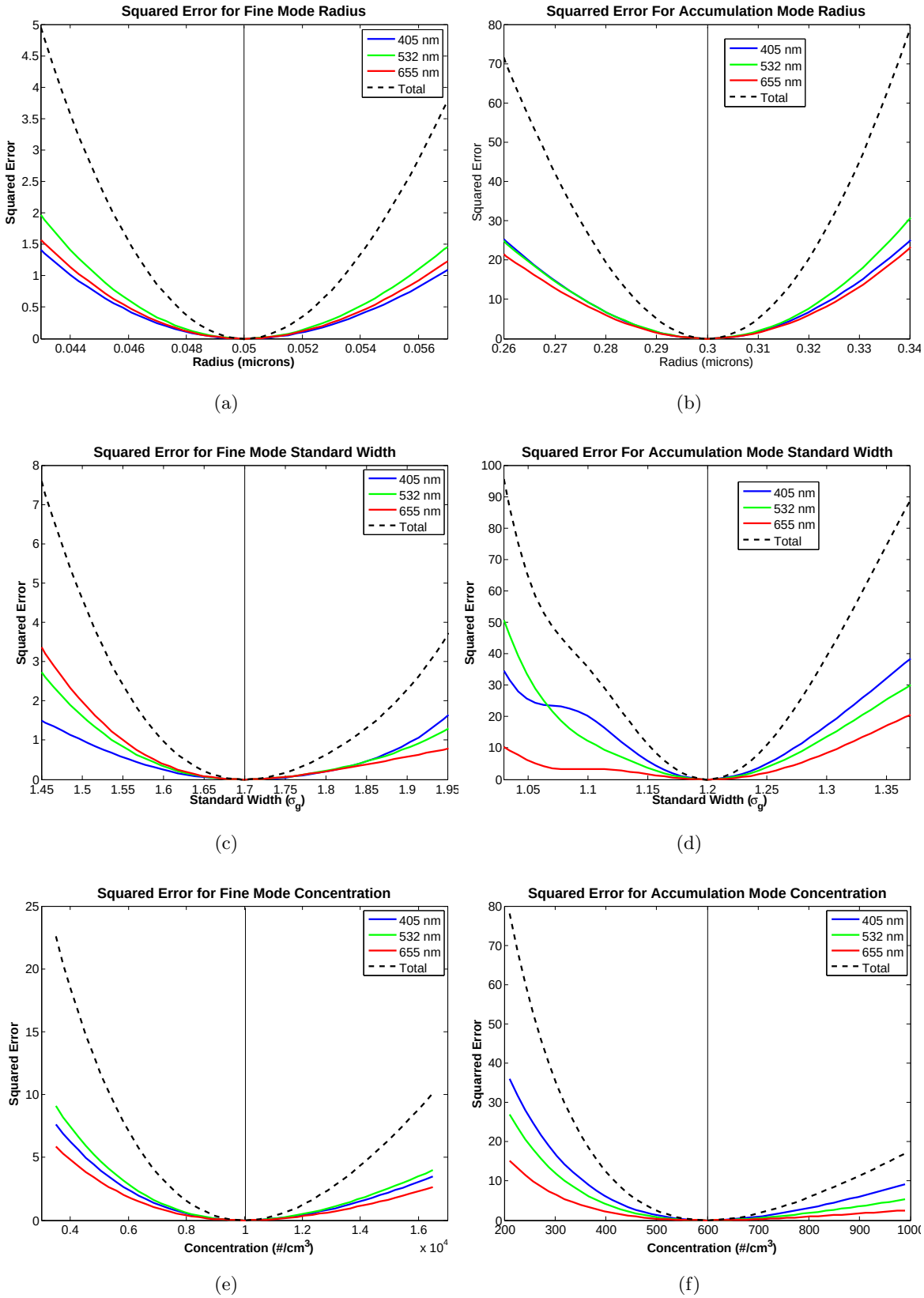

Figure 3.17: The six parameter squared-error analysis for the combined fine and accumulation mode distributions.

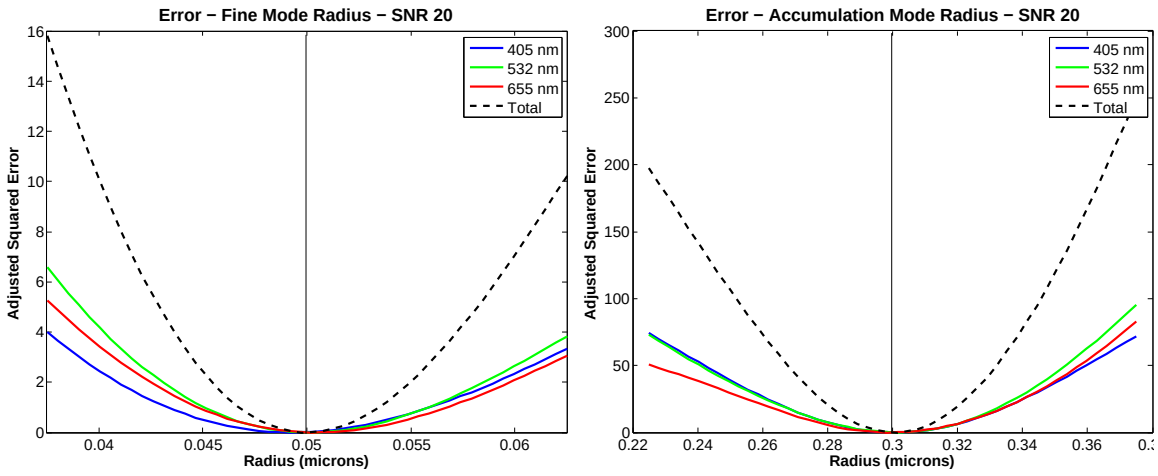

(a)

(b)

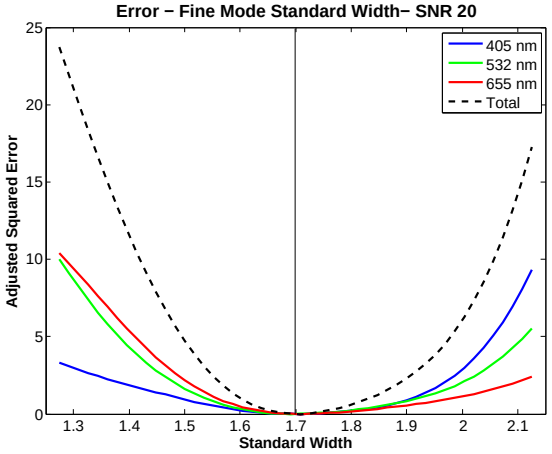

(c)

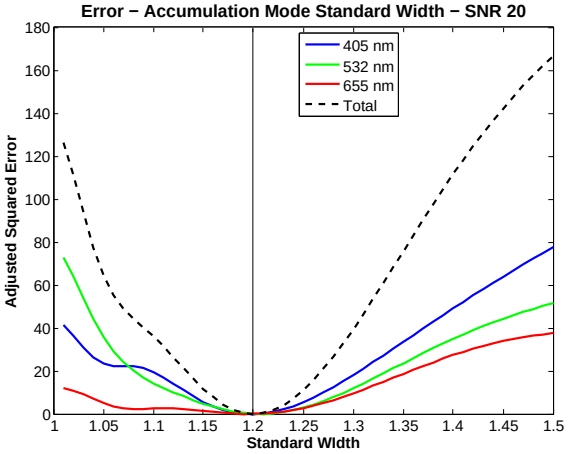

(d)

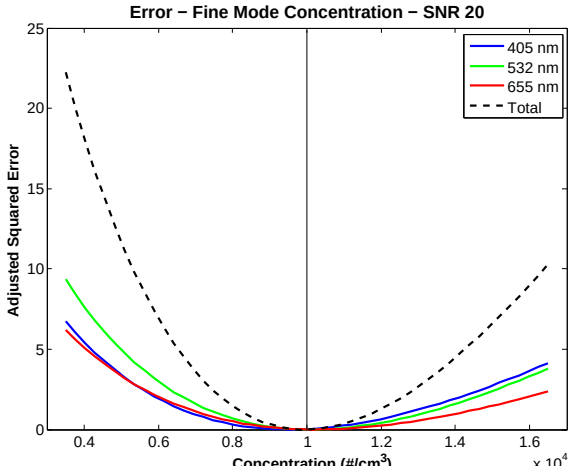

(e)

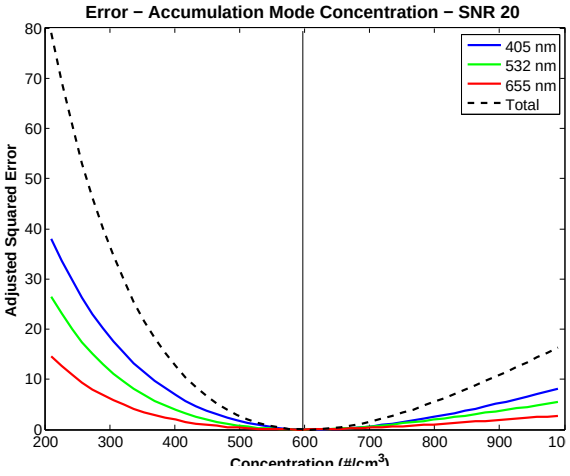

(f)

Figure 3.18: The same six parameters of the combination of fine and accumulation mode distributions with noise (SNR 20) added. The adjusted squared-error plotted is vertically shifted so the minimum for each wavelength and the total are zero.

The parameters still show good convergence except for the concentration in both modes. The fine mode standard width is slightly changed, it does not have the typical parabolic shape, the bottom is almost flat around 1.7 and the squared-error does not increase rapidly on either side of the minimum. The concentrations of the fine and accumulation modes show irregular convergence, as was the case with the single mode distribution; there is weaker convergence at higher concentrations than at lower concentrations. This implies that there will be a large error in this parameter in the presence of noise.

The ka values in Table 3.4 indicate that the mode that is best determined by these wavelengths is the accumulation mode because the ka values for the 405 and 532 nm wavelengths are close to the optimum ka value of 4.187. This is shown in the squared-error plots of Figure 3.18 by the steep convergence in the squared-error of the radius and standard width for the accumulation mode.

The combination of three wavelengths is always the most deterministic value for the parameter values. The shortest wavelength (405 nm) best determines the concentration for the accumulation mode, as evidenced by the closeness of the squared-error curves, The other five parameters do not show a closeness of any of the wavelengths to the total squared-error, re-emphesizing the importance to make a multi-wavelength measurement and selection of the optimum wavelengths based on the aerosol real index of refraction and the wavelength.

All three fine mode parameters are explored in Figure 3.19, where the noise in the polarization ratio was simulated 100 times and the parameter value corresponding to the minimum squared-error was totaled over all 100 runs and the results are shown.

The standard width of the fine mode shows the greatest standard deviation ($\approx 3\%$) in the parameter value obtained by the minimum squared-error. This behavior is expected due to the flat bottom nature of the standard width squared-error error in Figure 3.18(c).

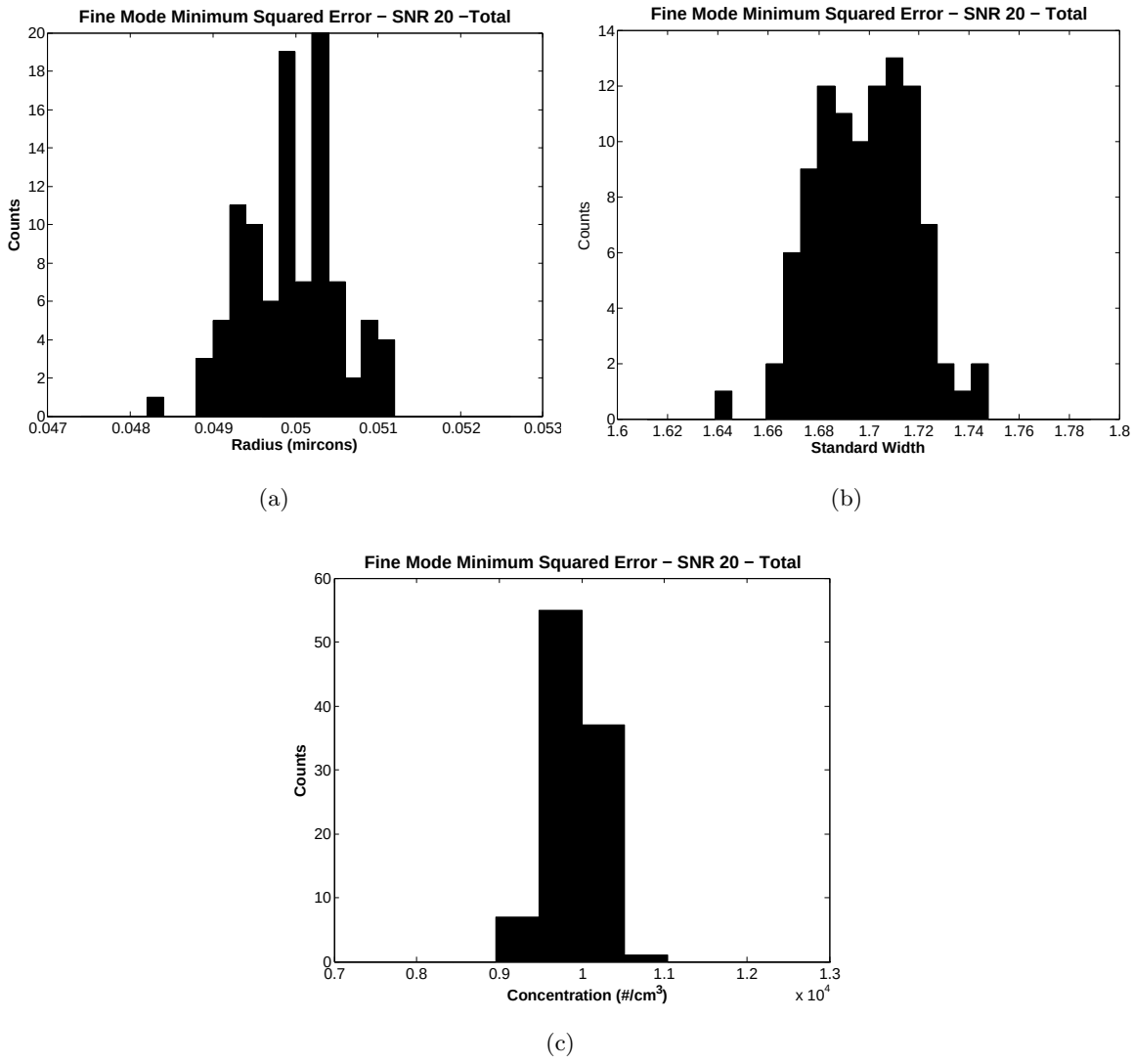

Figure 3.19: The total minimum squared-error for the Fine Mode parameters in the bi-modal combination of fine and accumulation distributions.

Accumulation and Coarse Modes

The size distribution and calculated polarization ratios for the bi-modal accumulation and coarse mode distributions are shown in Figures 3.20(a) and 3.20(b), based on the values listed in Table 3.3. The squared-error is evaluated to determine the convergence of each parameter at its input value, see Figure 3.21. Noise is then added to the ratios (SNR 20) and the squared-error is reevaluated. The result is shown in Figure 3.22. It is obvious that once the noise is added there is no longer convergence toward a proper value for parameters of the coarse mode.

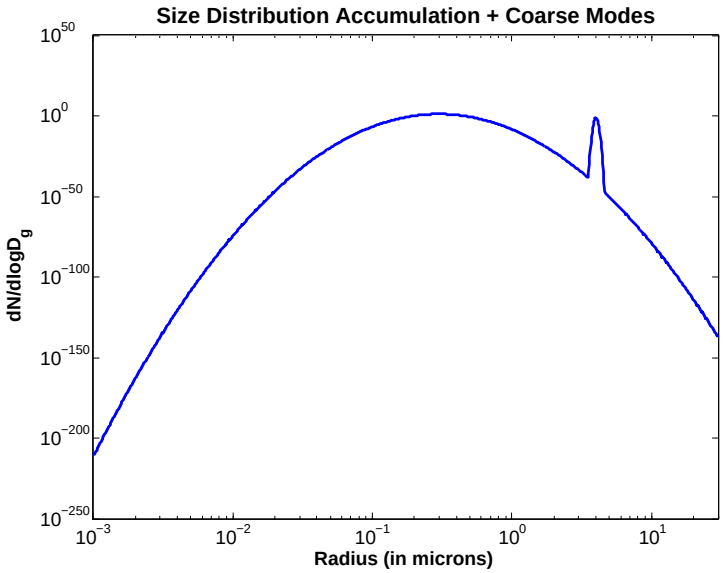

(a)

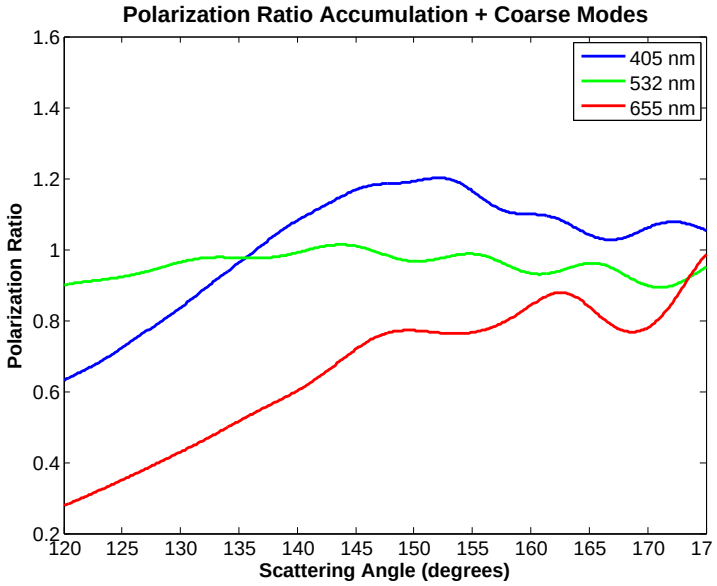

(b)

Figure 3.20: The bi-modal size distribution for the accumulation and coarse modes from Table 3.3.

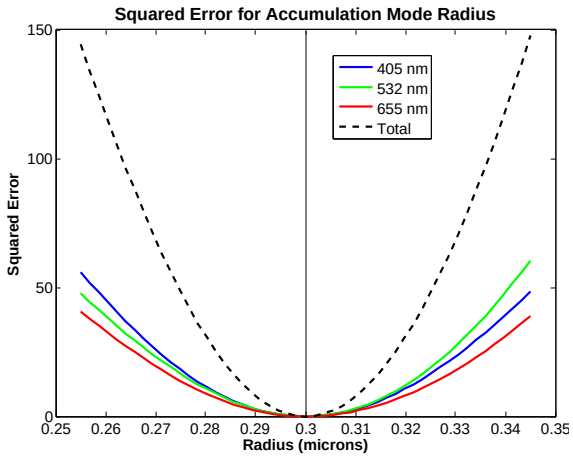

(a)

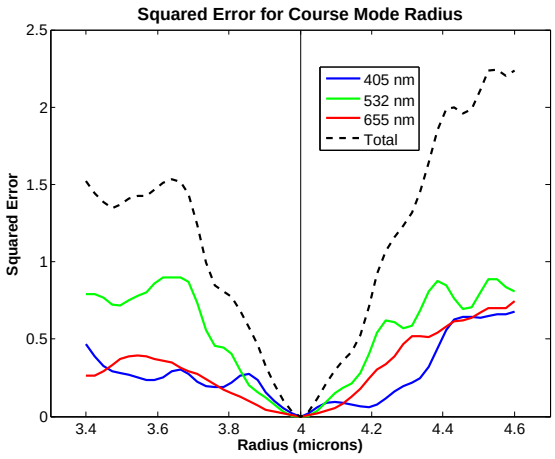

(b)

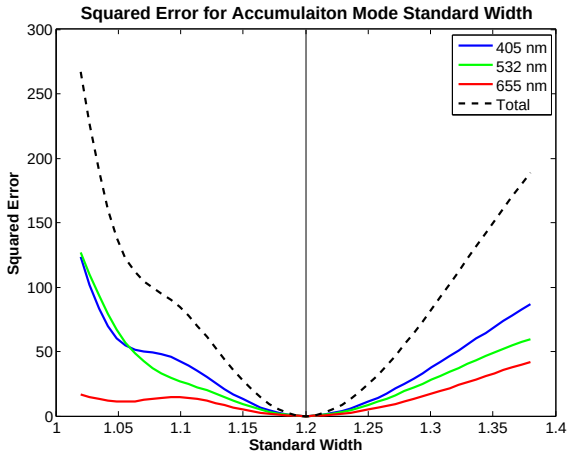

(c)

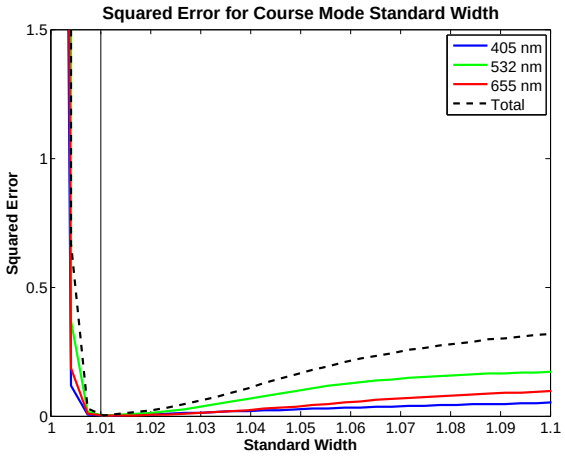

(d)

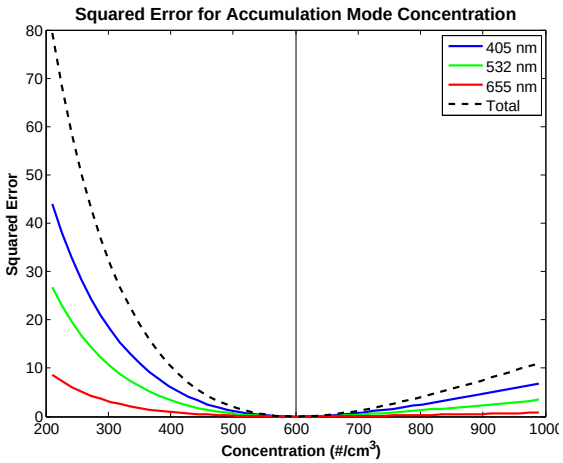

(e)

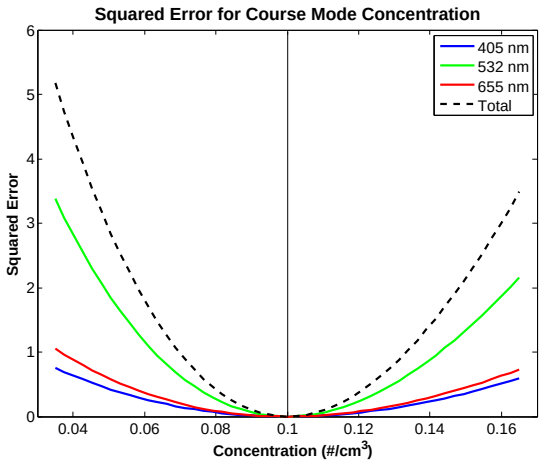

(f)

Figure 3.21: Squared-error for the parameters of accumulation and coarse bi-modal distribution.

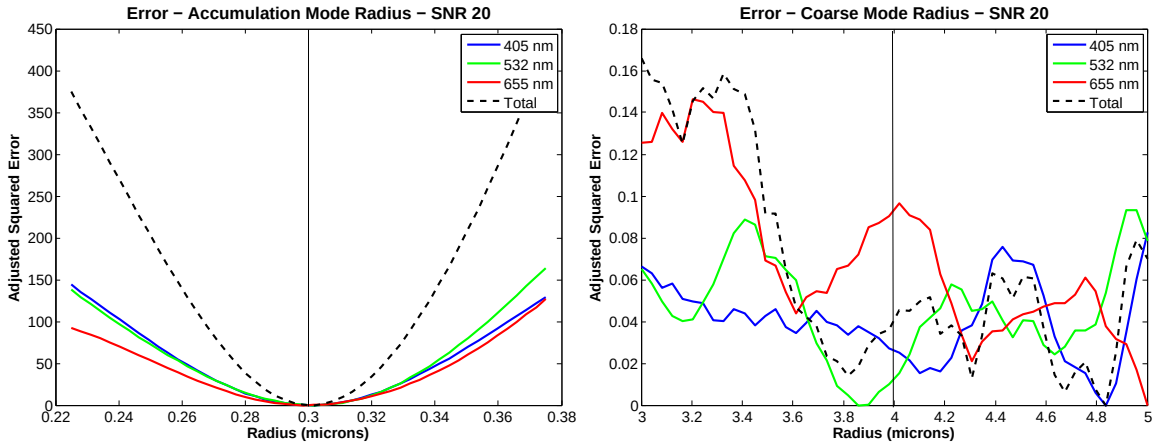

(a)

(b)

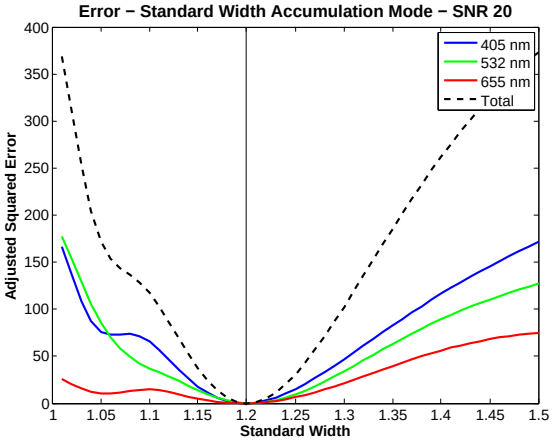

(c)

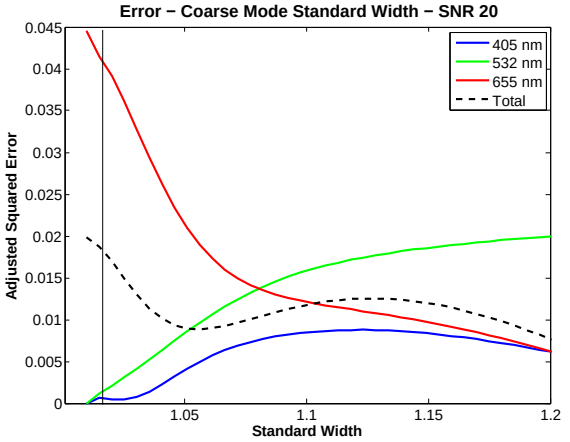

(d)

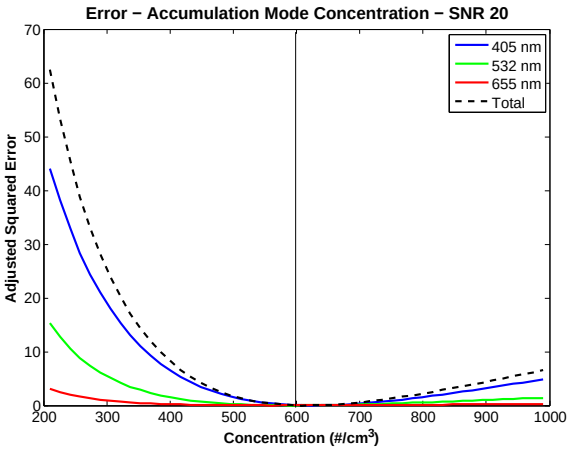

(e)

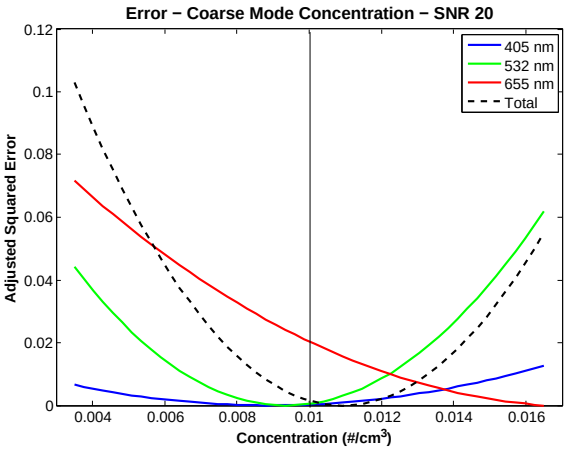

(f)

Figure 3.22: Adjusted squared-error for all parameters of accumulation and coarse modes in the bi-modal distribution when an SNR of 20 is added. The squared-error is vertically shifted, so the minimum for each wavelength and the total are zero.

The squared-error for the course mode standard width and radius can not be determined. In both cases, there is no clear minimum to show the convergence to a particular parameter value. Surprisingly, the concentration is determined by the total of all three wavelengths to a value slightly higher than the desired value by 20%, but close considering the other two course parameters are not determined, so the polarization ratio is sensitive to the larger size, it just cant determine the exact size when the aerosol is large compared with the wavelength.

Fine and Coarse Modes

The final bi-modal combination for the fine and course mode combination found in Table 3.3. This case tests the polarization ratio when mean radii are more separated than in the previous two cases. The sizedistribution obtained from combining the fine and course modes is shown in Figure 3.23(a), with their calculated polarization ratios in Figure 3.23(b). The six parameters are explored using the squared-error analysis for the case without noise and when noise is added, see Figures 3.24 and 3.25, respectively.

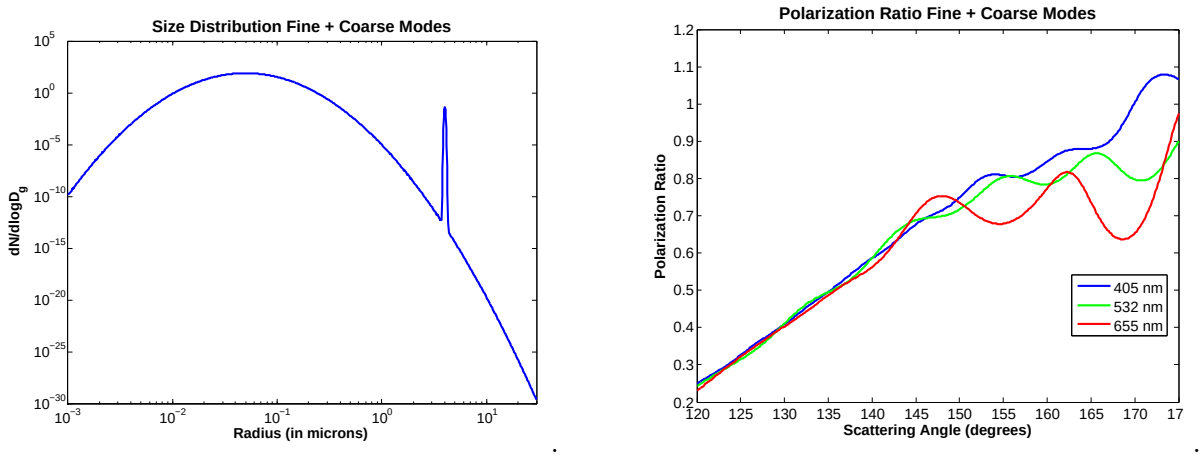

(a) (b)

Figure 3.23: The bi-modal size distribution for the fine and accumulation modes from Table 3.3.

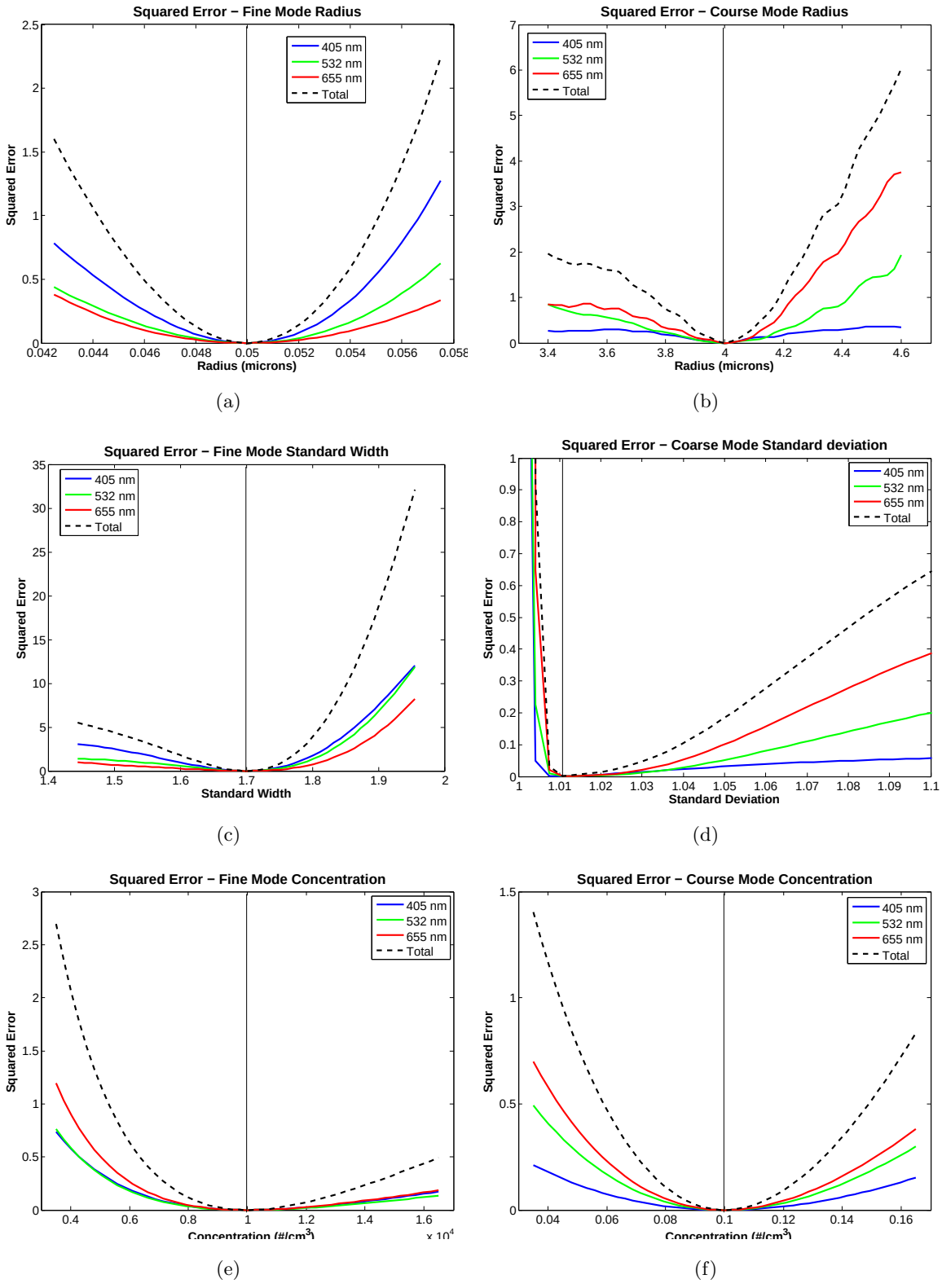

Figure 3.24: Squared-error for parameters of the fine and coarse bi-modal distribution combination.

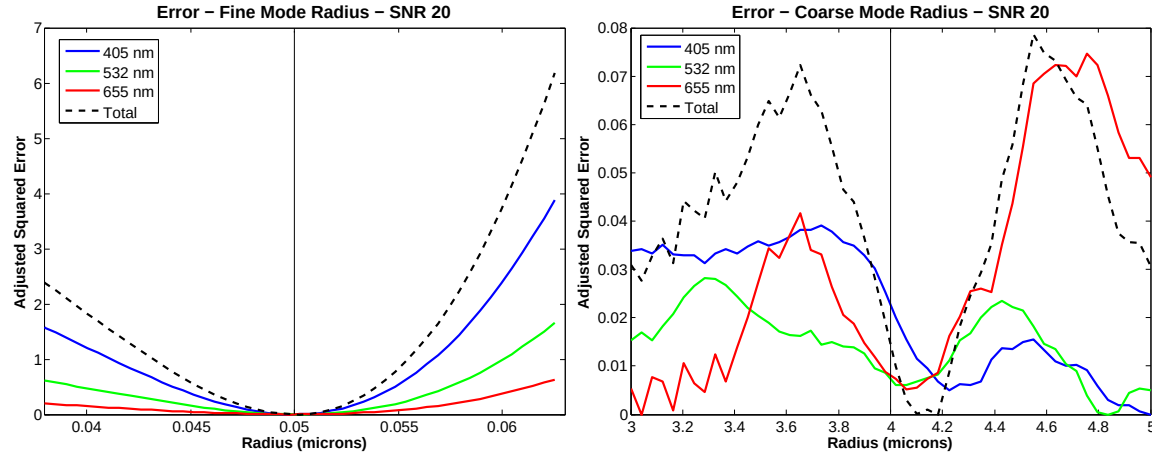

(a)

(b)

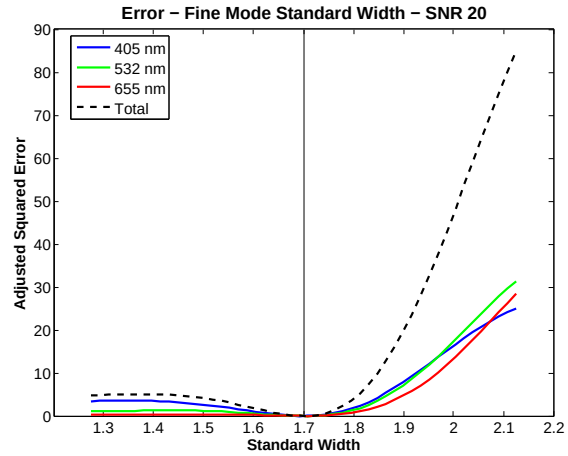

(c)

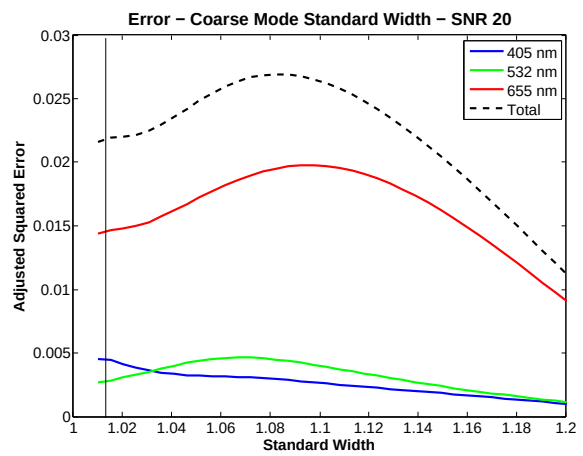

(d)

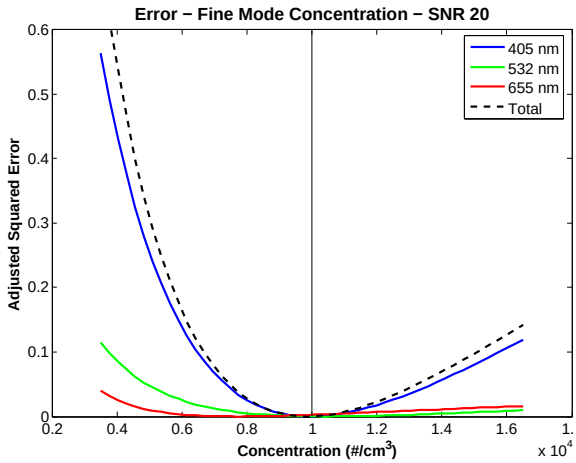

(e)

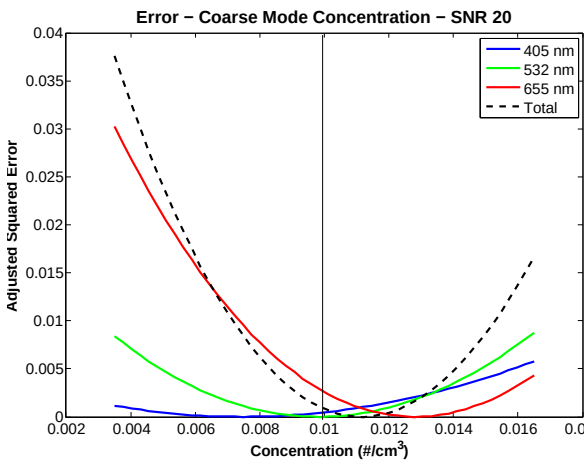

(f)

Figure 3.25: Adjusted squared-error for parameters of the fine and coarse bi-modal distribution when an SNR of 20 is added. The adjusted squared-error plotted is the squared-error minus the minimum for each wavelength and the total.

The fine mode parameters are well determined by the combination of the three wavelengths. The shortest wavelength, 405 nm, best determines the fine mode parameters, this is expected since the shortest wavelength would have the largest ka value of the three wavelengths. The course mode radius and standard width are not as well determined by these wavelengths, as before, since the ka values of the fine and coarse modes (see Table 3.4) are not close to the optimum ka value of 4.18. The fine mode distribution size is separated significantly from the coarse mode size, but the course mode radius and standard width are not well determined. The concentration of the coarse mode remains close due to the larger size scattering contribution from the large aerosols.

Tri-modal Distribution: Fine, Accumulation and Coarse Modes

The final configuration includes all three size distributions, the fine, accumulation and course modes. The combined size distribution and calculated polarization ratios are shown in Figure 3.26

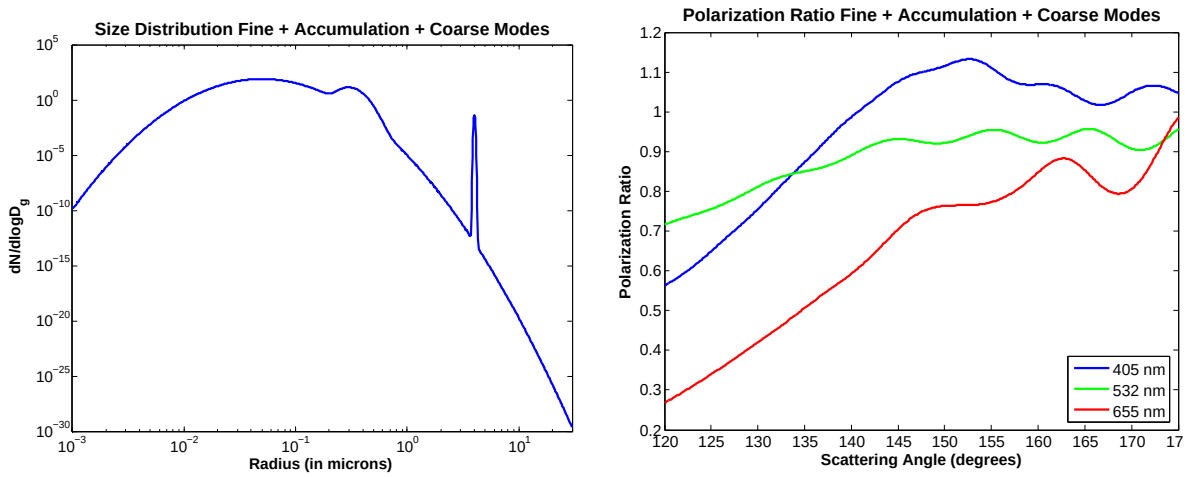

(a) (b)

Figure 3.26: The bi-modal size distribution for the fine and accumulation modes from Table 3.3.

Noise is added to the polarization ratios with a SNR of 20 and the squared-error for each parameter is examined (see Figures 3.27 - 3.29)

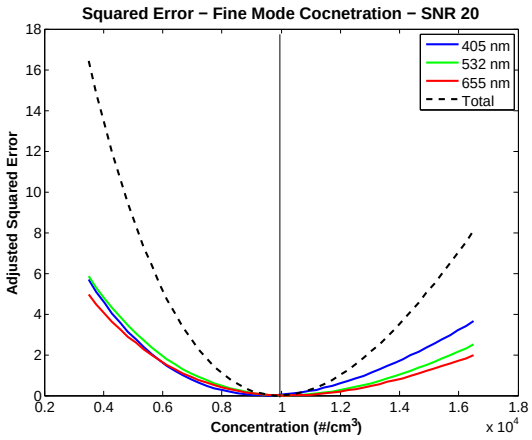

(a) Fine Mode Concentration

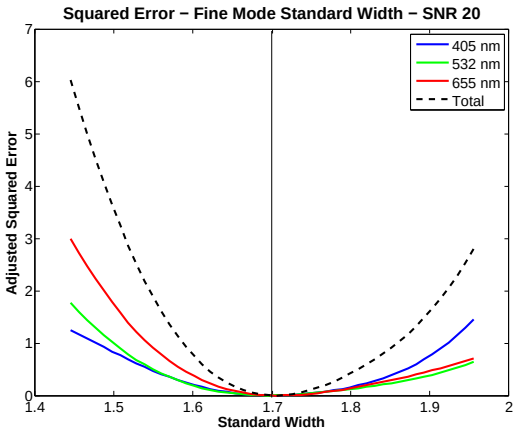

(b) Fine Mode Standard Width

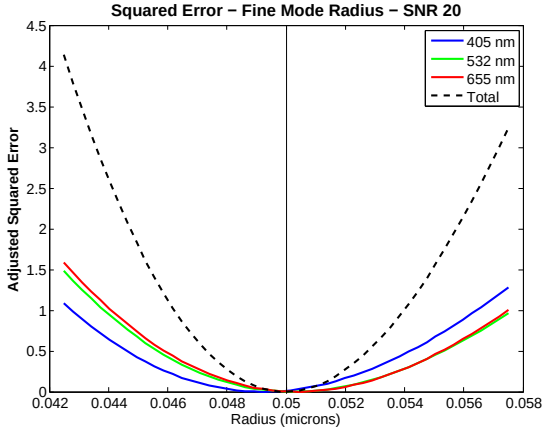

(c) Fine Mode Radius

Figure 3.27: Squared-error for fine mode parameters in tri-modal distribution polarization ratios with SNR of 20. The adjusted squared-error plotted is the squared-error minus the minimum for each wavelength and the total.

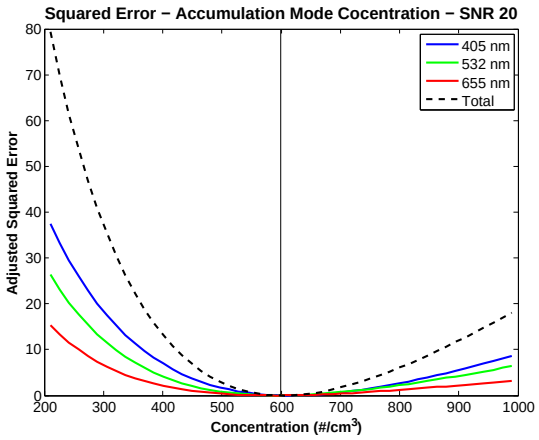

(a) Accumulation Mode Concentration

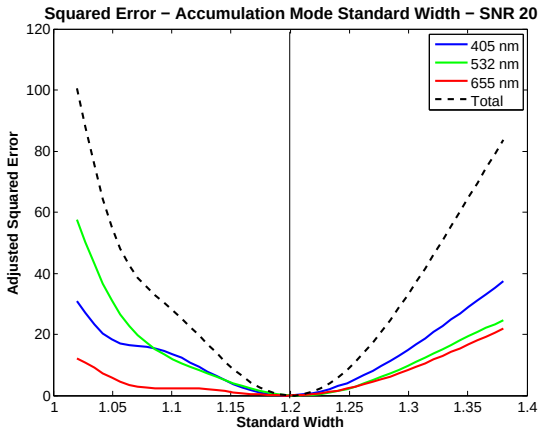

(b) Accumulation Mode Standard Width

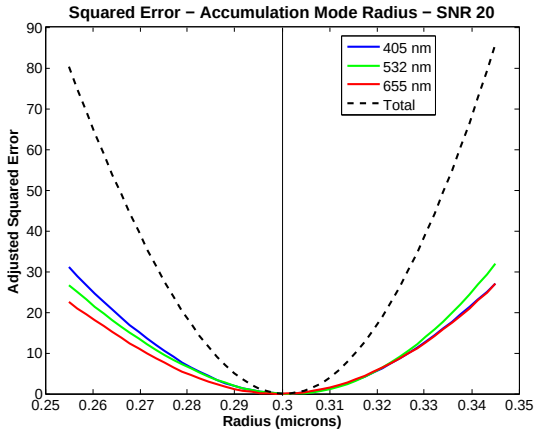

(c) Accumulation Mode Concentration

Figure 3.28: Squared-error for accumulation mode parameters in tri-modal distribution polarization ratio with SNR of 20. The adjusted squared-error plotted is the squared-error minus the minimum for each wavelength and the total.

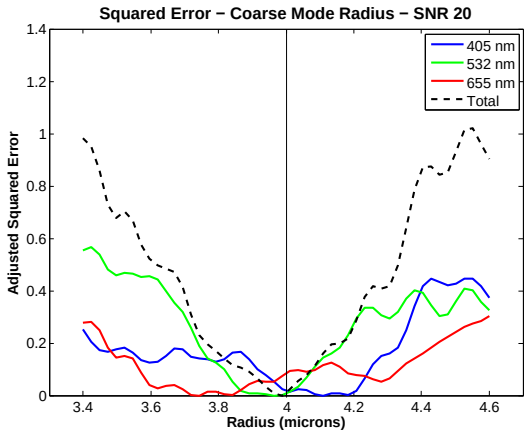

(a) Radius

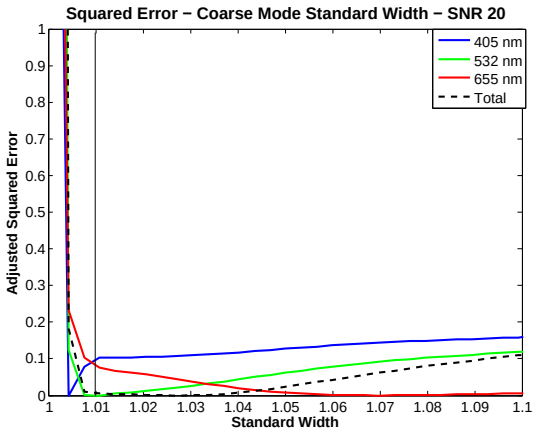

(b) Standard width

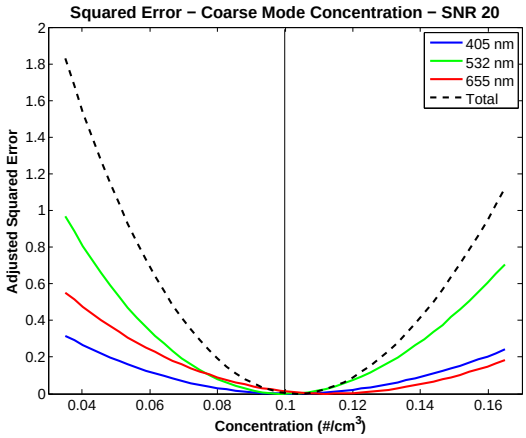

(c) Concentration

Figure 3.29: SE for coarse mode parameters in tri-modal distribution polarization ratio with SNR of 20. The adjusted squared-error plotted is the squared-error minus the minimum for each wavelength and the total.

The uncertainty in the coarse mode that was displayed in the squared-error plots of Figures 3.25 and 3.22, is no longer present in the tri-modal polarization ratio squared-error shown in Figure 3.29. The fine and accumulation modes converge to a value close to the correct value in the polarization ratio with SNR of 20, see Figures 3.27 and 3.28. This is again seen by looking at the ka values for each of the three modes in Table 3.4. The accumulation mode determination is the best, followed by the fine mode and then the coarse mode. The larger size

difference in ka value for the coarse mode suggest that it is the least determined by the ratio in all of the multi-mode configurations.

3.4 Selection of Transmitter Wavelengths

The wavelengths used in the above analysis are sufficiently sensitive to determine distribution parameters of the 0.3 micron radius (accumulation mode) aerosols, which are in the size range that are measured in the experimental chapter. Measured distributions have somewhat different aerosol sizes. Since the scattering signatures vary as a function of the wavelength and aerosol size, the smaller size distributions may need to be measured with even shorter wavelengths. This section examines the polarization ratio and evaluates it's sensitivity with various wavelengths to determine a combination of wavelengths to better measure this distribution. A study like this could be done before an experiment is conducted if the aerosol size and index of refraction are known. For an initial study of a typical size distribution, the rural distribution measured by Jaenicke[35] is selected, see Figure 3.30 and Table 3.5 .

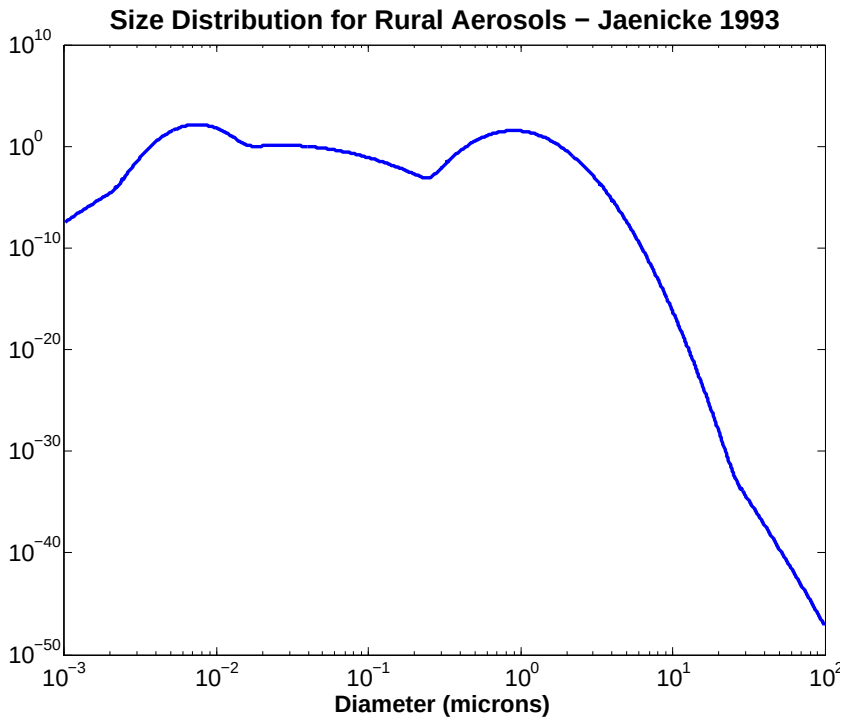

Figure 3.30: The typical size distribution for rural aerosols from Jaenike.[35]

Table 3.5: A typical rural size distribution taken from Jaenicke[35]

Mode	Mean Radius (microns)	Standard Width	Concentration (#/cc)
#1	0.0075	1.2523	6650
#2	0.027	1.7454	147
#3	0.9	1.3047	1990

The rural size distribution selected is made up of 94 % dust, 6 % water-soluable aerosols, and a trace of soot aerosols.[35,36] The polarization ratio is calculated as a function of wavelength in Figure 3.31. The refractive index values used are from D'Almeida[36] and Palmer.[37] These values are then interpolated for desired wavelengths. The selection of interpolated index values are shown in Table 3.6 for the fundamental, doubled, tripled and quadrupled wavelengths of an Nd:Yag laser.

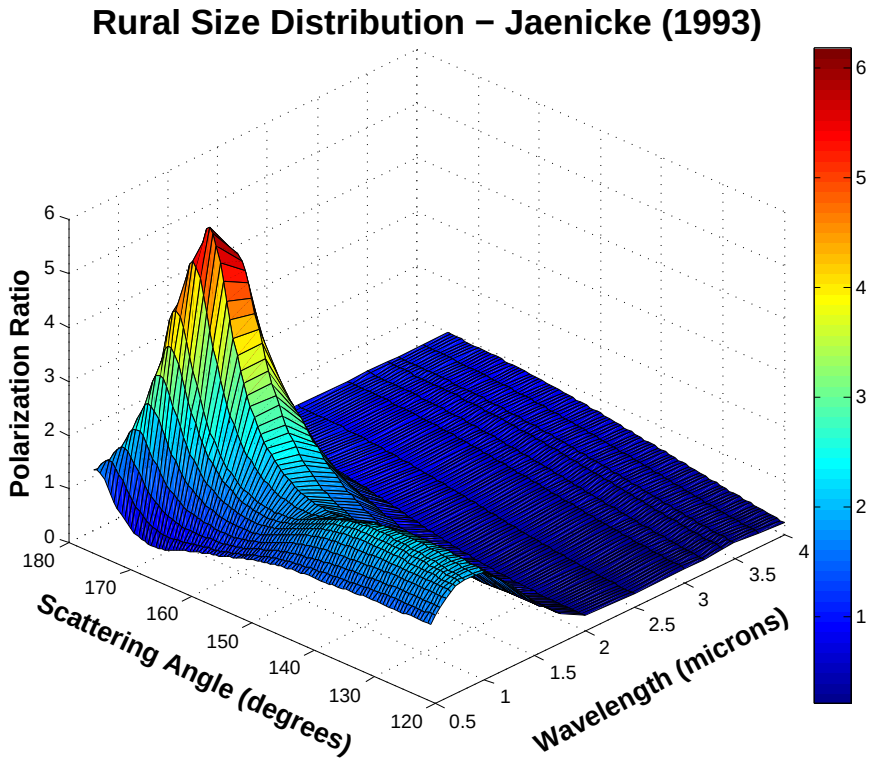

Figure 3.31: The polarization ratio shown over a large wavelength for a typical rural distribution as outlined in Jaenike.[35]

Table 3.6: Index of refraction for the components in the rural distribution shown at the Nd:Yag laser wavelengths, interpolated from from D'Almeida[36] and Palmer.[37]

Wavelength (nm)	**Dust**	**Water-Soluable**	**Soot**
1064	$1.50 + 0.008i$	$1.51 + 0.09i$	$2.00 + 0.44i$
532	$1.53 + 0.008i$	$1.53 + 0.01i$	$1.75 + 0.44i$
355	$1.53 + 0.008i$	$1.53 + 0.01i$	$1.75 + 0.46i$
266	$1.53 + 0.008i$	$1.53 + 0.01i$	$1.75 + 0.46i$

Figure 3.31 shows that the wavelengths that are most sensitive for this distribution of aerosols are near the visible (0.4 - 0.7 microns) and shorter near-infrared (1.0 - 2.0 microns) range. Once the wavelength gets beyond roughly 2 microns there is no structure in the polarization ratio. The squared-error for each of the parameter values are shown in Figures 3.32, 3.33, and3.34.

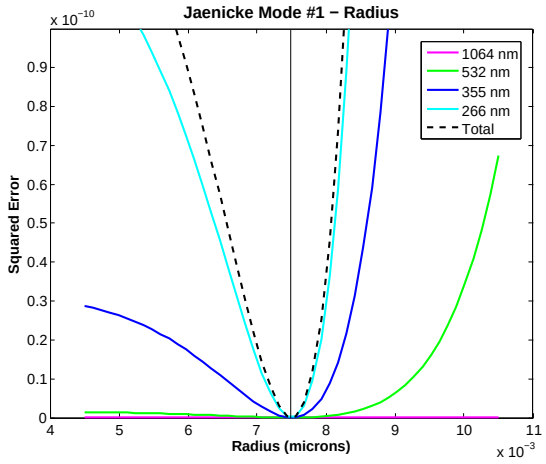

(a) Radius

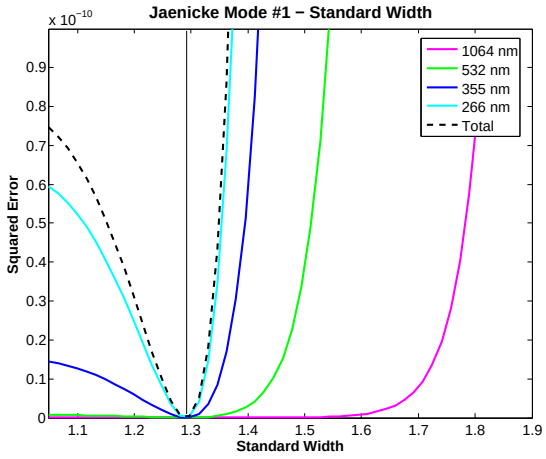

(b) Standard Width

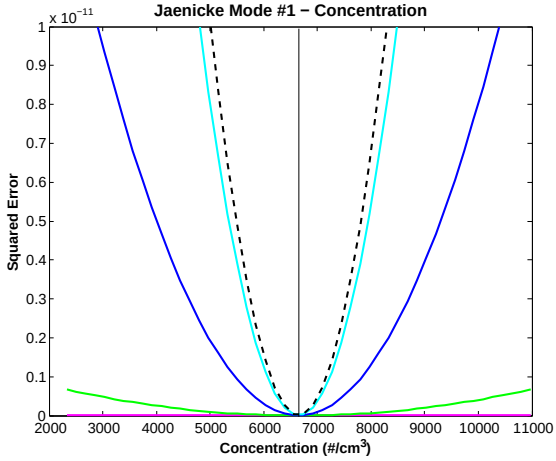

(c) Concentration

Figure 3.32: Squared-error for coarse mode parameters in tri-modal distribution polarization ratio with SNR of 20.

The first mode, with mean radius of 7.5 nm, is best measured by the shortest wavelength, 266 μm. The other wavelengths only provide weak addition to the convergence.

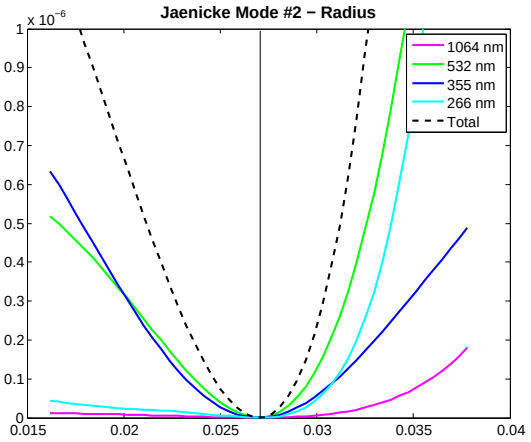

(a) Radius

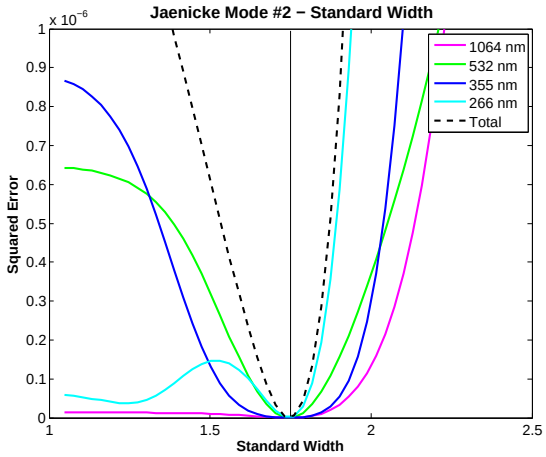

(b) Standard Width

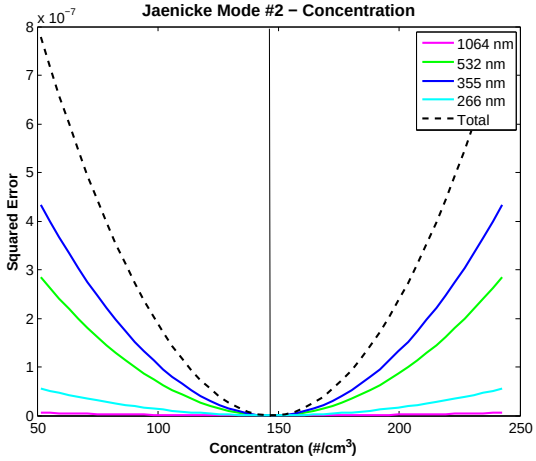

(c) Concentration

Figure 3.33: SE for coarse mode parameters in tri-modal distribution polarization ratio with SNR of 20.

The determination of the second mode (radius = 27 nm) parameters the determination of the radius is strongest for the 532 and 355 nm wavelengths. The standard deviaiton is the only second parameter whose convergence is greatly helped by the 266 nm wavelength.

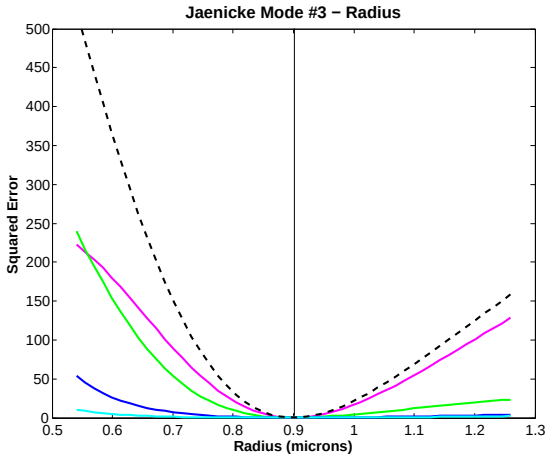

(a) Radius

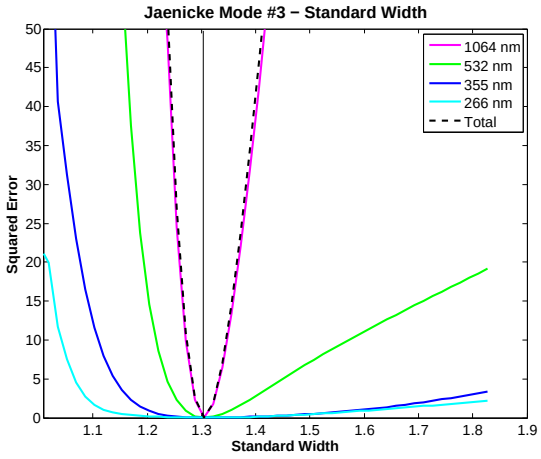

(b) Standard Width

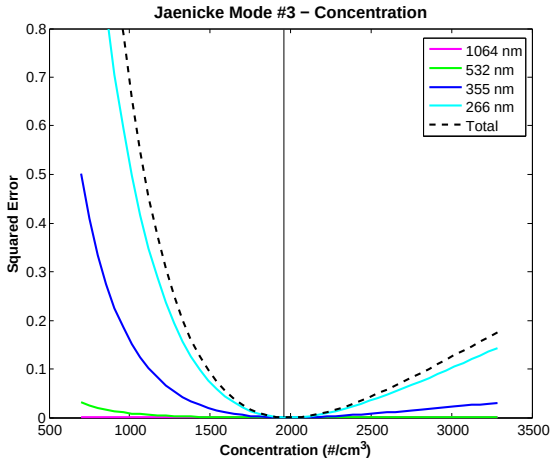

(c) Concentration

Figure 3.34: Squared-error for coarse mode parameters in tri-modal distribution polarization ratio with SNR of 20.

The third mode (radius = 0.9 μm) radius and standard width parameters are well determined by the 1064 nm wavelength. The concentration however, is determined the best by the shortest wavelengths. This is because the shorter wavelengths are more sensitive to the scattering by small particles and molecules. The scattering by molecules is needed to determine the concentration of the aerosols present.

From the multi-mode distributions explored, it is determined that the polarization ratio is not able to accurately determine aerosol parameters in all situations. The wavelengths must be tailored to each size range to accurately determine the parameters of each mode based on

the aerosol index of refraction and optimum ka value. The phase functions used to form the ratio are a relative measurement of intensity and are morse sensitive to the changes in each of the parameters, however because of experimental errors present in the intensity measurements that are not capable of being characterized with the current set up, the ratio is needed to eliminate these errors in the measurement. The selection of the polarization ratio over the phase functions is discussed in Appendix B.1 and a possible adjustment to the experimental set-up is suggested in Chapter 8. Since the current equipment is limited to the use of the polarization ratio, methods of inverting experimental ratios to match calculated Mie scattering ratio is explored.

Chapter 4

Inversion Routines

An inversion is the process of matching experimental data to theoretical calculations. In this particular instance, the angular scattering data is collected and an inversion routine is performed to determine the characteristics of the aerosols which caused the signature observed in the scatter.

The polarization ratio method requires measurement over an angle range of optical intensity of each polarization. Their ratio is used to analyze many of the parameters need to characterize particulates.[38] Stevens,[13] Novitsky,[15] Park[24] and Brown[25] found the polarization ratio to produce the best information to begin an inversion analysis technique. The inversion problem is extremely difficult because the ratio is affected by so many variables (Fig. 2.10 - 2.14). Thus, an efficient and reliable inversion technique is needed to make this instrument and measurement technique a more useful and efficient way of characterizing aerosols.

Stevens began with a method that depended heavily on an initial tri-modal distribution guess, then slightly varied the concentration, σ_g, and mean diameter parameters by hand to match the measured polarization ratio.[13] A gradient based method was used by Novitsky to arrive at a unique best solution for the size distribution and number concentration of the volume of aerosols based on the scattering phase function, he was unsuccessful in finding a gradient based inversion method that used the polarization ratio as its input measurement.[15] The failure of the gradient based method using the polarization ratio is due to extremely large derivatives in the solution space far away from the optimum solution. For this method to obtain a solution, and not become stuck in a local minima, it relies too heavily on information known before the inversion process begins.[39] Brown[25] sought find an inversion technique that would not get stuck in a local minima, but instead find the global minimum, using a genetic algorithm approach. This stochastic approach makes intelligent random steps to find a possible solution in a large solution space. Brown demonstrated the usefulness of this method to find several aerosol properties, such as size distribution, index of refraction and number density with good

accuracy. This inversion method is limited by the computational time it takes to invert the measurements to a solution, and it is critical to define the size of the discrete solution space that is searched.[25]

Other approaches to solve this type of inversion problem have been attempted. It is essential to stress that the solution to this problem is "ill-posed"[40] because there are many variables to optimize. The complexity of this inversion and the ill-posed nature of the polarization ratio was explored in the previous chapter, although it was determined that the ratio is a deterministic quantity in some cases when the ka value is close to being optimized. A simple monomodial aerosol distribution described by a log-normal distribution requires five variables: number concentration, mean radius(r_g), standard width (σ_g), real and imaginary index of refraction. Each of these variables effect the polarization ratio differently and must be optimized to obtain a meaningful solution.[41] However, there may be multiple best solutions depending on the combination of variables. In a real world situation, the aerosols in the lower atmosphere are usually described by a tri-modal size distribution. After the monomodial distribution, each distribution of particles add five more variables that need to be obtained to fully describe the properties of aerosols.

The inversion method used in an instrument like this must be very robust. The system parameters needed are defined by the transmitter and receiver, these include the laser wavelength and the angle range of scattered intensity. In addition, the background molecular scattering present in the lower troposphere must be included in the analysis. The size and concentration of the aerosols may produce scattering signals that cover up the scattering of the molecular background; thereby, preventing the use of molecular backscatter signals, which are often used in finding the concentration of aerosols.[25] In addition, more variables included in the inversion reduce confidence in the answer, since different combinations of multiple parameters can provide almost identical results, and could result in finding multiple best solutions. Finding the best solution may involve: using a genetic algorithm followed by a gradient based method. The discrete genetic algorithm approach of Brown[25] could be extended to a continuous genetic algorithm run on parallel processors to speed up the computation. Several problems need to be addressed to find a satisfactory inversion method. The approach selected must be automated and provide the correct answer in a reasonably short amount of time.

In addition, a Monte Carlo inversion was added. This is to test the genetic algorithm performance as a "smart" Monte Carlo inversion routine. The Monte Carlo routine is as simple as they come, it just takes a bunch of random guesses at the input parameters (μ_g, σ_g, N) with the assumed parameters (n, λ).

4.1 Monte Carlo (MC) Inversion Routine

A Monte Carlo routine is based on purely randomly generated numbers. The way the Monte Carlo routine is set up is to randomly generate a number between 0 and 1. This is then mapped to the desired variables, in this case μ_g, σ_g and N for a single mode aerosol distribution. The random number generator used randomly selects a decimal between 0 and 1. The randomly generated numbers are mapped to the solution space, see Table 4.1. The algorithm is written as shown in Figure 4.1. The terminology used here (see Table 4.2) is on purpose, to reflect the similarities to the genetic algorithm discussed in the next section.

Table 4.1: The range of possible values for Monte Carlo inversion, where s represents the randomly generated variable.

Parameter	**Range**	**Delta**	**Mapping**
μ_g	$0.01 \rightarrow 1.5\ \mu m$	1.49	$\mu_g(s) = s_1 * 1.49 + 0.01$
σ_g	$1.01 \rightarrow 1.80\ \mu m$	0.79	$\sigma_g(s) = s_2 * 0.79 + 1.01$
N	$10^{-2} \rightarrow 10^{3}\ \mu m$	10^5	$N(s) = s_3 * 10^3 + 10^{-2}$

Table 4.2: Explanation of variables used in Monte Carlo inversion routine

Terminology	**Explanation**
population size	number of randomly generated variables in each generation
max. generations	maximum number of generations per run

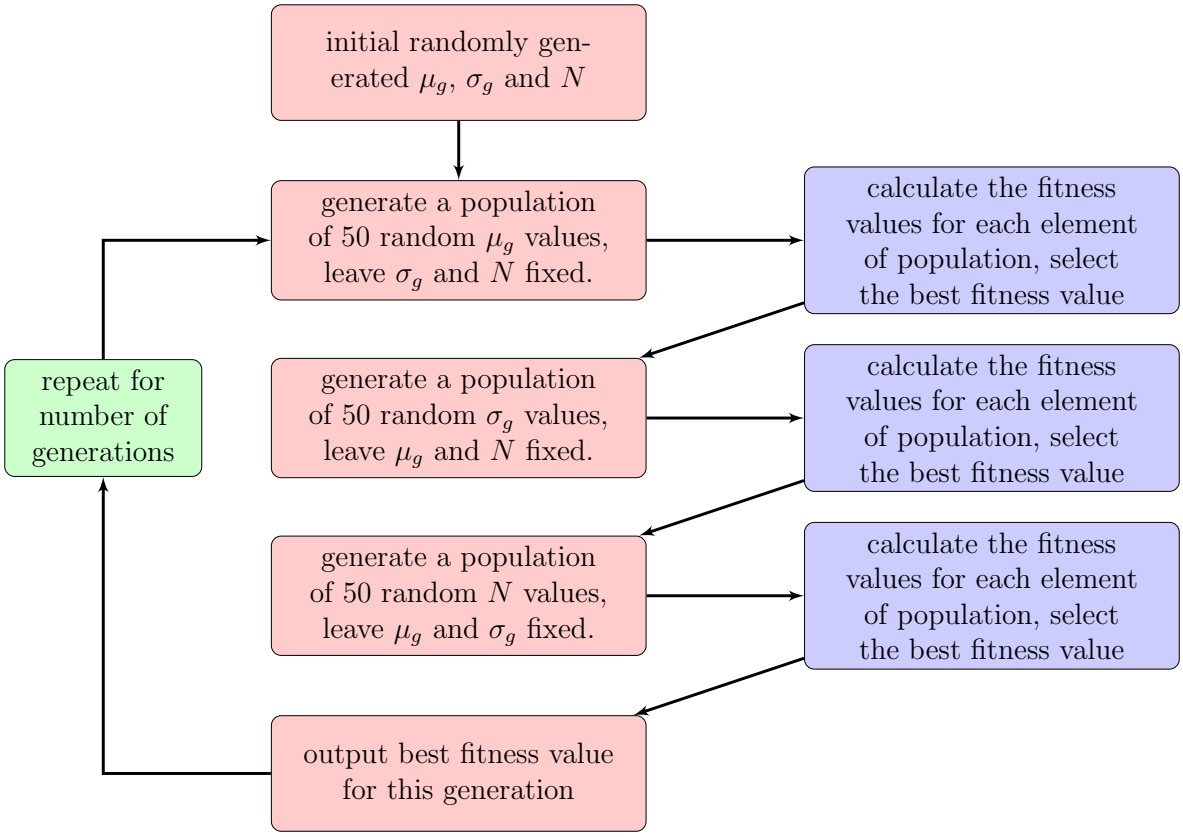

Figure 4.1: Representation of the Monte Carlo inversion routine.

This type of inversion algorithm would mimic the trial-and-error of a human changing the three inversion parameters by hand.

4.2 Binary Genetic Algorithm (BGA) Inversion Routine

A genetic algorithm is based on the way a population evolves. Therefore the terminology used mimics the terminology used when talking about population evolution, as described in Table 4.3.

A specific length chromosome is randomly generated representing a unique solution. Then a population of possible solutions is generated based on the first chromosome and a probability of mutation. Each new chromosome is evaluated using a fitness function. The chromosome that has the best fit function is then selected to be the parent chromosome for the next generation. This process is repeated until a predefined fit value is achieved or the predefined maximum number of generations is reached. A maximum number of generation criteria was used exclu-

sively because there was not a good feeling for a predefined fitness stopping value. This process is pictorially represented in Figure 4.2.

Table 4.3: Summarization of the terms used in the Binary Genetic Algorithm. (Descriptions greatly influenced by Haupt[42]).

Terminology	**Explanation**
chromosome	A string of binary numbers, $\{0, 1\}$, that represents a solution to the problem.
bit	These are the pieces, the 1's and 0's, that make up the chromosome. The *length* of a chromosome is the number of bits.
population	The number of chromosomes present in a generation.
generation	The number of times the inversion routine is performed.
fitness function	A function that compares the predicted solution to the measured data, i.e. the sum of the squared-error. Higher fitness values represent chromosomes further away from the measured data, lower fitness values represent chromosomes closer to the solution.
selection	This is survival of the fittest; the chromosomes that have the lowest fitness values (best solutions) are kept. The chromosomes kept are the ones that influence the next generation.
mutation	These occur to randomly change bits in a few chromosomes to make sure the global solution is found.
convergence	This is usually computed as the average fitness value of a population. To make sure you are converging on a solution the average fitness of the population should be decreasing.

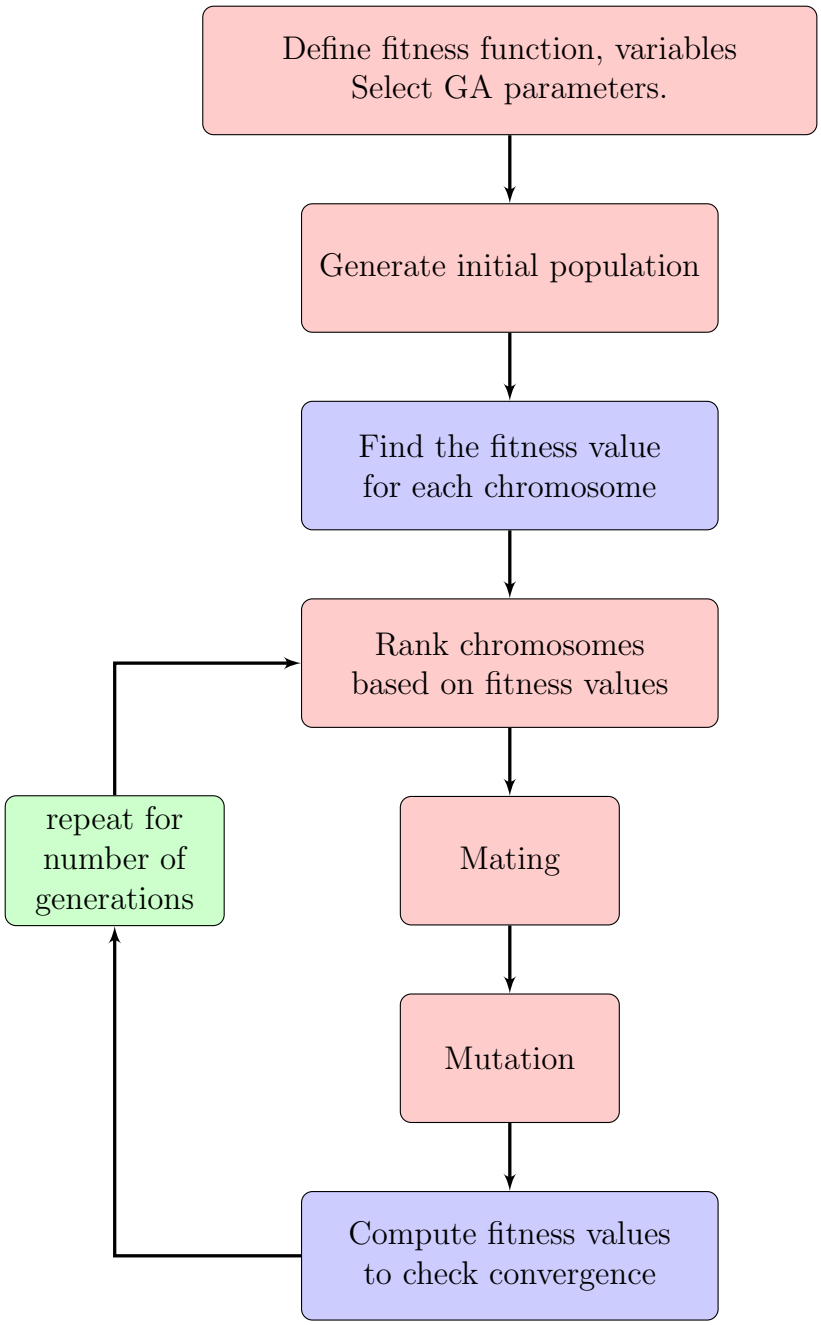

Figure 4.2: Representation of the Continuous Genetic Algorithm inversion routine.[42]

A chromosome of length of 24 bits is used for a single mode solution. An example chromosome of the form,

$$\underbrace{0011110}_{\mu_g}\ \underbrace{0011100}_{\sigma_g}\ \underbrace{1111010001}_{N}. \tag{4.1}$$

The mapping from the chromosome to the solution space of each variable is achieved in the following way; the random number that the section of the chromosome represents denoted by s, the number of possible numbers is 2^n, where n is the number of bits in that section of the chromosome. The mapping used for a single mode distribution is shown in Table 4.4.

Table 4.4: Binary Genetic Algorithm mapping from a 24-bit chromosome to the solution space of each variable.

Parameter	**Position**	**Possibilities**	**Mapping**	**Solution Space**
μ_g	$1-7$	$2^7 = 128$	$\mu_g(s) = s_1 * 0.01 + 0.01$	$0.01 \rightarrow 1.29\ \mu m$
σ_g	$8-14$	$2^7 = 128$	$\sigma_g(s) = s_2 * 0.005 + 1.01$	$1.01 \rightarrow 1.64$
N	$15-24$	$2^{10} = 1024$	$exp = linspace(-2, 3, 1024)$ creates 1024 linearly spaced points between -2 and 3 $N(s) = 10^{exp(s)}$	$10^{-2} \rightarrow 10^3\ \#/cm^3$

This inversion routine is similar to the one used by Brown,[25] but has a shorter section with the same resolution representing the mean radius, a higher resolution in the standard width and a longer string representing the concentration. The ranges of the mean radius and standard width were tightened around the input values to restrict the simulated polarization ratio, see Figure 3.1. This was done for efficiency while maintaining the discrete structure, which is characteristic of the binary genetic algorithm.

4.3 Continuous Genetic Algorithm (CGA) Inversion Routine

This inversion is written almost identically to the Binary Genetic Algorithm described in the previous section. However, this has a string of randomly generated numbers between 0 and 1, noninclusive, representing the chromosome.

$$\underbrace{0.8147}_{\mu_g}\ \underbrace{0.9058}_{\sigma_g}\ \underbrace{0.1270}_{N} \tag{4.2}$$

These random numbers are then mapped to the solution space for each variable as shown in Table 4.5.

Table 4.5: Continuous Genetic Algorithm Mapping of chromosome to range of possible solutions, where r stands for the randomly generated number.

Parameter	**Minimum**	**Maximum**	**Mapping**
μ_g	0.01 μm	1 μm	$\mu_g(s) = r_1 * 0.99 + 0.01$
σ_g	1.01	1.80	$\sigma_g(s) = r_2 * 0.79 + 1.01$
N	10^{-2}	10^3	$N(s) = r_3 * (10^3 - 10^{-2}) + 10^{-2}$

After many inversion attempts with experimental data from narrow log-normal size distributions ($\sigma_g < 1.1$) measured in Chapter 6, the parameter mapping for the standard width was changed to have a log type scaling.

4.4 Accuracy, Convergence, and Efficiency

A polarization ratio was then calculated at 750 linearly spaced points between 120 and 170 degrees, these were selected to resemble the angle range of an imager and the number of pixels in the imager where a polarization ratio could be calculated. All three methods (Monte Carlo, Binary Genetic, and Continuous Genetic) are stochastic methods based on random sampling of a solution space. Their convergence, accuracy and efficiency will be tested by adding noise to the simulated polarization ratio, as was done in Section 3.2.1, to model experimental input to each of the inversion routines.

Accuracy

First, an exact polarization ratio will be used to test the accuracy of each inversion routine when there is no noise in the data. Before the data can be fed into the inversion routine it needs to be sampled and smoothed at every half-degree angle, as shown in Figure 4.3.

The inversion routines are used to find the one unique solution in the solution space. Since the ratios are generated from known input values there is a unique solution for each parameter when the inversion of the polarization ratio with no noise is conducted. Figures 3.4, 3.5 3.6, demonstrate the uniqueness of all three parameter vales when one parameter is fixed; the fitness values converge to the input parameters of the other two parameters. Each was run for 50 generations with a population of 50. To obtain the result, each was run 20 times and the value reported is the average output and the standard deviation of the inverted results for each of the three parameters found in the inversion, see Table 4.6.

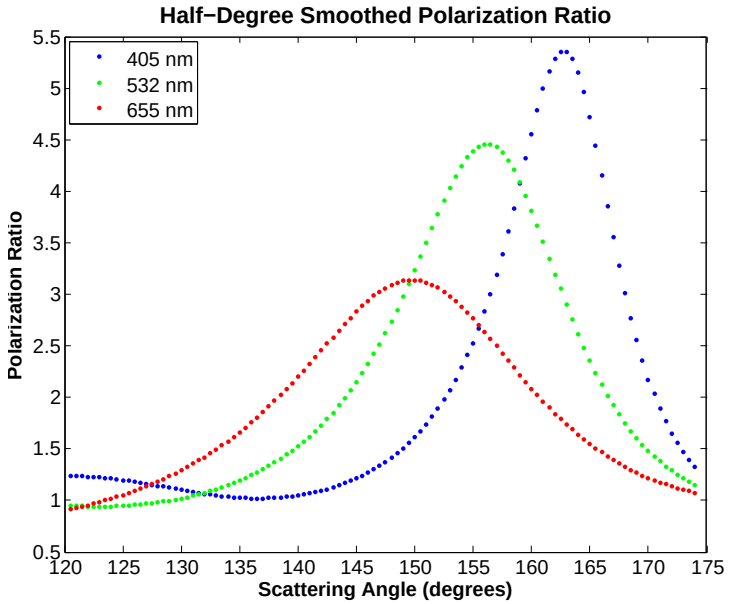

Figure 4.3: The half-degree sampled polarization ratio used for the inversion tests.

Table 4.6: The accuracy of the inversion routines with NO noise in the polarization ratio.

(a) Radius (μ_g) and Standard Width (σ_g).

Inversion	**Radius** (μm)	**Error**	**Standard Width**	**Error**
MC	$\mu_g = 029147 \pm 0.02736$	-2.844%	$\sigma_g = 1.2243 \pm 0.06194$	2.027 %
BGA	$\mu_g = 0.3095 \pm 0.0173$	3.167 %	$\sigma_g = 1.1855 \pm 0.03186$	-1.208 %
CGA	$\mu_g = 0.29999 \pm 0.002823$	-0.0033%	$\sigma_g = 1.1996 \pm 0.0068$	-0.033%

(b) Number Concentration and Fitness Value.

Inversion	**Conc. (#/cc)**	**Error**	**Fitness**
MC	$N = 657.20 \pm 261.714$	9.5338 %	43.83 ± 38.416
BGA	$N = 514.64 \pm 222.9612$	-14.23 %	26.602 ± 28.7803
CGA	$N = 609.63 \pm 81.141$	1.605%	4.734 ± 3.0222

Table 4.6 displays the closeness of each parameter value obtained by the three inversion routines. The continuous genetic algorithm shows the strongest agreement with the input parameters, as demonstrated by the low percent error obtained.

Convergence

To quickly obtain the best fitness value, the convergence of each method was tested. The convergence is important so that the same solution is obtain when the inversion routine is run multiple times. The convergence of each method is show in Figure 4.4.

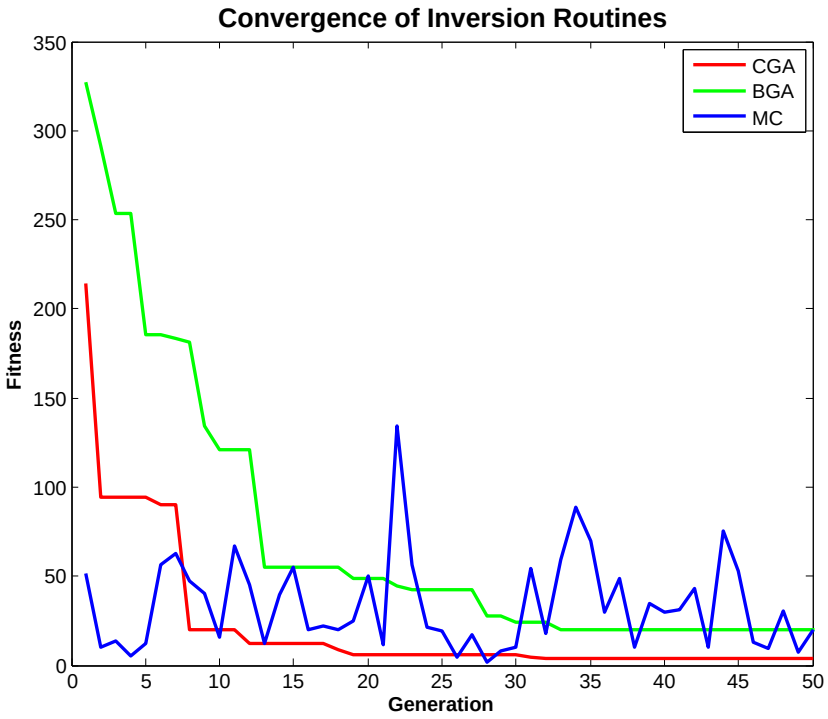

Figure 4.4: The convergence of each method is displayed.

From this study, the Continuous Genetic Algorithm routine produces the most consistent accurate results and have converges fastest. The Continuous Genetic Algorithm's performance is tested on simulated data, noise is added to the polarization ratio. as was outlined in Section 3.2.1. Figure 4.4 shows the instability of the Monte Carlo method and the convergence of the Genetic Algorithms. There is a clear advantage to using the Continuous Genetic Algorithm (CGA).

Efficiency

The disadvantage of the continuous Genetic algorithm is the computation time. The approximate computation times are shown in Table 4.7. This table was create when all there routines were run 50 generation with a population of 50.

Table 4.7: Computation times for each inversion method.

Method	**Computation Time**
Monte Carlo	1.5 hr
Binary Genetic Algorithm	20 min
Continuous Genetic Algorithm	30 min

The CGA takes longer to run than the BGA, but has a huge advantage over the Monte Carlo method, which takes three times longer that the CGA. Continuous Genetic Algorithm accuracy and convergence is strong enough that computation time is overlooked and the CGA is selected as the method to run inversion routines on experimentally obtained data.

Chapter 5

Design and Construction of Aerosol Characterization Instrument

This chapter describes the setup that is used for the experiments conducted in this work. The basic design consists of co-aligned laser beams emitted into a volume of aerosols, which are subsequently imaged to obtain intensity measurements across a range of angles.

5.1 Emission of a Co-aligned Beams

The transmitter shown in Figure 5.1 uses three diode laser beams, which are coaligned. Each of the three laser beams is reflected from specially coated dichroic mirrors that reflect the wavelength particular to the laser, but transmit the other wavelengths. Each mirror is mounted in a kinematic 2-axis mount to adjust its reflection angle to co-align the beams as they travel through the measured aerosol volume. The co-aligned beams pass through a polarization splitting cube where the horizontal polarization is transmitted and the vertical polarization is reflected at 90 degrees. The horizontally transmitted polarized beam then goes through the polarization rotator, which is a broadband waveplate used to flip the polarization between horizontal and vertical. The rotator shown is computer controlled for speed and precision of this rotation. A manual polarization rotator was initially used in some of the early experiments. The final optical element is an aperture (iris), which blocks the extra beam spray created by reflections off other optical elements in the transmitter.

Optical elements on the transmitter, shown in Figure 5.1, that affect the polarization are the polarization splitting cube and the polarization rotator, and there specific efficiencies are precisely quoted below in Table 5.1. These efficiencies can be taken into account when looking at the scattered intensities before forming the polarization ratio.

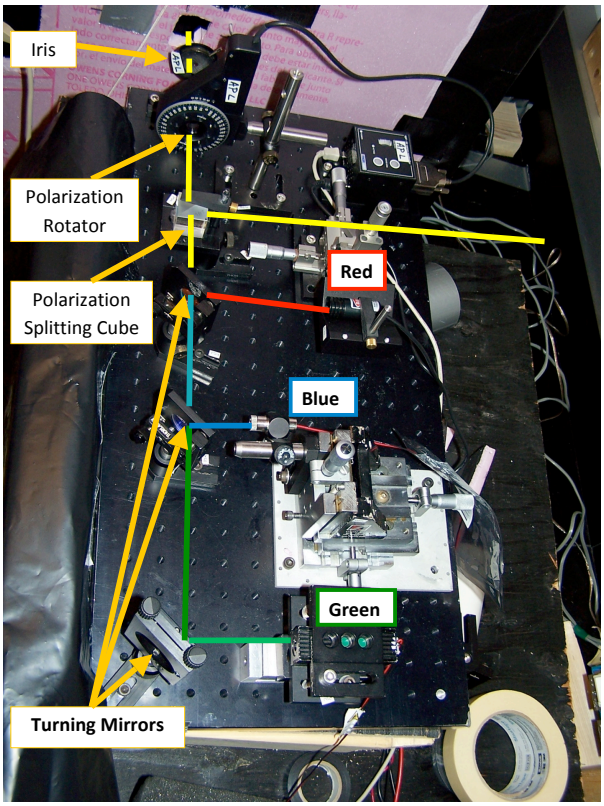

Figure 5.1: The transmitter consists of three coaligned visible wavelength lasers used in all experiments.

Table 5.1: The experimentally measured polarization efficiencies of the splitting cube and the rotator.

Element	**wavelength (nm)**	**Efficiency**
Polarization Splitting Cube	405	> 0.95
	532	> 0.90
	655	> 0.85
Polarization Rotator (half-wave plate)	405	0.9686
	532	0.9921
	655	0.9921

Once the efficiency of the transmitter elements are known they are used to scale the measured intensities before the ratio process. Additionally, the imaging optics (diffraction grating and camera) must be polarization insensitive to obtain the true polarization ratio.

5.2 Imaging of Scattered Beam Intensity

The co-aligned beams are directed through a volume of aerosols where scattering angles in the 120 to 175 degree range are imaged. A diffraction grating is placed in front of the camera as shown in Figure 5.2. The grating spatially separates the beams into different wavelengths in the image. Each image contains the scattering data for the transmitted wavelengths in the selected range of angles.

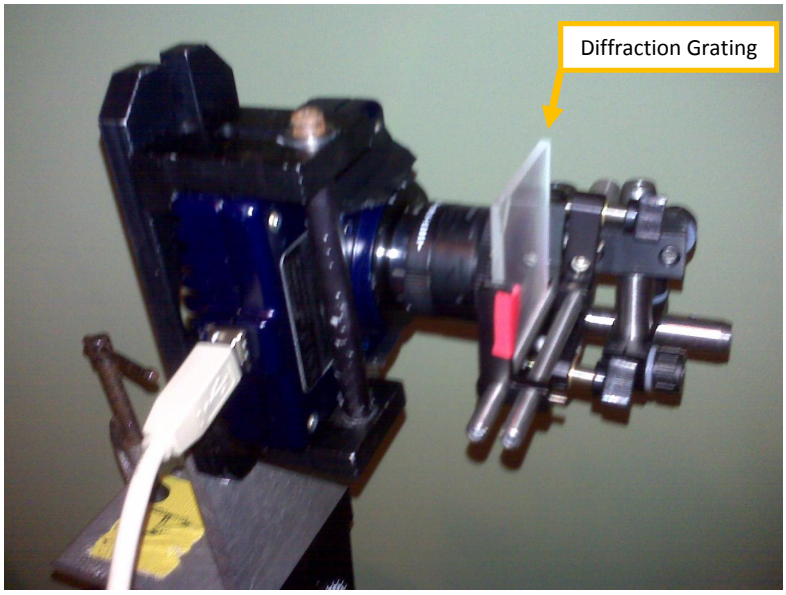

Figure 5.2: The diffraction grating is in front of the imager.

The gratings were chosen to be polarization insensitive, so they should exhibit no optical performance difference between the polarization components. This allows the ratio to be taken without a calibration of the diffraction grating.

The diffraction grating is claimed to be polarization insensitive by the supplier, Thor Labs. A 600 lines/mm grating was selected for a number of reasons; it has a similar transmission efficiency for all three visible wavelengths, see Figure 5.3, the beams are spread enough to separate and image the beams near the middle half of the CCD chip, and it exhibits severe

curvature in the diffracted beams. The beam curvature affects the intensity measured across the imager because of the addition and subtraction of dead space in the imager, this is discussed in more detail in Appendix B.2.

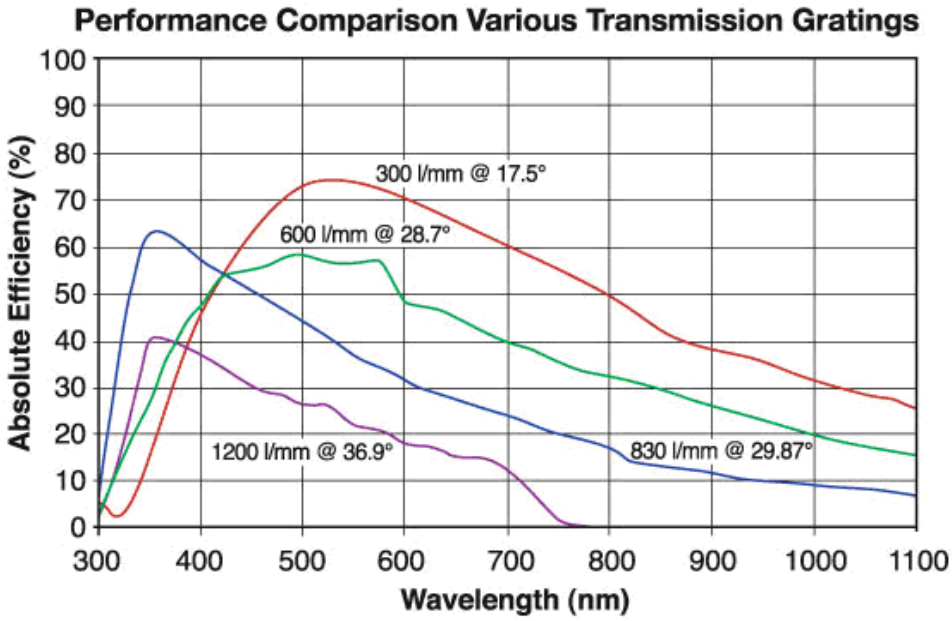

Figure 5.3: Transmission data of the diffraction gratings provided by Thor Labs, including the 600 lines/mm grating used.

A Computar 8.5 mm focal length coated lens focuses the image on the CCD chip. The coated lens loses some light and the efficiency of the light transmitted changes slightly between the center of the lens and the edges. This effect is largely ignored and assumed minimal, but its presence is acknowledged. This lens can be adjusted to focus on different parts of the beam path as it goes through the scattering volume. Imaging a large scattering volume when the camera sufficiently far away from the beam (8 ft or more) captures the majority of the beam. However, when the camera is close to the beam (within 6 ft) it is impossible to focus the whole beam in focus, in this instance the end of the beam is chosen to be in focus. This is the portion of the beam where the largest scattering angles are imaged and the most information is contained.

The light passes through the lens and is focused directly on the CCD chip. The CCD chip response is shown in Figure 5.4, the inverse of this curve is an indication of the relative power that the transmitted wavelengths should have. For instance, the 532 nm and 655 nm wavelengths have a similar response on the CCD chip, so their powers should be similar. However,

the 405 nm wavelength laser would need to be about 1.5 times more powerful in order to be registered equally on the CCD and obtain accurate scattering data for all three wavelengths in one image. By matching the CCD response for all three beams sufficient scattering intensities, which are not over-saturated, are measured. The Meade Instruments Deep Sky Imager II monochromatic imager uses a Sony ICX429ALL chip described in Table 5.2.

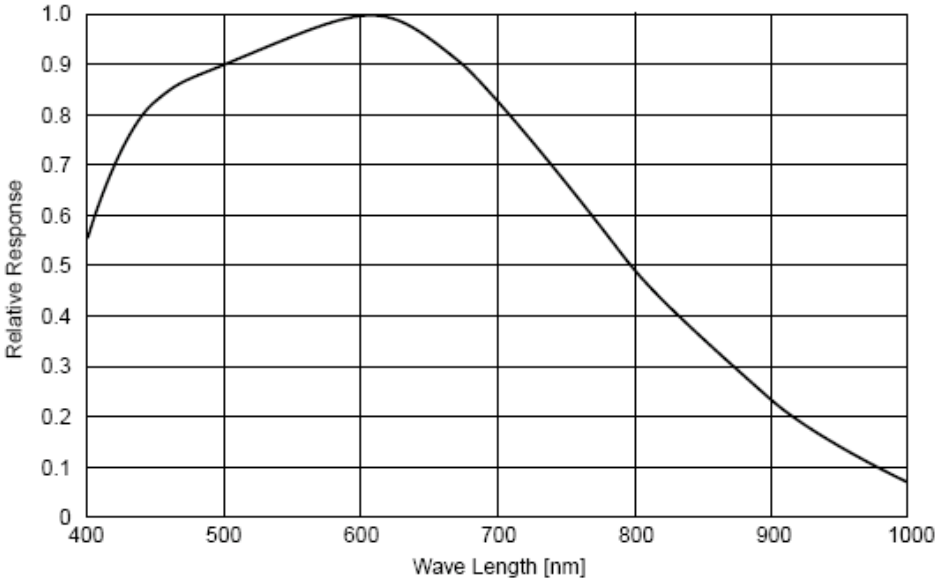

Figure 5.4: Response of the CCD chip, provided by Meade instruments.

Table 5.2: Imager specifications (provided by Sony and Meade Instruments).

Chip Size	5.59 mm (w) x 4.68 mm (h) 8 mm diagonal (type)
Pixels	8.3 microns (w) x 8.6 microns (h) 752 x 582 pixels (437,664 pixels) Built in temperature sensor measures degrees in celsius and matches it to each dark frame
Data Transition	16-bit (greater image depth and contrast) 1/10,000 of a second to one hour

5.3 Calculation of Scattering Angle

In order to calibrate the scattering angle for any given point in the CCD image, wires hanging on a string are placed in the beam at pre-measured distances before experimental measurements are taken, see Figure 5.5. This figure illustrates the triangulation method used to determine the scattering angle in the CCD image. The ovals denote the CCD imager lens and the faded area represents the field of view of the imager. The black dotted lines represent the reference points taken in the image. The yellow circles represent the dangles (metal wire) suspended from a string into the laser beam for the alignment pictures.

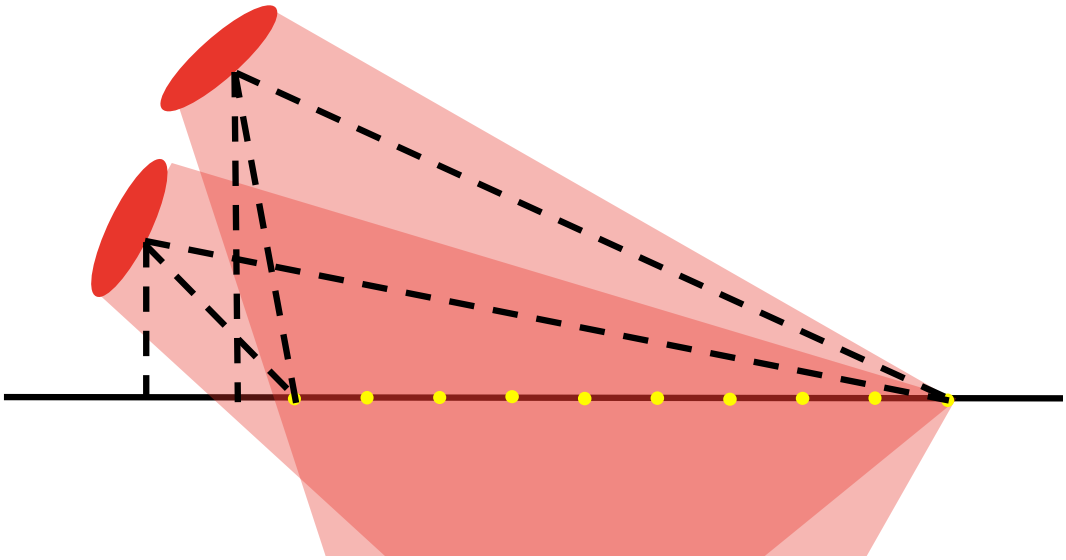

Figure 5.5: Triangulation method use to find scattering angle.

Figure 5.6 is a photo showing of the inside of the chamber, as the CCD imager would see the alignment string. Each dangle produces a "star" in the CCD alignment image (see Figure 5.7) allowing correlation of the CCD pixel number to a specific scattering angle. Before the experiment is conducted the alignment string is used to obtain an alignment picture and then the string is dropped out of the field of view of the camera.

Figure 5.7 was taken with the imager in the NCSU chamber. The colored lines are superimposed to represent the location of the first diffracted order of the blue, green and red beams. The zeroth order is located above and the second order diffracted beams are observed below. This alignment picture is the type used to find the scattered angle corresponding to each pixel.

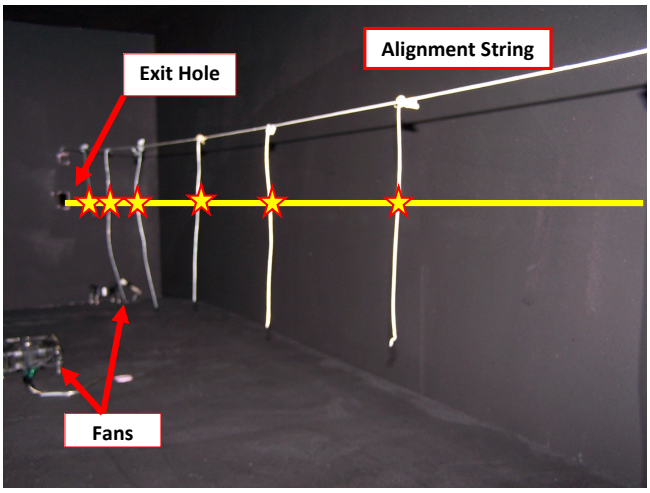

Figure 5.6: Picture of alignment process, metal alignment wires are clearly visible, the co-aligned beam and scattering created by metal alignment wires are superimposed..

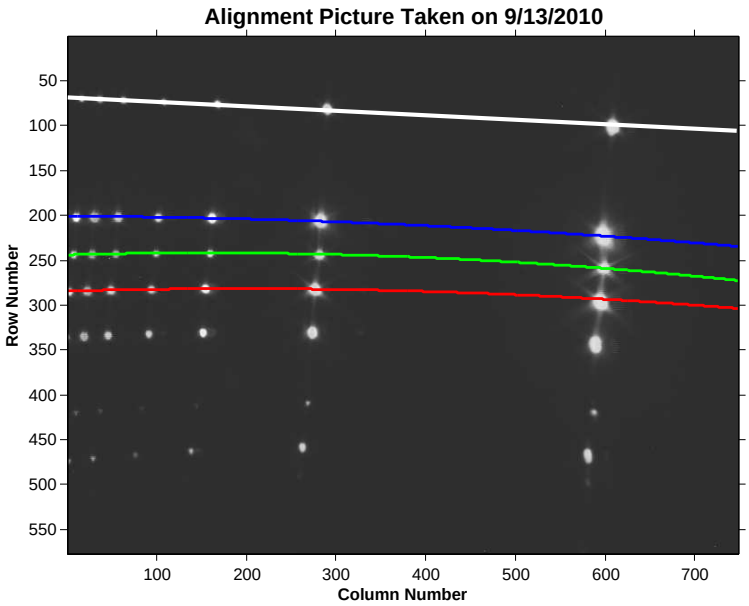

Figure 5.7: Picture taken by imager during alignment process to find location of diffracted beams.

The scattering angle is found by simply finding the perpendicular distance from the beam to the imager and then measuring the distance down the beams from the perpendicular to the imager, see Figure 5.8. During the calibration, measurements are taken to the nearest 1/2 in, making the uncertainties 1/4 of an inch. The uncertainty in the scattering angle is estimated below:

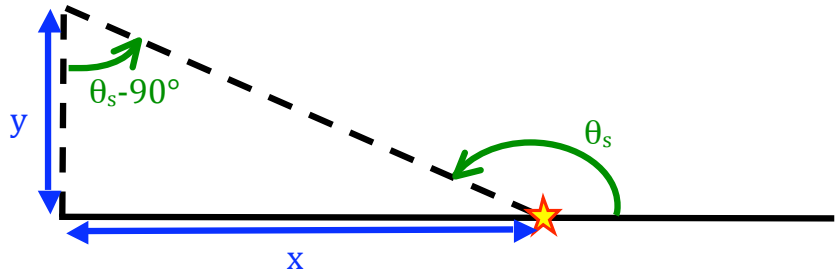

Figure 5.8: The scattering angle.

$$(\theta_S - 90^\circ) = \tan^{-1}\left(\frac{x}{y}\right) \tag{5.1}$$

The uncertainty in $(\theta_S - 90^\circ)$ is examined in Equation 5.1 and the propagation of errors equation in Bevington.[34] The squared error in θ is:

$$\sigma_{\theta_S}^2 = \sigma_x^2\left(\frac{\partial\theta_S}{\partial x}\right)^2 + \sigma_y^2\left(\frac{\partial\theta_S}{\partial y}\right)^2, \tag{5.2}$$

where,

$$\frac{\partial\theta_S}{\partial x} = \frac{1}{1+\left(\frac{x}{y}\right)^2}\left(\frac{1}{y}\right), \qquad \frac{\partial\theta_S}{\partial y} = \frac{1}{1+\left(\frac{x}{y}\right)^2}\left(\frac{-x}{y^2}\right),$$

$$\left(\frac{\partial\theta_S}{\partial x}\right)^2 = \frac{y^2}{(x^2+y^2)^2}, \qquad \left(\frac{\partial\theta_S}{\partial y}\right)^2 = \frac{x^2}{(x^2+y^2)^2}.$$

The values of x and y have the same uncertainty ($\sigma_x = \sigma_y = \sigma$). Therefore equation 5.2 simplifies to,

$$\sigma_{\theta_S}^2 = \frac{\sigma^2}{x^2+y^2}.$$

The uncertainty in θ_S is

$$\sigma_{\theta_S} = \frac{\sigma}{\sqrt{x^2 + y^2}}. \tag{5.3}$$

An example from one instance in the chamber at NCSU is considered. The distance between the camera and the first dangle (closest to the transmitter) was measured to be $y = 9\ in$ and $x = 11\ in$, therefore the uncertainty is

$$\sigma_{\theta_S} = \frac{0.25}{\sqrt{11^2 + 9^2}} = 0.0175\ radians = 1\ degrees.$$

However, when the distances measured the the last dangle is $y = 9in$ and $x = 83in$, the uncertainty at the higher angles is much smaller, as calculated here.

$$\sigma_{\theta_S} = \frac{0.25}{\sqrt{83^2 + 9^2}} = 0.003\ radians = 0.15\ degrees.$$

This means that the location of most of the structure in our polarization ratio is fairly well known. Figure 5.9 shows the polarization ratio simultaneously measured by two different cameras.

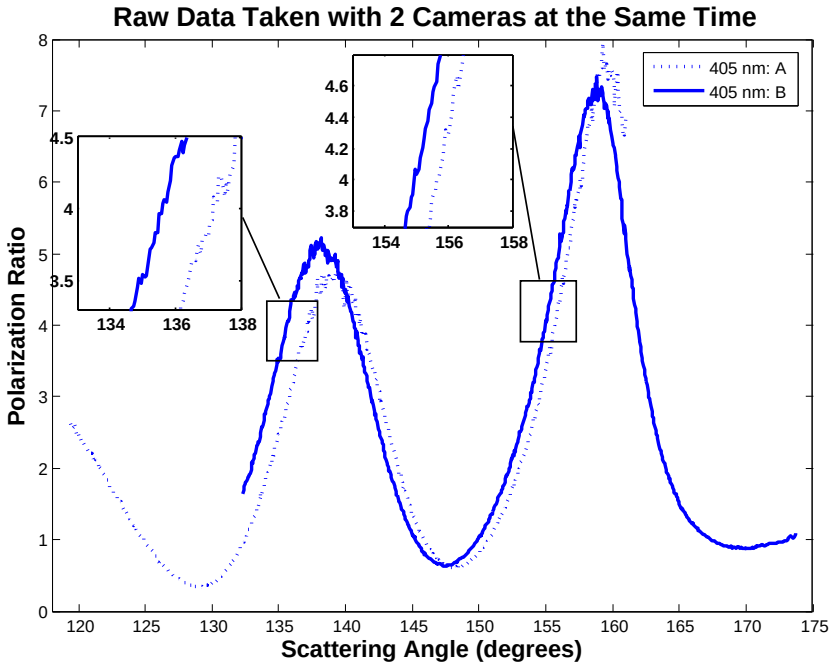

Figure 5.9: The polarization ratio measured by two separate cameras at the same time shows larger differences at the lower angles and less of a separation at the higher angles illustrating that the uncertainty in the higher angles is less than in the smaller angles.

The scattering angle was determined independently for each camera. Portions of the result are expanded at a range of smaller angles and larger angles illustrating that the polarization ratios are better determined at the higher angles. The location and magnitude of the polarization ratios are most important at higher scattering angles, because those angles contain more information for aerosol characterization.

The differences in the measured scattering angle for the two cameras in Figure 5.9 are larger than expected. This is due to the fact that the uncertainties calculated only include 68% of the possible measured values, the other 32% of the measured values fall outside this range, this is just a case where these fall slightly outside the calculated uncertainty range.[34]

Chapter 6

Chamber and Outdoor Measurements

This chapter starts with detailed descriptions of the three experiment locations. Then a discussion of resampling the measured data before inversion. Finally, the Continuous Genetic Algorithm (CGA) routine is used on the resampled measurements to determine aerosol distribution characteristics.

Measurements are made on commercially available on well-known aerosol sizes. These aerosols are manufactured spheres that have a specific size and very small standard width (≤ 1.05). Significant testing of well known sizes of aerosols has not been included in previous students' work, so testing of the polarization ratio and the inversion technique should be valuable in evaluating the polarization ratio method with the multistatic multiwavelength instrument.

6.1 Experimental Chamber Setup

Experiments were conducted using selected narrowly distributed polystyrene spherical aerosols in a testing chamber at Johns Hopkins Applied Physics Laboratory (APL), and in a small aerosol chamber at North Carolina State University (NCSU). Non-spherical biological aerosols were also measured in the APL chamber to investigate possible future application of an aerosol scattering instrument. Outdoor measurements of a radiation fog were attempted in Raleigh, NC.

6.1.1 Johns Hopkins University Applied Physics Laboratory (APL)

Tests were conducted in the aerosol chamber at Johns Hopkins Applied Physics Lab in Laurel, Maryland. During the tests, an Aerodynamic Particle Sizer (APS) is used simultaneously with the optical scattering instrument to measure the aerosol properties. The five wavelengths were split into two sets of wavelengths, visible (405 nm, 532 nm, and 655 nm) and near-infrared (670 nm and 780 nm). These tests evaluate the instrument performance using known size distributions and number densities that could be derived from the results of the Mie inversion routines.

An overall picture of the chamber and the important components is shown in Figure 6.1. Computer work stations controlled the data collection while aerosols were dispersed and portals were used to feed the USB cables for imaging, polarization rotation and APS data transfer. The evacuation tube is controlled from in an adjoining room and used to clean the aerosols from the chamber before and after all experiments.

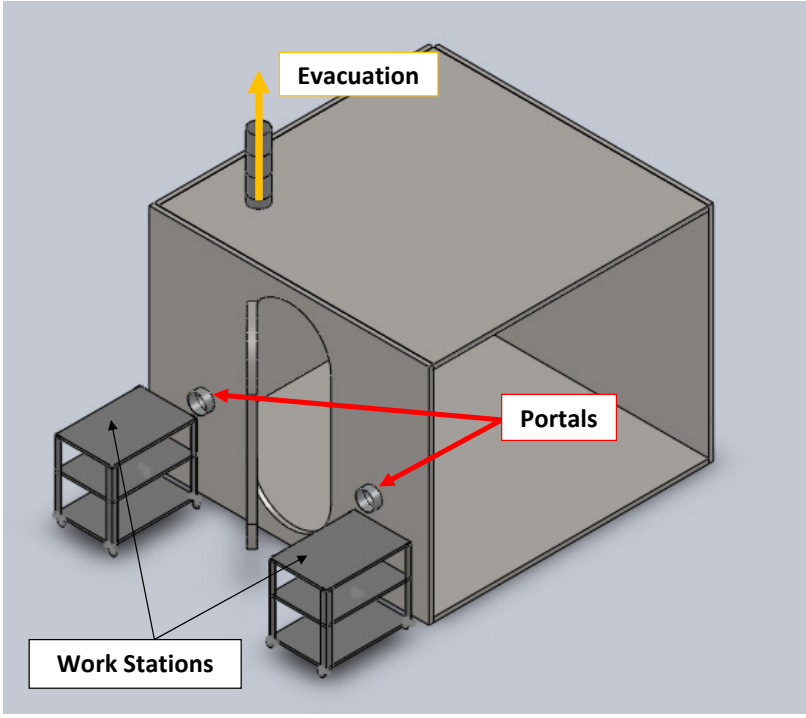

Figure 6.1: Schematic drawing of the 10 ft × 10 ft × 8 ft APL aerosol chamber.

The aerosol dispersal unit and the multistatic instrument were placed in the chamber as shown in Figure 6.2 and schematically in Figure 6.3. The wavelengths are separated into the visible and near-infrared (NIR) wavelengths, these transmitters are operated as independent measurements of the same aerosols. The height of the NIR and visible beams are the same, but the APS is located a meter below, and between the beams. Each of the beams are terminated at the corner of the chamber using a beam stop to reduce the amount of stray light in the chamber.

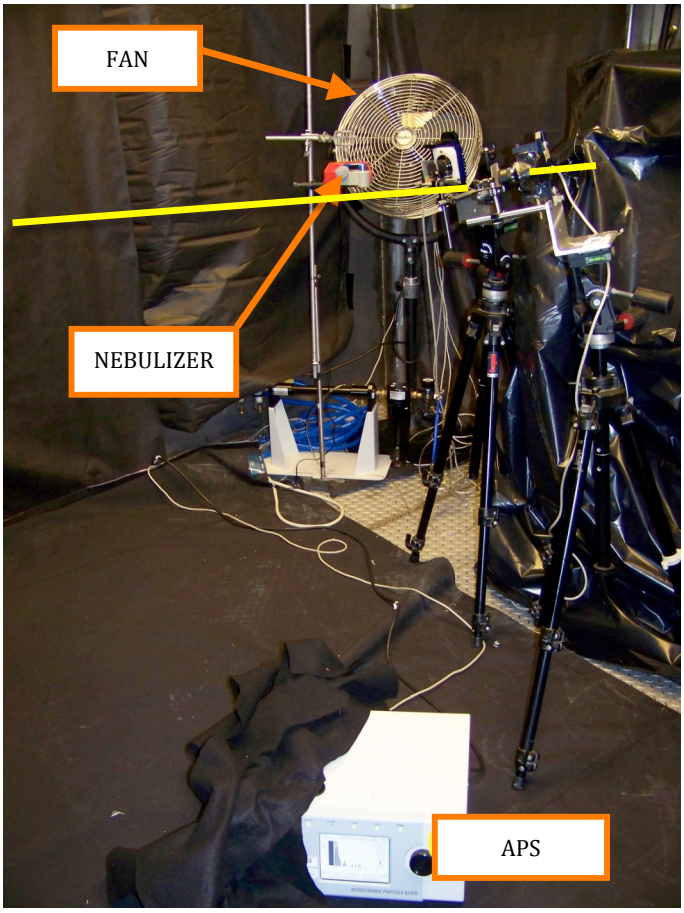

Figure 6.2: Picture taken from inside the chamber looking across the position of the visible beam (indicated as a yellow line in the image).

The chamber is highly reflective stainless steal and reflections can be a huge problem when measuring the scattering intensity, see discussion by Brown. Black felt was placed on the walls and floor of the chamber and beam stops were placed at the end of the beams to reduce reflections, this can be seen in Figure 6.2. Felt was also placed over the APS because its white color; in this image, the felt is peeled back to show the instrument. Figures 6.2 and 6.3 also show the arrangement of the nebulizer, fan and APS in the chamber. The APS is placed on the floor and it measures through a small intake valve on the top of the instrument.

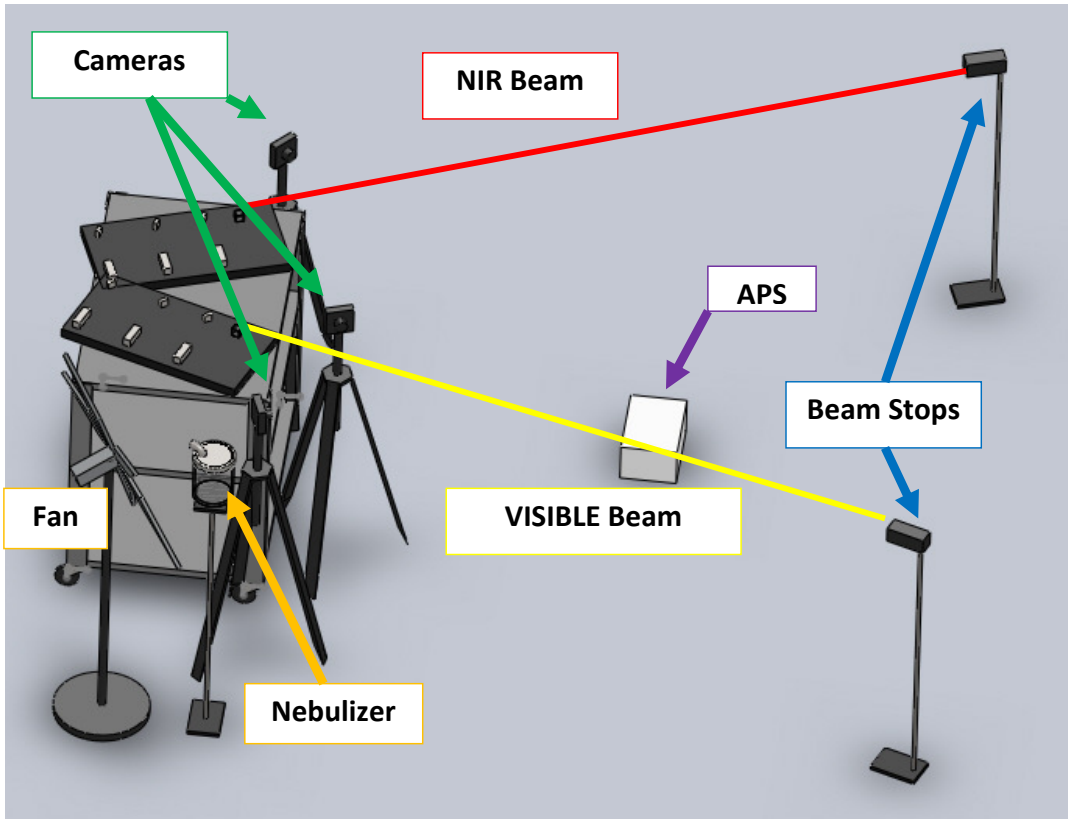

Figure 6.3: Instrument elements inside the chamber during the experiments at APL.

An APS one of the most advanced particle sizing instruments currently used for aerosol research. It uses a pump to draw in a small volume of air and characterize the aerosols it collects. The aerosols are sized based on falling rate and light scattering within the chamber. This measurement method only gives a measurement for a small volume within the larger

chamber volume. Experiments conducted with both instruments available allow a unique way to study their agreement.

Once the equipment was set up removable posts to suspend an alignment string are placed behind the transmitter and in front of the beam stop and alignment images were taken. The spatial relation between each imager and the alignment wires is measured and recorded below in Figure 6.4.

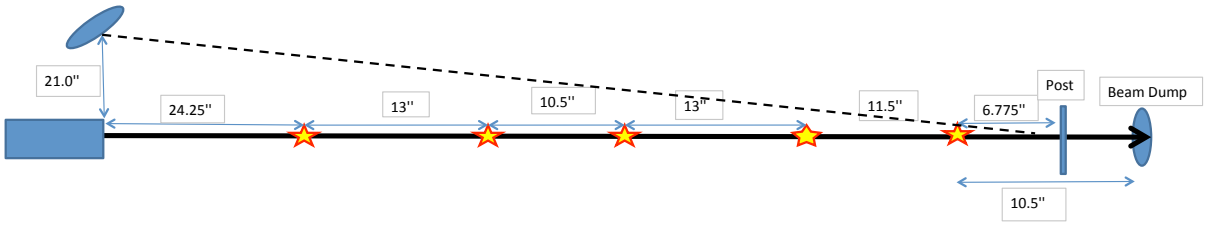

(a) NIR Alignment

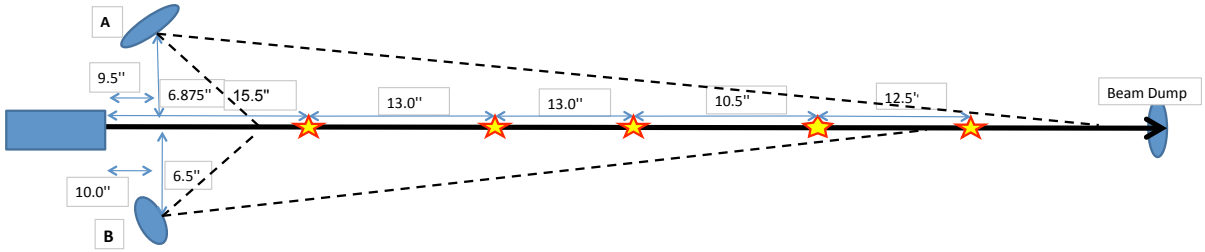

(b) Visible Alignment

Figure 6.4: The alignment measurements for APL setup.

Since the larger scattering angles contain more information for aerosol characterization, the spatial relation between the imagers and the beam is similar.

In the chamber an Aerodynamic Particle Sizer(APS) was used to continuously monitor the size distribution of the particles, see Figure 6.2. The size distribution is summed over a 10 second time period. After the data is collected it is averaged into one minute intervals to decrease the file size. This down sampling is still at a higher data rate than the sequential pictures used in the aerosol scattering instrument.

6.1.2 North Carolina State University (NCSU)

The cameras are placed next to each other on the same side of the beam in these experiments, as shown in Figure 6.5. The spatial relation between the imagers and the beams are measured

using the alignment wire technique, the measurements are recorded in inches as shown in Figure 6.6. The chamber is made of styrofoam with a flat black water-based paint on the inside to reduce reflections. Holes are cut providing windows for the imagers to view the scattering inside the chamber, evacuation of the chamber, as well as beam entrance and beam exit. The hole between the cameras in Figure 6.5 is used to input aerosols to the chamber and for evacuation of the chamber volume after experiment runs. This opening is covered with a spare piece of painted styrofoam during the experiment to prevent aerosols from escaping the chamber. After the experiment is completed the ventilation tube is added (see Figure 6.7). Ventilation after experiment runs is used because the particle sizes used are small enough to be breathed into the lungs, which is unhealthy. Masks and goggles are worn during the experiment run, since the holes in the chamber allow aerosols to escape.The transmitter, cameras and fans are controlled from outside the chamber, as shown in Figure 6.8. Placement of the controls for the experiment outside the chamber allows them to be controlled without disturbing the aerosols inside the chamber.

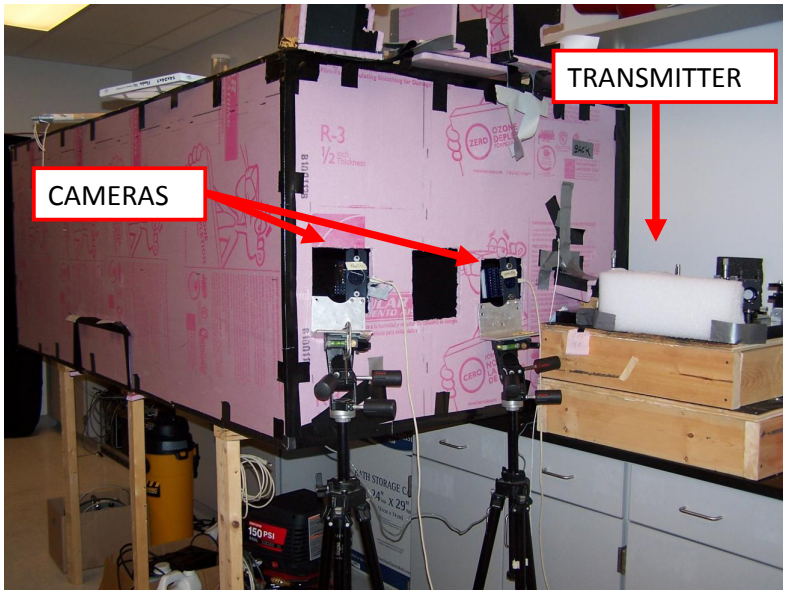

Figure 6.5: Transmitter and imager placement.

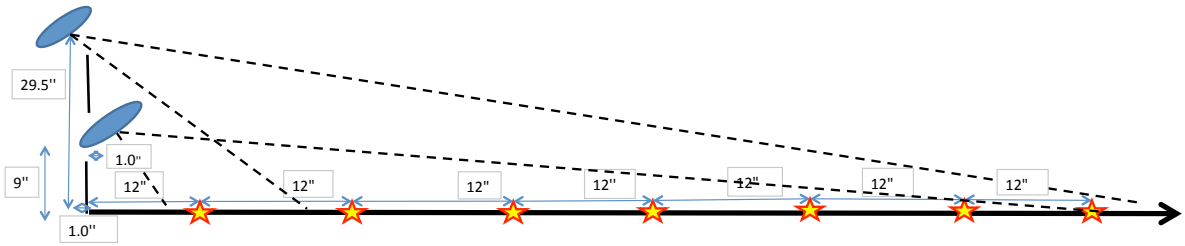

Figure 6.6: This shows the alignment process used to determine the scattering angles for both cameras in the NCSU chamber.

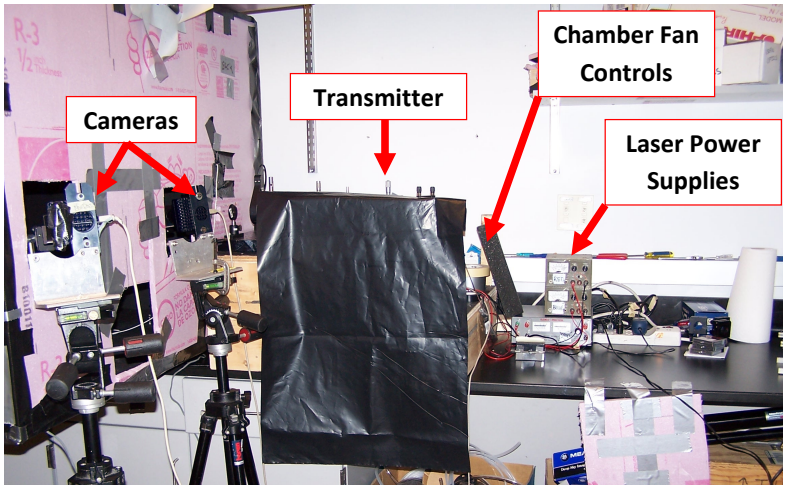

Figure 6.8: The transmitter, fans, and cameras controls located outside the chamber.

6.1.3 Nebulizer System for Aerosol Dispersal System

At APL, the aerosols were dispersed by a 24 jet collision nebulizer, and at NCSU the aerosols were desprused using a 6 jet collision nebulizer. These units are identical scale models of each other (jets remain the same size). The placement of the nebulizer int he APL chamber can be seen in Figures 6.3 and 6.2. The nebulizer set up for the NCSU chamber is shown in Figures 6.9 and 6.10.

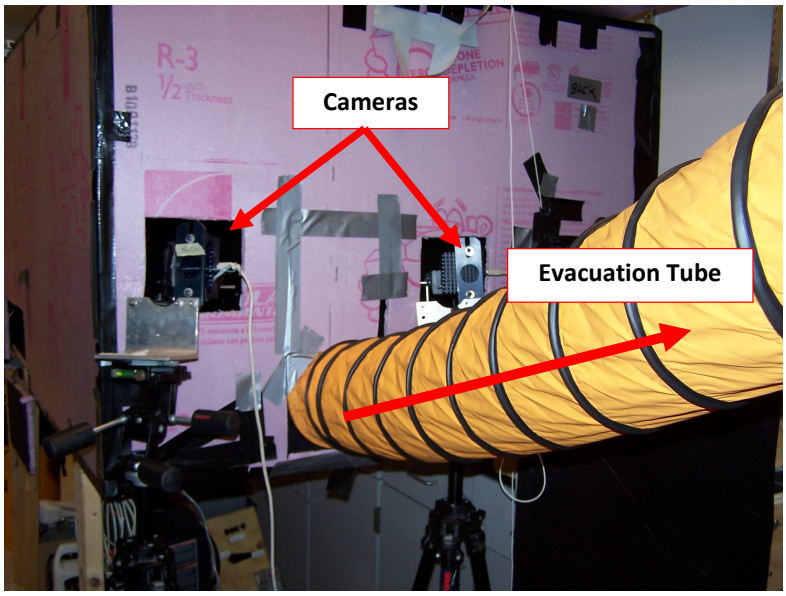

Figure 6.7: The evacuation tube was used with an industrial fan to quickly evacuate the chamber of aerosols.

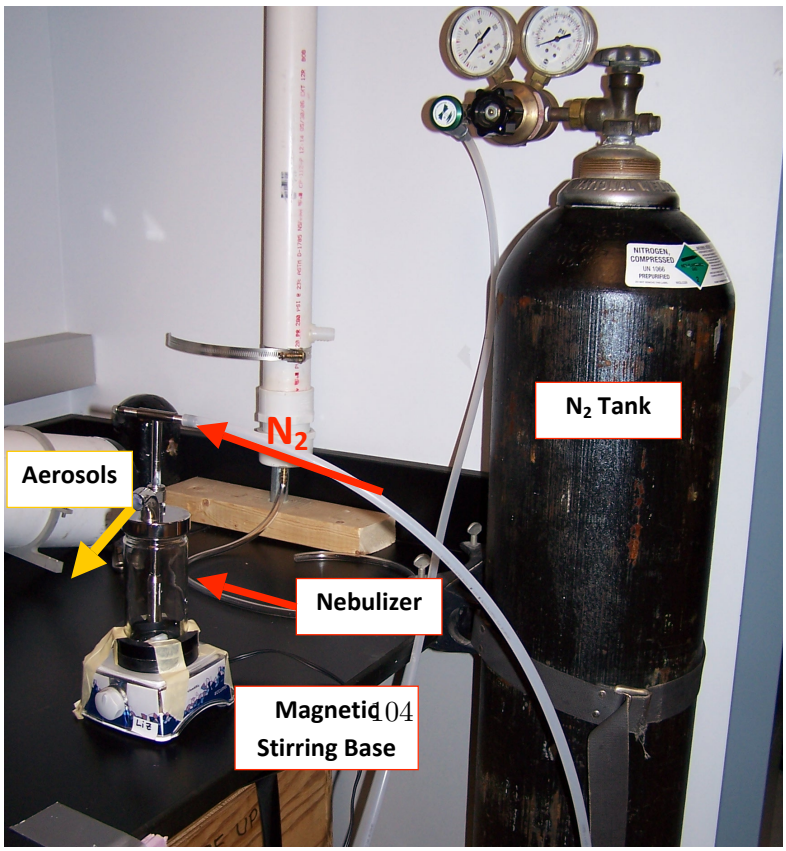

Figure 6.9: Nebulizer set-up.

A nebulizer forces compressed nitrogen down a spout and uses jets of the nitrogen gas to spray the aerosols which are suspended in water toward the walls. A magnetic stirring base is used to keep the sample in the nebulizer well mixed throughout the experiment. The large dropplets blown from in the spray are fractured with one particle inside a liquid dropplet, the droplets are then forced out the top of the nebulizer and into the air. Once released into the air, any water coating rapidly evaporates from the aerosol. A fan is placed near the out spout of the nebulizer mix the aerosols in the chamber and uniformly disperse them. The NCSU chamber uses six fans throughout the chamber to uniformly mix the aerosols before measurements are taken. The aerosols used are not harmful, but should not be ingested, so the APL chamber and the NCSU chamber have evacuation tubes. The placement of these tubes can be seen in Figures 6.1 and 6.7, respectively. Both evacuation systems have a large tube connected to high flow fans to quickly remove aerosols from the chamber.

Before experiment runs begin the nebulizer set-up is placed inside the chamber to disperses the aerosols from an aqueous solution, as shown in Figure 6.10. A fan is placed near the nebulizer to quickly blow the aerosols into the chamber. Additional fans in the chamber are turned on during aerosol dispersal, but all are turned off during experiment runs while the aerosols settle naturally. The aerosols are inserted near the cameras but blown toward the other end of the chamber, this is the maximize the most useful pieces of data, at larger scattering angles, and to try and keep the aerosols away from the cameras, to keep them as clean as possible.

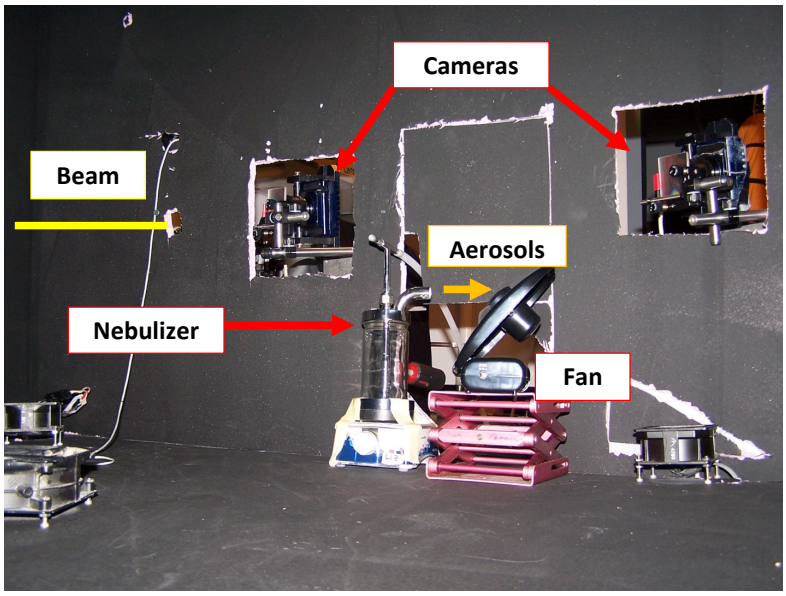

Figure 6.10: Equipment placement inside the chamber.

The nebulizer may output droplets that do not contain a particle. If small water droplets stay suspended in the air or the water stays on the particle, it will affect the scattering that is measured. Tiny water droplets affect the intensity measured by the 405 nm wavelength, since it has the highest ka value. In Figure 6.11(a) the scattering by the molecules that exist in the lab air. Figure 6.11(b) the intensity of scattering is measure when the nebulizer was filled with purely water. The small peak of intensity present in all intensity measurements is due to a scratch on the diffraction coating of the grating, where an increased intensity is transmitted. Large intensity measurements at the largest scattering angles are due to a large amount of light reflected off the sides of the beam exit hole. From Figure 6.11 the intensity scattered by the lab air and from the lab air with the dispersed water are essentially identical in shape and intensity for both polarizations. The lab air at NCSU, where this test was conducted, and at APL was air conditioned, so the relative humidity is low enough to quickly evaporate water from the particles. Therefore, the water droplets output by the nebulizer are not expected to effect the scattering measured by this instrument.

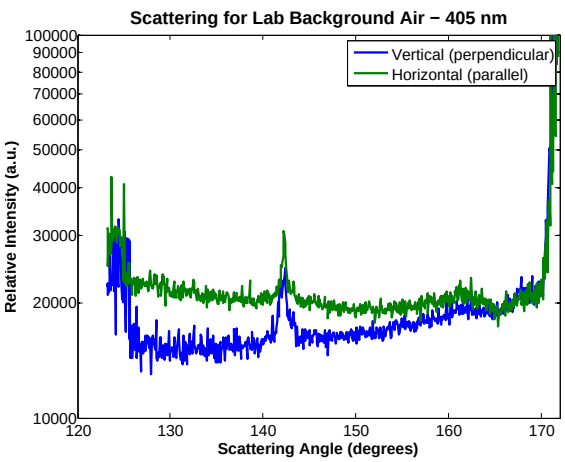

(a)

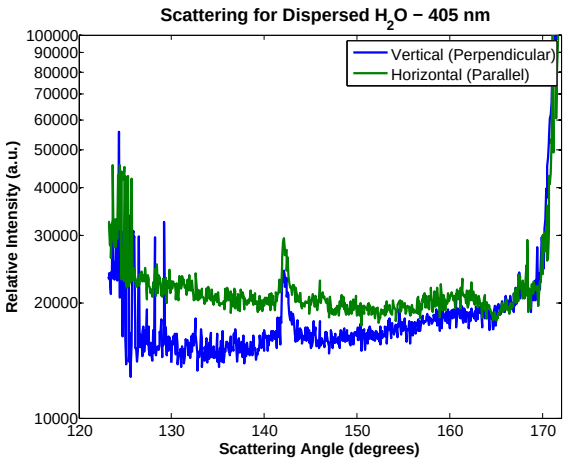

(b)

Figure 6.11: Intensity measurements for lab background air (a) and water dispersed by the nebulizer (b).

6.2 Outdoor Experimental Setup

A beam path over a small hog lagoon was selected because of its remoteness and available moisture for fog formation, see Figure 6.12(a).

(a) Location

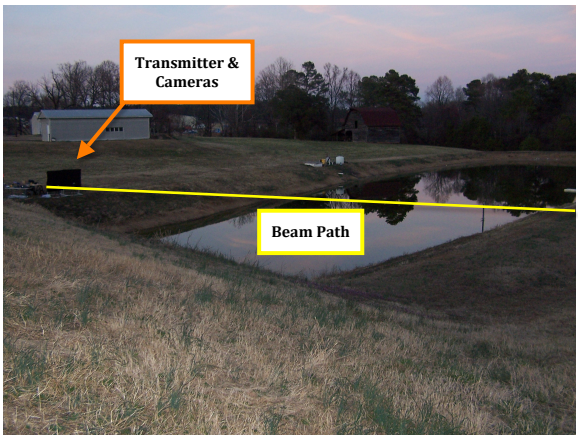

(b) Beam Path

Figure 6.12: The location and beam path selection for the fog experiment.

The beam path selected is across the lagoon (see Figure 6.12(b)), where the fog would form first if the dew point to temperature ratio approaches one. This is also where the fog showed stay the most uniform because it is continuously generated by the moisture of the lagoon. Imagers are place on the bank next to the transmitter, the alignment string is hung between the banks of the lagoon.

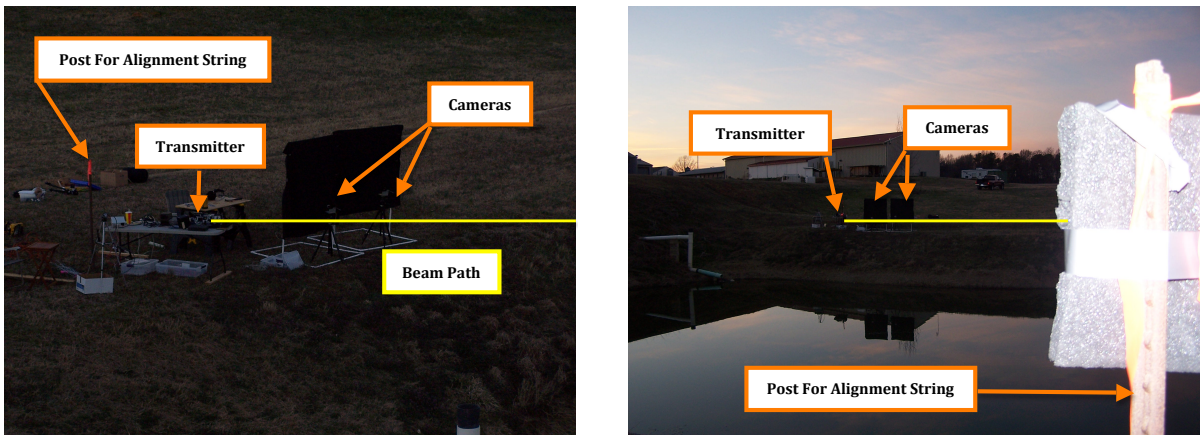

(a) (b)

Figure 6.13: Instrument component placement for the fog experiment.

Previous fog experiments were hindered by background lights through trees.[25] This location is at a lower elevation surrounded by small hills, so background light is not a problem.

6.3 Data Preparation for Inversion

Before the experimental data can be analyzed it must be prepared for the inversion process. Brown[25] determined that the resolution needed for polarization ratio inversion is approximately one degree. However she implemented a half-degree resolution without sacrificing much efficiency. Images during the alignment process correlate the locations on the image to the scattering angle. The field of view of the camera determines the range of scattering angles and the number of pixels determine the resolution of the angle measurements.

Weighted-averaging is selected to accurately down-sample the measured polarization ratio at each half degree. This method is selected over a decimation method because decimation would select one point as a representative value disregarding the nearest neighbor measured points allowing a larger amount of noise in the resampled data.

The particular weighted average method used here is a 7-point method based on a binomial distribution around the midpoint.[34] The point nearest to the desired half-degree scattering angle is selected as the "mid-point" to preform this procedure. The averaging procedure uses the three points on either side of the midpoint and their binomial weight to calculate the re-sampled representative value of the half-degree measurement. Symbolically, given seven points: $\{p_1, p_2, p_3, p_4, p_5, p_6, p_7\}$. Let p_4, be the measured value at the pixel nearest to the desired half-degree measurement. Then the new resampled value, p'_4, would be calculated as follows....

$$p'_4 = \frac{p_1}{64} + \frac{p_2}{16} + \frac{p_3}{4} + \frac{11p_4}{32} + \frac{p_5}{4} + \frac{p_6}{16} + \frac{p_7}{64}.$$

A representative intensity measurement across the captured scattering range is shown in Figure 6.14(a). The ratio formed from these intensity measurements is shown in Figure 6.14(b), where the resolution remains the same. This ratio is then resampled through interpolation and weighted averaging to for the ratio in Figure 6.15.

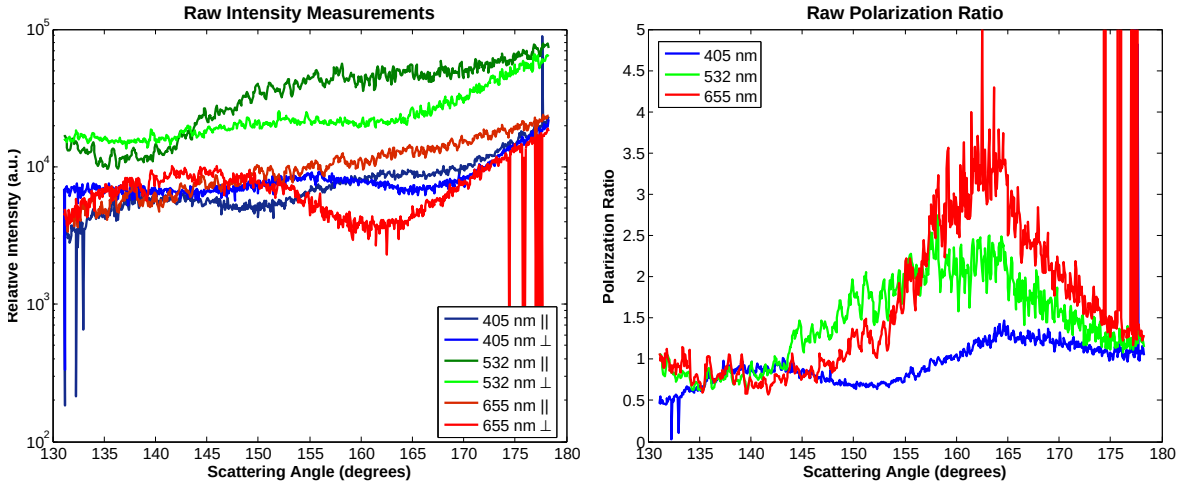

(a) (b)

Figure 6.14: (a) Example of raw intensity measurement, (b) Polarization ratio formed from the raw intensity measurements in (a)

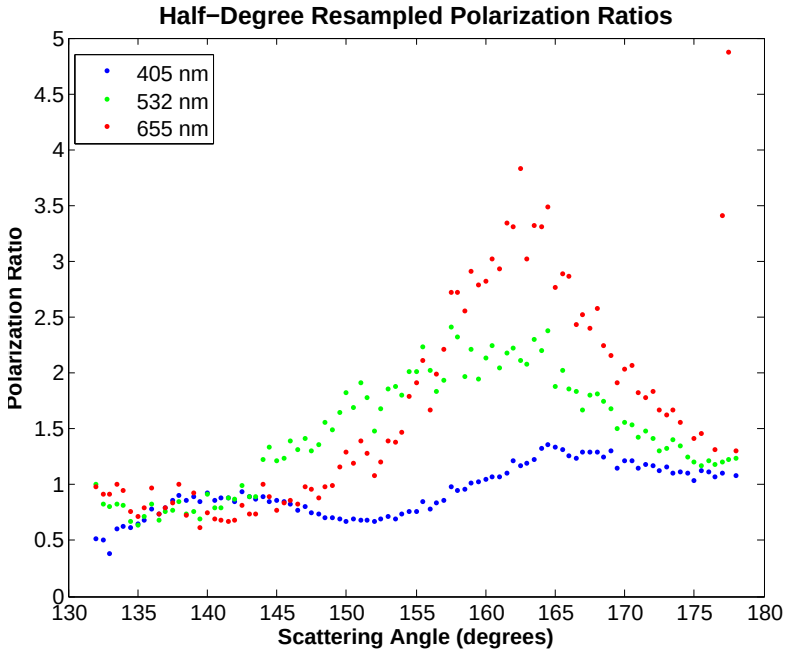

Figure 6.15: The raw polarization ratio from Figure 6.14(b) is interpolated with a weighted 7-point average at every half degree.

6.4 Single Mode Polystyrene Latex (PSL) Aerosol Distributions

Polystyrene Latex (PSL) spheres are selected as a spherical aerosol that could be purchased and dispersed by a nebulizer. These spheres are readily available in many different narrowly distributed sizes in the 10 nm to 10 micron diameter range. The sizes selected for this analysis are 0.5, 1.0 and 2.0 μm in diameter.

Fro analysis the index of refraction of the PSL spheres was assumed from Ma,[43] see Figure 6.16. The index for the specific wavelengths is outlined in Table 6.1. The concentration, mean radius, μ_g, and standard width, σ_g, where found by the continuous genetic algorithm routine using the measured polarization ratios.

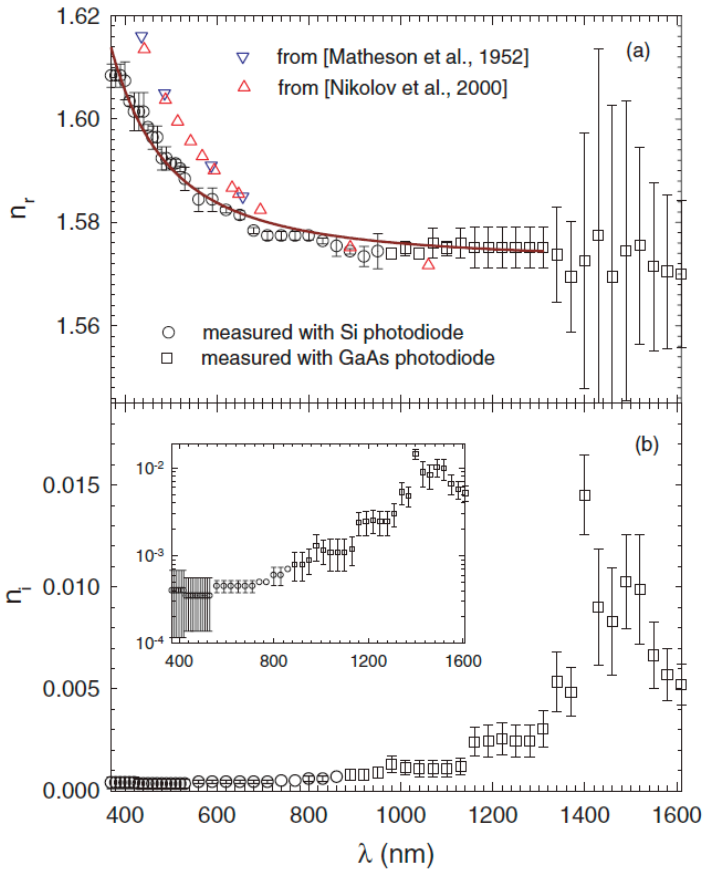

Figure 6.16: Refractive indices of the polystyrene microspheres as a function of wavelength: (a) n_r with solid line as the fitting curve based on the Cauchy dispersion formula; (b) n_i (inset: n_i on a log scale). Figure and caption taken from Ma,[43] references are to Matheson et al.[44] and Nikolov et al.[45]

Table 6.1: The index of refraction values for PSL spheres selected for the wavelengths used.[43]

Wavelength [λ(nm)]	Index of Refraction [n]
405	1.61 + 0.001i
532	1.59 + 0.001i
655	1.58 + 0.001i
670	1.58 + 0.001i
780	1.575 + 0.001i

6.4.1 One Micron Diameter PSL Spheres.

To study the polarization ratio as the concentration changes, it is important to calculate the expected ratios for each wavelength at two concentrations. The concentrations of 100 and 25 $/cm^3$ were selected as they are typical concentrations for measurements performed, see Figure 6.17.

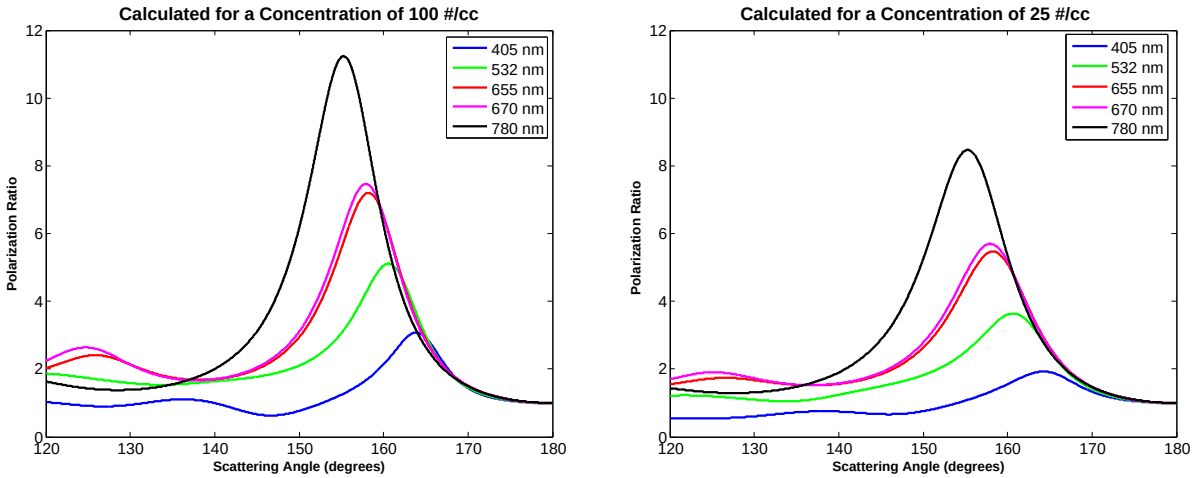

(a) (b)

Figure 6.17: Calculated polarization ratio for all five wavelengths with different concentrations of 1.0 micron diameter PSL spherical aerosols using the index of refraction values in Table 6.1.

Figures 6.17(a) and 6.17(b) show the magnitude of the polarization ratio changes based on concentration. Notice the scattering angle where the polarization ratios peak does not change as a function of concentration. It is beneficial to check the concentration sensitivity for the wavelengths used. Figure 6.18 indicates the detectable concentration range for the shortest wavelength, 405 nm. According to this figure the lowest concentration for one micron PSL sphere that is detectable is 1 sphere/cm^3 and the highest detectable concentration is 10^4 spheres/cm^3. The concentrations obtained by the APS are within the detectable range, so the polarization ratio method can be used to accurately determine the concentration.

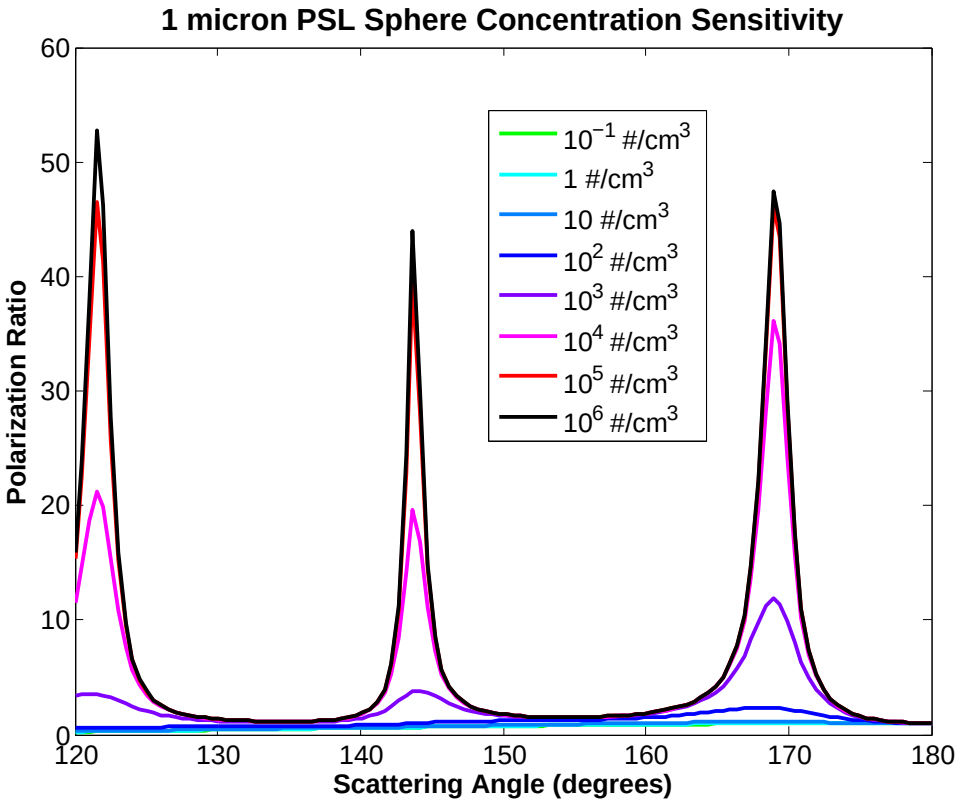

Figure 6.18: The polarization ratio sensitivity for 1 micron diameter PSL spheres based on the shortest wavelength of the visible transmitter, 405 nm.

Experimental Measurement at APL

The first experimental measurements are on Sunday August 22, 2010 using Polystyrene Latex(PSL) spheres. The chamber was filled to about 150 $particles/cm^3$ as measured by the APS then measurements were taken over the next few hours as the concentration dropped to about 20 $particles/cm^3$ on the APS (see Figure 6.19. The aerosols were dispersed by a 24 jet collision nebulizer. Nebulizers are described in Section 6.1.3. A large fan placed near the spout of the nebulizer mixes the aerosols in the chamber to disperse them.

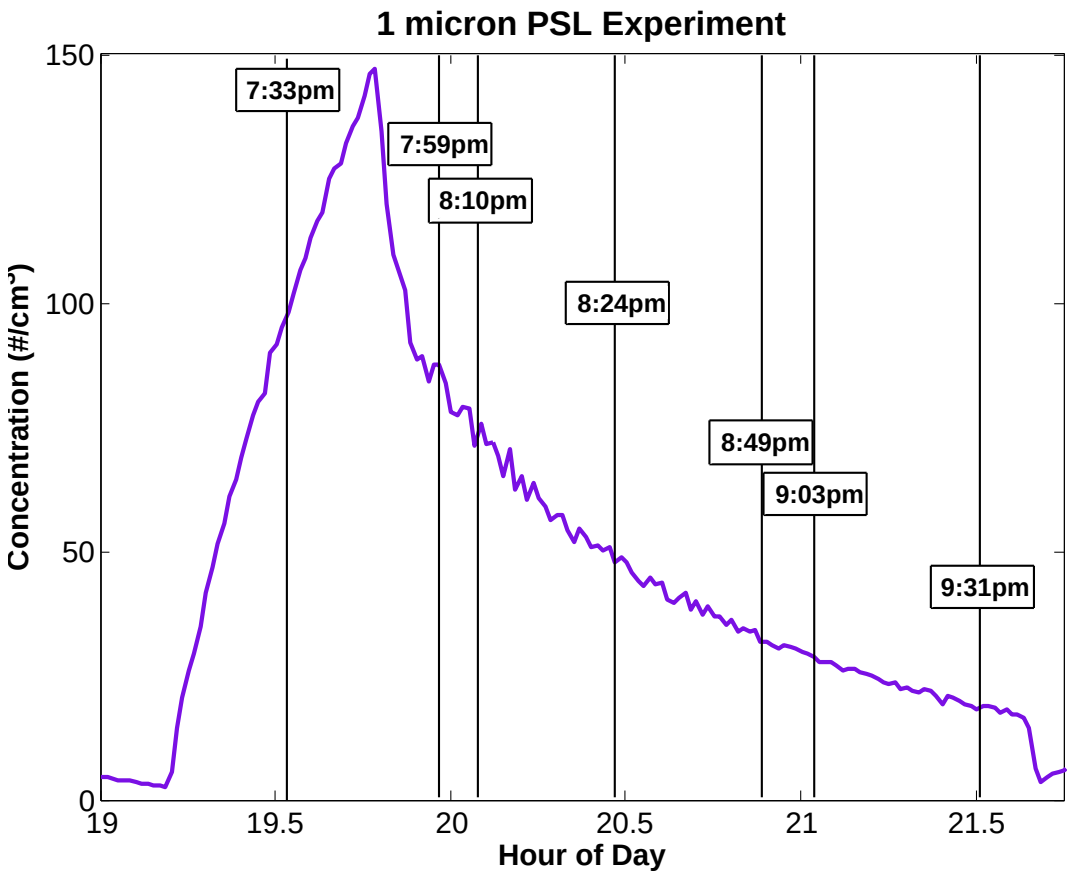

Figure 6.19: The total concentration measured by the APS during the one micron diameter PSL experiment is shown. The times are shown when the polarization ratio measurements are analyzed using the aerosol scattering collection method.

The first time analyzed was 7:33pm, the measured polarization ratios for the three visible wavelengths as well as the inverted solution are shown in Figure 6.20. The inversion results are shown in Table 6.2. The NIR wavelengths (670 nm and 780 nm) are taken at this time as well, but a problem in the camera software did not allow the beams to be accurately analyzed. Later in the experiment, the NIR wavelengths are analyzed.

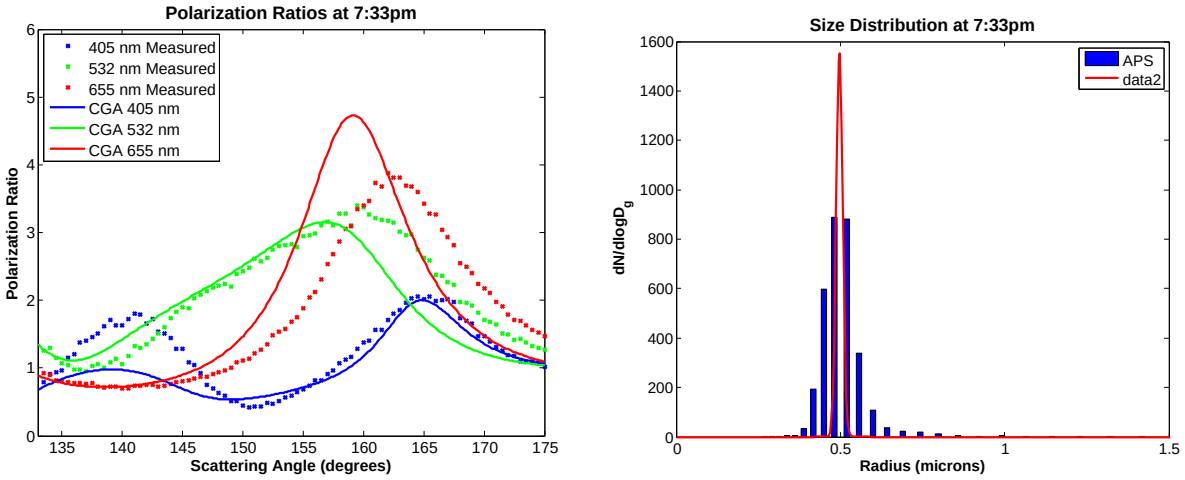

(a) (b)

Figure 6.20: (a) Measured polarization ratios are plotted using the CGA inversion; (b) Measured size distribution from APS, both at 7:33pm while the fans were still running and aerosols being added to the chamber.

Table 6.2: The quoted results form the CGA inversion routine and the measured values for the size distribution at 7:33 pm.

7:33pm	**Radius** (μm)	**Standard Width**	**Conc.** ($\#/cm^3$)	**Fitness**
CGA	$\mu_g = 0.497 \pm 0.0029$	$\sigma_g = 1.02 \pm 0.005$	$N = 34.1 \pm 7.71$	101.5 ± 4.45
APS	$\mu_g = 0.498$	$\sigma_g = 1.14$	$N = 101.84$	
% diff.	0.201 %	11.1 %	99.7 %	

The results shown in Figure 6.20, show that the inversion routine is trying to match the structure of the measured polarization ratio. The size distribution measured by the APS stays very consistent over the experiment run, with the concentration decreasing as the aerosol fall. Notice the large discrepency in the concentration in Table 6.2, this could be due to the placement of the APS unit 1 meter below the scattered beams, as shown in Figure 6.2. The measured polarization ratios and CGA inverted solutions are shown for several times after the fans are shut off in Figure **??**. All of these plots are with the same range on the y-axis to easily compare subfigures (a) to (f) as the magnitude of the polarization ratios decrease in magnitude while the concentration decreases.

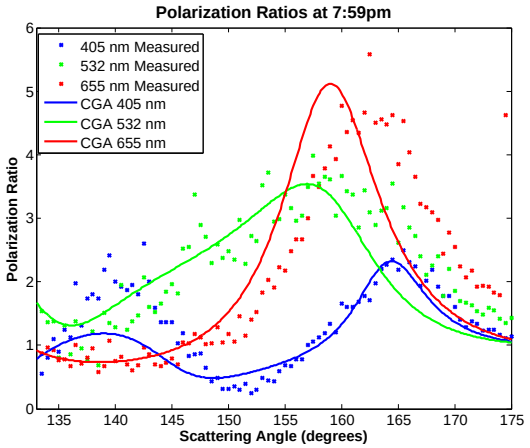

(a)

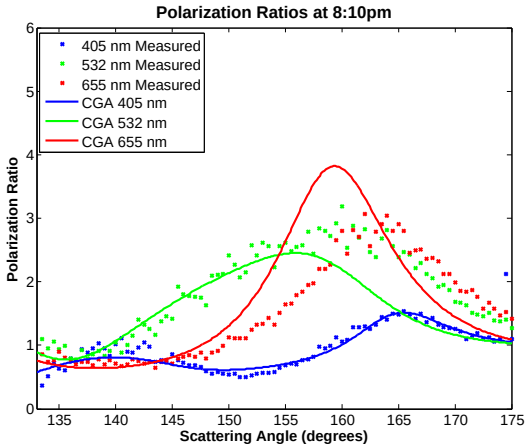

(b)

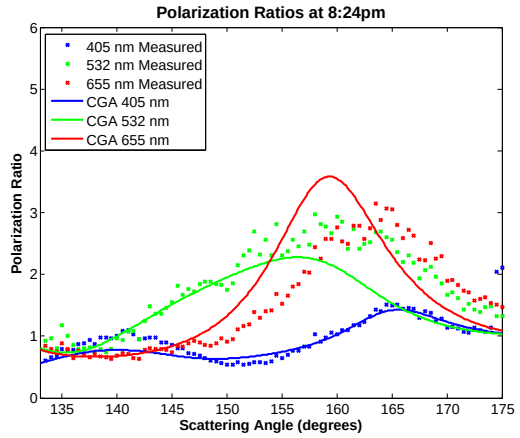

(c)

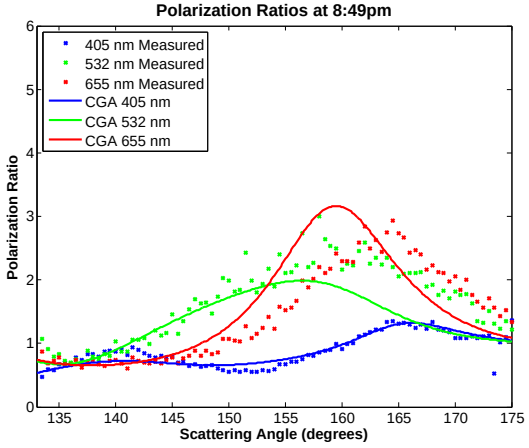

(d)

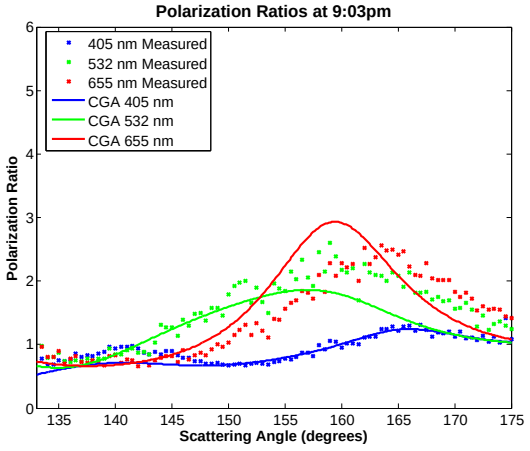

(e)

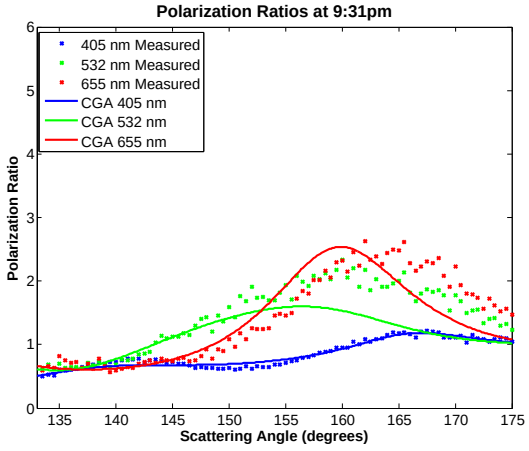

(f)

Figure 6.21: (a) - (f) show the measured polarization ratios with the CGA inverted solutions as quoted in Table 6.3.

Table 6.3: Comparison of parameters for visible wavelength scattering measurements.

7:59pm	**Radius (μm)**	**Standard Width**	**Conc. ($\#/cm^3$)**	**Fitness**
CGA	$\mu_g = 0.497 \pm 0.0037$	$\sigma_g = 1.02 \pm 0.008$	$N = 53.7 \pm 11.52$	178.5 ± 5.37
APS	$\mu_g = 0.503$	$\sigma_g = 1.13$	$N = 83.75$	
% diff.	1.20 %	10.2%	43.7%	

8:10pm	**Radius (μm)**	**Standard Width**	**Conc. ($\#/cm^3$)**	**Fitness**
CGA	$\mu_g = 0.498 \pm 0.0005$	$\sigma_g = 1.01 \pm 0.0044$	$N = 14.8 \pm 1.45$	80.5 ± 0.58
APS	$\mu_g = 0.504$	$\sigma_g = 1.13$	$N = 70.46$	
% diff.	1.20%	11.2 %	131 %	

8:24pm	**Radius (μm)**	**Standard Width**	**Conc. ($\#/cm^3$)**	**Fitness**
CGA	$\mu_g = 0.498 \pm 0.0038$	$\sigma_g = 1.01 \pm 0.010$	$N = 12.2 \pm 1.86$	87.8 ± 5.54
APS	$\mu_g = 0.501$	$\sigma_g = 1.13$	$N = 50.72$	
% diff.	0.60 %	11.2 %	122%	

8:49pm	**Radius (μm)**	**Standard Width**	**Conc. ($\#/cm^3$)**	**Fitness**
CGA	$\mu_g = 0.498 \pm 0.0022$	$\sigma_g = 1.01 \pm 0.006$	$N = 8.71 \pm 1.888$	71.3 ± 3.94
APS	$\mu_g = 0.498$	$\sigma_g = 1.13$	$N = 33.84$	
% diff.	0.00 %	11.2 %	118 %	

9:03pm	**Radius (μm)**	**Standard Width**	**Conc. ($\#/cm^3$)**	**Fitness**
CGA	$\mu_g = 0.499 \pm 0.0030$	$\sigma_g = 1.02 \pm 0.003$	$N = 7.09 \pm 2.038$	66.0 ± 2.45
APS	$\mu_g = 0.499$	$\sigma_g = 1.12$	$N = 27.58$	
% diff.	0.00%	9.45 %	118 %	

9:31pm	**Radius (μm)**	**Standard Width**	**Conc. ($\#/cm^3$)**	**Fitness**
CGA	$\mu_g = 0.498 \pm 0.0022$	$\sigma_g = 1.01 \pm 0.005$	$N = 5.02 \pm 0.818$	56.6 ± 2.88
APS	$\mu_g = 0.496$	$\sigma_g = 1.12$	$N = 19.0$	
% diff.	0.40 %	10.3 %	116 %	

Addition of Near-Infrared (NIR) Wavelengths During APL Measurements

Unfortunately a software problem preventing the polarization ratios for the NIR wavelengths from being measured during much of this experiment. Figure 6.22 shows results from the 780 nm and 670 nm wavelengths plotted with the visible wavelengths and the inversion is run on

all five wavelengths, results are shown in Table 6.4.

The two times analyzed are 9:05pm and 9:31pm. These times are selected because the NIR and visible instruments provide independent, but simultaneous measurements. The measured polarization ratios for the five wavelengths are shown in Figure 6.22. Each of the measured polarization ratios are resampled at every half-degree and only the angles present in both the NIR and visible measurements are used in the inversion process. The inversion routine is written to have measurements of all polarization ratios at the same angle range, so the truncation is necessary.

Table 6.4: Comparison of parameters for visible and NIR wavelength scattering measurements.

9:05pm	**Radius** (μm)	**Standard Width**	**Conc.** ($\#/cm^3$)	**Fit**
CGA	$\mu_g = 0.486 \pm 0.0408$	$\sigma_g = 1.06 \pm 0.112$	$N = 7.67 \pm 2.708$	95.6 ± 26.69
APS	$\mu_g = 0.450$	$\sigma_g = 1.13$	$N = 27.7$	
% diff.	7.69%	6.39 %	113%	

9:31pm	**Radius** (μm)	**Standard Width**	**Conc.** ($\#/cm^3$)	**Fit**
CGA	$\mu_g = 0.497 \pm 0.4580$	$\sigma_g = 1.05 \pm 0.111$	$N = 6.04 \pm 2.330$	80.8 ± 28.18
APS	$\mu_g = 0.496$	$\sigma_g = 1.12$	$N = 19.0$	
% diff.	0.20%	6.45%	104%	

Comparison of the 9:31pm inverted results from Table 6.3 and 6.4 show that the inversion routine obtains similar results when the additional NIR wavelengths are added. The radius values are in good agreement with the expected radius values and the standard widths are very narrow as expected from the well-known narrow distribution of the manufactured spheres. Recall Figure 6.3, the visible and NIR wavelengths and imagers were mounted at the same height, but spanned a different diagonal path across the chamber. The agreement between the combined wavelengths and the visible wavelengths in quantitive value suggest that the aerosols were dispersed uniformly across the chamber and fell at a constant rate. The visual agreement between the polarization ratio scattering for all five wavelengths dispite the difference in measurement location of the NIR and visible beams suggests agreement between the instruments.

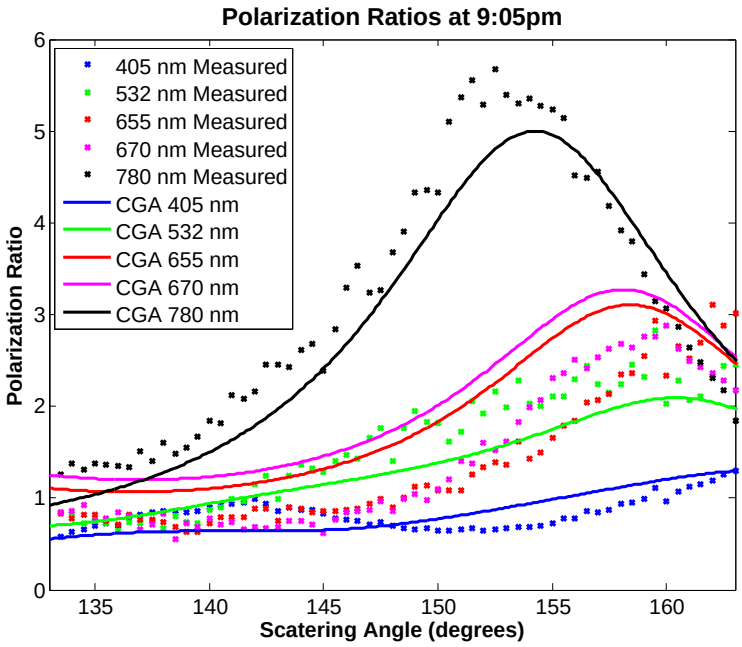

(a)

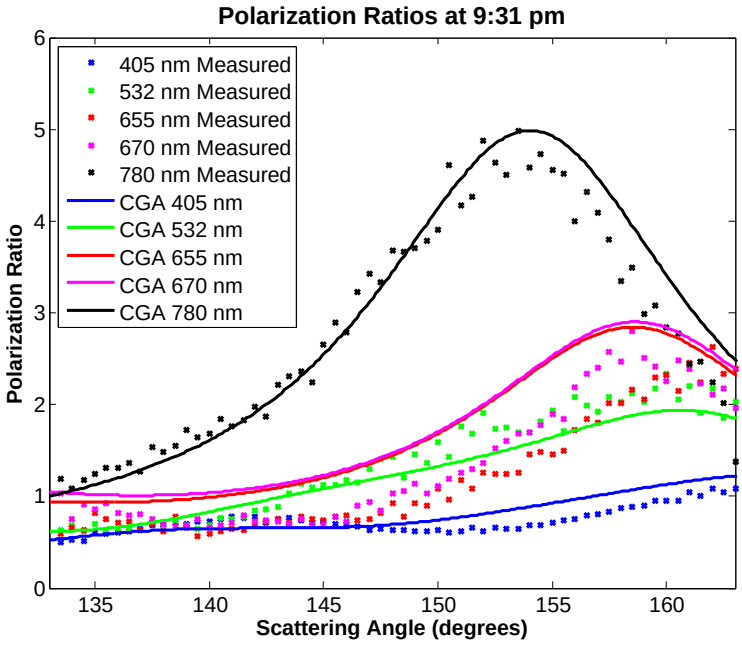

(b)

Figure 6.22: The polarization ratio at visible and NIR wavelengths are shown with the calculated ratios found by CGA inversion.

Experimental Measurement at NCSU

Figure 6.23 shows the inversion routine solution that combines the best solution for the three polarization ratios (see Table 6.1). Measured ratios obtained by both cameras are shown and measurements are compared directly in Figure6.24. Calculated polarization ratios for the inverted solutions are also shown with the measurements in Figure 6.23 and the inversion results for each camera individually are shown in Table 6.5.

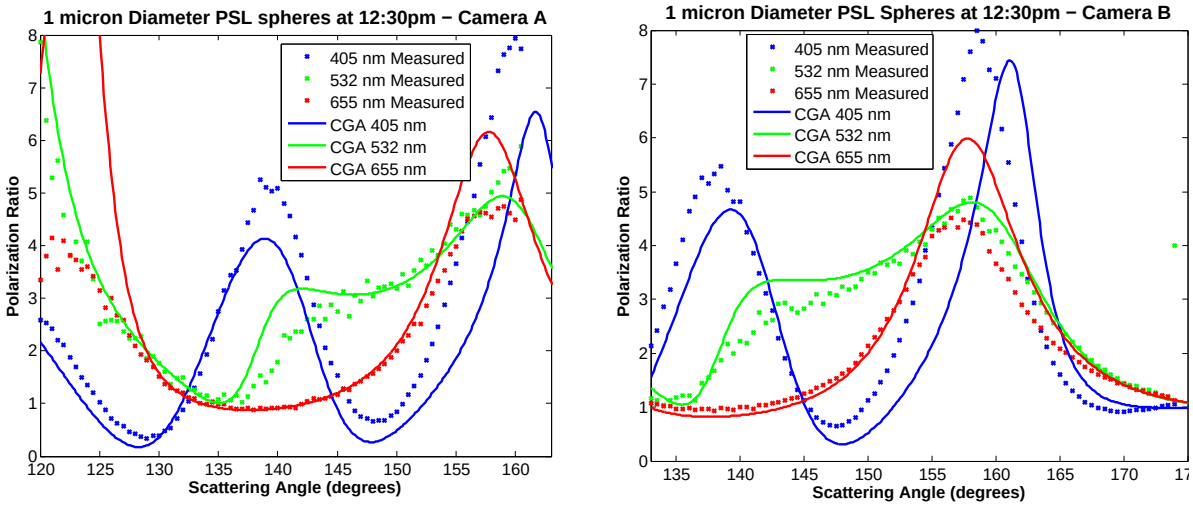

(a) (b)

Figure 6.23: Measured polarization ratio from camera A and B as compared to the polarization ratio obtained by the CGA at 12:30pm.

Table 6.5: The results of the CGA inversion routine on the polarization ratios measured by cameras A and B at 12:30pm.

	Radius(μm)	**Standard Width**	**Conc.**($\#/cm^3$)	Fit
Camera A	$\mu_g = 0.508 \pm 0.0047$	$\sigma_g = 1.02 \pm 0.006$	$N = 216 \pm 127.7$	261 ± 42.1
Camera B	$\mu_g = 0.508 \pm 0.0019$	$\sigma_g = 1.01 \pm 0.004$	$N = 155 \pm 64.6$	220 ± 0.09
% Difference	0 %	0.985 %	32.9 %	

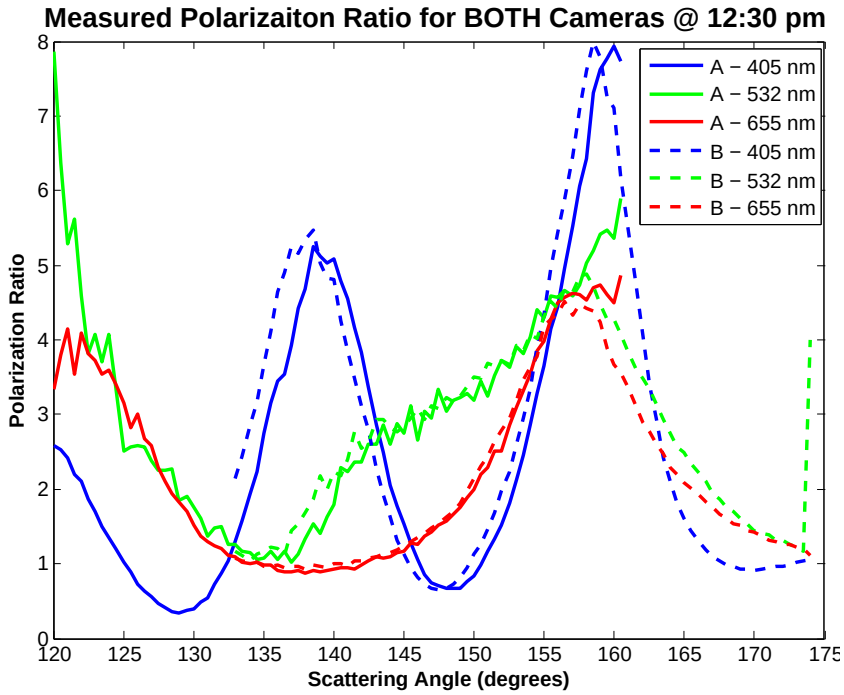

Figure 6.24: Measured polarization ratio from camera A and B, taken at 12:30pm.

The measured polarization ratios for both cameras show strong agreement in magnitude, shape, and structure. The inverted results for each camera show strong agreement for the radius and standard width. A small discrepancy in the average concentration between the cameras is obtained, but the values fall within the others uncertainty. The concentrations found have a large uncertainty for both cameras and the mean concentration obtain for one camera falls within the uncertainty of the the camera. The lower scattering angles captured by camera A leads to a higher concentration, since the angle range does not include measurements on both sides of the higher scattering angle peak of the 405 nm wavelength. In addition, both sides of the 532 nm and 655 nm wavelength peaks are not captured, so a magnitude of the polarization ratio peak can not be determined, which is directly related to the concentration. The importance of capturing the larger scattering angles is affirmed.

Figure 6.25 shows additional polarization ratios measured at 1:00pm as the concentration decreased. The calculated polarization ratios for the inversion results are shown in Figure 6.25 and the results are reported in Table 6.6.

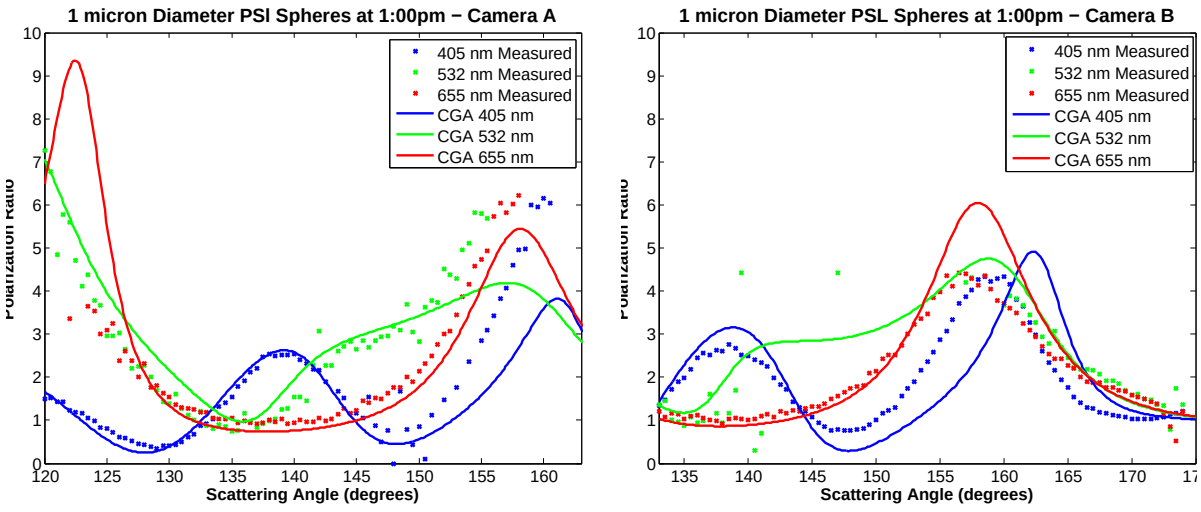

(a) (b)

Figure 6.25: Measured polarization ratio from camera A and B as compared to the polarization ratio obtained by the CGA at 1:00pm.

Table 6.6: The results of the CGA inversion routine on the polarization ratios measured by cameras A and B at 1:00pm.

	Radius (μm)	**Standard Width**	**Conc.** ($\#/cm^3$)	**Fit**
Camera A	$\mu_g = 0.510 \pm 0.0012$	$\sigma_g = 1.01 \pm 0.005$	$N = 64.1 \pm 13.68$	1100 ± 9.8
Camera B	$\mu_g = 0.506 \pm 0.0033$	$\sigma_g = 1.02 \pm 0.006$	$N = 203 \pm 112.6$	33230 ± 6.4
% Difference	1.18 %	0.99 %	104 %	

The radius and standard width obtained agree with the values expected. There is a large discrepancy in the concentration obtained, this is due to the lack of higher scattering angle measurement. The ka values for all the wavelengths with a one micron PSL sphere are shown in Table 6.7. Index of refraction values for all five wavelengths are similar, so the optimum ka value for all wavelengths is about 2 based on Figure 3.11. The table value for all wavelengths are too short to match with the best solution for the 1 micron PSL aerosol size distribution.

Table 6.7: *ka* values for the wavelengths used in the one micron PSL experiment.

Wavelength (microns)	***ka* value**
0.405	7.757
0.532	5.905
0.655	4.796
0.670	4.689
0.780	4.028

6.4.2 Comparison of One Micron Experiments

One micron PSL spherical aerosols are used at both locations to provide a verification that this instrument would reliably preform in different locations and configurations. There were unanticipated differences in the results from the two locations; discrepancies are found in the location of the peaks in the measured polarization ratios, and the type of materials used to manufacture the spheres.

Difference in Aerosol Material

The PSL spheres used in the APL experiments contained a dye to make them fluoresce green (508 nm) and blue (468 nm) when UV light strikes them. The 405 nm wavelength was low enough to activate the florescent dye inside the spheres, so this means the 405 nm index of refraction probably has a higher imaginary component, i.e. the spheres will absorb more of this light than a standard PSL sphere. The wavelengths of the fluorescence are close enough to the wavelengths of the beams that after diffraction the fluorescence light and the scattered light overlap. The angular scattering intensity that is measured has a higher cross section by a factor of 10^2 than the florescence cross section of the dye. The effect of a higher imaginary component in the index of refraction can be seen in Figure 6.26, the higher absorption leads to more structure in the polarization ratio for the 405 nm wavelength.

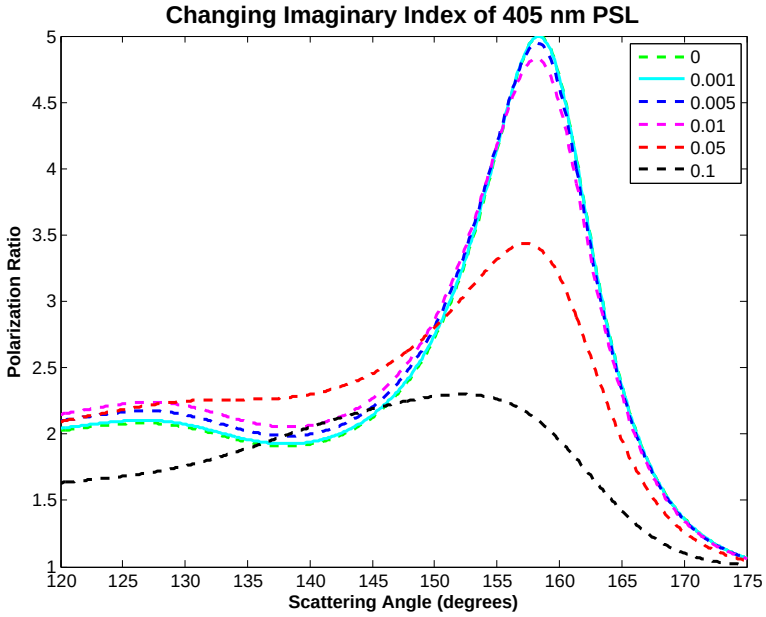

Figure 6.26: The higher imaginary component of the index of refraction results in less structure the polarization ratio for the 405 nm wavelength ($\mu_g = 0.5\mu m$, and $n_{real} = 1.61$).

From Figure 6.26 it appears that as the absorption (imaginary index) of the spheres increases above 0.01 show a decrease in the polarization ratio structure. Although this seems a likely explanation for some of the discrepancies between the calculated and the measured polarization ratio, consider how this effects the ratio formed in Equation 2.29.

$$PR(\theta) = \frac{I_{||}}{I_{\perp}} = \frac{\int N|S_2(x,\theta)|^2 y(x)dx + (2.54 \times 10^{19})S_{2molecules}(\theta) + \mathbf{I_f}(\theta)}{\int N|S_1(x,\theta)|^2 y(x)dx + (2.54 \times 10^{19})S_{1molecules}(\theta) + \mathbf{I_f}(\theta)}, \tag{6.1}$$

where $\mathbf{I_f}(\theta)$ is the intensity scattered due to the fluorescence based on the fluorescence cross section and the concentration of the spheres (assuming all the spheres have identical dye density). The ratio cancels out a lot of the experimental errors, but the fluorescence is inherent to the aerosol, so it is not canceled by taking the ratio (see Equation 6.1) . This would change the measured polarization ratio for the 405 nm and 532 nm wavelengths, since the spheres used absorbed in the UV and fluoresced around the green and blue wavelengths.

Discrepancies in Structure Locations Suggest Refractive Index Variation

The location of the scattering peak is normally an indication of the size of an aerosol. Aerosol size was very similar between the experiments; however, the peak locations in the polarization ratios measured at the three wavelengths are different, as shown in Figure 6.27.

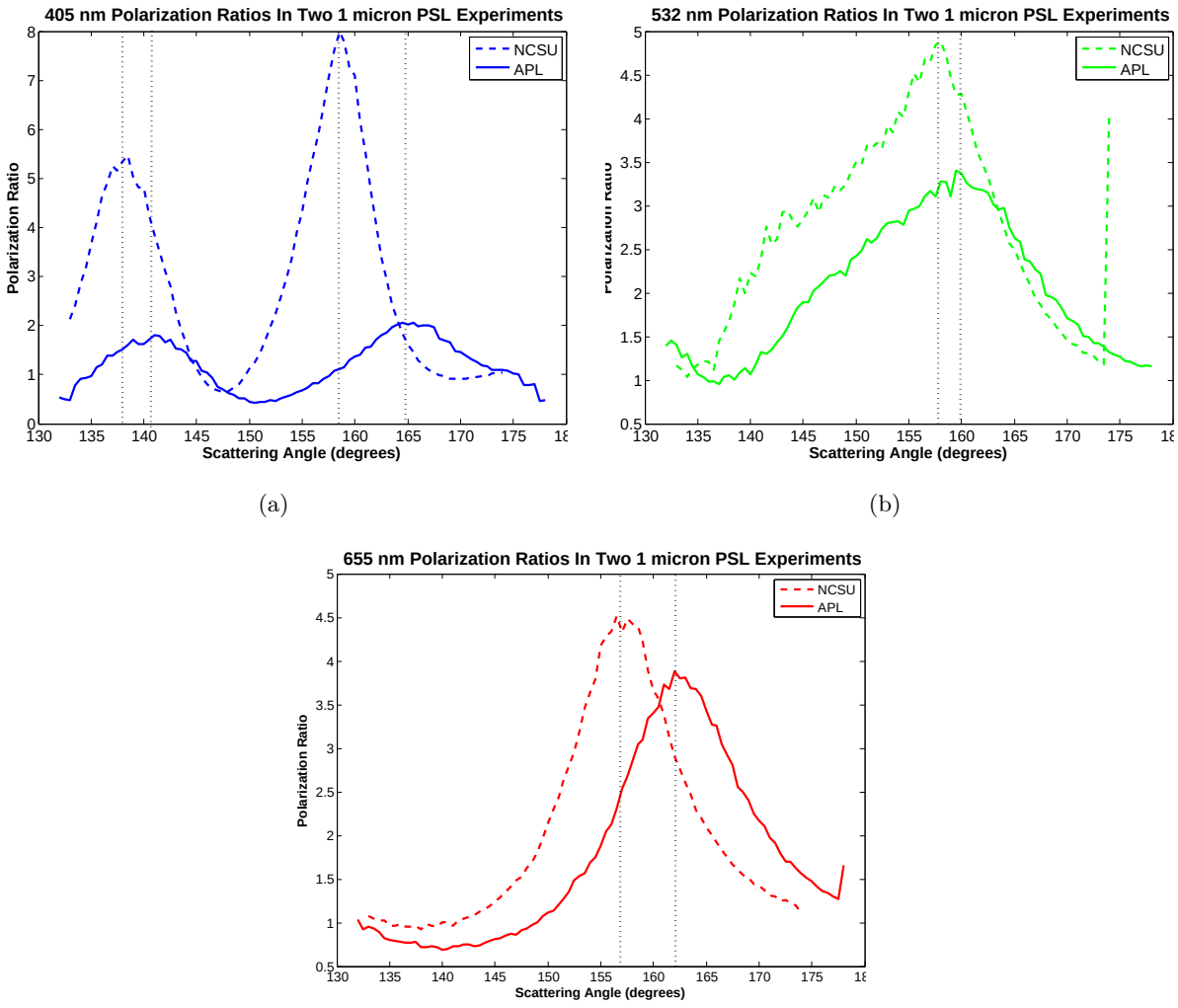

Figure 6.27: Comparison of the measured polarization ratio structure in the one micron diameter PSL experiments at NCSU and APL.

The sensitivity plot of concentration in Figure 6.18 shows that the magnitude of the polarization ratios change, but not the location of its peak. The location of the peaks in the polarization ratio for 405 nm occur around 144 degrees and 168 degrees, but neither the locations is observed in the measured ratio at NCSU or APL.

6.4.3 One-Half Micron Diameter PSL Spheres

Half micron diameter ($\mu_g = 0.25\mu m$) polystyrene latex (PSL) spheres were dispersed into the chamber using the nebulizer. The concentration sensitivities for the 405 nm wavelength are shown in Figure 6.28. This figure indicates that a concentration between 10 and 10^5 aerosols per cm^3 are detectable by this instrument. At 2:48pm the nebulizer was turned off, data was taken at 2:50pm, 2:53pm and 2:56pm as the spheres naturally settled, see Figure 6.29. The continuous genetic algorithm inversion routine was then run 20 times for 50 generations with a population of 50. The results are show in Table 6.8, the polarization ratios that correspond to these values were plotted in Figure 6.29.

The results obtained by the inversion show a decreasing concentration as the spheres settle out, but none of the sizes obtained in the inversion are very close to the $0.25\mu m$ radius that was expected.

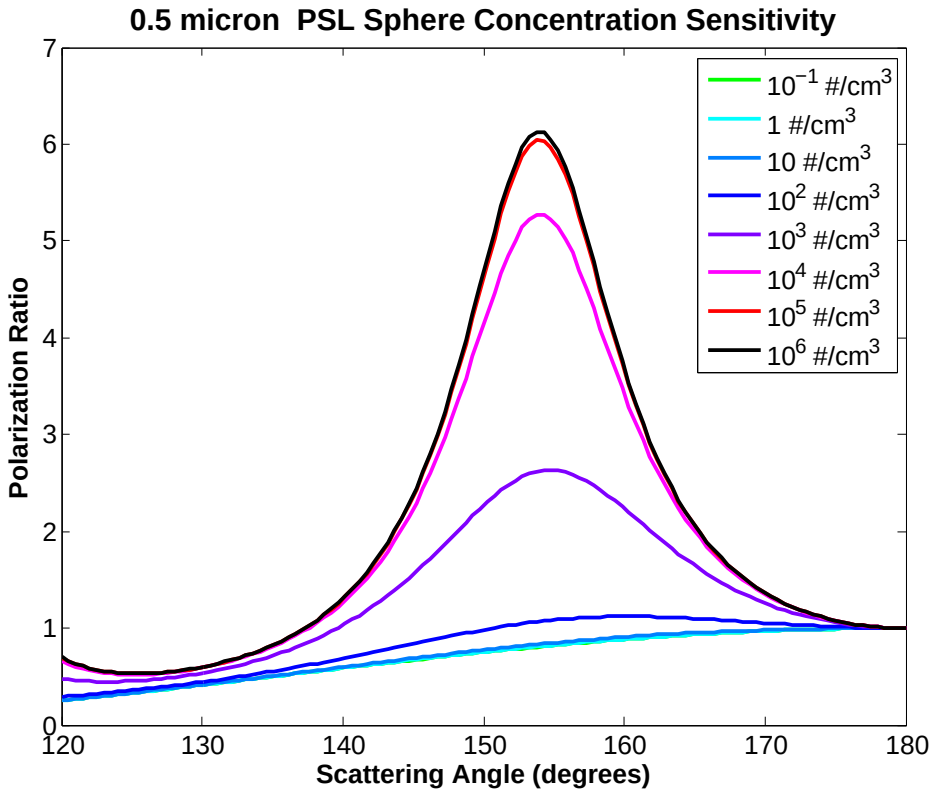

Figure 6.28: Calculated 0.5 micron concentration sensitivity.

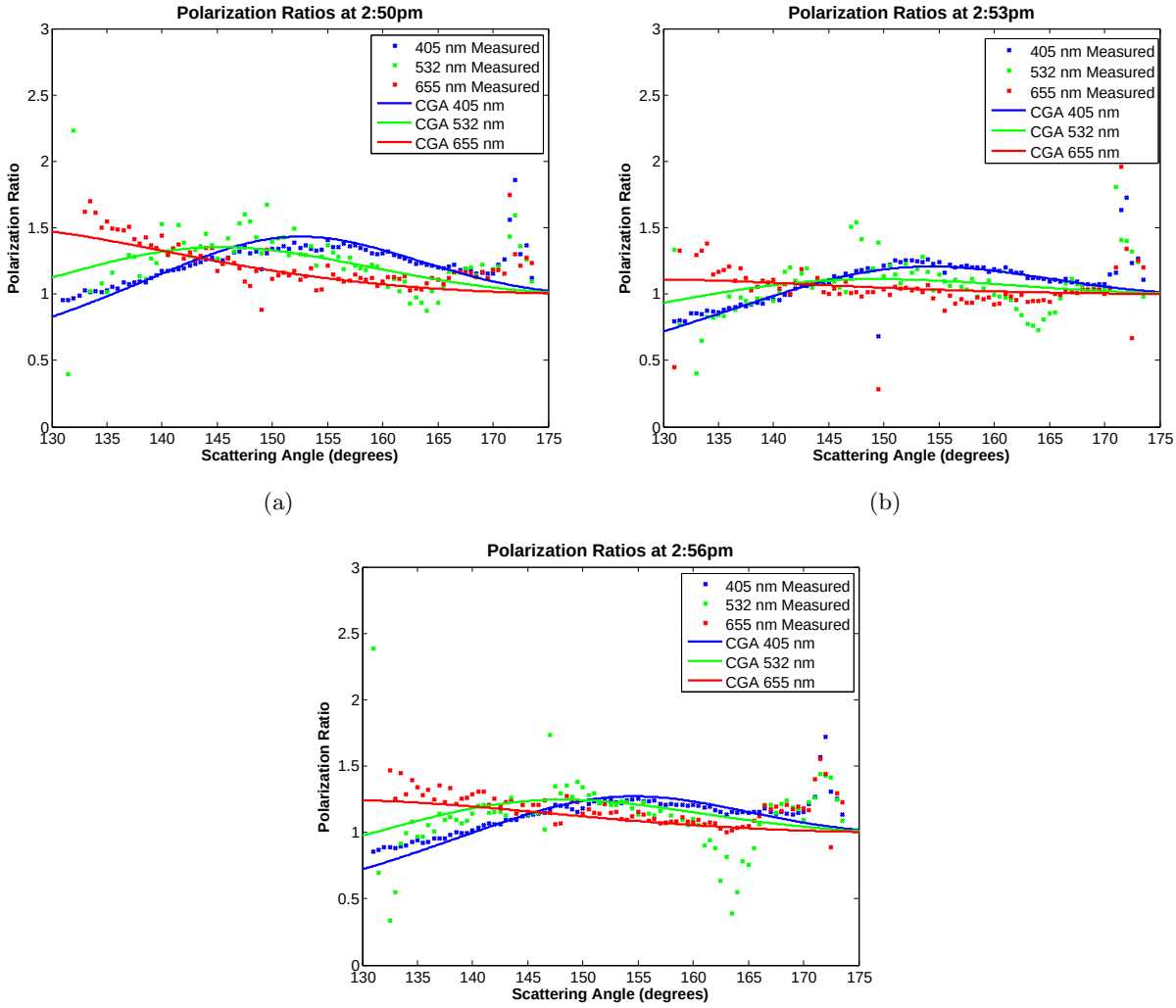

(a) (b)

(c)

Figure 6.29: The measured polarization ratios of 0.5 micron diameter PSL aerosols shown with the CGA inversion results, with values summarized in Table 6.8.

Table 6.8: Inversion results for the 0.5 micron diameter PSL sphere experiment.

Time	**Radius** (μm)	**Standard Width**	**Conc.** ($\#/cm^3$)	**Fit**
2:50pm	$\mu_g = 0.198 \pm 0.0078$	$\sigma_g = 1.14 \pm 0.032$	$N = 107 \pm 24.4$	171 ± 1.5
2:53pm	$\mu_g = 0.193 \pm 0.0102$	$\sigma_g = 1.14 \pm 0.040$	$N = 75.2 \pm 23.36$	38.9 ± 1.16
2:56pm	$\mu_g = 0.200 \pm 0.0147$	$\sigma_g = 1.15 \pm 0.066$	$N = 73.7 \pm 13.65$	167 ± 1.3

The ka values for all the wavelengths with a one half micron PSL sphere are shown in Table 6.9. Index of refraction values for all five wavelengths are similar, so the optimum ka value for all wavelengths is about 2 based on Figure 3.11. As seen in the table all wavelengths are too short to optimally find the 1 micron PSL aerosol size distribution, although the 655 nm wavelength is close to the optimum value.

Table 6.9: ka values for the wavelengths used in the one half micron PSL experiment.

Wavelength (microns)	***ka* value**
0.405	3.879
0.532	2.95
0.655	2.398

6.4.4 Two Micron Diameter PSL Spheres

Two micron diameter ($\mu_g = 1.00\mu m$) polystyrene latex (PSL) spheres were dispersed, Figure 6.30 shows the concentration sensitivity of the 405 nm laser that is present on the transmitter. A concentration between 10^{-1} and 10^{3} should be discernible in the polarization ratios. The ranges for the parameters in the inversion routine (shown in Figure 4.5) had to be changed to accomidate the 2 micron diameter size, see Table 6.10.

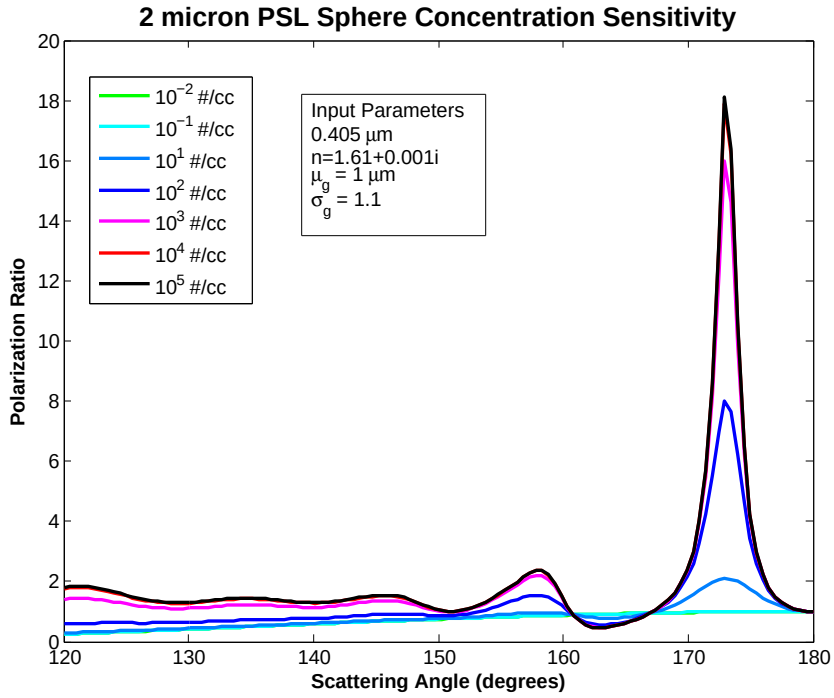

Figure 6.30: The polarization ratio sensitivity for 2 micron diameter PSL spheres.

Table 6.10: Here r stands for the random number generated in the piece of the chromosome that represents each variable. This maps each variable to a continuous range between the input minimum and maximum values.

Parameter	**Minimum**	**Maximum**	**Mapping**
μ_g	0 μm	2 μm	$\mu_g(s) = r_1 * 2$
σ_g	1.01	1.80	$\sigma_g(s) = r_2 * (1.80 - 1.01) + 1.01$
N	10^{-2}	10^3	$N(s) = r_3 * (10^3 - 10^{-2}) + 10^{-2}$

Measurements taken at NCSU

During this experiment two micron spherical PSL aerosols were dispersed by a nebulizer. At 1:04pm the nebulizer was turned off, measured polarization ratios are shown at 1:08 pm, 1:17 pm and 1:25 pm in Figure 6.31. The concentration and magnitude of the polarization ratio peaks decrease as the spheres naturally settled.

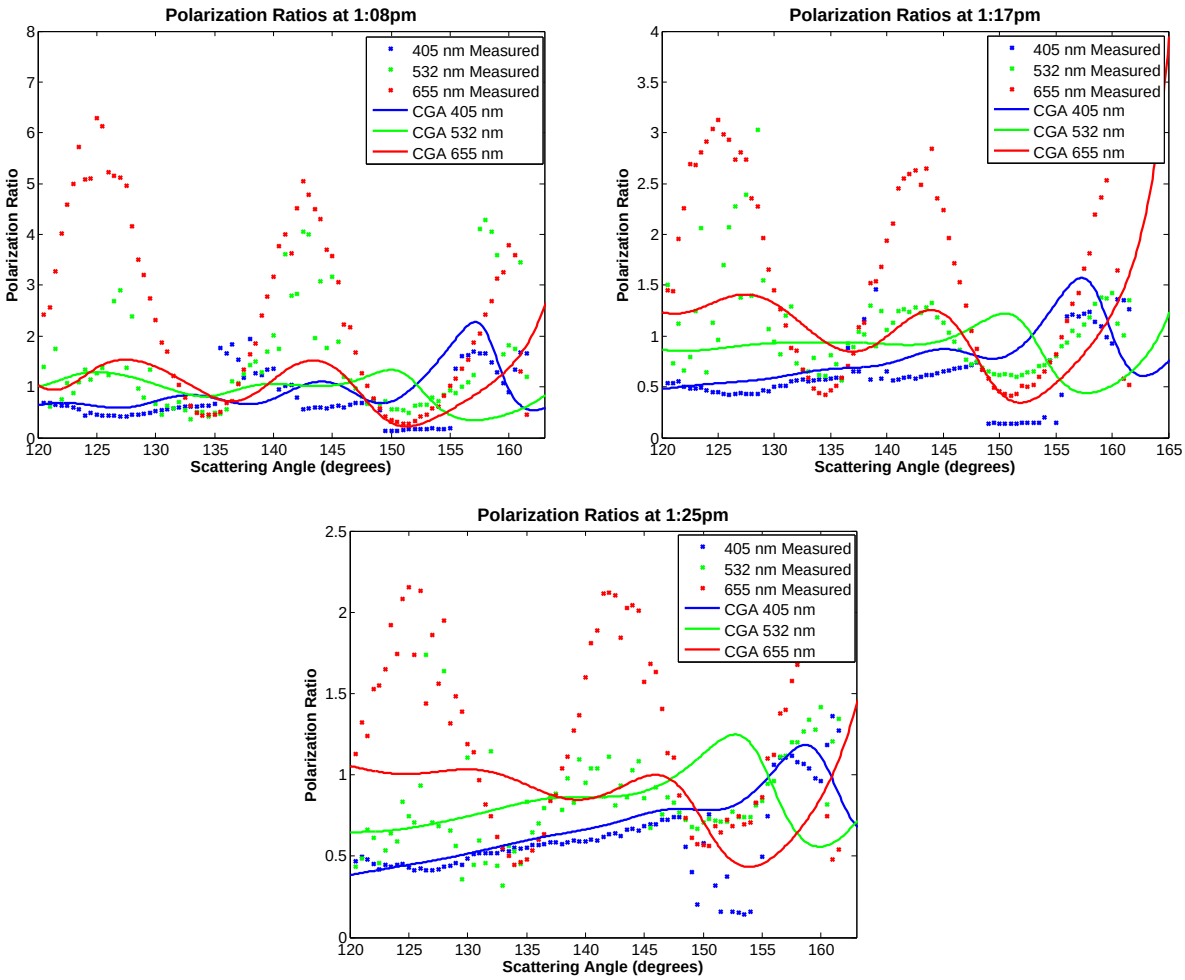

Figure 6.31: Measured polarization ratios are shown with the CGA inversion results for three different times as the concentration of 2.0 μm spheres decreased.

The continuous genetic algorithm inversion routine was then run 20 times for 50 generations with a population of 50. The results are shown in Table 6.11, the polarization ratios that correspond to these values are plotted in Figure 6.31.

Table 6.11: Inversion results for the 2.0 micron diameter PSL sphere experiment.

Time	**Radius** (μm)	**Standard Width**	**Conc.** ($\#/cm^3$)	**Fit**
1:08pm	$\mu_g = 0.961 \pm 0.2356$	$\sigma_g = 1.04 \pm 0.022$	$N = 20.6 \pm 6.01$	193 ± 23.0
1:17pm	$\mu_g = 0.975 \pm 0.2284$	$\sigma_g = 1.07 \pm 0.073$	$N = 11.3 \pm 2.86$	99.8 ± 8.53
1:25pm	$\mu_g = 1.039 \pm 0.3086$	$\sigma_g = 1.10 \pm 0.090$	$N = 5.39 \pm 1.763$	66.0 ± 3.90

The structure in the polarization ratios shown in Figure 6.31 should allow the inversion routine to determine the size accurately. However, the plotted polarization ratios form the CGA results do not show the same lever of structure. This is troubling until the measured polarization ratios and the locations of the peaks of a calculated ratio are compared. Figure 6.32 shows the measured polarization ratio for the 655 nm wavelength compared with the calculated concentration sensitivity of the 655 nm wavelength (using the PSL index values given in Table 6.1). Structure peaks in the measured ratio are located at 125 and 142 degrees these locations are translated to the simulation in Figure 6.32(b). The peak at 125 degrees in the measured polarization ratio occurs at a trough in the calculated ratio. Additionally, the magnitude of the peak at this scattering angle is greater in magnitude. When the fitness is minimized in the inversion routine, this peak would contribute more error. This explains why the inversion solution with the least structure has the lowest fitness value and is selected for the solution. Since the results obtained by the inversion are close to the expected size, this suggests that the assumed index of refraction is incorrect. The effect of decreasing the polarization ratio is shown in Figure 6.33(a) and the effect of increasing the real index value is shown in Figure 6.33 (b). The dotted lines are transferred from Figure 6.32(a) to show the location of the measured polarization ratio peaks. A shift in index of refraction is explored because the radii values obtained are very close to those expected. From the slight shift in the location of the polarization ratio peak by shifting the index for the two micron spheres in combination with the previous study in Chapter 3, a size range where the index must be assumed should be determined in a future study.

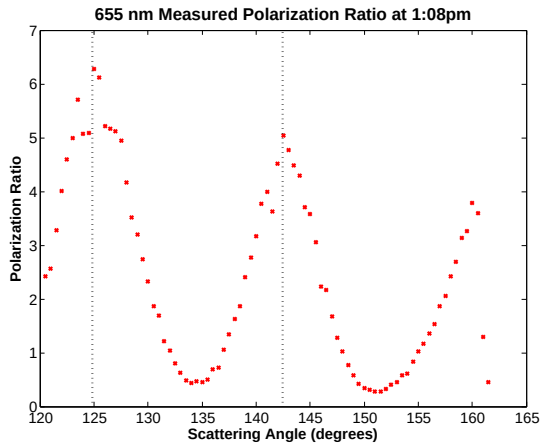

(a) Measured Locations

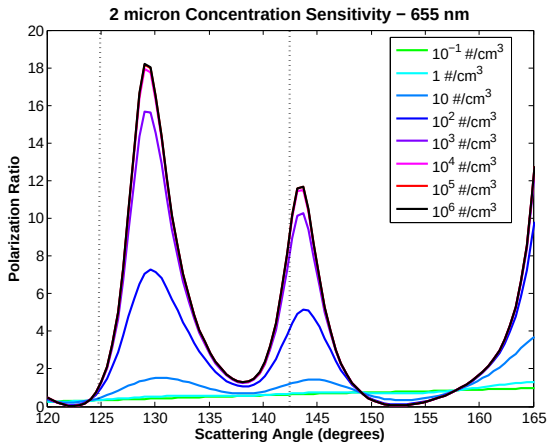

(b) Locations of Calculated Ratios

Figure 6.32: The location of the polarization ratio structure measured and calculated as a function of concentration.

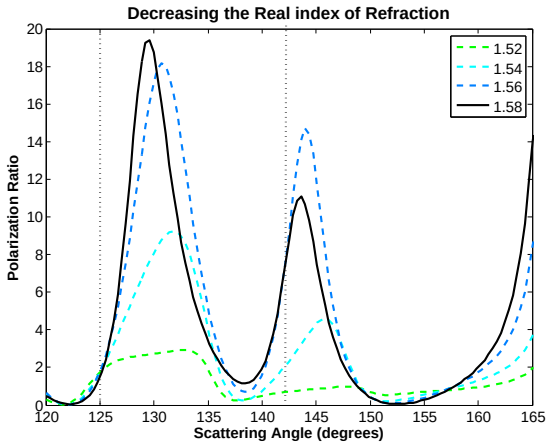

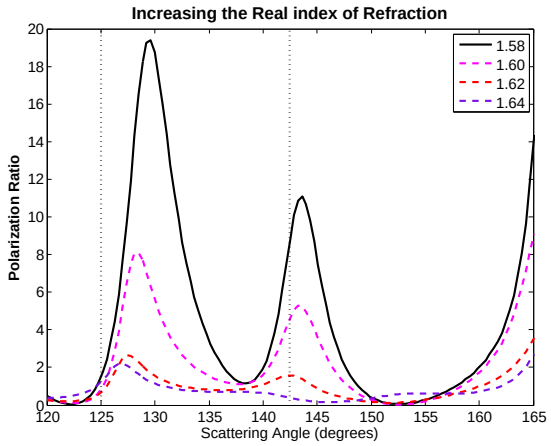

Figure 6.33: Possible variation in the index of refraction for a two micron PSL spherical distribution to better match the measured ratios..

Figure 6.33 suggests that increasing the index of refraction would shift both structure features in the ratio to lower scattering angles; this result would be in better agreement with the measured structure. The *ka* values for all the wavelengths with a two micron PSL sphere are shown in Table 6.12. Index of refraction values for all five wavelengths are similar, so the

optimum ka value for all wavelengths is about 2 based on Figure 3.11.

Table 6.12: ka values for the wavelengths used in the two micron PSL experiment.

Wavelength (microns)	***ka* value**
0.405	15.514
0.532	11.81
0.655	9.592

As seen in the table all wavelengths are too short to optimally find the two micron PSL aerosol size distribution. To achieve the optimum ka value to measure the 2 micron PSL spheres the wavelength must be increased by a factor of more than four.

6.5 Bi-Modal PSL Aerosol Distributions

6.5.1 One-Half and One Micron PSL Spheres

A mixture of one micron and one half micron diameter spheres is measured to investigate the polarization ratio method to seperate bi-modal distributions. The parameter ranges for the CGA inversion routine (see Figure 4.5) had to be changed to accomidate the bi-modal distribution and these values are listed inTable 6.13.

Table 6.13: Mapping used in one-half and one micron mixture, where r stands for a randomly generated number.

Parameter	**Minimum**	**Maximum**	**Mapping**
μ_g (mode 1)	0 μm	0.5 μm	$\mu_g(s) = r * 0.5$
μ_g (mode 2)	0.3 μm	1 μm	$\mu_g(s) = r * 0.5 + 0.5$
σ_g (both modes)	1.01	1.80	$\sigma_g(s) = r * (1.80 - 1.01) + 1.01$
N (both modes)	10^{-2}	10^3	$N(s) = r * (10^3 - 10^{-2}) + 10^{-2}$

Measurements at NCSU

Aerosols were dispersed into the chamber at 10:54 am and data collection began. Results are shown in Figure 6.34 at 10:55am and 11:06am, as the spheres settled from the volume.

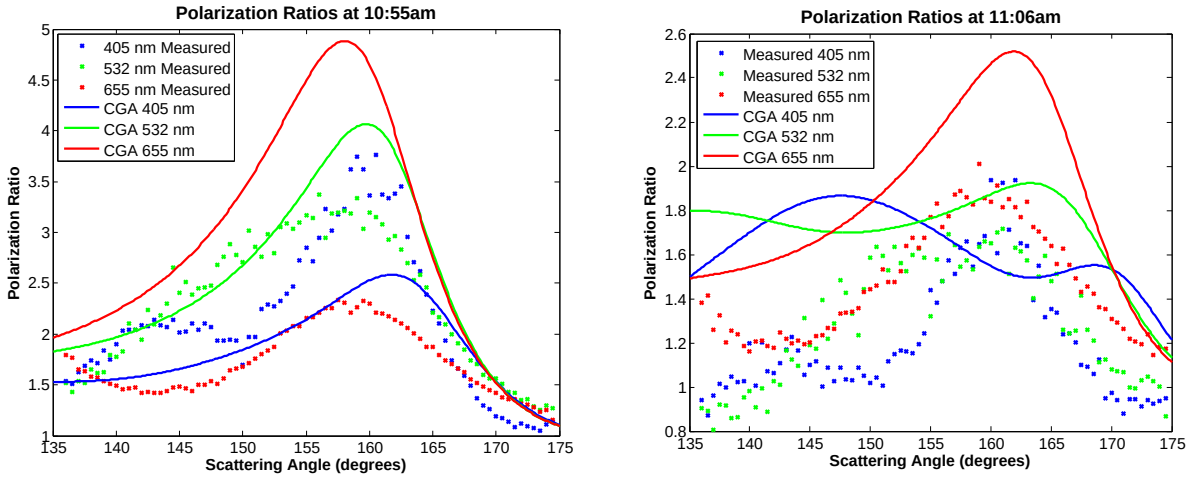

(a) (b)

Figure 6.34: Measured ratios compared with the CGA inversion results for the bi-modal mixture of one-half and one micron PSL spheres.

The inversion routine was run 10 times (to obtain all 6 parameters) for 100 generations with a population of 50 on the measured polarization ratios and the inversion results are shown in Table 6.14.

Table 6.14: Inversion results for the one and one half micron diameter PSL sphere mixture experiment.

Time	**Radius** (μm)	**Standard Width**	**Conc.** ($\#/cm^3$)	**Fit**
10:55am	$\mu_g = 0.105 \pm 0.0013$	$\sigma_g = 1.79 \pm 0.007$	$N = 971 \pm 26$	76.8 ± 0.2
	$\mu_g = 0.683 \pm 0.2231$	$\sigma_g = 1.47 \pm 0.218$	$N = 503 \pm 348$	
11:06am	$\mu_g = 0.168 \pm 0.1127$	$\sigma_g = 1.20 \pm 0.072$	$N = 450 \pm 355.8$	34.2 ± 5.24
	$\mu_g = 0.476 \pm 0.1262$	$\sigma_g = 1.44 \pm 0.286$	$N = 23.9 \pm 22.06$	

The mixture of one-half and one micron PSL spheres show polarization ratios that are unlike the individual measurements of the one-half and the one micron spheres measured previously. The calculations of the polarization ratios from the CGA results are visibly very different. There is a large deviation in the parameter values, but not the fitness values, which suggest a non-converging bi-modal distribution solution.

6.5.2 One and Two Micron PSL Spheres

A bimodal mixture of one micron and two micron spheres require changes in the parameter ranges for the CGA inversion routine, the values selected are shown in Table 6.15.

Table 6.15: Mapping values fro the genetic algorithm applied to the one and two micron mixture, where r stands for a randomly generated number.

Parameter	Minimum	Maximum	Mapping
μ_g (mode 1)	0 μm	1.0 μm	$\mu_g(s) = r_1 * 1.0$
μ_g (mode 2)	0.5 μm	1.5 μm	$\mu_g(s) = r_2 * 1.0 + 0.5$
σ_g (both modes)	1.01	1.80	$\sigma_g(s) = r_3 * (1.80 - 1.01) + 1.01$
N (both modes)	10^{-2}	10^3	$N(s) = r * (10^3 - 10^{-2}) + 10^{-2}$

Measurements at NCSU

At 9:36am measurements began on a dispersed mixture of one and two micron diameter PSL spheres. Measurements shown in Figure 6.35 are taken at 10:55am and 11:06am, as the spheres naturally settled out of the volume.

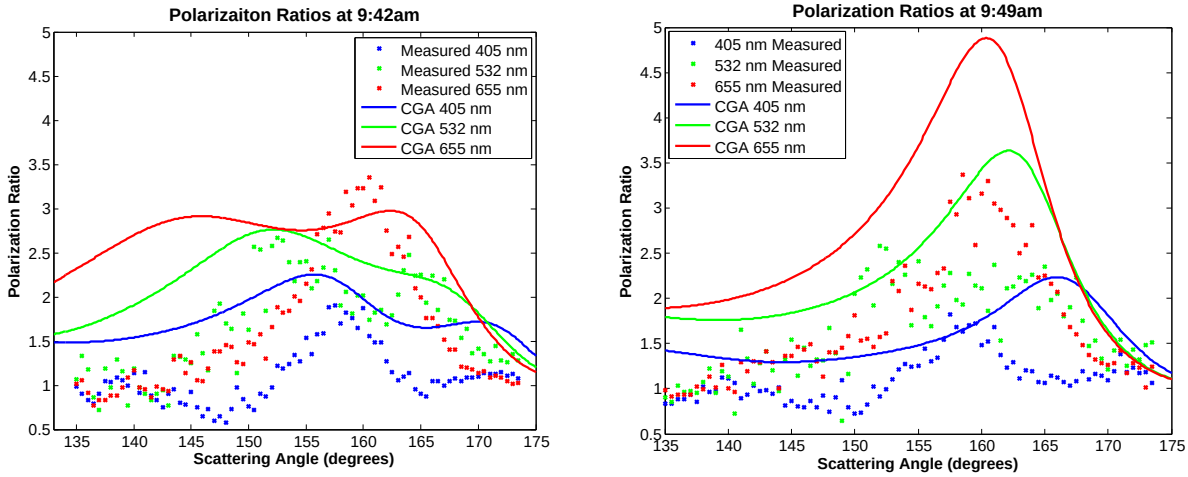

(a) (b)

Figure 6.35: Measured ratios for the one and two micron mixture, shown with the inverted results.

The inversion routine was run 10 times (to obtain all 6 parameters) for 100 generations with a population of 50 on the measured polarization ratios and the inversion results are shown in Table 6.16.

Table 6.16: Inversion results for the one and two micron diameter PSL sphere mixture experiment.

Time	**Radius** (μm)	**Standard Width**	**Conc.** ($\#/cm^3$)	**Fit**
9:42am	$\mu_g = 0.323 \pm 0.194$	$\sigma_g = 1.14 \pm 0.145$	$N = 299 \pm 267.3$	71.7 ± 6.63
	$\mu_g = 0.635 \pm 0.0868$	$\sigma_g = 1.37 \pm 0.260$	$N = 82.8 \pm 130$	
9:49am	$\mu_g = 0.393 \pm 0.0750$	$\sigma_g = 1.38 \pm 0.244$	$N = 7.78 \pm 2.835$	60.3 ± 1.84
	$\mu_g = 0.938 \pm 0.2977$	$\sigma_g = 1.41 \pm 0.208$	$N = 401 \pm 341$	

The radii obtained for the 9:42am time are not close for the smaller or larger mode. For both distributions obtained the standard width is much larger than expected. The larger radius obtained by the inversion for 9:49am is close to the expected radius($\mu_g = 1.0\mu m$), but the smaller radius obtained for the one micron diameter aerosols is not close to the expected value ($\mu_g = 0.5$). Also, these aerosols were mixed in a one-to-one ratio before dispersal, so the vastly different concentrations obtained is unexpected. The two micron particles are expected to fall faster than the one micron aerosols, but the huge discrepancy in the concentration is still somewhat surprising. The large deviation in the concentrations and the small variance in the fitness values obtained are indicative of a solution space that is not converging, since vastly different solutions obtained have similar fitness values.

6.6 Non-Spherical Particle Distribution

Bacillus Globigii (BG) spores are included in the data sets studied at APL. These spores are used as a non-harmful aerosols, which simulate harmful biological agents. This experiment is conducted in the same manner as the one micron PSL aerosol experiment. The chamber is filled to a concentration of about 250 $particles/cm^3$ as measured by the APS, then measurements were taken over the next few hours as the concentration dropped to about 50 $particles/cm^3$ as shown in Figure 6.36.

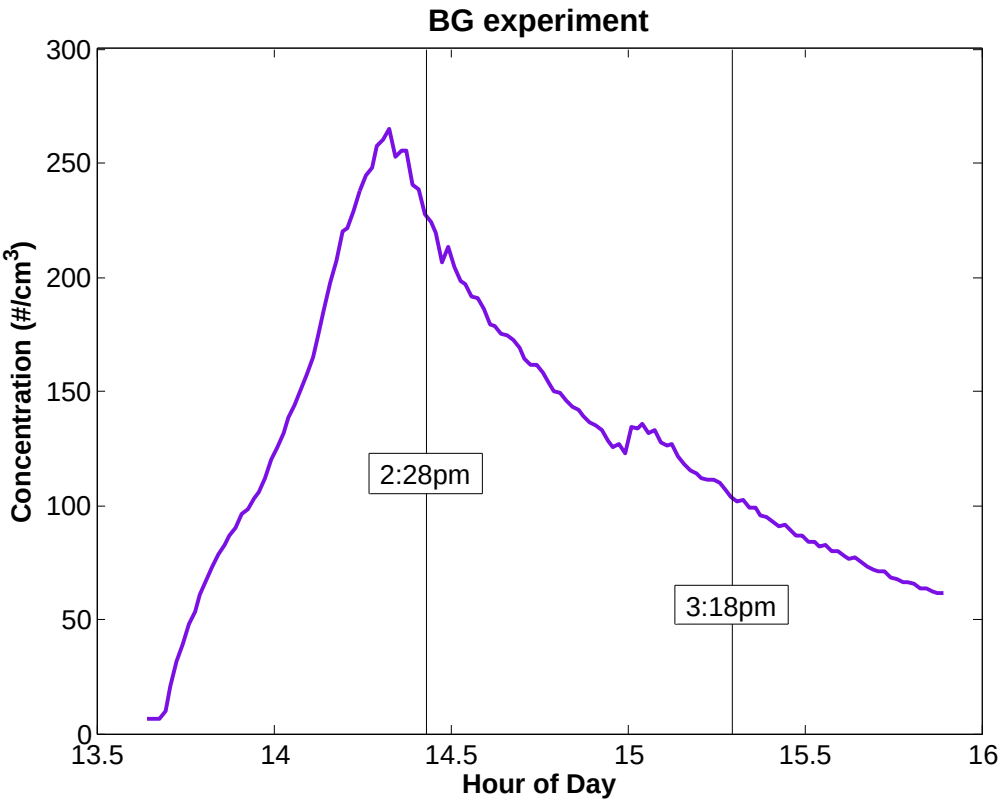

Figure 6.36: This shows the total concentration as measured by the APS in the APL aerosol chamber when BG was released by a nebulizer.

The index of refraction for BG, following exposure to an aqueous solution, is shown in Table 6.17. BG spores were suspended in an aqueous solution before being dispersed by the nebulizer. Spores begin taking on water and swell, the index of refractions shown assume a 15% uptake of water.

Table 6.17: The index of refraction values for BG.[46]

Wavelength [λ(nm)]	Index of Refraction [n]
405	1.545+0i
532	1.545+0i
655	1.545+0i
670	1.545+0i
780	1.545+0i

Measurements at APL

The measured polarization ratios during the experiment are shown in Figures 6.37 and 6.40. These times were selected because measurement times for the visible and NIR instruments matched. The 405 nm, 532 nm and 655 nm wavelengths are on the visible transmitter, the 670 nm and 780 nm wavelengths are on the NIR transmitter. The CGA inversion results are shown in Table 6.18 and 6.19.

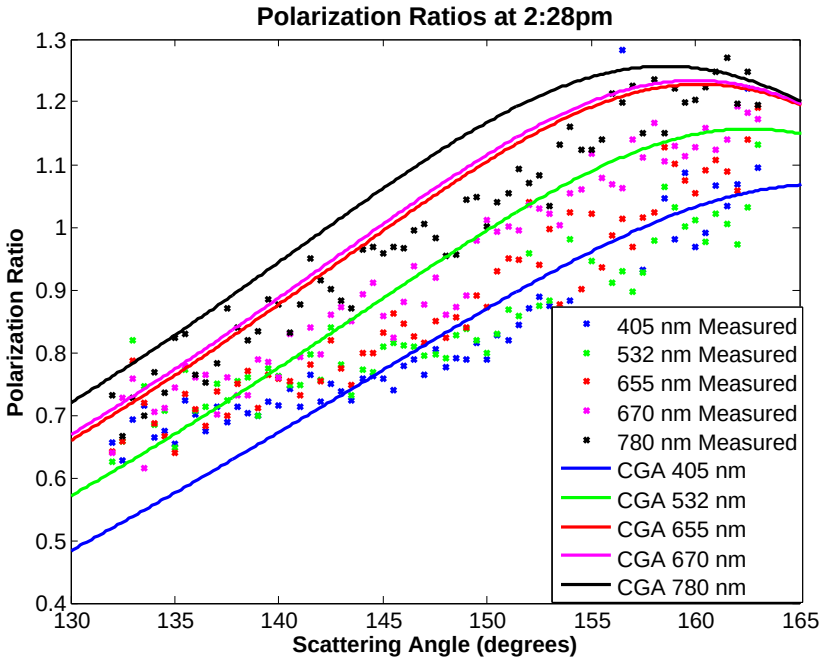

Figure 6.37: The polarization ratios measured are compared with the best-fit from the CGA single mode inversion for a high concentration of BG at 2:28pm.

The size distribution as measured by the APS is shown in Figure 6.38(a). The APS reports a single mode log-normal distribution, this does agree with the measured sizes. The calculated polarization ratios for the reported size distribution are shown in Figure 6.38(b).

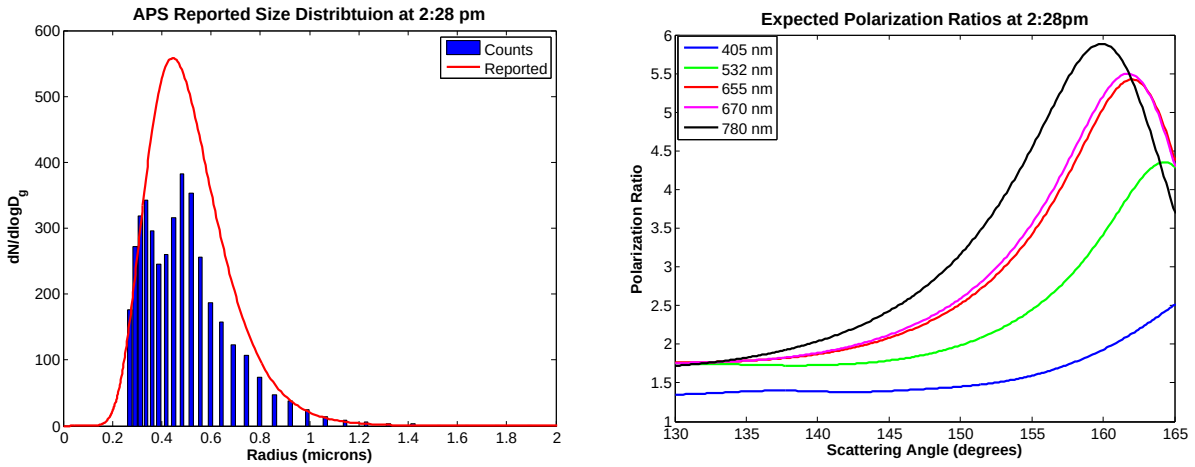

(a) (b)

Figure 6.38: The size distribution measured by the APS at 2:28pm is shown together with the single mode log-normal distribution that the APS reports in (a). The calculated polarization ratio that is expected based on this size distribution are plotted in (b).

Since the APS only reports a single log-normal distribution that seems to not match the bi-modal type structure, a bi-modal distribution was found to better model the measured sizes and is shown in Table 6.18. The bi-modal distribution found is shown with the APS measured sizes in Figure 6.39(a). The polarization ratio corresponding to the bi-modal distribution found are shown in Figure 6.39(b).

Table 6.18: The size distribution reported by the APS, two mode distribution found to match the measured sizes, and the CGA inverted results at 2:28pm.

	Radius (microns)	Standard Width	Concentration ($\#/cm^3$)	Fitness
APS Reported	0.4450	1.37026	191.342	N/A
2 Mode Found	0.3 0.48	1.15 1.35	30 120	N/A
CGA	0.12 ± 0.027	1.72 ± 0.058	41 ± 46.3	18 ± 1.0

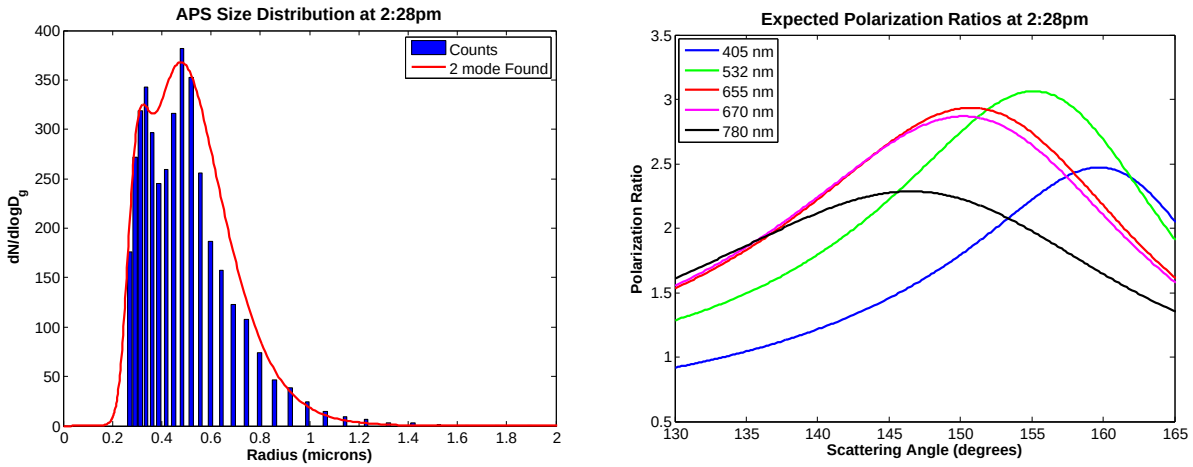

(a) (b)

Figure 6.39: Improved size distribution fit to the APS data at 2:28pm is shown together with the single mode log-normal distribution that the APS reports in (a). The calculated polarization ratio that is expected based on this size distribution are plotted in (b).

Neither the single or two mode distributions match the measured polarization ratios. Another time was explored later in the experiment run, the measured polarization ratios are shown in Figure 6.40. Notice, the similar shape structure and magnitude in the measured polarization ratios. There are a few points in the measured ratio for 405 nm that seem to be outliers in the overall trend, these points are due to unknown experimental noise and should be ignored.

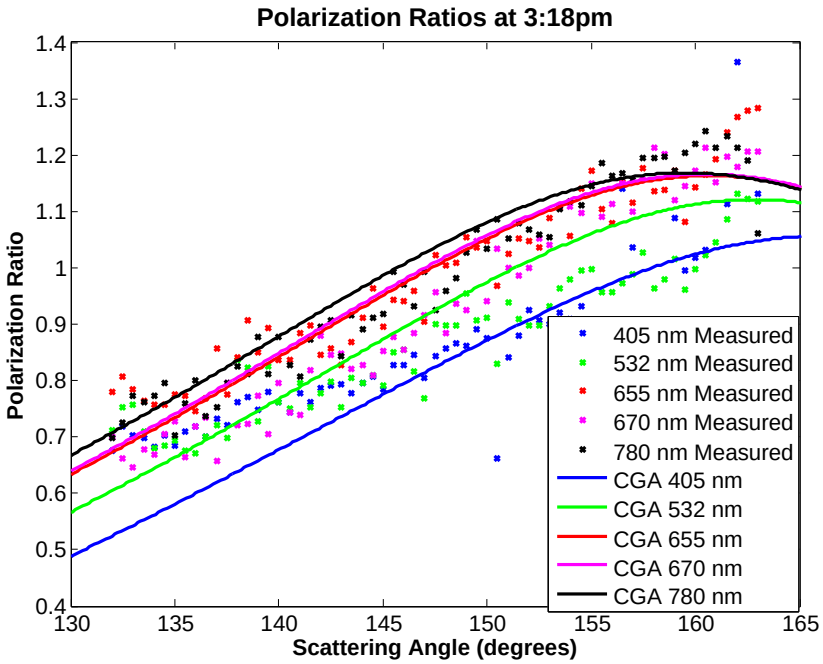

Figure 6.40: The polarization ratios measured are compared to with the best-fit from the single mode CGA with a low concentration of BG at 3:18pm.

The size distribution reported by the APS is shown in Figure 6.41(a). Again, the reported single mode log-normal distribution reported by the APS is not a good indication of the sizes measured by the APS. However, these polarization ratios are calculated with the assumption that the distribution reported is for spherical aerosols (see Figure 6.41(b)). The APS measured sizes show a bi-modal structure, so a bi-modal distribution was found to model this as shown in in Figure 6.42(a). The polarization ratio corresponding to the found bi-modal distribution is shown Figure 6.42(b); however the calculated ratios are not similar to the measured ratios in Figure 6.40 in shape or magnitude.

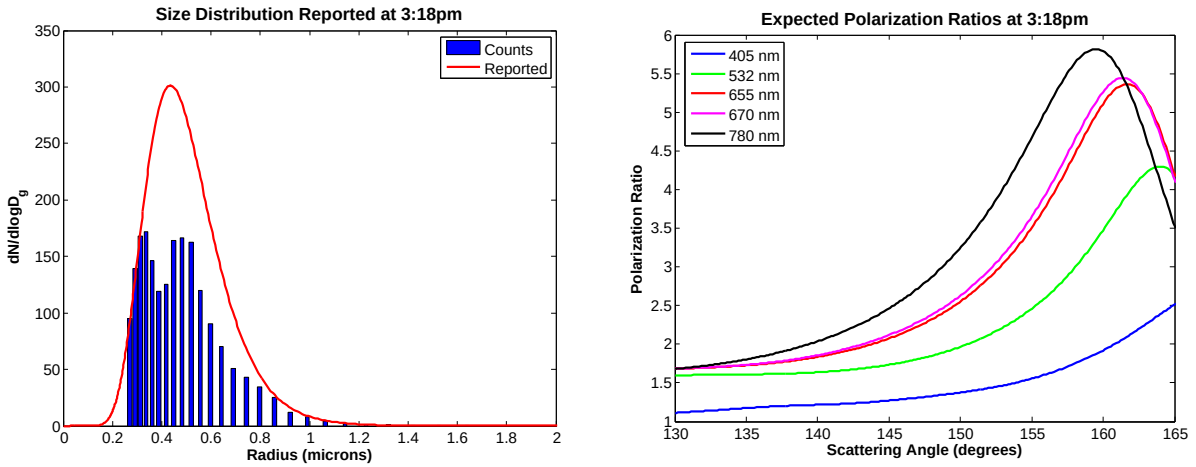

(a) (b)

Figure 6.41: The size distribution measured by the APS at 3:18pm is shown together with the single mode log-normal distribution that the APS reports in (a). The calculated polarization ratio that is expected based on this size distribution is plotted in (b).

Table 6.19: The size distribution reported by the APS, two mode distribution found to match the measured sizes and the CGA inversion results at 3:18pm.

	Radius (microns)	Standard width	Concentration ($\#/cm^3$)	Fitness
Reported	0.4356	1.36325	101.596	N/A
2 Mode Found	0.3 0.48	1.15 1.35	18 55	N/A
CGA	0.10 ± 0.015	1.76 ± 0.036	74 ± 32.3	18 ± 0.3

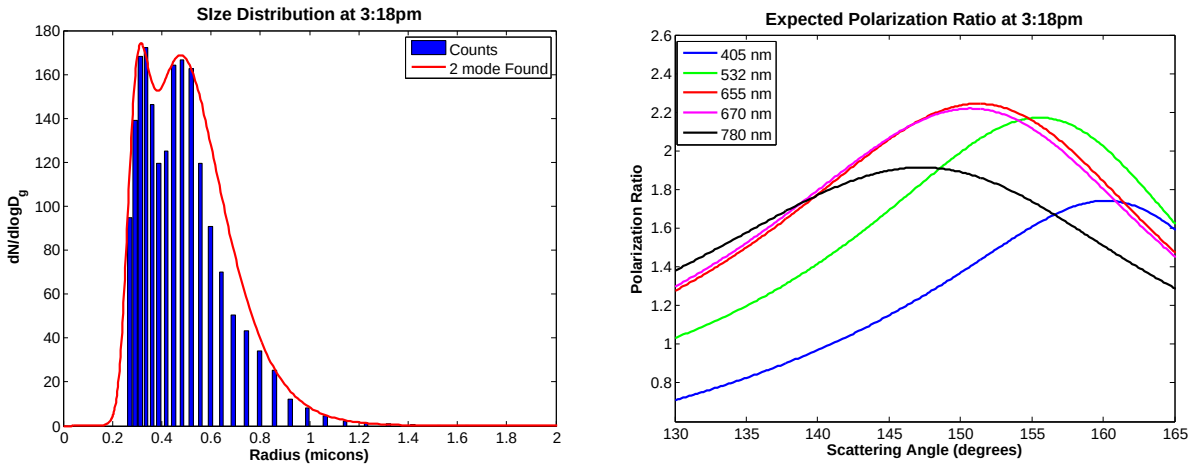

(a) (b)

Figure 6.42: The size distribution measured by the APS at 2:28pm is shown together with the single mode log-normal distribution that the APS reports in (a). The calculated polarization ratio that is expected based on this size distribution is plotted in (b).

Clearly the measured polarization ratios do not match the expected polarization ratios with a one or two mode distribution of spherical particles in shape or magnitude. This was somewhat expected since the BG spores are non-spherical aerosols, thus the measured scattering is clearly different. Non-spherical scattering has been calculated using T-matrix code.

Scattering Calculations: T-matrix

Code was developed by Mishchenko and Travis[47] to calculate the scattering for non-spherical particles. Instead of the scattering matrix found in Equation 2.23, the T-matrix is used,

$$\begin{pmatrix} E_{s||} \\ E_{s\perp} \end{pmatrix} = \begin{pmatrix} T^{11} & T^{12} \\ T^{21} & T^{22} \end{pmatrix} \begin{pmatrix} E_{i||} \\ E_{i\perp} \end{pmatrix}, \tag{6.2}$$

where the E_s represents the scattered electric field, E_i represents the incident electric field, $||$ and $\perp$ represent the polarization. This code has been used to calculate the scattering of spheroids, the shape of the BG aerosols. A BG aerosol can be represented as a prolate spheroid, as shown Figure 6.43. A spheroid is always rotated around its minor axis, here the minor axis is the longer one, producing a "football" shaped particle. The aspect ratio refers to the ratio of the major to minor axis, BG spores are known to have an aspect ratio of about 1/2.

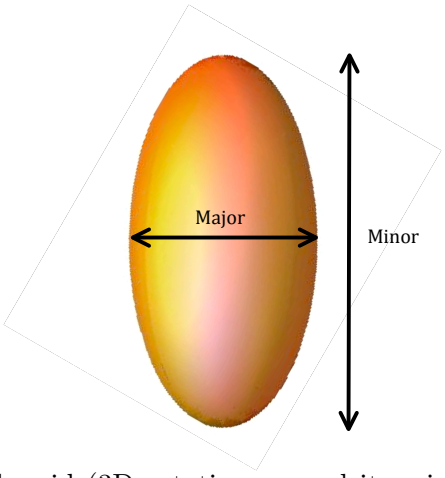

Figure 6.43: A prolate spheroid (3D rotation around its minor axis) with an aspect ratio of 1/2.

The T-matrix code calculates the angular scattering of randomly oriented non-spherical particles.[47] The code can calculate the phase functions for randomly oriented non-spherical particles, thus it can calculate a polarization ratio. This study is not intended to use the T-matirx code in an inversion routine, but to simply show that this code could be useful for future to this type of instrument if its use was extended to include non-spherical particles. The calculated polarization ratios for the three visible wavelengths (405 nm, 532 nm and 655 nm) are shown Figure 6.44(a), with no concentration or molecular contribution included. The backscatter region measured in this experiment is shown in Figure 6.44(b).

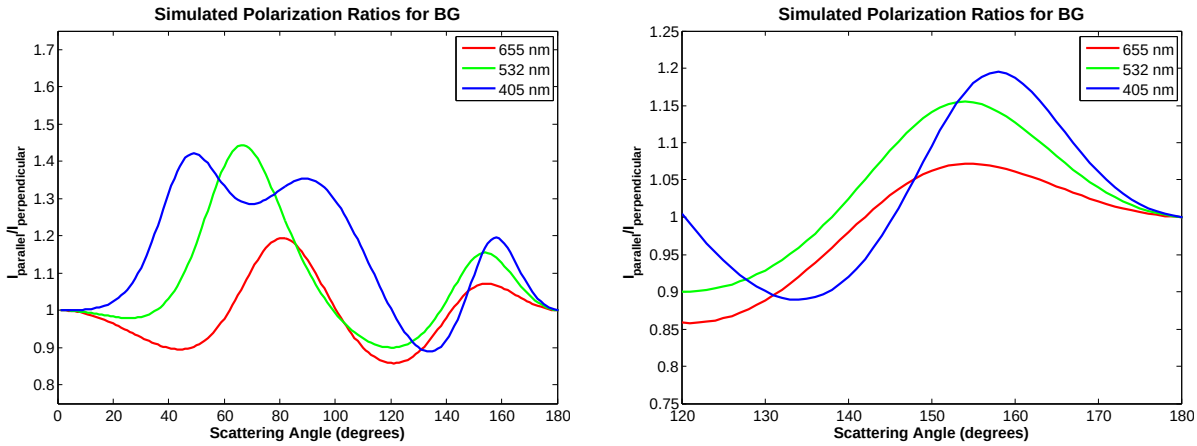

(a) Polarization Ratio

(b) Backscatter Region

Figure 6.44: The calculated polarization ratio for BG aerosols using T-matrix code with an aspect ratio of 1:2, and radius of 0.25 microns.

As seen in Figure 6.44(b), the magnitude of the 405 nm and 532 nm wavelengths is larger than the red wavelength. If molecular scattering were added as with the previous Mie calculations (see Chapter 2), the polarization ratio of the shorter wavelength would increased in this backscatter region. Measured polarization ratios shown in Figures 6.37 and 6.40 do not show this polarization ratio magnitude order or shape. Adding the T-matrix capabilities to the inversion routine, is something left for future work, however this is used for randomly oriented particles, and the discrepancies in shape and magnitude order measured could be due to a preferred falling orientation. This is the most likely explanation since the APS measures the size of the sporse based on their falling rate, the bi-modal distribution shown is close to having mean radii at 0.25 and 0.5 micron which would be the radius measurements for each axis of the spore. If the falling spores have a preferred orientation a new calculation would need to be preformed to calculate the scattering taking into account the physics of why the non-spherical particles this preferred orientation. There is T-matrix code available to calculate oriented non-spherical particles, but this would add another parameter to determine, the orientation ratio, at least for prolate spheroid aerosols.

6.7 Outdoor Fog Measurements

Measurements with a beam path across a hog lagoon in Raleigh, NC were made when the dew point and temperature approached each other. A temperature close to the dew point

indicates when the moisture in the air begins condensing on aerosols. The alignment image used in one of the fog measurements is shown in Figure 6.45. The instrument was reassembled each day before measurement and alignment images were taken each day.

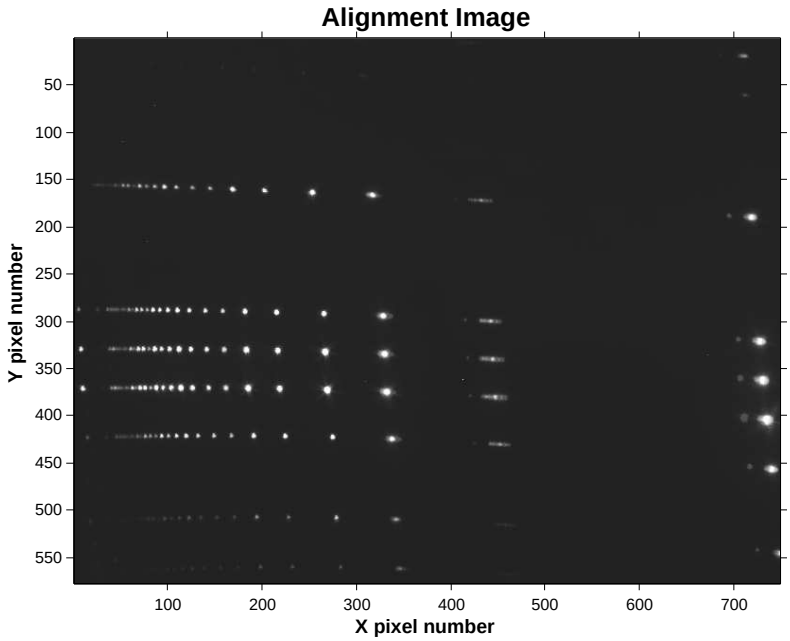

Figure 6.45: Alignment Image taken during fog experiment.

Measurements in Raleigh, NC

Before the image was taken hot air was blown across the gratings in front of the cameras to dry the condensation off. However, condensation formed on the grating while the image was taken, see Figure 6.46. This image was taken during a fog experiment, the condensation shown formed on the grating while the image was taken and interferes with the first order diffracted 405 nm beam The increased intensity cause by the condensation smearing the light is shown quantitatively in Figure 6.47 for a vertical column of the image. This also shows the limitations of the sequential picture technique, the small clouds of fog moved along the beam, but would be in different spatial (and angular) positions when the two images were taken.

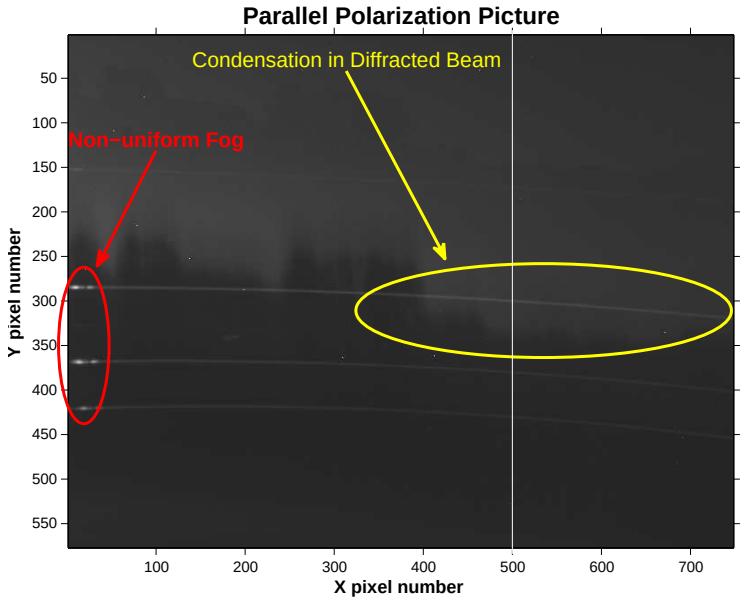

Figure 6.46: Image taken during fog experiment, shows the condensation formed on the grating and the presence of a non-uniform fog. The white line represents the selected column intensity shown in Figure 6.47.

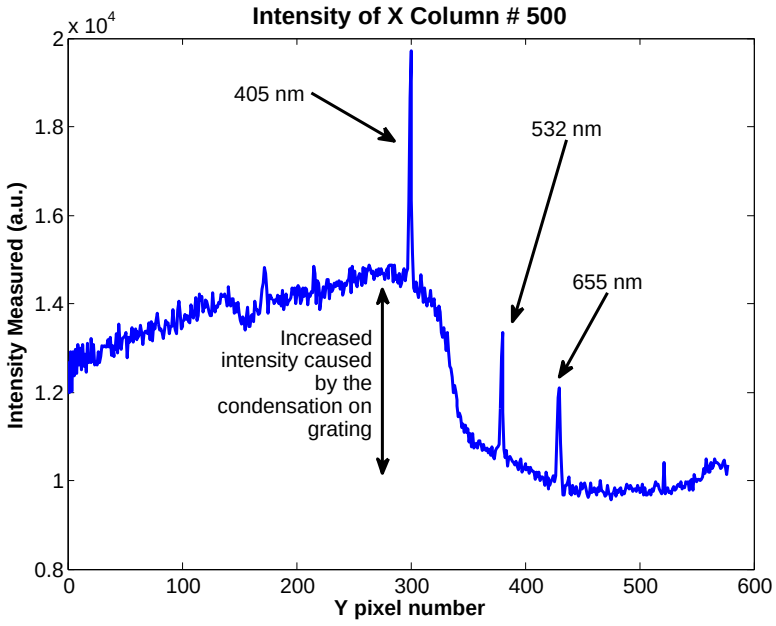

Figure 6.47: Intensity measured on the #500 X column from Figure 6.46.

The other problem with this instrument set up is that unless you have a uniform fog that lasts for a long time, measurements are impossible. This is due to the fact that the pictures are taken sequentially, so the fog must be uniform for the length of the first picture, time of polarization rotation and the length of the second picture. This could be overcome if the cameras were mounted on perpendicular axes and the pictures could be taken simultaneously, this is initially explored and implementation left to future work. Figure 6.46 shows a non-uniform fog that was unable to be measured because only sequential pictures were available not simultaneous pictures. See chapter 8 for the instrument improvements to make fog measurements possible.

Chapter 7

Conclusions

A multistatic multiwavelenth optical scattering instrument to measure volume resolved aerosols characteristics is the focus of this research. This instrument employs the polarization ratio method to obtain aerosol characteristics for the optical scattering measurements. Work involved in a extensive mathematical exploration of the sensitivity and measurement range of the polarization ratio method for single mode, bi-modal and tri-modal distributions of aerosols. The convergence of inversions is analyzed through simulations and squared-error analysis. Experimental results from the polarization ratio techniques are explored and known distributions are calculated to demonstrate the capability of such an instrument. This study leads to a key result; given the index of refraction, an optimum ka value can be found to maximize sensitivity of the polarization ratio method in determining aerosol characterizations.

In a successful attempt, a continuous genetic algorithm was developed to more accurately match measured polarization ratios to theoretical Mie scattering calculations. Sensitivity of the ratio method and inversion technique are experimentally investigated through measurements of well known aerosol distributions and results show strong agreement for single mode aerosol distributions when the index of refraction is correct. Measurements of polystyrene latex spheres of one half, one and two micron diameter are reported and data is analyzed. It is confirmed that the polarization ratio is sensitive to concentration as previously hypothesized by Brown.[25] Exploration into aerosol properties give added insight to the discrepancies in ratios of measured data and inverted results. Additional experiments are reported with mixtures of one-half and one, as well as one and two micron spheres, which show mixed results due to the size similarity and wavelengths used. The results could be improved in future work with optimized ka values and larger size range combinations.

Measurement and calculation for a distribution of non-spherical particles is reported. The measured ratios lack structure found in the spherical calculations of equivalent size distribution. The measured ratios do not match randomly oriented non-spherical T-matrix calculations,

which is conjectured to be due to preferred orientation of gravitational flight. A set of fog measurements were performed without significant results because non-uniformity in fog formation and development of condensation on optics. Experimental improvements are suggested for future work chapter.

As concerns about human impact on climate has grown an understanding of aerosols has become increasingly important yet aerosol continue to be one of the least understood components of the global climate picture. Current systems are mainly point measurements and are not practical for larger scale volumetric measurements needed for climate modeling and human impact analysis. Instrument improvements and reliability testing of the multistatic multiwavelength technique is expected to provide polarization ratio measurements for future studies of atmospheric aerosols. The sensitivity to the ka values based on the index of refraction, as first shown is this work, when in combination with improved laser technologies is expected to expand the range of aerosol measurement capabilities in all future aerosol studies.

Chapter 8

Future Work

This instrument and data analysis could benefit from improvements. The instrument could benefit from a fixed diffraction grating to better characterize the relative intensities measured. Mounting the cameras at a 90° angle from each other would allow simultaneous pictures. Data analysis improvements are also needed to speed up the inversion process.

8.1 Instrument Improvements

8.1.1 Fixed Mounting for the Diffraction Grating

Figure 8.1 shows the diffraction grating mounted in front of the imager. While the experiment is conducted this grating is fixed, but to transport the imager the diffraction grating and the optical mounts to hold the gratings are taken off. The diffraction gratings could get scratched and will fall out if the mounting turned upside down during transport. Thus, the grating should be remounted in a more rugged way. A fixed mounting would allow a completely calibrated scatter receiving system that does not change.

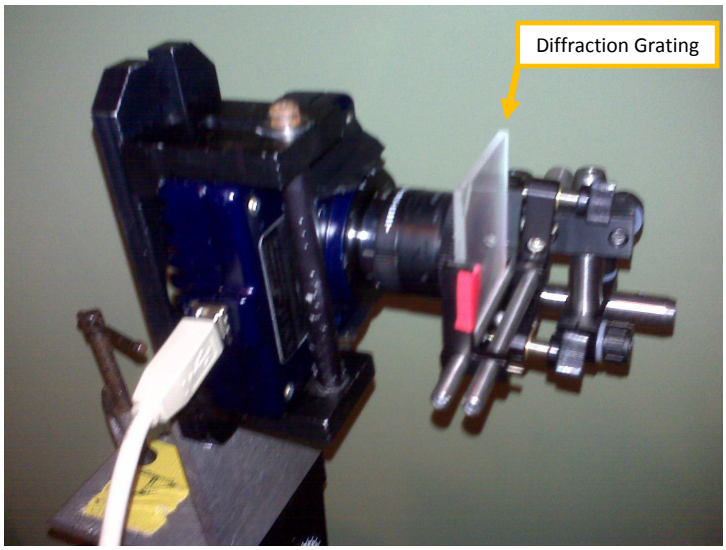

Figure 8.1: The diffraction grating is mounted in front of the imager (reprint of Figure 5.2.

Mounting a housing around the entire imager and diffraction grating that would hold them fixed for all experiments would mean relative intensity measurements could be explored. The relative intensity measurement provide scattering phase functions that contain the experimental/optical errors canceled by the ratio method (see Appendix B). Once a fixed mounting is developed for the grating the optical errors can be determined and adjusted for to obtain true scattering phase functions. These true functions could be used in the analysis process to directly determine concentration.

The main error present in the measured phase functions is the entrance angle of the photon to the grating, which could be accounted for with calibration using molecular scatter. In addition, the camera lens could be characterized and a function involving the response of the imager, integrating time, transmission efficiency and the focusing lens could be found to convert the relative intensities to true scattering phase functions. The phase functions measured in conjunction with the polarization ratio could be used in the analysis to better determine characteristics of aerosols.

8.1.2 Simultaneous Pictures From Perpendicular Scattering Planes

Images from two orthogonal polarization directions are needed simultaneously to improve the data collection in a rapidly changing environment. The current technique assumes that the aerosols have the same characteristics between the two orthogonal polarization pictures. However, in environments where the aerosol distributions are changing the time between images to

to flip the rotation is a hindrance, especially with a rapidly changing concentration. Therefore, configuration for the two cameras to be mounted 90 degrees apart is suggested, so that pictures of the beams polarized parallel and perpendicular components can be taken simultaneously. The set-up was altered in the NCSU chamber to mount the cameras 90 degrees apart, see Figures 8.2 and 8.3.

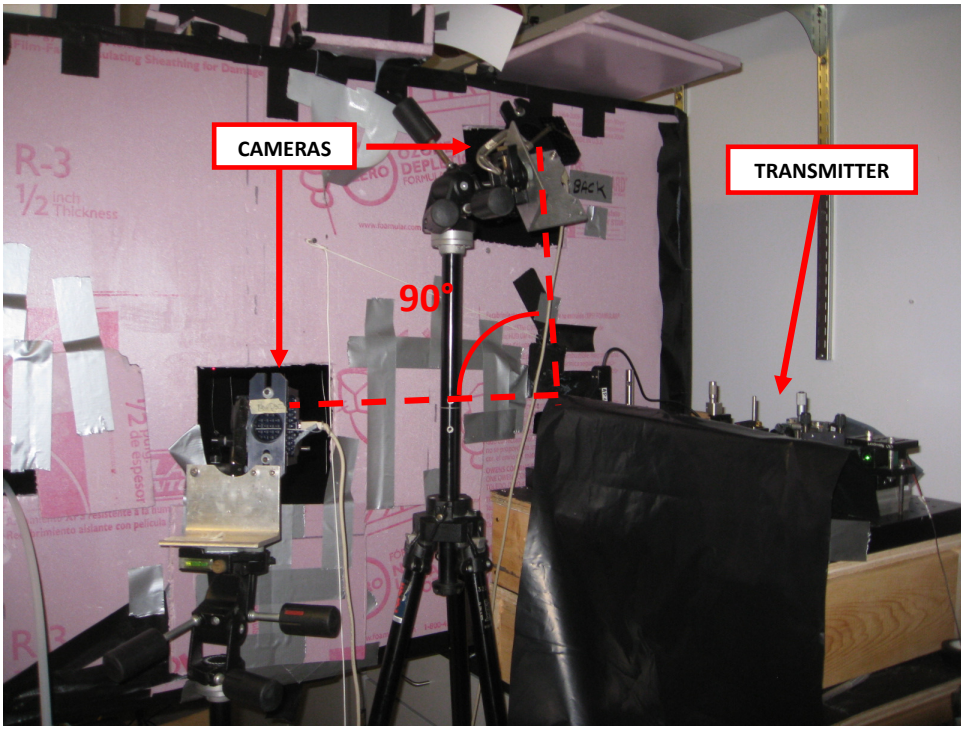

Figure 8.2: Picture of the back of the chamber shows the camera placements to obtain pictures at the two perpendicular scattering planes.

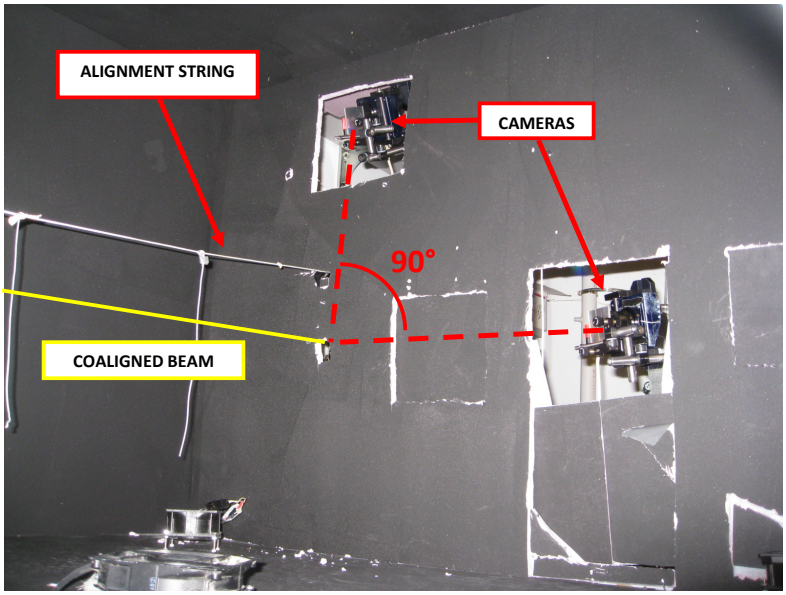

Figure 8.3: Picture taken from inside the chamber, showing the cameras relative to the beam with the alignment sting.

One micron PSL spheres are dispersed to measure the scattering with both cameras simultaneously. During these measurements the polarization is flipped 90 degrees to compare in each camera's result using the polarization ratios obtained. Sequential and simultaneous pictures are obtained, the corresponding polarization ratios are shown in Figure 8.4. The ratios shown are at the resolution of the pixels, they have not been down-sampled.

A calibration procedure is developed to form polarization ratios from cameras oriented at a 90° angles:

1. Verify that the cameras are lined up relative to the beam and are capturing the same wires in the alignment pictures, this ensures the range of angles collected by each imager are approximately equal.

2. Verify that the diffracted images land approximately in the same place on the CCD image in both cameras, near the middle of the CCD chip seems to give the best intensity measurements.

3. Collect molecular scattering pictures on both cameras with the same integration time

4. The perpendicular scattering intensity for each wavelength on each camera gives a numerical intensity conversion of the efficiency of each camera is at each wavelength.

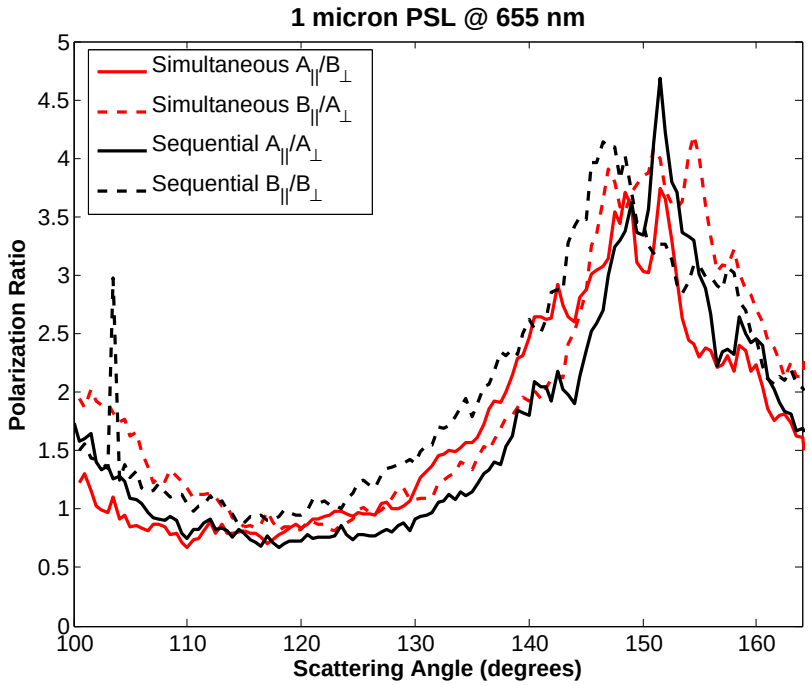

Figure 8.4: The measured polarization ratio when using perpendicular cameras is comparable when using one camera and taking simultaneous pictures.

The fact that the polarization ratios are all similar in height and shape means that the method of simultaneous pictures with the cameras mounted at 90 degrees is a viable method to obtain the polarization ratio quicker than taking sequential pictures.

The disadvantage of this is that if the exact experimental set-up can not be calibrated with molecular scattering pictures there is no way to calibrate the intensities in a rapidly changing environment. This picture must be taken every time because the intensity measured by the camera is a function of the distance that the beam is from the imager. This method will be useful in an environment that is rapidly changing, such as a turbulent fog, as long as the background molecular pictures can be taken.

The relative intensities at each wavelength in the two cameras can measure the polarization ratio simultaneously. Measurements reported are taken in a very non-turbulent environment, a controlled chamber with no air motion, where the aerosol environment could be considered the same in the sequential pictures. However, in a turbulent fog the method of simultaneous pictures will speed up the data acquisition and expand the applicability of this instrument. Figures 8.6 and 8.5 show a Solid Works drawing of the transmitter, beam expander and arms to hold the cameras at 90°. The cameras can be fixed to the transmitter and this instrument can be changed in angle of inclination to measure a larger volume.

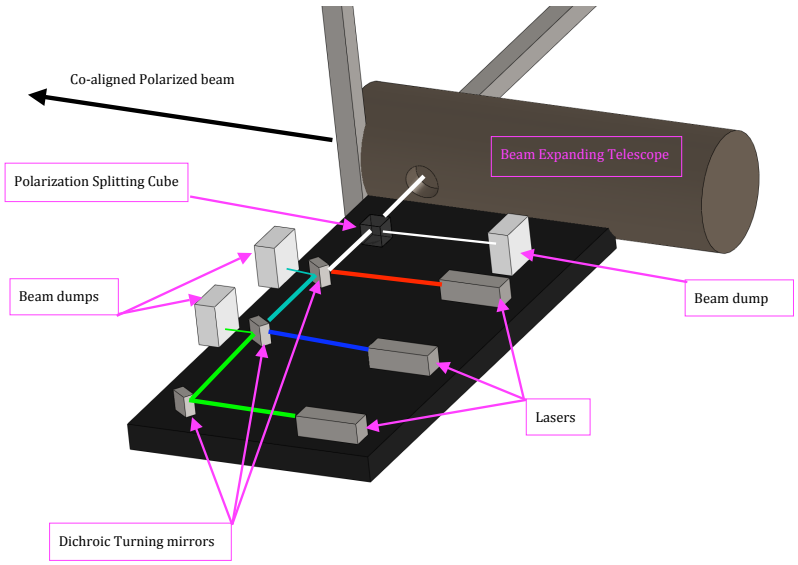

Figure 8.5: Schematic diagram of the transmitter sub-system, which includes using dichroic mirrors to co-align the beam and a beam expanding telescope.

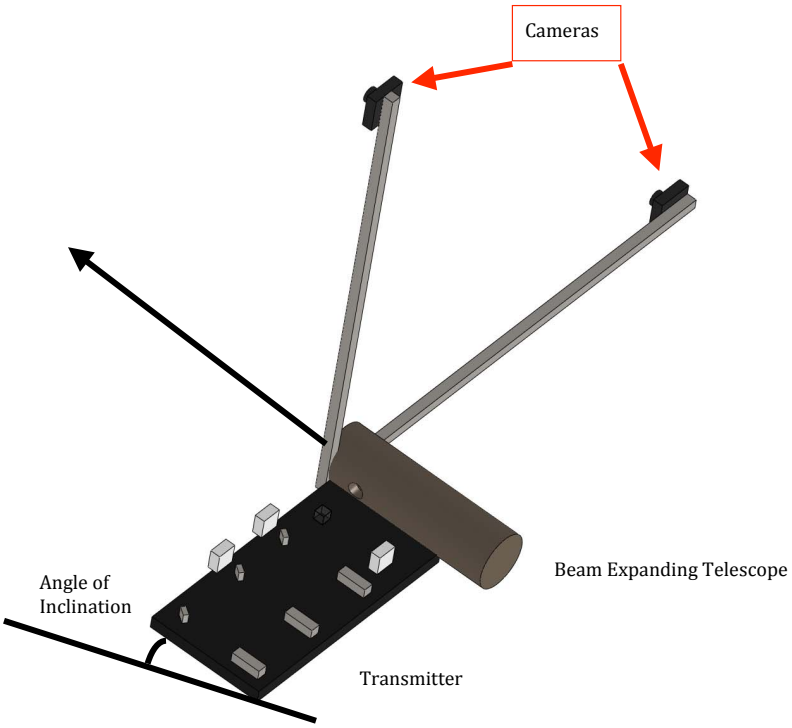

Figure 8.6: Diagram shows the co-aligned transmitter (see Figure 5.1) combined with cameras mounted at 90 degrees to image both polarization components at the same time. This setup can adjust the angle of elevation to obtain horizontal and vertical profiles in the lower troposphere.

8.2 Computational Data Analysis Improvements

Major computational limitations were found during this work. One way to relieve of these limitations is to build a parallel processing computer and break up the Continuous Genetic Algorithm processing. Figure 8.7 shows a diagram of the continuous genetic algorithm with the fitness value computation broken up between five processors. This approach could always be expanded to have more than five processors to improve the inversion time requirements. The computational inversion time could also be reduced by writing the algorithm in another computational language, such as C++.

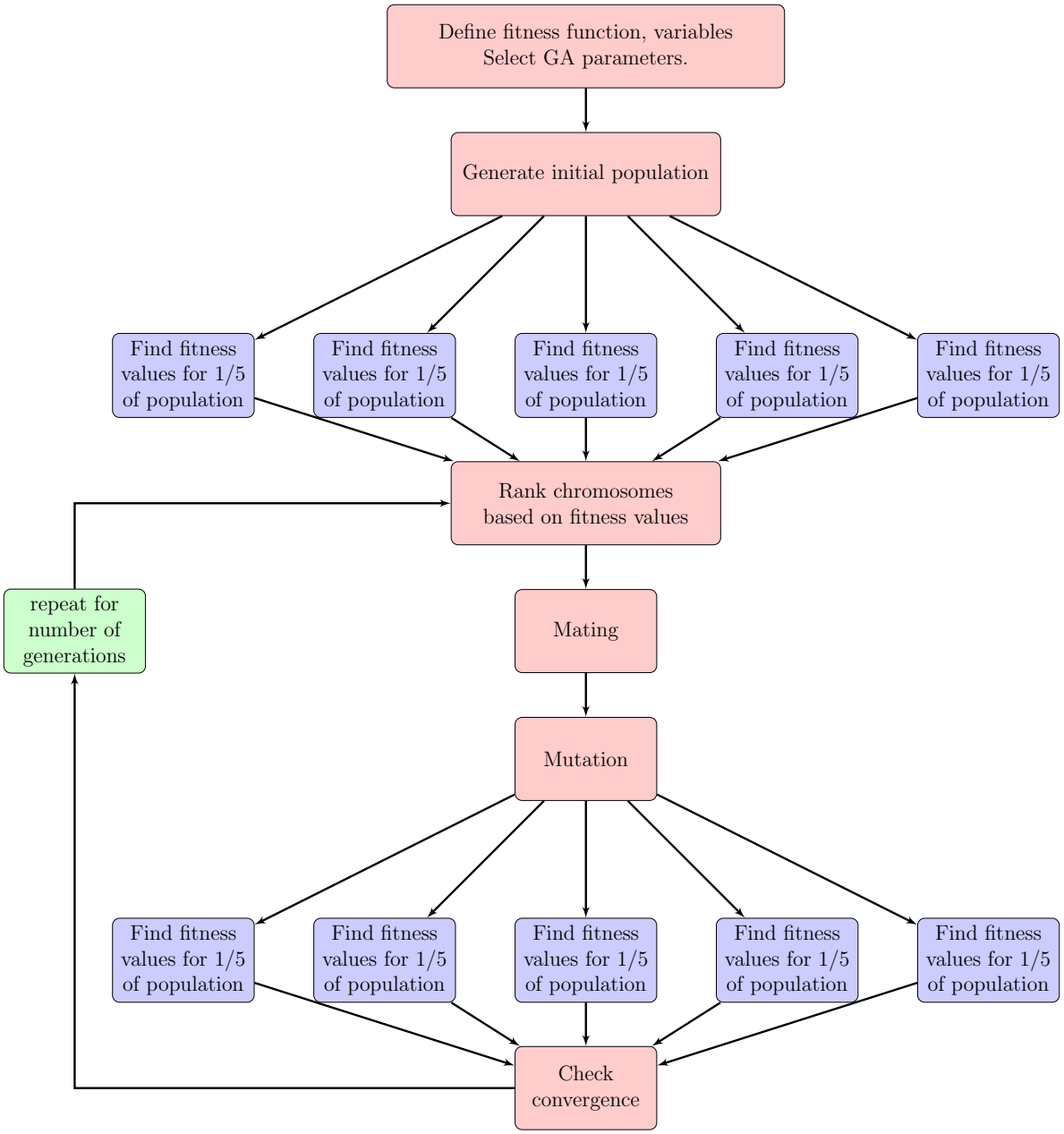

Figure 8.7: Diagram of breaking up the continuous genetic algorithm computation into parallel processing on 5 processors.

REFERENCES

[1] G.J. Jenkins J.T. Houghton and J.J Ephraums, editors. *Climate Change: The IPCC Scientific Assessment*, Cambridge, 1990. Cambridge University Press.

[2] P. Forster, V. Ramaswamy, P. Artaxo, T. Berntsen, R. Betts, D.W. Fahey, J. Haywood, J. Lean, D.C. Lowe, G. Myhre, J. Nganga, R. Prinn, G. Raga, M. Schulz, and R. Van Dorland. *Changes in Atmospheric Constituents and in Radiative Forcing. In: Climate Change 2007: The Physical Science Basis. Contribution of Working Group I to the Fourth Assessment Report of the Intergovernmental Panel on Climate Change*. Cambridge, United Kingdom and New York, NY, USA, 2007.

[3] W Johnson. Lidar applications in air-pollution research and control. *Journal of Air Pollution Control Association (JAPCA)*, 19:176–180, 1969.

[4] John H. Seinfield and Spyros N. Pandis. *Atmospheric Chemistry and Physics: From Air Pollution to Climate Change*. John Wiley & Sons,Inc, 1998.

[5] J. Levy. *New Findings Highlight the Significance of Aerosols in the Earth's Climate System*, spotlight feature articles edition, 2000. *Retrieved August 2 2010*`http://www.oar.noaa.gov/spotlite/archive/spot_aero.html`.

[6] S. Twomey. Pollution and the planetary albedo. *Atmospheric Environment*, 8:1251–1256, 1974.

[7] R. Pincus and M. Baker. Precipitation solar absorption, and albedo susceptibility in marine boundary layer clouds. *Nature*, 372:250–252, 1994.

[8] B. A. Abrecht. Aerosols, cloud microphysics, and fractional cloudiness. *Science*, 245:1227–1230, 1989.

[9] S.A. Ackerman and H. Chung. Radiative effects of airborne dust on regional energy budgets at the top of the atmosphere. *Journal of Applied Meterorology*, 31:223–233, 1992.

[10] James Haywood and Olivier Boucher. Estimates of the direct and indirect radiative forcing due to tropospheric aerosols: A review. *Reviews of Geophysics*, 38(4):513–543, 2000. copyright held by the American Geophysical Union.

[11] S. Twomey. The influence of pollution on the shortwave albedo of clouds. *Journal of the Atmospheric Sciences*, 34:1149–1152, 1977.

[12] John A. Reagan, Dale M. Byrne, and Benjamin M. Herman. Bistatic LIDAR: A tool for chacterizing atmospheric particles: Part i - the remote sensing problem. *IEEE Transactions on Geoscience and Remote Sensing*, GE-20(3):229–235, July 1982.

[13] Timothy D. Stevens. *Bistatic Lidar Measurements of Lower Tropospheric Aerosols*. PhD dissertation, Pennsylvania State University, Department of Electrical Engineering, May 1996.

[14] C. R. Philbrick and K. R. Mulik. Application of Raman lidar to air quality measurements. In G. W. Kamerman, U. N. Singh, C. H. Werner, & V. V. Molebny, editor, *Society of Photo-Optical Instrumentation Engineers (SPIE) Conference Series*, volume 4035 of *Society of Photo-Optical Instrumentation Engineers (SPIE) Conference Series*, pages 22–33, September 2000.

[15] Edward J. Novitsky. *Multistatic Lidar Profile Measurements of Lower Tropospheric Aerosol and Particulate Matter: Multiple Scattering Measurements using Multistatic Lidar*. PhD dissertation, Pennsylvania State University, Department of Electrical Engineering, May 2002.

[16] Graham Feingold. First measurements of the Twomey indirect effect using ground-based remote sensors. *Geophysical Research letters*, 30(6):20–1 – 20–4, 2003.

[17] K. Meki, K. Yamaguchi, X. Li amd Y. Saito, T.D. Jawahara, and A. Nomura. Range-resolved bistatic imaging lidar for the measurement of the lower atmosphere. *Optics Letters*, 21(17):1318–1320, 1996.

[18] R. M. Welch, M. G. Ravichandran, and S. K. Cox. Prediction of quasi-periodic oscillations in radiation fogs. part i: Comparison of simple similarity approaches. *Journal of the Atmospheric Sciences*, 43(7):633–651, 1986.

[19] Roland B. Stull. *An Introduction to Boundary Layer Meteorology*. Kluwer Academic Publishers, Dordecht, The Netherlands, 1988.

[20] Adolph S. Jursa, editor. *Handbook of Geophysics and the Space Enviroment*. Hanscom Airforce Base, MA., 1985.

[21] H. Gerber. Supersaturation and dropplet spectral evolution in fog. *Journal of Atmospheric Sciences*, 48(24):2569–2588, 1991.

[22] H. Gerber. Liquid water content of fogs and hazes from visible light scattering. *Journal of Climate and Applied Meteorology*, 23:1247–1252, 1984.

[23] H.E. Gerber. Microstructure of a radiation fog. *Journal of Atmospheric Sciences*, 38:454–458, 1980.

[24] Jin H. Park. *Multiple Scattering Measurements Using Mutistatic Lidar*. PhD dissertation, Pennsylvania State University, Department of Electrical Engineering, May 2008.

[25] Andrea M. Brown. *Multiwavelength Multistatic Optical Scattering For Aerosol Characterization*. PhD dissertation, Pennsylvania State University, Department of Electrical Engineering, August 2010.

[26] Raymond M. Measures. *Laser Remote Sensing: Fundamentals and Applications*. John Wiley and Sons,Inc, reprint 1992 Kreiger Publishing Company Malabar, Florida, 1984.

[27] Craig F. Bohren and Donald R. Huffman. *Absorption and Scattering of Light by Small Particles*. WILEY-VCH Verlag GmbH & Co. KGaA, Weinheim, 2004.

[28] H. C. van de Hulst. *Light Scattering by Small Particles.* Courier Dover Publications, 1981.

[29] Michael I. Mischenko, Larry D. Travis, and Andrew A. Lacis. *Multiple Scattering of Light by Particles: Radiative Transfer and Coherent Backscattering.* Cambridge University Press, New York, 2006.

[30] von Gustav Mie. Beiträge zur Optik rrüber Medien, speziell kolloidaler Metallösungen. *Annalen Der Physik*, 25(3):377–445, 1908.

[31] Lord Rayleigh. On the light from the sky, its polarization and colour. *Philosophy Magazine*, 41:107–120, 274–279, 1871. (reprinted in *Scientific Papers by Lord Rayleigh*, Vol. I: 1869-1881, No.8, Dover, New York, 1964).

[32] M. Born and E. Wolf. *Principle of Optics.* Pergamon Press, New York, 1980.

[33] Andrea M. Wyant, David M. Brown, Perry S. Edwards, and C. Russell Philbrick. Multi-wavelength, multi-angular lidar for aerosol characterization. In Gary W. Kamerman Monte D. Turner, editor, *Laser Radar Technology and Applications XIV*, pages 1–8. Proc. of SPIE Vol. 7323, 73230R, 2009.

[34] Philip R. Bevington and D. Keith Robinson. *Data Reduction and Error Analysis for the Physical Sciences.* McGraw-Hill, Inc. New York, NY, 2003.

[35] R. Jaenicke. Tropospheric aerosols. In P.V. Hobbs, editor, *Aerosol-Cloud-Climate Interactions.* Academic Press, 1993.

[36] Guillaume A. D'Almeida, Peter Koepke, and Eric P. Shettle. *Atmospheric Aerosols: Global Climatology and Radiative Characteristics (Studies in Geophysical Optics and Remote Sensing).* A. Deepak Publishing, January 1991.

[37] F. Palmer, B. Kopcewicz, C. Nagamoto, R. Schnell, P. Sheridan, C. Zhu, and J. Harris. Aerosol particles in the kuwait oil fire plumes: Their morphology, size distribution, chemical composition, transport and potential effect on climate. *Journal of Geophysical Research*, 97:15867–15992, 1992.

[38] John A. Reagan, Dale M. Byrne, and Benjamin M. Herman. Bistatic LIDAR: A tool for chacterizing atmospheric particles: Part ii - the inversion problem. *IEEE Transactions on Geoscience and Remote Sensing*, GE-20(3):236–243, July 1982.

[39] N. T. O'Neill and J. R. Miller. Constrained linear inversion of optical scattering data for particle size spectra: an approach to angular optimization. *Applied Optics*, 21(7):1231–1235, 1982.

[40] Igor Veselovskii, Alexei Kolgotin, Vadim Graiznov, Detlef Mü ller, Ulla Wandinger, and David N. Whiteman. Inversion with regularization for the retrieval of tropospheric aerosol parameters from multiwavelength lidar sounding. *Applied Optics*, 41(18):3685–3699, 2002.

[41] Grzegorz Miecznik, Raner Illing, Shelley Petroy, and Irina N. Sokolik. Sensitivity metric approach for retrieval of aerosol properties from multiangular and multispectral polarized radiances. *Applied Optics*, 44(20):4186–4204, 2005.

[42] Randy L. Haupt and Sue Ellen Hupt. *Practical Genetic Algorithms*. John Wiley & Sons, Inc. Hoboken, New Jersey, 2004.

[43] Xiaoyan Ma, Jun Q Lu, R. Scott Brock, Kenneth M. Jacobs, Ping Yang, and Xin-Hua Hu. Determination of complex refractive index of polystyrene microspheres from 370 to 1610 nm. *Phys. Med. Biol.*, 48:4165–4172, 2003.

[44] L. A. Matheson and J. L. Sanderson. Optical and electrical properties of polystyrene. In R. H. Boundy and R.F. Boyer, editors, *Styrene: It's Polymers, Copolymers, and Derivatives*. Reinhold: New York, 1952.

[45] I. D. Nikolov and C. D. Ivanov. Optical plastic refractive measurements in the visible and the near-infrared regions. *Applied Optics*, 39:2067–2070, 2000.

[46] E. Thrush, D. M. Brown, N. Salciccioli, J. Gomes, A. Brown, K. Siegrist, M.E. Thomas, N.T. Boggs, and C. C. Carter. Optical properties and cross-sections of biological aerosols. In Augustus W. Fountain III and Patrick J. Gardner, editors, *Chemical, Biological, Radiological, Nuclear, and Explosives (CBRNE) Sensing XI*, pages 1–9. Proc. of SPIE Vol. 7665, 766507, 2010.

[47] Michael I. Mishchenko and Larry D. Travis. Capabilities and limitations of a current fortran implementation of the T-matrix method for randomly oriented, rotationally symmetric scatterers. *J. Quant. Spectrosc. Radiat. Transfer*, 60(3):309–324, 1998.

[48] Image sensors world. Website, accessed on February 12, 2011. `http://image-sensors-world.blogspot.com/2010/05/sony-shrinks-ccd-pixel-to-143um.html`.

[49] Monita cctv-faq's. Website, accessed on February 12, 2011. `http://www.monitacctv.com/faq.php`.

APPENDICES

Appendix A

Selection of Simulated Noise

In most exercises to simulate measured quantities, noise is added to the measured quantity to evaluate the performance of analysis tools. The relative intensities are measured and used to form the polarization ratio on a pixel -by-pixel basis. Therefore, an attempt was made to add noise directly to the calculated phase functions. The calculated phase functions are related to the measured intensities, and used to form the calculated theoretical polarization ratio.

White Gaussian noise is added to the calculated phase functions in the following way:

1. First, calculate the parallel (horizontal) and perpendicular (vertical) phase functions;
2. Add noise to the phase functions;
3. Calculate the polarization ratio;
4. Sample ratio using a 7-point weighted-average-down-sampling routine, as described in Section 6.3.

Noise is added at a SNR level of 20 to the phase functions. Figure A.1 (a), (c) and (e) show the addition of noise to the horizontal (parallel) phase function for each of the three wavelengths, 405 nm, 532 nm and 655 nm. Small black lines indicate the calculated phase function, before noise was added. The plots on the right hand side (b) (d) and (f) show the addition of noise to the vertical (perpendicular) phase functions.

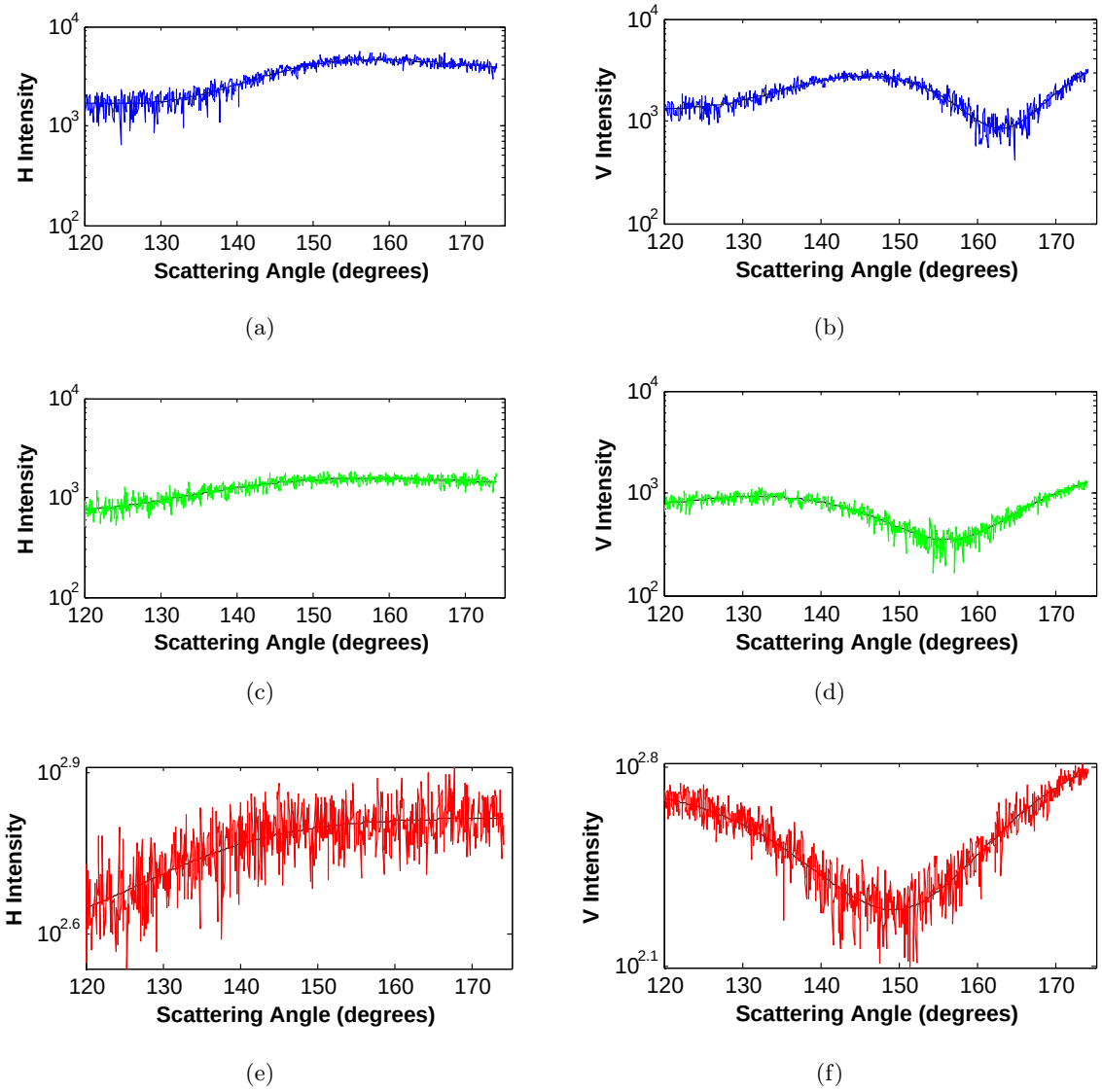

Figure A.1: The addition of white Gaussian noise at a SNR of 20 to the phase functions.

Figure A.2 (a), (c) and (e) show the polarization ratios formed from the phase functions shown in Figure A.1 for all three wavelengths. In subfigures (b), (d) and (f) the simulated ratios are downsampled using the interpolation-weighted averageing method. The calculated ratios with no noise added are shown by the thin black lines.

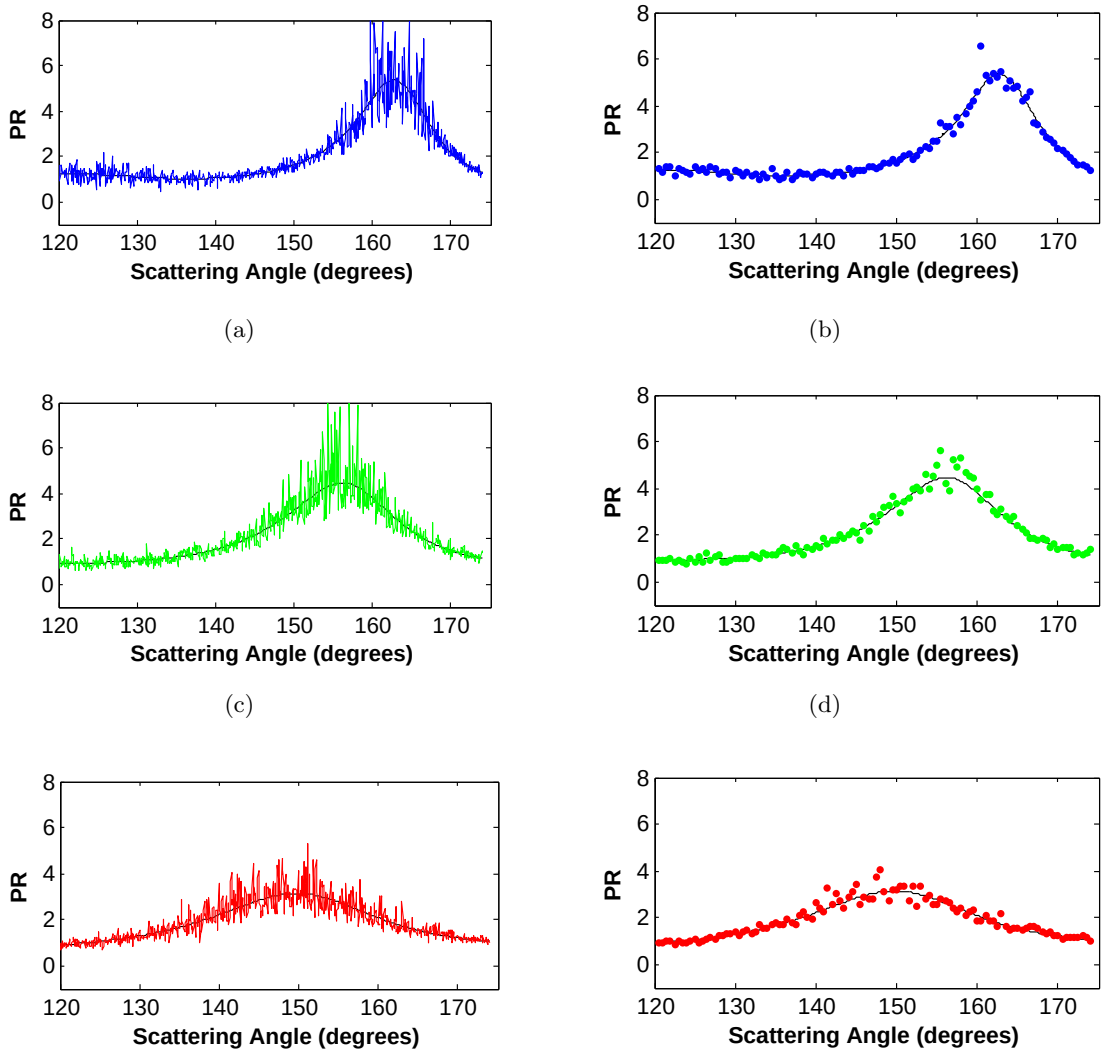

Figure A.2: Polarization ratios formed from the phase functions with a SNR of 20, plotted with the downsampled ratios used in the analysis process.

From the ratios in Figure A.2, an uneven amount of noise is added to the polarization ratio. There appears to be more noise in the peaks of the polarization ratios than in the tails. Decreasing the snr value was also tested and the unevenness of the noise in the polarization ratio was amplified. In the experimental measurements there appears to be a consistent amount of noise throughout the polarization ratio, therefore noise is added directly to the polarization ratio.

Appendix B

Additional Experimental Complications

Experimental complications and insight are added here to provide future researches additional insight. Many of the experimental improvements mentioned in Chapter 8 would correct these problems. For this instrument to be a more efficient and reliable way of characterizing aerosols several equipment selections and modifications can be made.

B.1 Mounting of Diffraction Grating and Imaging Lens

The diffraction grating and imager lens are two elements of the instrument that change from application to application. The diffraction grating is removed after experiments to prevent breaking or scratching. Once the grating is replaced it needs to be retightened, so the angle and relationship to the imager is changed. When the instrument is moved from location to location, the mounting of the grating is removed from the camera mount completely, leading to an even larger variation in placement of the diffraction grating. Additionally, when the instrument is moved, the relation between the scattered beam and the imager changes. The iris and focus knob on the imager lens are changed to maximize the camera efficiency at the largest scattering angles. This leads to slightly different efficiencies in the imager lens between experiments, which needs to be calibrated before the relative intensity measurements can be exploited.

B.1.1 Measuring Molecular Intensity

Experimentally measured scattered intensities from a volume of air clear of large aerosols are shown in Figure B.1, which should represent pure dipole scattering.

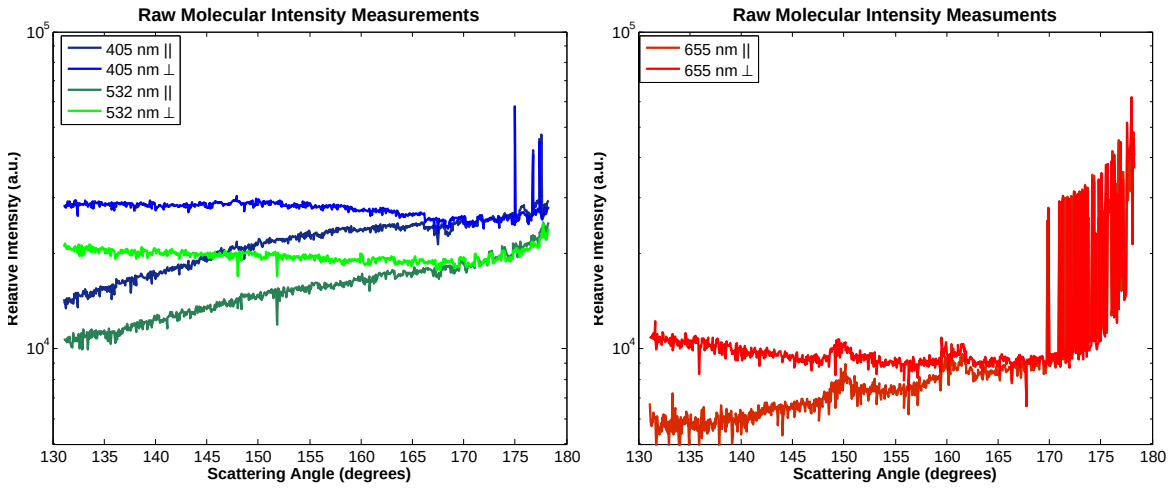

(a) (b)

Figure B.1: The raw intensity measurements for molecular scattering. The red is shown separately in (b) because the stray intensity measurements at the higher angles would cover up the intensity of the blue and green in (a).

A discrepancy in the measured quantities and the calculated phase functions can be seen in the perpendicular scattering intensity. Theoretically this should be a horizontal line with one intensity for all scattering angles, as for a dipole (see Figure 2.4). In fact, the tendency of the beam to decrease in intensity (see Table B.1) at the end of the path would suggest extinction along the path. However, there should not be extinction due to molecules over the 8 foot path that this measurement was taken. Extinction due to molecules over this path was measured to be less than 1 %.

Table B.1: The difference in intensity of the perpendicular measured intensity in Figure B.1.

Wavelength	**Angle (degrees)**	**Intensity (a.u.)**	**Percent Difference**
405 nm	135	2.7571×10^4	13.26 %
	165	2.4142×10^4	
532 nm	135	1.9334×10^4	8.711 %
	165	1.7720×10^4	
655 nm	135	9.3708×10^3	1.90 %
	165	9.1943×10^3	

B.1.2 Selection of the Polarization Ratio

The ratio formed from the molecular intensity measurements in Figure B.1 is shown in Figure B.2. The $cos^2(\theta)$ line is shown in this figure to represent the theoretical molecular polarization ratio from the calculated phase functions in Figure 2.4. The polarization ratio shows very good agreement with the theoretical polarization ratio in the measurement range. This means that the experimental factors that created the shape discrepancies between the measured intensities in Figure B.1 and the predicted intensity shape are canceled out in this ratio process.

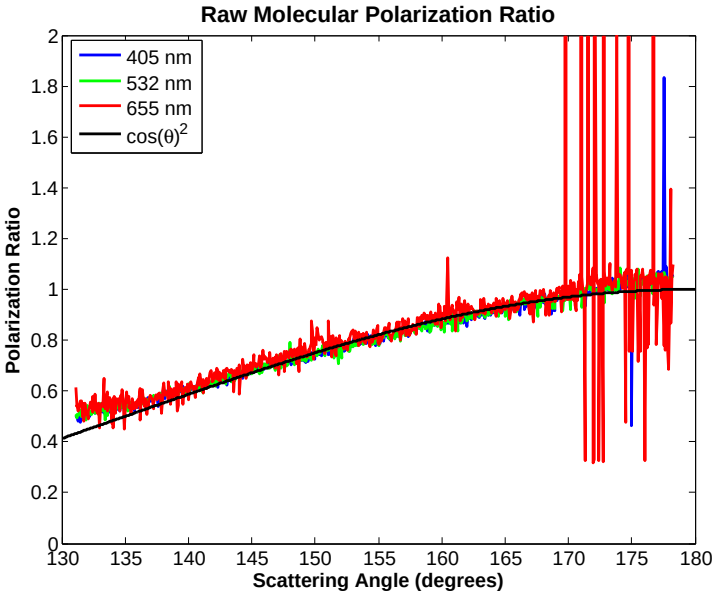

Figure B.2: The polarization ratio for all three wavelengths shows good agreements with the predicted molecular polarization ratio, represented by the $cos^2(\theta)$.

The explanation for the discrepancies in the molecular measured intensities and the theoretical phase functions is optical efficiency of the camera lens and the diffraction grating. The scattering is striking the diffraction grating and camera lens at very high angles, so some intensity must be lost to reflection. Again, this is something that could be corrected for through calibration, if the imager and diffraction grating were in fixed orientation and the lens knobs were precisely controlled.

Experimental complications have effects that can not be overcome computationally overcome untill there are major changes in the imager and diffraction gratings used. The reason to use the polarization ratio as the primary measurement to find all aerosol characteristics is affirmed.

B.2 Error Due to Interlined-Interlaced CCD Imager

The CCD chip in this camera is not a full framed imager, there are spaces between the pixels on the chip. The scattered intensity measured should have a smooth curvature across the field of view of the camera based on Mie calculations. This smoothness in intensity is not always found due to the spaces between pixels on the imager chip. The CCD imager chip used in the Meade imager is the Sony ICX677 depicted in Figure B.3. One row of the grid created by the pixels and spaces is show in Figure B.4.

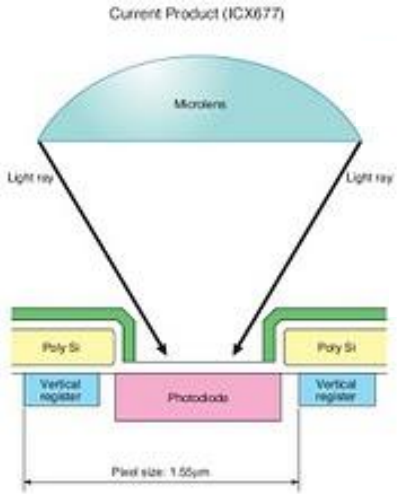

Figure B.3: The ICX677 is the same series as the ICX429 used in the Meade imagers used in this instrument.[48]

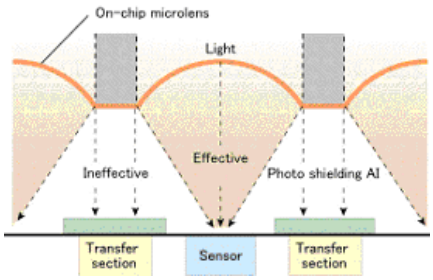

Figure B.4: This shows the traditional structure of a CCD imager, where the pixels and spaces are clearly visible. Some of the scattered light MUST be lost to the spaces.[49]

The chip consists of rows of pixels separated by a small space for the electronics, therefore it is classified as an interline interlace traditional CCD imager chip. The manufacturer tries to minimize the effect of this by added micro lenses on top of the pixels, see Figure B.3. These Meade imagers are typically used by amateur astronomers for telescope images. Experimental difficulties are present in this application because the intensity measurement needs to be taken at every angle. If the beam is aligned horizontally across the CCD imager, then the captured beam always includes the same number of pixels and adjoining spaces; however this is difficult to obtain with one beam and impossible when the diffraction grating is incorporated due to the curvature of the diffracted beams. Thus parts of the imaged beam may contain more pixels or more spaces in the total intensity scattered at a particular angle. This translates to an unnatural structure in the captured intensity of the beam (see Figure B.5) when a narrow image is formed on the chip. This structure can be attributed to the space between the pixels

and the curvature of the beam created by the diffraction grating.

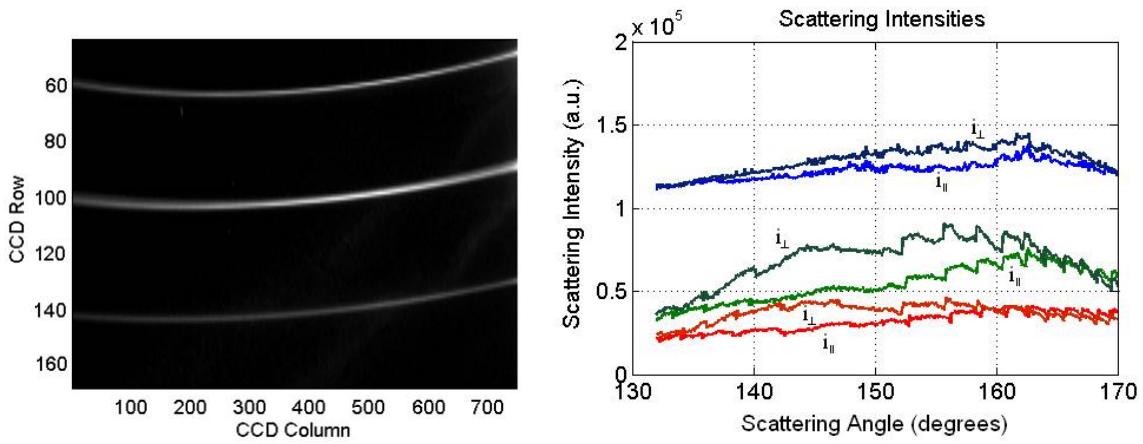

(a) CCD image

(b) Raw Scattered Intensities

Figure B.5: The curvature of the beams created by the location of the grating and the camera lens (these images are taken from Brown's dissertation.[25])

A Matlab routine was created to simulate this problem. A Gaussian beam profile is assumed and it is imaged on a background grid of pixels with "dead space" between them. The beam profile is a normalized Gaussian profile, so that the total intensity under the curve is one. For example, if only 90 percent of the intensity is captured it would be reported as 0.9. The background grid of pixels and spaces is shifted from a starting position between -10 and -7. As the grid starts the intensity measured by each simulated pixel bin captures a different intensity based on the number of pixel bins and spaces present in the beam profile. Shifting the starting position simulates the way a Gaussian beam profile would curve over the image. In Figure B.5 the beam becomes more severely curved on the right side of the image and the structure created is similar to that in Figures B.6 and B.7. By comparing the pattern of intensity captured in Figures B.6 and B.7 the stagard intensity has less variation between the minimum and maximum intensity capture when more pixels capture the beam intensity.

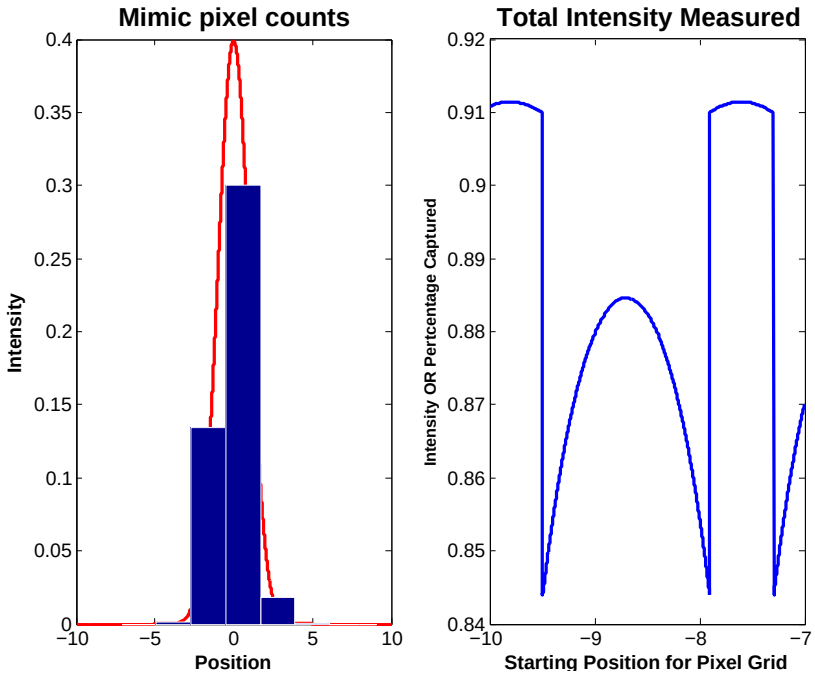

Figure B.6: The intensity captured by the pixels in a Gaussian beam.(pixsize = 2.0 and pixspace = 0.2, Gaussian beam: mean = 0, standard deviation = 1).

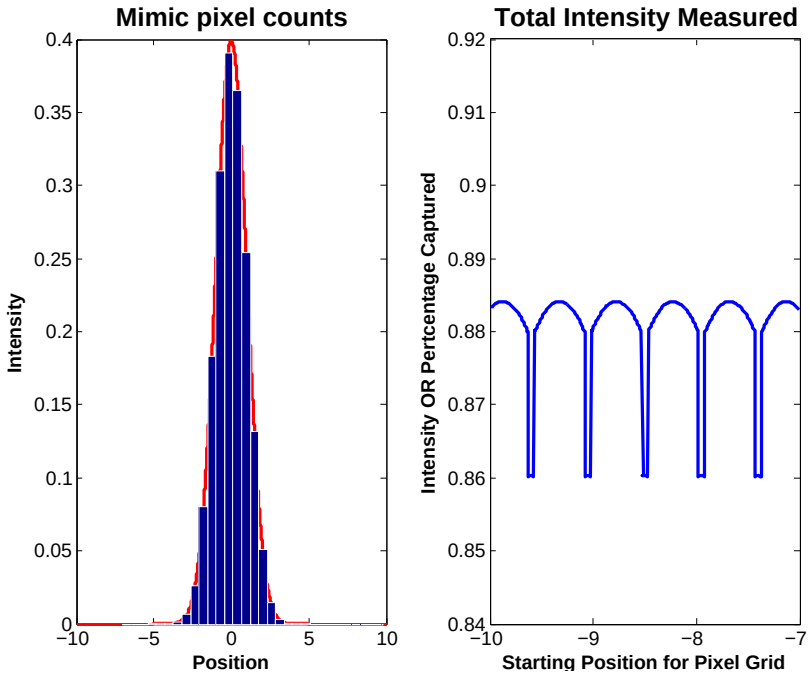

Figure B.7: Simulation using more pixels smooths the intensity captured by the imager (pixsize = 0.5 and pixspace = 0.05, Gaussian beam: mean = 0, standard deviation = 1).

If the beam is expanded, then the structure present in the intensity measurements is lessened. Suppose the beam is expanded; then the maximum intensity decreases and the beam spreads out. The highest intensity would be captured less often, as shown in Figure B.8, so the unnatural structure in the data is less, but less intensity is captured over all. If the beam is expanded and more pixels incorporated in the beam the CCD would measure greater "valleys" of lower intensity and more structure. This means that in an environment where the beam is close to the imager (i.e. inside a chamber) it is not advantageous to expand the beam, but in an environment where the beam is further away expanding the beam can be beneficial (i.e. outside), this is simulated in Figure B.9.

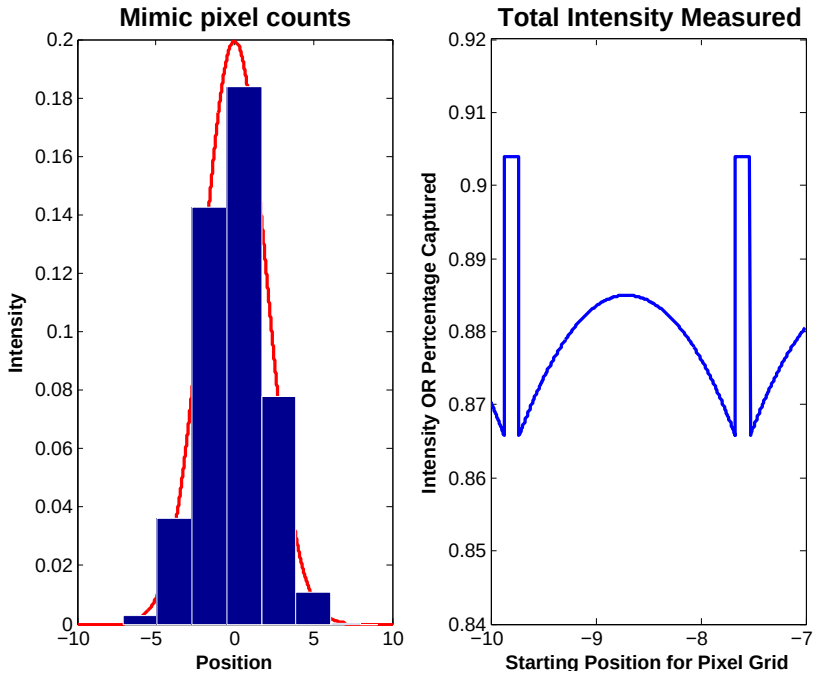

Figure B.8: Simulated intensity captured by the pixels in a Gaussian beam (pixsize = 2.0 and pixspace=0.2, Gaussian beam: mean = 0, standard deviation = 2).

There is a limitation to this expansion based on the diffraction grating. The diffraction grating spatial spreads the beams across the imager, but there is a limited amount of space between the diffracted beams before they will overlap in the image. An example of the limited amount of space on the imager is indicated in Figures B.10 and B.11.

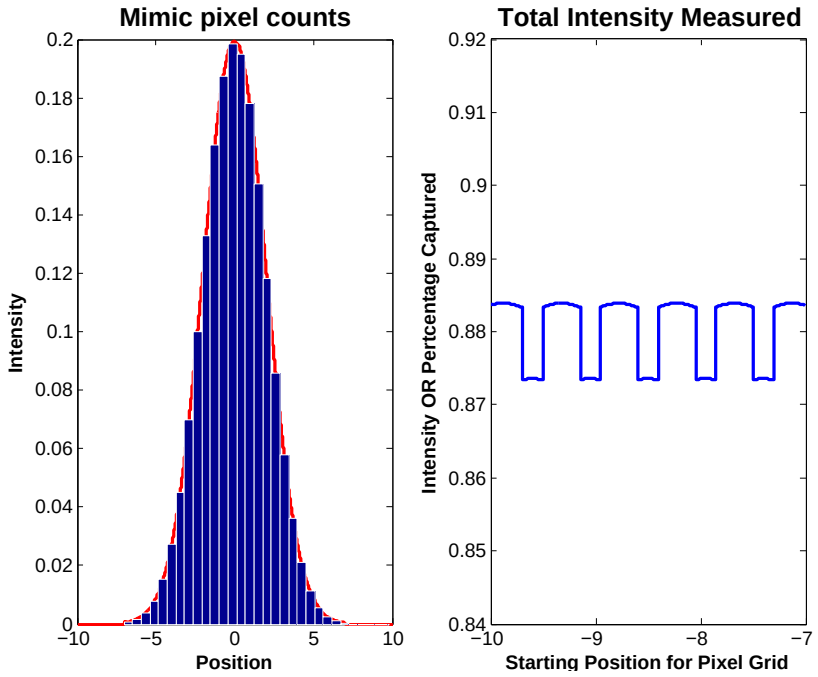

Figure B.9: This simulates using more pixels to capture the beam (pixsize = 0.5 and pixspace=0.05, Gaussian beam: mean = 0, standard deviation = 2)

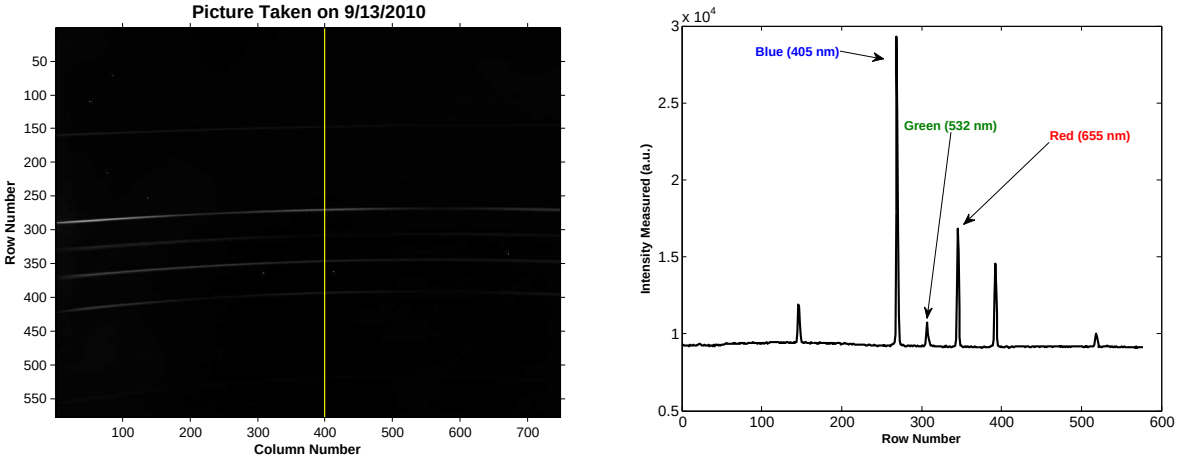

(a) Picture

(b) Profile of Column 400

Figure B.10: The spacing along the indicated contours show the location of the diffracted beams (NCSU chamber on 9/13/2010).

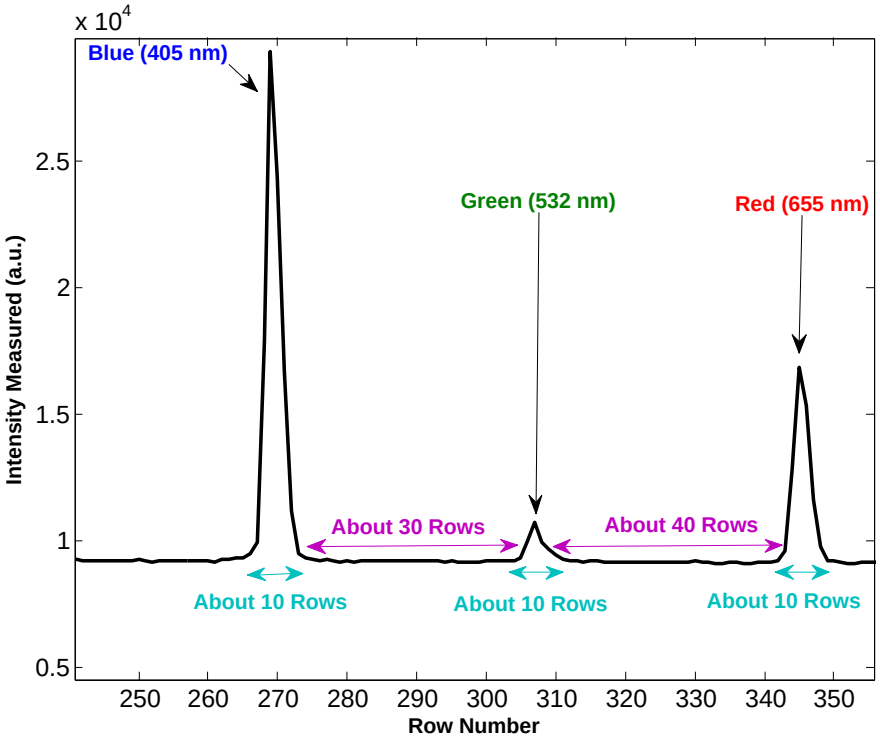

Figure B.11: Zoomed in on diffracted beam section of Figure B.10b shows the limited amount of space between each of the diffracted beams.

The small space between the diffracted beams leaves little room for expansion. For instance, if the beam were expanded by 3 then 10 rows of intensity would be added on each side of each beam. This would be about the limit of beam expansion that could be used before the diffracted beams ran together because of pixel bleeding. This makes the expansion a way to decrease the unnatural structure levels due to the interlace interline nature of the CCD imager for the images taken; however this is limited by the width of the beam as it cross the field of view of the imager and the amount of space between the diffracted beams.